

Iron Dominated Electromagnets

Design, Fabrication, Assembly and Measurements

Jack Tanabe

January 6, 2005

Stanford Linear Accelerator Center, Stanford Synchrotron Radiation Laboratory, Stanford, CA 94025

Work supported in part by Department of Energy contract DE-AC02-76SF00515

Dedicated with Love to Sumi, for her support and devotion. For our beautiful grand-daughter, Sarah.

Abstract

Medium energy electron synchrotrons (see page 15) used for the production of high energy photons from synchrotron radiation is an accelerator growth industry. Many of these accelerators have been built or are under construction to satisfy the needs of synchrotron light users throughout the world. Because of the long beam lifetimes required for these synchrotrons, these medium energy accelerators require the highest quality magnets of various types. Other accelerators, for instance low and medium energy boosters for high energy physics machines and electron/positron colliders, require the same types of magnets.

Because of these needs, magnet design lectures, originally organized by Dr. Klaus Halbach and later continued by Dr. Ross Schlueter and Jack Tanabe, were organized and presented periodically at biennial classes organized under the auspices of the US Particle Accelerator School (USPAS). These classes were divided among areas of magnet design from fundamental theoretical considerations, the design approaches and algorithms for permanent magnet wigglers and undulators and the design and engineering of conventional accelerator magnets. The conventional magnet lectures were later expanded for the internal training of magnet designers at LLNL at the request of Lou Bertolini. Because of the broad nature of magnet design, Dr. S. Y. Lee, the former Director of the Particle Accelerator School, saw the need for a specialized course covering the various aspects of the design, engineering and fabrication of conventional magnets. This section of the class was isolated and augmented using the LLNL developed material resulting in the class on conventional magnet design. Conventional magnets are defined (for the purposes of this publication) as magnets whose field shape is dominated by the shape of the iron magnet yoke and are excited by coils, usually wound from solid or hollow water-cooled copper or aluminum conductors.

Dr. S. Y. Lee and Dr. Helmut Wiedemann, past and current Directors of USPAS, encouraged the author to write a text for the purpose of consolidating the lecture notes used in the USPAS course. This publication collects the lecture notes, written for the first course in the USPAS conventional magnet design course and evolved over subsequent presentations of this same course, and organizes the material roughly divided among two parts. One part is theoretical and computational and attempts to provide a foundation for later chapters which exploit the expressions and algorithms for the engineering and design calculations required to specify magnet conceptual designs. A chapter is devoted to the description and use of one of many magnet codes used to characterize the two dimensional field resulting from various magnet cross-sections. A chapter is included which exploits the two-dimensional theory and applies the mathematics to techniques and systems for magnet measurement. The second part of this publication ranges to practical issues associated with the fabrication of components, assembly, installation and alignment of magnets. This section also includes fabrication practices which respond to personnel and equipment protection needs.

Required design calculations are supplemented by examples and problems. A CD is included with tools provided to simplify the computation of some of the more tedious relationships. This CD also includes useful photographs and pictures describing the high volume production of typical magnet types, which if included in the publication will add too many pages and increase the cost of publication.

Styles among those facing similar problems will result in a wide variation of individual magnet designs. Designs and technologies will evolve and improve. This publication provides a snapshot of the present technology and presents as examples the magnet designs developed in response to the needs of several projects, the Advanced Light Source at LBNL, PEP-II Low Energy Ring and SPEAR3 synchrotron light source at SLAC and the Australian Light Source, currently under construction in Melbourne. In each example, the reasons for fabrication design decisions are itemized and rationalized as much as is reasonable. The examples presented in this publication are provided as starting points which can be used as a design basis for magnets required for future projects. It is hoped that the listing of some design choices and the motivation for these choices will be useful. It is the intention of the author to publish a document collecting and archiving the tools and techniques learned from the past masters in the craft and to provide a useful reference for future magnet designers.

Acknowledgements

This work would not have been possible without the creativity, guidance and patience of Dr. Klaus Halbach. Klaus mentored, taught and guided the efforts of many individuals at Lawrence Berkeley National Laboratory (LBNL) as well as making major contributions to numerous fields including the field of synchrotron light. His generosity and wisdom in supplying hints rather than answers made it possible for the author of this work to own knowledge rather than merely learn it.

Two examples of Klaus' creative work among a much broader spectrum are relevant to the field of particle accelerators. His development of permanent magnet circular arrays made it possible to design and install compact permanent magnet quadrupoles in linac drift tubes as well as multipole magnet arrays for circular storage rings. His work on the use of permanent magnets in longitudinal arrays has resulted in the proliferation of numerous wigglers and undulators at electron synchrotron light facilities throughout the world. Indeed, this means of exploiting electrons to produce high energy and high intensity synchrotron light has stimulated the construction of numerous electron synchrotrons throughout the world. In addition to contributions in the area of permanent magnets, Klaus formulated and documented relationships invaluable to the design and fabrication of electromagnets. The accelerator community misses his presence and remains in his debt.

I am grateful for the opportunities to participate in important accelerator projects at LBNL. Alan Jackson, Ron Yourd and Dr. Alan Paterson trusted me to lead the magnet design, fabrication and measurement program for the Advanced Light Source (ALS). Dr. Ross Schlueter and Dr. Steve Marks encouraged an academic approach and rigor in my written work. Dr. Michael I. Green at LBNL and Dr. Zack Wolf at SLAC helped me become familiar with the intricacies of magnetic measurements. John Meneghetti and Tom Henderson taught me about capabilities and limitations of machine shops and fabrication techniques and prevented the design of unbuildable hardware. Someone once said, "the toughest boss you have is the one who works for you". In that regard, I am indebted to many engineers and designers whose creativity reflected any success I have achieved. John Milburn's successful ALS designs have been mirrored at Pohang in Korea and scaled for numerous other projects. Collaborative design work with James Osborn, Johanna Swann and Dr. Matt Kendall resulted in the design and fabrication of important final focus magnets for PEPII. Conversations and notes from contacts with Jack Jagger at FNAL and Hank Hsieh when he was at BNL were important in the development of specifications for the manufacture of large numbers of magnets. Frequently, during the course of designing magnets, one comes across especially difficult problems. This was the case for the design of rapidly cycling correctors magnets for feedback of the beam orbits for SPEAR3. I am indebted to Glen Lambertson of LBNL for his help in simplifying my understanding of transient fields providing insight into eddy current effects on magnetic fields.

Finally, the author has gained enormously from contacts with scientists

and engineers, especially at the Stanford Synchrotron Radiation Laboratory (SSRL), for their patience in sharing knowledge of the physics of accelerators. Dr. Tom Elioff and Richard Boyce were instrumental in my participation in SLAC projects providing an opportunity to contribute to the design of magnets for PEPII and SPEAR3. It was a pleasure working with Nanyang Li in collaborations with IHEP in China during the manufacture of the PEPII and SPEAR3 magnets. During trips to China, contacts with Mrs. Rui Hou of IHEP were especially profitable and memorable. Dr. Max Cornacchia's and Dr. Hermann Winnick's enthusiasm for physics was infectious. The generosity of Dr. Jeff Corbett and Dr. Bob Hettel is especially appreciated. Their patient and generous explanations provided new insight into the physics of accelerators and greatly expanded my understanding and appreciation of the performance specifications that drive magnet design. Jim Sebek helped me through difficult mathematics and helped minimize my frustration working with difficult computer codes. I was also fortunate in sharing an office during the last months of Dr. Moohyun Yoon's sabbatical from the Pohang Light Source in Korea while he spent a year participating in the SPEAR3 commissioning. He made it possible to understand the fundamental physics which are the genesis of the simple differential equations whose solutions form the basis for magnet theory. In addition, Dr. Yoon, Dr. S. Y. Lee at the University of Indiana and Dr. Helmut Wiedemann at SLAC generously consented to provide their time and knowledge to edit early versions of this work. Their suggestions and recommendations have been incorporated into the final version of this text.

Undoubtedly, many more colleagues and friends not named in this acknowledgement have influenced me and have contributed in a real way to this text. A work such as this is indeed built on the shoulders of others.

Contents

1 Basic Concepts	15
1.1 Introduction	15
1.2 Magnet Types	16
1.3 Pictures	16
1.4 Conventions	20
1.5 The Field from a Line Current (Biot-Savart law)	20
1.6 Magnetic Force on a Line Current	21
1.6.1 MKS Units	21
1.6.2 Force Directions	22
1.6.3 Dipole Magnet	22
1.6.4 Quadrupole Magnet	22
1.6.5 Sextupole Magnet	23
1.6.6 Corrector Magnets	24
1.6.7 Specialized Magnets	25
1.6.8 More Polarity	28
1.6.9 Alternate Polarity Convention	29
1.7 Chapter Closure	29
1.8 Problems	31
2 Theory	33
2.1 Introduction	33
2.2 Maxwell's Magnet Equations	33
2.2.1 Continuity	33
2.2.2 Units	34
2.3 The Function of a Complex Variable	34
2.4 The Two-Dimensional Fields	35
2.4.1 Fields from the Two-Dimensional Function of a Complex Variable	36
2.5 Two Dimensional Fields in a Vacuum	36
2.5.1 Multipoles	36
2.5.2 Laplace's Equation	37
2.5.3 Solutions to Laplace's Equation	37
2.6 Two-Dimensional Vector and Scalar Potentials	38

2.6.1	Magnetic Fields from the Two-Dimensional Potentials	38
2.7	A Particular Function of the Complex Variable, $F = C_n z^n$	40
2.7.1	Ideal Two-Dimensional Multipole Magnets	40
2.7.2	Two-Dimensional Flux Lines and Poles	40
2.7.3	Pole Contours	43
2.7.4	Complex Extrapolation	45
2.8	Magnetic Fields Using the Function of the Complex Variable	46
2.8.1	$n=1$, the Dipole Magnet	46
2.8.2	$n=2$, the Quadrupole Magnet	47
2.8.3	$n=3$, the Sextupole Magnet	47
2.9	Multipole Errors	48
2.9.1	The Error Spectrum	48
2.9.2	“Allowed” or Systematic Multipole Errors	49
2.9.3	Multipole Field Errors	51
2.10	Simple Conformal Maps	51
2.10.1	Mapping Functions	52
2.10.2	Quadrupole to Dipole Map	52
2.10.3	Dipole to Quadrupole Map	52
2.10.4	Sextupole to Dipole Map	53
2.10.5	Dipole to Sextupole Map	53
2.10.6	Gradient Magnet to Dipole Map	54
2.10.7	Dipole to Gradient Magnet Map	54
2.11	Chapter Closure	54
2.12	Problems	56
3	Pole Tip Design	57
3.1	Understanding the Dipole Magnet	57
3.1.1	The Orthogonal Analog Model	57
3.1.2	The Orthogonal Analog Model and the Quadrupole	60
3.1.3	The “H” Dipole Geometry	62
3.1.4	H-Magnet Uniformity	64
3.2	Understanding the Quadrupole Magnet	67
3.2.1	Quadrupole Uniformity	67
3.3	Understanding the Gradient Magnet	71
3.3.1	Gradient Magnet Uniformity	71
3.4	Mapping an Existing Gradient Magnet Design	74
3.4.1	Baseline Optimized Pole	76
3.4.2	New Unoptimized Pole	77
3.4.3	Baseline Mapped Pole	77
3.4.4	New Mapped Unoptimized Pole	77
3.4.5	Scaling and Shifting	78
3.4.6	Center Expansion	79

3.4.7	Mapping Back into the Quadrupole Space	81
3.5	Chapter Closure	81
3.6	Problems	84
4	Perturbations	87
4.1	Introduction	87
4.2	Algorithms and Tables	88
4.2.1	Quadrupole Pole Error Coefficients, N=2	88
4.2.2	Sextupole Pole Error Pole Error Coefficients, N=3	88
4.2.3	Computing Error Multipoles	89
4.3	Two Piece Quadrupole	91
4.3.1	Magnet Assymetry	92
4.3.2	Differences in Lengths of the Upper and Lower Halves	94
4.3.3	Sorting	97
4.3.4	Two Piece Quadrupole Errors	98
4.3.5	Tolerances (Examples of Computations)	100
4.3.6	Alignment Error	100
4.3.7	Excitation Error	102
4.3.8	Random Multipole Error	102
4.4	Sextupole Trim Windings	104
4.4.1	Orthogonality	104
4.4.2	Horizontal Steering Trim	105
4.4.3	Vertical Steering and Skew Quadrupole Trim	106
4.4.4	Trim Excitations	108
4.5	Chapter Closure	109
4.6	Problems	111
5	Magnetic Excitation and Coil Design	113
5.1	Introduction	113
5.2	Maxwell's Inhomogeneous Equation	113
5.2.1	Continuity	114
5.3	Magnet Excitations	115
5.3.1	Magnet Efficiency	115
5.3.2	Dipole Magnets	116
5.3.3	Quadrupole Magnet	122
5.3.4	Sextupole Magnet	124
5.4	Coil Design	125
5.4.1	Coil Power	126
5.5	Coil Cooling	129
5.5.1	Pressure Drop	130
5.5.2	Flow Velocity	130
5.5.3	Units	131

5.5.4	Coil Cooling	135
5.5.5	Calculations	137
5.5.6	Sensitivities	141
5.6	Chapter Closure	142
5.7	Problems	144
6	POISSON	147
6.1	Elements of the Family of Codes	149
6.2	Documentation	150
6.3	Problem Flow	150
6.4	AutoMesh	152
6.4.1	Boundary Conditions and Constraints	152
6.4.2	Geometry	155
6.4.3	Setting Up and Testing the Geometry	156
6.5	Symmetries	158
6.5.1	Example - Collins or Figure Eight Quadrupole	158
6.5.2	Coil Geometry	159
6.5.3	Yoke Geometry	161
6.6	The Vector Potential Boundary Condition	162
6.6.1	Simple Dipole	162
6.6.2	The Simple Dipole with Vector Potential Boundary Conditions	164
6.6.3	The Vector Potential Boundary Condition for Optimizing the Quadrupole Pole	167
6.6.4	Other Applications of the Vector Potential Boundary Conditions	178
6.7	Chapter Closure	181
6.8	Problems	185
7	Stored Energy, Magnetic Forces and Dynamic Effects	187
7.1	Force on Coils	187
7.2	Force on a Pole	189
7.2.1	Units	189
7.2.2	A Reference Point	190
7.3	Magnet Stored Energy	190
7.3.1	Inductance	191
7.4	Eddy Currents	193
7.4.1	Field Attenuation due to Eddy Currents in a Semi-infinite Conductive Horizontal Plate	194
7.4.2	Field Attenuation due to Eddy Currents in a Pair of Semi-infinite Conductive Vertical Plates	198
7.4.3	Field Attenuation due to Eddy Currents in a Closed Rectangular Chamber	200
7.4.4	Field Amplification	201

7.5 Chapter Closure	208
7.6 Problems	209
8 Magnetic Measurements	213
8.1 The Vector Potential	214
8.1.1 Fourier Analysis	216
8.2 Output Voltage	218
8.3 The Compensated Coil	220
8.3.1 The Quadrupole Coil	221
8.3.2 The Dipole Coil	222
8.3.3 The Sextupole Coil	222
8.4 “Spilldown” and Magnetic Center	223
8.4.1 Quadrupole Magnetic Center	224
8.4.2 Sextupole Magnetic Center	226
8.5 Rotating Coil Magnetic Measurements	227
8.5.1 The Measurement System	227
8.6 Fourier Analysis	230
8.6.1 Uncompensated Signal	231
8.6.2 Compensated Signal	231
8.6.3 Expressions for the Integrated Multipole Fields	232
8.6.4 Excitation and Transfer Function	233
8.6.5 Relative Phases	234
8.6.6 Units	235
8.7 Measurements and Output	235
8.7.1 Measurement Plan	235
8.7.2 Raw Data Output	236
8.7.3 Bucking Ratio	236
8.7.4 Normalized Multipole Errors	237
8.7.5 Error Spectrum Normalized to the Required Good Field Radius	238
8.7.6 Magnetic Center	238
8.8 Measurement Output	239
8.8.1 Tabular Output	240
8.9 Analog Output (Iso-Error Plots)	240
8.10 Chapter Closure	243
8.11 Problems	244
9 Magnet Yoke Design and Fabrication	249
9.1 Introduction	249
9.2 Saturation	249
9.3 Two Dimensional Design	251
9.4 Three Dimensional Design	252
9.4.1 Dipole Fringe Field	252

9.4.2	Quadrupole Fringe Field	254
9.5	Solid Iron or Steel Laminations	258
9.5.1	Reproducibility and Symmetry	258
9.5.2	Solid Iron Cores	258
9.5.3	Laminated Steel Cores	259
9.5.4	Economics	260
9.5.5	Laminated Yoke Fabrication	261
9.6	Yoke Assembly/Fabrication Techniques	262
9.6.1	Gluing	264
9.6.2	Welded Laminated Yokes	271
9.6.3	Mechanically Assembled Laminated Yokes	273
9.7	Core Grounding	281
9.8	Chapter Closure	281
9.9	Chapter Appendix	284
10	Magnet Coil Fabrication	287
10.1	Introduction	287
10.1.1	Conductor Size and Turn to Turn Insulation	287
10.1.2	Coil Winding	288
10.1.3	Coil Potting (Encapsulation)	291
10.2	Coil Failures	298
10.2.1	Specifications	298
10.2.2	Measurements and Tests	299
10.3	Chapter Closure	303
11	Magnet Assembly	305
11.1	Introduction	305
11.2	Coil Supports and Bussing	305
11.2.1	Bussing	306
11.2.2	Magnet Tests	313
11.3	Chapter Closure	315
12	Magnet Installation and Alignment	317
12.1	Introduction	317
12.2	Magnet Support	318
12.2.1	Predetermined Alignment	318
12.2.2	Generic Fiducialization	319
12.2.3	Adjusted Alignment	320
12.2.4	Adjustable Struts	323
12.2.5	Adjustable Support Blocks	326
12.2.6	Pedigreed Fiducialization	328
12.3	Chapter Closure	330

CONTENTS	13
Solutions	331
References	345
index	347

Chapter 1

BASIC CONCEPTS

1.1 Introduction

Conventional iron dominated electromagnets are components of low/medium energy accelerator systems and also used for low/medium energy charged beam transport. Low/medium energy particle accelerators are those whose beam stiffness, $B\rho$, is limited to a few tens of Tesla-meters. The beam stiffness is given in many physics texts including Livingood[1] by

$$B\rho = \frac{1}{qc} \sqrt{T^2 + 2TE_0}, \quad (7.01)$$

where q = charge in Coulombs, c = the speed of light in $\frac{m}{sec}$, T = beam energy and E_0 = the particle rest mass energy. Written in conventional accelerator units

$$B\rho \approx \frac{1}{299.8Z} \sqrt{T^2 + 2TE_0}, \text{ where} \quad (7.02)$$

Z is the number of charge units,
 $B\rho$ (*Tesla – meters*),
 T (*MeV*),
 $E_0 = \begin{cases} 0.51Mev & \text{for electrons} \\ 938MeV & \text{for protons} \end{cases}$.

High energy accelerators and beam transport lines for accelerators whose beam stiffness is greater than a few tens of Tesla-meters require higher fields not achievable with iron dominated magnets and must rely on superconducting technology.

The conventional magnets described herein are those whose fields are shaped by iron poles, where the maximum field level in the yoke is less than the iron saturation level and whose excitation is provided by current carrying coils. Understanding the function of these magnets requires understanding the forces and the force directions on charged particle beams with conventionally defined magnet polarities. This chapter introduces the different magnet types, describes the forces and defines the polarities for different magnets used for particle beams. Means of electrically connecting separate coils in different type magnets to achieve the desired polarities are

also described. The physics accelerators using different magnets can be found in other Physics texts[2][3].

Since it is difficult to explain all concepts of magnetic fields without some basic background, some expressions, developed more fully in later chapters, are used to describe relationships of the electrical current flowing in a single conductor, the magnetic field it generates and the forces the field exerts on moving charged particles. Other conventions are used to identify the polarities of magnet poles and the flux directions determined by these polarities.

1.2 Magnet Types

Many of the magnet types and their functions are described in a chapter written by Dr. Neil Marks of Daresbury in Great Britain in a collection of articles covering various aspects of synchrotron radiation accelerators edited by Dr. Herman Winick[4].

Conventional electromagnets can be divided among several different types.

- Dipole Magnets
 - Gradient Magnet
- Quadrupoles
- Sextupoles
- Correctors
 - Vertical and Horizontal Steering
 - Skew Quadrupole
- Specialized Magnets
 - Current Sheet Septum (Horizontal Bend)
 - Lambertson Septum (Vertical Bend)
 - Bump and Kicker Magnets

1.3 Pictures

The photographs reproduced in this chapter are those of magnets manufactured for the PEPII and SPEAR3 projects. The PEPII accelerator at SLAC is an electron positron asymmetric collider, constructed to investigate the fundamental nature of subatomic particles. The SPEAR3 project is an upgrade of an existing 3GeV electron synchrotron at SLAC, constructed to exploit the synchrotron radiation emitted by electrons bent through magnetic fields.

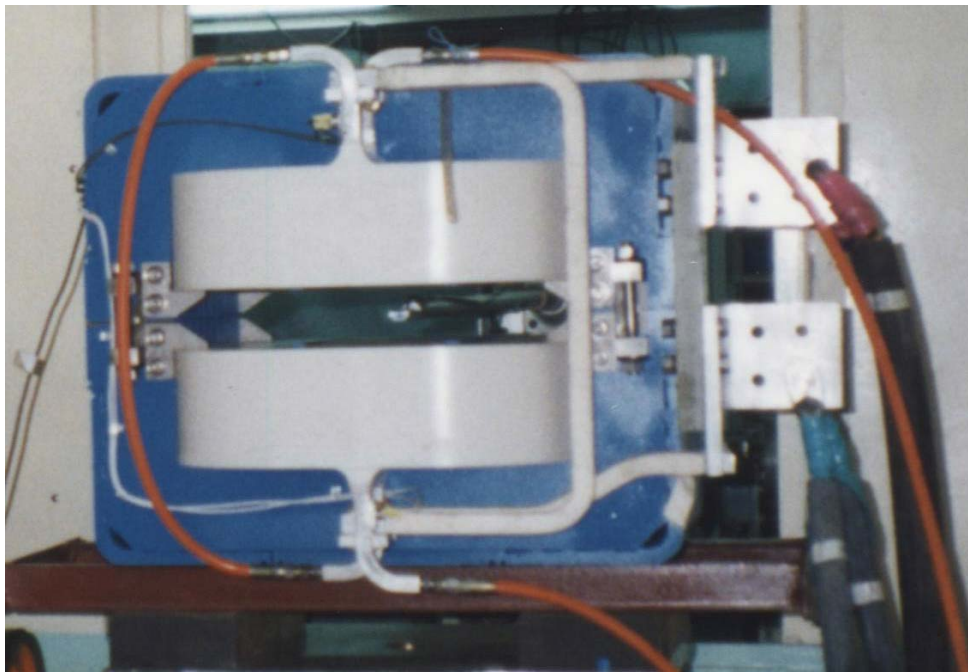


Figure 1 PEPII Low Energy Ring Dipole



Figure 2 SPEAR3 Gradient Dipole Magnet

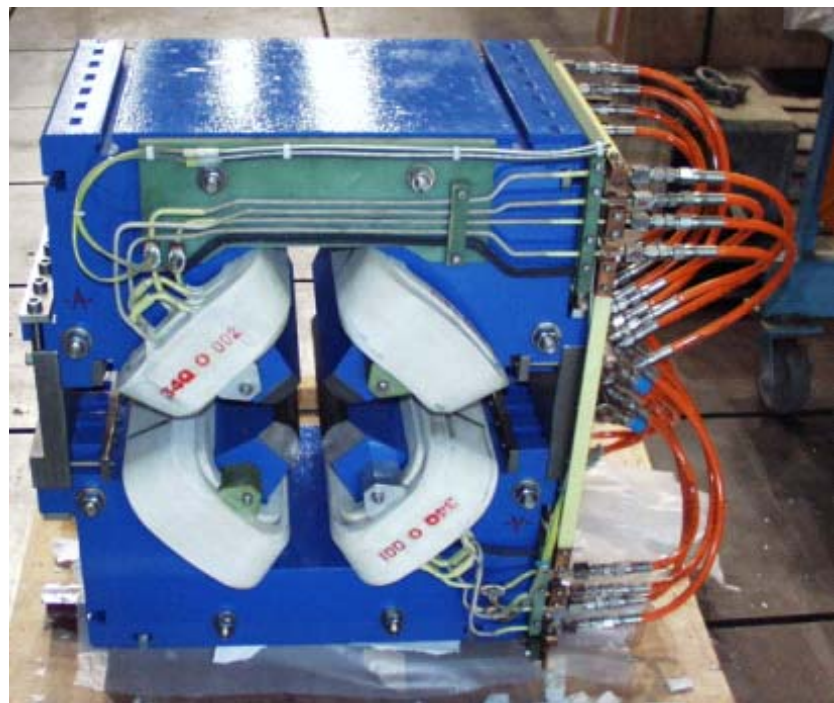


Figure 3 SPEAR3 Quadrupole Magnet

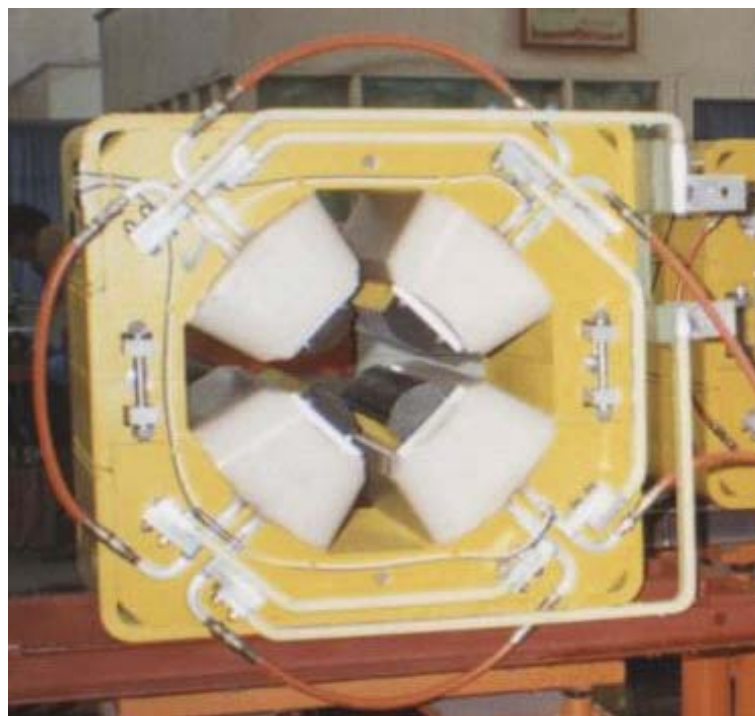


Figure 4 PEPII Quadrupole

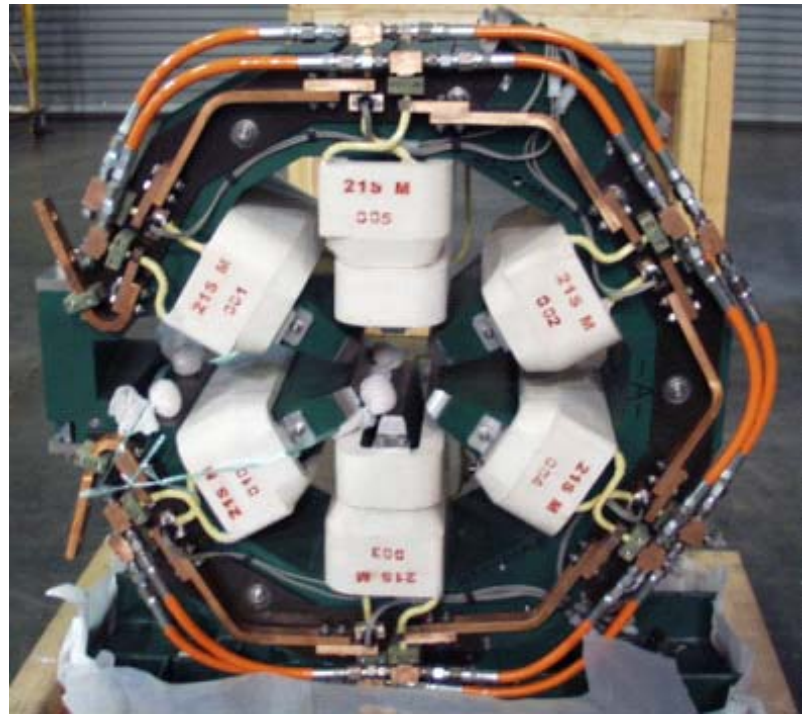


Figure 5 SPEAR3 Sextupole Magnet with Skew Quadrupole Trim Coils



Figure 6 SPEAR3 Combined Horizontal and Vertical Steering Corrector

Fig. 1 illustrates a PEPII Low Energy Ring dipole. A dipole magnet has two poles and has a constant field in the magnet aperture. Fig. 2 illustrates the SPEAR3 gradient dipole magnet. In the gradient dipole, the field shaped by the pole combines a constant dipole field with a field linearly distributed along the transverse and vertical directions. The SPEAR3 gradient magnet simultaneously bends and horizontally defocuses the charged beam.

Fig. 4 illustrates a PEPII Low Energy Ring quadrupole magnet. Fig. 3 illustrates a SPEAR3 quadrupole magnet. The two illustrated quadrupoles differ in design and construction details. The PEPII magnet uses a welded core. Its conductors are large and require separate busses for the coil to coil electrical connections. The SPEAR3 quadrupole employs a glued core. The coil conductors are bent to an electrical manifold at both ends of the magnet, used to make the coil to coil electrical connections. Alternate coils are manifolded together at each end of the magnet to reduce the congestion due to the crossover topology. A quadrupole has four poles and a null field at its center. Its field magnitude varies linearly with the distance from the magnet center.

Fig. 5 illustrates the SPEAR3 sextupole magnet. A sextupole magnet has six poles and a null field at its center. Its field magnitude varies quadratically with the distance from the magnet center. Two extra coils installed on the vertical poles of the sextupole are added to produce a skew quadrupole trim field (a linearly distributed field rotated so that the field directions are parallel to the horizontal and vertical magnet axes).

Fig. 6 illustrates a combined horizontal and vertical corrector magnet. The corrector is a low field dipole magnet whose function is to correct the angle orbit of the charged particle beam by steering the beam horizontally and vertically. For the illustrated corrector example, the vertical field is shaped by the poles. In this example, the horizontal field is shaped by the placement of individual conductors.

1.4 Conventions

The right hand rule describes positive directions in vector relationships. Positive current flows from the positive (+) lead of a power supply to the negative (-) lead of a power supply. The flux direction due to positive current flowing in a coil surrounding a magnet pole is determined by the right hand rule. This convention also determines the polarity. Magnetic flux flows from the positive to the negative pole of a magnet. In the two dimensional illustrations shown in fig. 8, a \circlearrowright is used to describe the positive charge direction out of the page and an \times is used to describe the positive charge direction into the page.

1.5 The Field from a Line Current (Biot-Savart law)

The amplitude of the magnetic field is computed using the line integral form of the magnetic field equation (see page 114)

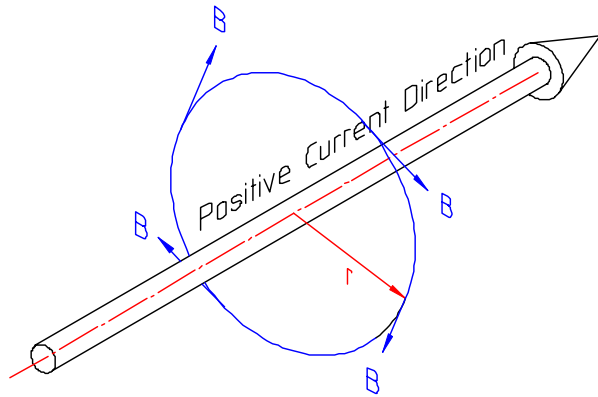


Figure 7 Magnet field due to a line current

$$\oint \vec{H} \cdot d\vec{l} = \frac{B}{\mu_0} 2\pi r = I,$$

$$B = \frac{\mu_0 I}{2\pi r}.$$

The direction of the magnetic field is described in fig. 7

1.6 Magnetic Force on a Line Current

The vector expression for forces on a particle beam is given by the vector cross product equation

$$\vec{F} = e \vec{v} \times \vec{B}. \quad (7.1)$$

1.6.1 MKS Units

Unless otherwise specified, all expressions in this text are expressed in the MKS system of units

$$\begin{aligned} \vec{F} &= \text{Newtons}, \\ e &= \text{coulombs}, \\ \vec{v} &= \frac{m}{\text{sec}}, \\ \vec{B} &= \text{Tesla}. \end{aligned}$$

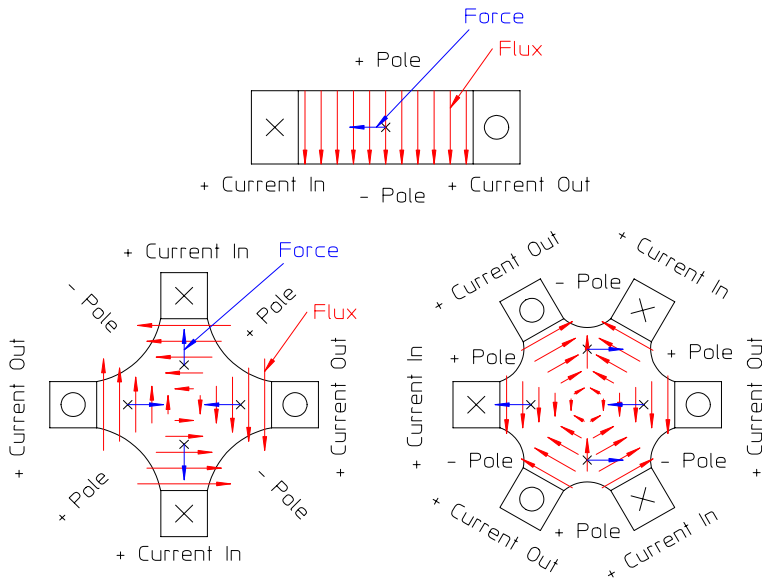


Figure 8 Coil Currents, Polarities and Force Directions for a Positive Beam Current

1.6.2 Force Directions

The right hand rule force direction on a positive particle beam is described in vector form in eq. (7.1) and is illustrated for the different magnet types in fig. 8. In this illustration, the coils have been simplified so that the dipole, quadrupole and sextupole appear to have one, two and three coils. Later chapters will show that the number of coils is equal to the number of magnet poles or multiples thereof.

1.6.3 Dipole Magnet

The dipole magnet has two poles and a uniform field. Applying the right hand convention for the coil current flowing in the indicated direction, the magnetic flux flows downward. Since the convention requires the magnetic flux to flow from the positive to negative poles, the upper pole is positive and the lower pole is negative. For positive beam current into the page, force direction, using the right hand convention, is to the left.

Gradient Magnets Gradient magnets are specialized dipole magnets which, in addition to a bend field at its center, has a linear gradient. This magnet is a combined function magnet which simultaneously defocuses (or focuses) and bends the beam.

1.6.4 Quadrupole Magnet

The quadrupole magnet has four poles and a zero field at its center. The field is normal to the horizontal and vertical centerlines and its distribution is linear with

distance from the center. Applying the right hand convention for the coil current flowing in the indicated directions, the magnetic flux flows outward from the poles at $\frac{\pi}{4}$ and $\frac{5\pi}{4}$ and inwards to poles at $\frac{3\pi}{4}$ and $\frac{7\pi}{4}$. Since the convention requires the magnetic flux to flow from the positive to negative poles, the poles at $\frac{\pi}{4}$ and $\frac{5\pi}{4}$ are positive and the poles at $\frac{3\pi}{4}$ and $\frac{7\pi}{4}$ are negative. For the illustrated positive beam currents at 0 and π planes into the page, along the horizontal centerline, the force direction is toward the center of the magnet. For the illustrated positive beam currents at $\frac{\pi}{2}$ and $\frac{3\pi}{2}$ planes into the page, along the vertical centerline, the force direction is away from the center of the magnet. The illustrated magnet is considered an F quadrupole for positively charged beam. Using the conventional definition, the F quadrupole focuses the beam in the horizontal plane and defocuses the beam in the vertical plane. The D quadrupole defocuses the beam in the horizontal plane and focuses the beam in the vertical plane.

1.6.5 Sextupole Magnet

The sextupole magnet has six poles and a zero field at its center. The field is normal to the horizontal centerline and centerlines at angles $\frac{\pi}{3}$ and $\frac{2\pi}{3}$. Its distribution is quadratic ($\propto r^2$) with distances from the center. Applying the right hand convention for the coil current flowing in the indicated directions, the magnetic flux flows outward from the poles at $\frac{\pi}{6}$, $\frac{5\pi}{6}$ and $\frac{3\pi}{2}$. The magnetic flux flows inwards to poles at $\frac{\pi}{2}$, $\frac{7\pi}{6}$ and $\frac{11\pi}{6}$. Since the convention requires the magnetic flux to flow from the positive to negative poles, the poles at $\frac{\pi}{6}$, $\frac{5\pi}{6}$ and $\frac{3\pi}{2}$ are positive and the poles at $\frac{\pi}{2}$, $\frac{7\pi}{6}$ and $\frac{11\pi}{6}$ are negative. For the illustrated positive beam currents at 0 and π , along the horizontal centerline, the force direction is to the left of the magnet. For the illustrated positive beam currents at $\frac{\pi}{2}$ and $\frac{3\pi}{2}$, along the vertical centerline, the force direction is to the right of the magnet.

The function of a sextupole magnet is to correct for the chromatic aberration due to dispersion in a dipole caused by the momentum spread in the beam. For a beam with energy spread traversing a dipole magnet, the higher energy particles are bent less than the lower energy particles, causing the dipole magnet to disperse a beam with point distribution into a beam with line distribution along the horizontal plane. The line beam leaving the illustrated dipole magnet (bending the beam to the left) is populated with higher energy particles on the right side of the beam and the lower energy beam on the left side of the beam (looking in the beam direction). The effect of a quadrupole on this dispersed beam is to longitudinally spread the focal point of the quadrupole lens, focussing the higher energy beam downstream and the lower energy beam upstream from the desired focal point. The sextupole magnet is designed to compensate for this effect. The illustrated magnet is designated an F sextupole for positively charged beam. The F sextupole selectively bends the beam on the right side of the magnet towards the beam centerline (shortening the focal length) and the beam on the left side of the beam away from the beam centerline (lengthening the focal length), restoring the desired single focal point. Since the sextupole also steers the vertically displaced beam in the opposite direction, it is

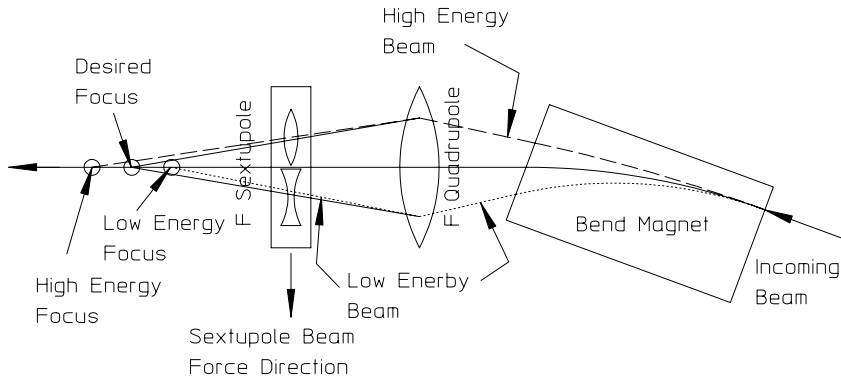


Figure 9 Dispersion and Chromatic Aberration Correction

usually located in positions in the synchrotron lattice where the beam is vertically small. Using the conventional definition, the F sextupole bends the beam toward the center of the accelerator ring and the D sextupole bends the beam away from the center of the accelerator ring. The orbits are illustrated in fig. 9.

1.6.6 Corrector Magnets

Steering Correctors

Steering corrector magnets are used to provide minor horizontal and vertical steering ($\lesssim 1.5 \text{ mrad}$) of the charged particle beam. They are normally located upstream from main ring quadrupoles and are used to steer the beam to the center of the quadrupole. Unwanted beam steering occurs when the charged particle beam is not centered in the quadrupole. In order to conserve lattice space and to simplify operation, horizontal and vertical steering are often combined in a single magnet.

Skew Quadrupole Correctors

Skew quadrupole corrector magnets are used to correct for the integrated effects of rotationally misaligned main ring quadrupoles. When the main ring magnets are rotationally misaligned, radial components of the magnetic field proportional to the sine of the misalignment angle are introduced along the horizontal and vertical planes. These small radial fields rotate the beam and mix the horizontal and vertical beam phases, causing instabilities. The skew quadrupole trims are used to compensate for these radial field errors. Corrector magnets are normally powered with bipolar power supplies so that corrections can be made in all directions and angle misalignments for different magnet polarities. Schematic illustrations of the three types of corrector magnets are shown in fig. 10.

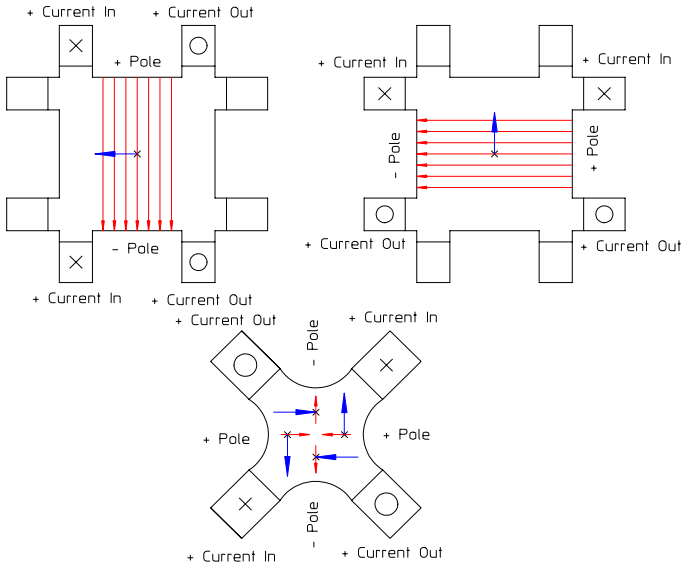


Figure 10 Horizontal/Vertical and Skew Quadrupole Correctors

1.6.7 Specialized Magnets

Specialized magnets are used for injection and/or extraction of charged particle beams into/out of accelerator rings. Normally, injection requires the buildup of current into the ring and occurs after previously stored beam is circulating in the ring. In order to ensure that the injected beam is stored (incorporated with the previously injected beam), it must be injected as transversely close to the central orbit of the circulating beam as possible. This is accomplished by using a combination of several bump magnets to momentarily move the circulating beam transversely close to the injected beam. When the bump magnets are turned off, the beam is restored to its central orbit. A good explanation of this process is described in an article by Dr. Gottfried Mülhaupt of Grenoble (in section 3.6.1 of reference [4]) covering synchrotron injection taking advantage of the transverse phase space in an accelerator with a fractional tune of approximately 1/4.

Bump Magnets

The bump magnet is a dipole usually with a laminated yoke or a yoke made from high resistive permeable material. This material is selected since it does not carry eddy currents. The magnetic field in the bump magnet must be raised to its required field and reduced again to zero in the shortest possible time (usually the time required to make a single orbit around the ring). Power supply voltage constraints often limit the rate at which the magnetic field can be changed. Thus, the previous article by Mülhaupt describes a system which takes advantage of the accelerator fractional tune

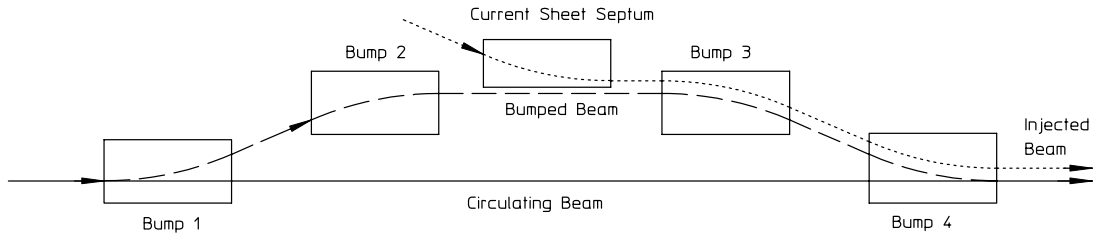


Figure 11 Bumped Beam Orbit

to increase the required time to change the bump magnet field.

The rapid change in the magnetic field excites eddy currents in low electrically resistive permeable material. Because of the rapid change in the magnetic field, the bump magnets are normally installed in boxes which are part of the vacuum chamber. The field for bump magnets with metallic vacuum chambers installed within the gap will be excluded from the interior of the chamber (the beam space) because of eddy currents. A simplified illustration of the bumped beam orbit is shown in fig. 11.

Current Carrying Septum

The external field (fringe field) of the injection septum must be as small as possible to avoid affecting the circulating beam. The current in the outer coil of the current carrying septum magnet divides the high field region of the magnet from the low field region. This type of magnet is often operated in the persistent mode and left on for long periods after injection. The cross section of a current carrying septum, typically operated in the persistent mode, is shown in fig. (12). The fringe field in the current carrying septum can adversely affect the orbit of the circulating beam. Its magnitude is dependent on the design of the iron yoke and is discussed in a later chapter (see discussion on page 119).

Eddy Current Septum

Another injection septum design (the eddy current septum) is employed for higher fields requiring higher currents and a very limited space for the septum. The eddy current septum magnet, illustrated in fig. (13), employs a pulsed current in the coil around the back leg of the yoke. Eddy currents generated by the rapidly changing magnetic flux exclude the field from regions outside of the high conductivity copper eddy current box. In particular, the currents generated in the septum minimizes the field penetrating into the region of the bumped and circulating beam. In practice, the eddy current septum has a longer time constant than the pulse width of the

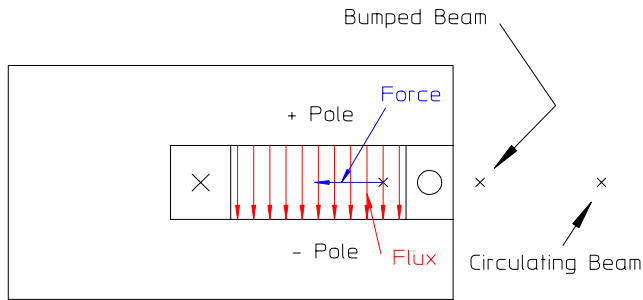


Figure 12 Current Carrying Septum

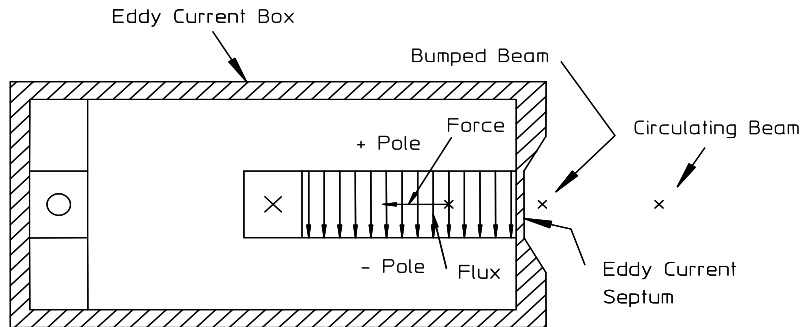


Figure 13 Eddy Current Septum

excitation and the fringe field persists longer than the magnet field.

Lambertson Septum

The Lambertson septum magnet is used to inject the beam from above or below the plane of the accelerator. Its cross section is shown in fig. (14). As in the case of the current carrying septum, the magnet is left on and its external field must be as small as possible in the region of the circulating beam. Its fringe field is horizontal rather than the vertical fringe field for the current carrying and eddy current septa. Thus, the unwanted vertical steering is a bit more difficult to deal with than the horizontal orbit perturbations from the horizontally steering septa. Means of estimating the size of the fringe field is covered in a later chapter in this book (see discussion on page 120). In general, a larger opening angle in the septum causes an intensification of the gap H-field in the septum. Since the H-parallel field is continuous across the iron air boundary, this intensification causes a larger fringe field.

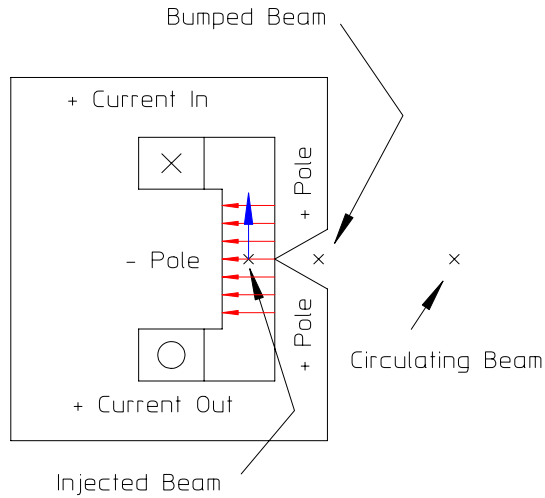


Figure 14 Lambertson Septum

1.6.8 More Polarity

All the previous figures showing the direction of magnetic flux and the direction of forces for positive beam flowing “into the paper” employ the conventions outlined in the beginning of this chapter. However, it is often difficult to remember and/or employ all the conventions when connecting a power supply or determining the correct intercoil bussing to connect the two coils for a dipole, the four coils for a quadrupole or the six coils for a sextupole. Moreover, since all the conventions were defined for a positively charged circulating beam, one can become confused when considering electron accelerators with negatively charged beam. One has to remember that the right hand rule becomes a left hand rule to determine the direction of the magnetic forces or to reverse the power supply leads assuming positively charged particles to obtain the correct magnet polarities for electrons. One of the most common errors in the final stages of accelerator construction projects is the reversing of polarities on isolated magnets. Another less common error is the mis-connection of the leads connecting the separate coils of a single magnet.

A simpler means of determining the correct magnet polarities exists.

Magnetostriiction

Using the right hand rule force and magnetic flux direction convention, it can be seen that the magnetic flux and force directions for a series of conductors carrying parallel positive currents in the same direction are as shown in fig. 15. The forces on parallel conductors, carrying the same charges in the same direction, are towards each other. This phenomenon is familiar to those dealing with multi-strand cables. The separate

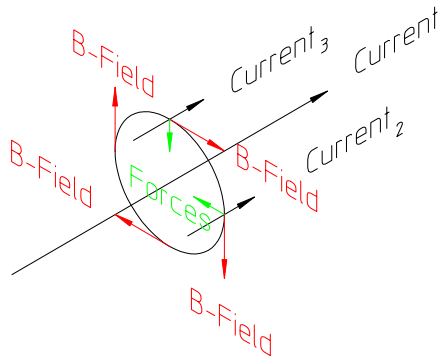


Figure 15 Forces on Parallel Conductors

strands of a cable attract each other and the cable cross-section compresses when the power is turned on. One can take advantage of this behavior and develop a simpler set of polarity conventions.

1.6.9 Alternate Polarity Convention

- Currents with the same charge travelling in the same direction attract.

Corollaries

- Currents with opposite charges travelling in the same direction repel.
- Currents with the same charge travelling in opposite directions repel.
- Currents with opposite charges travelling in the opposite direction attract.

By considering the charged particle beam as a line current with appropriate signs, one can use this alternate convention and/or its corollaries to determine the direction of the power supply currents through the different coils of the magnet to ensure the proper magnet polarities for positively or negatively charged beams. One does not have to figure out the polarities of the magnet poles.

1.7 Chapter Closure

This chapter introduces and describes the functions and characteristics of different types of conventional iron dominated electro-magnets used for low and medium energy charged particle accelerators and beam transport lines. The main magnet types are the dipole, quadrupole and sextupole whose field are uniform, linear and quadratic whose functions are to bend, focus and correct the chromaticity of the beam. Other magnets are described which correct beam orbits and compensate for the effects of installation/alignment errors. Some specialized magnets required for beam injection/extraction are described. Descriptions of the charged particle beam

orbits through the different magnet types is beyond the scope of this work. The physics of beam orbits through magnets can be found in texts by Wiedemann [2] and Lee [3].

Conventions and definitions are introduced to identify the force direction on moving positively charged particle beams. These conventions are restated using the principal of magnetostriction to simplify the concepts and to avoid confusion when attempting to establish the correct polarity for beams with different charges.

For modern accelerators, especially for storage rings and colliders whose beam lifetimes are measured in hours, the properties of magnets are crucial to the accelerator performance and beam lifetime. Magnets need to be installed and aligned precisely, the excitation of individual magnets must be precise and predictable and the magnetic field shape must be free of errors to satisfy the requirements needed by the physics of accelerators. The quality of the magnets depend on the extent that the fields have the desired shapes. The shapes of the magnetic fields depend on the iron pole shapes, the mechanical fabrication precision of the construction of the poles and the assembly of the parts making up the magnet yoke. Later chapters describe means of satisfying the physics requirements for high quality accelerator magnets. The task of the magnet designer is to design magnets which satisfy the physics requirements and can be translated into mechanical components and magnet assemblies accurately, reliably and economically.

1.8 Problems

Problem 1.1 (Solution)

Using the eq. (7.1) and the MKS system of units, show that the units for force are expressed in Newtons.

Problem 1.2 (Solution)

Why are there no forces between two line currents a distance d apart and perpendicular to each other?

Problem 1.3 (Solution)

What is the expression for the magnitude of the force per unit length on one conductor due to the magnetic field generated by a parallel conductor where the distance separating the two conductors is given by d ?

Chapter 2

SOLUTIONS OF THE MAGNET EQUATIONS

2.1 Introduction

An understanding of magnets is not possible without reviewing some of the mathematics underpinning the theory of magnetic fields. The development starts from Maxwell's equation for the three-dimensional distribution of magnet fields in the presence of steady currents both in vacuum and permeable material. For vacuum and absence of current sources, the fields satisfy the homogeneous equation. A function, F , is introduced and the Laplace equation is derived from Maxwell's homogeneous equation. Although three-dimensional fields are discussed, the mathematical solutions for the differential equations developed in this text is limited to two dimensional functions and field distributions. Understanding the mathematics of two dimensional fields is important since the three dimensional fields linearly integrated perpendicular to the plane over the region where the magnetic field is non-zero obey the same two dimensional differential equation and can be characterized by the same two-dimensional relationships.

The discussion in this chapter finds two different forms for solutions of the two dimensional Laplace equation for magnetic fields in vacuum. A solution for the more general condition with current sources and with permeable material is developed in a later chapter.

2.2 Maxwell's Magnet Equations

The three-dimensional vector form of Maxwell's steady state magnet equations in the MKS system is

$$\vec{\nabla} \times \vec{B} = \begin{cases} \mu\mu_0 \vec{J} \\ 0 \text{ in the absence of sources} \end{cases} \quad (2.1)$$

$$\vec{\nabla} \cdot \vec{B} = 0. \quad (2.2)$$

2.2.1 Continuity

A later chapter will use Stoke's theorem applied to eq. (2.1) to develop an integral form for Maxwell's two dimensional magnet equation (see page 114). This integral

form will be used to establish the continuity of $H\parallel$, the parallel H vector across an iron/air boundary. Since we have described the second of Maxwell's magnet equations, $\vec{\nabla} \cdot \vec{B} = 0$, it is convenient to develop the concepts that establish the continuity of $B \perp$, the perpendicular B vector across an iron/air boundary in this chapter. Eq. 2.2 can be rewritten as

$$\frac{\partial B_x}{\partial x} + \frac{\partial B_y}{\partial y} + \frac{\partial B_z}{\partial z} = 0,$$

or $\frac{\partial \vec{B}_n}{\partial \vec{x}} = 0$.

Another way to state the second expression is that the B field is continuous along its vector direction. Thus the perpendicular component of the B field does not change across material interfaces.

2.2.2 Units

The MKS units (which are used throughout this text) are

$$\begin{aligned}\vec{B} &= (\text{Tesla}) \\ \vec{J} &= \left(\frac{\text{Amps}}{\text{m}^2} \right) \\ \mu &= (\text{Relative Permeability}) = 1 \text{ in vacuum,} \\ \mu &\approx 1000 \text{ in high permeable material} \\ \text{and } \mu_0 &= (\text{Permeability of vacuum}) 4\pi \times 10^{-7} \frac{\text{Tm}}{\text{Amp}}.\end{aligned}$$

2.3 The Function of a Complex Variable

A function of a complex variable introduced in this section is

$$F = \vec{A} + iV \quad (2.3)$$

consisting of a real part, the vector potential, \vec{A} , and an imaginary part, the scalar potential, V . The magnetic field vectors are defined by the curl of the vector potential and the divergence of the scalar potential;

$$\vec{B} = \vec{\nabla} \times \vec{A} = \begin{vmatrix} \hat{i} & \hat{j} & \hat{k} \\ \frac{\partial}{\partial x} & \frac{\partial}{\partial y} & \frac{\partial}{\partial z} \\ A_x & A_y & A_z \end{vmatrix} \quad (2.4)$$

$$\vec{B} = -\vec{\nabla} V = -\hat{i} \frac{\partial V}{\partial x} - \hat{j} \frac{\partial V}{\partial y} - \hat{k} \frac{\partial V}{\partial z}. \quad (2.5)$$

Taking eq. (2.4) applying eq. (2.1) with no sources, the homogeneous equation, and using the vector identity,

$$\vec{\nabla} \times \vec{B} = \vec{\nabla} \times (\vec{\nabla} \times \vec{A}) = \vec{\nabla} (\vec{\nabla} \cdot \vec{A}) - \nabla^2 \vec{A} = 0.$$

In the previous expression, the Coulomb condition, $\vec{\nabla} \cdot \vec{A} = 0$, is assumed. \vec{A} satisfies the Laplace equation

$$\nabla^2 \vec{A} = 0. \quad (2.6)$$

Taking eq. (2.5) and applying eq. (2.2)

$$\vec{\nabla} \cdot \vec{B} = 0 = -\nabla^2 V.$$

Thus, V also satisfies the Laplace equation

$$\nabla^2 V = 0. \quad (2.7)$$

and the function, $F = \vec{A} + iV$ must also satisfy the Laplace equation

$$\nabla^2 F = 0. \quad (2.8)$$

2.4 The Two-Dimensional Fields

At this point, the generality of three dimensional fields is abandoned and the discussion is limited to mathematical expressions describing two dimensional fields in the (x, y) plane. Expanding eq. , the three-dimensional Maxwell's magnet equation describing the magnetic fields are

$$\begin{aligned} & \hat{i} \left(\frac{\partial B_z}{\partial y} - \frac{\partial B_y}{\partial z} \right) \\ & + \hat{j} \left(\frac{\partial B_x}{\partial z} - \frac{\partial B_z}{\partial x} \right) = \mu \mu_0 \left(\hat{i} J_x + \hat{j} J_y + \hat{k} J_z \right). \\ & + \hat{k} \left(\frac{\partial B_y}{\partial x} - \frac{\partial B_x}{\partial y} \right) \end{aligned}$$

The two-dimensional fields in the (x, y) plane satisfy the scalar equation,

$$\frac{\partial B_y}{\partial x} - \frac{\partial B_x}{\partial y} = \mu \mu_0 J_z, \quad (2.9)$$

where J_z describes the current density in the (x, y) plane in the z direction and can be treated as a scalar quantity.

2.4.1 Fields from the Two-Dimensional Function of a Complex Variable

The function, $F = A + iV$, can be written in two dimensions as a function of a complex variable, $z = x + iy$ where the complex conjugate of the field is given by eq. (2.10)

$$\begin{aligned} B^* &= B_x - iB_y = iF'(z), \\ &= i \frac{dF}{dz} = i \left(\frac{\partial F}{\partial x} \frac{dx}{dz} + \frac{\partial F}{\partial y} \frac{dy}{dz} \right), \\ &= i \left(\frac{\partial F}{\partial x} - \frac{\partial F}{\partial y} i \right) = \frac{\partial F}{\partial y} + i \frac{\partial F}{\partial x}. \end{aligned} \quad (2.10)$$

Equating the real and imaginary parts of the expression;

$$B_x = \frac{\partial F}{\partial y} \quad \text{and} \quad B_y = -\frac{\partial F}{\partial x}.$$

Substituting into eq. (2.9), we get Poisson's equation;

$$\frac{\partial^2 F}{\partial x^2} + \frac{\partial^2 F}{\partial y^2} = -\mu\mu_0 J_z. \quad (2.11)$$

2.5 Two Dimensional Fields in a Vacuum

The following sections develop the mathematical conventions used to describe the distribution of two-dimensional magnetic potentials satisfying the homogeneous Poisson's equation. Expressions for the two-dimensional magnetic fields and the ideal boundary conditions required to produce these fields are derived from these potentials. Mathematics of complex variables are used for describing magnetic fields as the sum of multipole terms and performing simple conformal maps. The conformal maps are used in a later chapter to generalize the knowledge of one type of magnet to other magnets.

Since the relationships developed for two dimensional fields fully describe three dimensional integrated fields, the mathematics can be exploited for the design of data acquisition systems and algorithms used to reduce the measurement data and characterize the field integral and the integrated harmonic error contents in various magnets.

2.5.1 Multipoles

In the following sections and chapters, the term “multipole” is used. In the context of magnets, multipoles can be used to designate the number of poles in a magnet or the harmonic content of the magnetic field. A multipole magnet can be a dipole, quadrupole, sextupole, octopole or a general multipole magnet where the terms refer

to a magnet with two, four, six, eight or any number of poles. The term is also used to describe the harmonic content of the field. Thus, a physical dipole magnet can have error terms which consist of harmonics called multipole errors. Certain properties of the multipole content of the magnetic field are derived using the conditions of rotational symmetry for different magnet types.

2.5.2 Laplace's Equation

Interaction of charged particles with magnetic fields occur in the magnet gaps. The gaps are regions where current sources and permeable material are absent. These are regions where two-dimensional magnet fields can be derived from potential functions which are the solutions to the homogeneous Poisson's differential equation, Laplace's equation,

$$\nabla^2 F = \frac{\partial^2 F}{\partial x^2} + \frac{\partial^2 F}{\partial y^2} = 0. \quad (2.12)$$

In this section, two different forms for the solutions are discussed.

2.5.3 Solutions to Laplace's Equation

Any analytic function of the complex variable $z = x + iy$ where $i = \sqrt{-1}$ satisfies Laplace's equation which can be verified using $\partial z / \partial x = 1$ and $\partial z / \partial y = i$.

$$\begin{aligned} \frac{\partial F}{\partial x} &= \frac{dF}{dz} \frac{\partial z}{\partial x} = \frac{dF}{dz} \\ \frac{\partial^2 F}{\partial x^2} &= \frac{\partial}{\partial x} \frac{dF}{dz} = \frac{d^2 F}{dz^2} \frac{\partial z}{\partial x} = \frac{d^2 F}{dz^2} \\ \frac{\partial F}{\partial y} &= \frac{dF}{dz} \frac{\partial z}{\partial y} = \frac{dF}{dz} i \\ \frac{\partial^2 F}{\partial y^2} &= \frac{\partial}{\partial y} \frac{dF}{dz} i = \frac{d^2 F}{dz^2} i \frac{\partial z}{\partial x} = \frac{d^2 F}{dz^2} i^2 = -\frac{d^2 F}{dz^2}. \end{aligned}$$

Thus,

$$\nabla^2 F = \frac{\partial^2 F}{\partial x^2} + \frac{\partial^2 F}{\partial y^2} = \frac{\partial^2 F}{\partial z^2} - \frac{\partial^2 F}{\partial z^2} = 0,$$

satisfying the Laplace's equation, eq. (2.12) for all functions of the complex variable $z = x + iy$.

Since all functions of the complex variable satisfy Laplace's equation, two particular forms, $F = A + iV$ and $F = Cz^n$, both satisfy Laplace's equation. Either form is useful with each providing different insights.

2.6 Two-Dimensional Vector and Scalar Potentials

The vector and scalar potentials are parts of a function of a two-dimensional complex coordinate, $z = x + iy$. However, the expressions derived from the three-dimensional curl and divergence expressions, summarized in section (2.4), are completely consistent in two-dimensions.

The function of a complex variable is divided among two quantities, the vector and scalar potentials. The function of the complex variable in two dimensions is given by the expression $F = A + iV$ where A , the real part of the complex function, is the vector potential and V , the imaginary part of the complex function, is the scalar potential:

$$A = \operatorname{Re}(F) \quad V = \operatorname{Im}(F). \quad (2.13)$$

In general, \vec{A} is a vector. Since two-dimensional fields in the (x, y) plane require $A_z \neq 0$ where A_z is the vector component normal to the (x, y) plane, $A = A_z$ is treated as a scalar quantity in the (x, y) plane. (Non-zero fields in the (y, z) and (z, x) planes require $A_x \neq 0$ and $A_y \neq 0$.)

The parts of an analytic function of the complex variable must satisfy the Cauchy-Riemann conditions,

$$\frac{\partial A}{\partial y} = -\frac{\partial V}{\partial x} \quad \text{and} \quad \frac{\partial A}{\partial x} = \frac{\partial V}{\partial y}. \quad (2.14)$$

2.6.1 Magnetic Fields from the Two-Dimensional Potentials

In two-dimensions, the magnetic fields are computed using eq. (2.10),

$$B^* = B_x - iB_y = iF'(z)$$

where * indicates the complex conjugate and ' indicates the derivative with respect to the complex variable, z . Computing the derivative of the function F with respect to the complex coordinate z ;

$$F'(z) = \lim_{\Delta z \rightarrow 0} \frac{\partial F(z)}{\partial z} = \lim_{\Delta z \rightarrow 0} \frac{\partial A + i\partial V}{\partial x + i\partial y} \quad (2.15)$$

Dividing the numerator and denominator of eq.(2.15) by ∂x ;

$$F'(z) = \lim_{\Delta z \rightarrow 0} \frac{\frac{\partial A}{\partial x} + i\frac{\partial V}{\partial x}}{1 + i\frac{\partial y}{\partial x}}$$

But $\frac{\partial y}{\partial x} \equiv 0$ since x and y are orthogonal. Therefore,

$$B^* = B_x - iB_y = iF'(z) = i\frac{\partial A}{\partial x} - \frac{\partial V}{\partial x}. \quad (2.16)$$

Similarly, taking eq. (2.15) and dividing both the numerator and denominator by ∂y ;

$$\begin{aligned} F'(z) &= \lim_{\Delta z \rightarrow 0} \frac{\frac{\partial A}{\partial y} + i\frac{\partial V}{\partial y}}{\frac{\partial x}{\partial y} + i}, \\ &= \frac{\frac{\partial A}{\partial y} + i\frac{\partial V}{\partial y}}{i} = -i\frac{\partial A}{\partial y} + \frac{\partial V}{\partial y}. \end{aligned}$$

But $\frac{\partial x}{\partial y} \equiv 0$ since x and y are orthogonal. Therefore,

$$F'(z) = \frac{\frac{\partial A}{\partial y} + i\frac{\partial V}{\partial y}}{i} = -i\frac{\partial A}{\partial y} + \frac{\partial V}{\partial y},$$

and

$$\begin{aligned} B^* &= B_x - iB_y = iF'(z) \\ &= i\left(-i\frac{\partial A}{\partial y} + \frac{\partial V}{\partial y}\right) = \frac{\partial A}{\partial y} + i\frac{\partial V}{\partial y}. \end{aligned} \quad (2.17)$$

Equating the real and imaginary parts of the expression,

$$\text{from eq. (2.16), } B_x = -\frac{\partial V}{\partial x} \quad \text{and} \quad B_y = -\frac{\partial A}{\partial x} \quad (2.18)$$

$$\text{or from eq. (2.17), } B_x = \frac{\partial A}{\partial y} \quad \text{and} \quad B_y = -\frac{\partial V}{\partial y}. \quad (2.19)$$

Either the vector or scalar potentials can be used. The Cauchy-Riemann conditions are satisfied for the complex conjugate of the field, B^* , but not for $B = B_x + iB_y$. The expressions in two dimensions are consistent with the more general three-dimensional expressions.

2.7 A Particular Function of the Complex Variable, $F = C_n z^n$

Since all functions of a complex variable satisfy Laplace's equation, a particular function satisfying LaPlace's equation, useful in the characterization of magnetic fields, is the function $F = C_n z^n$, where C_n is, in general, a complex constant.

2.7.1 Ideal Two-Dimensional Multipole Magnets

The convention used to describe multipole magnet types is to use a prefix to specify the number of poles. Thus, a dipole has two poles, a quadrupole has four poles, a sextupole has six poles, an octopole has eight poles and so on. (The numbers of poles in a symmetric multipole magnet is always even.) When describing the fields in a magnetic multipole using the function of a complex variable $F = C_n z^n$, the index of the function, the integer n , is half the number of poles. Thus, $n = 1, 2, 3$, and 4 correspond to a dipole, quadrupole, sextupole and octopole, respectively.

In the following sections, the two dimensional vector and scalar potentials computed using the complex function, $F = C_n z^n$, are used to describe ideal two-dimensional magnet types.

2.7.2 Two-Dimensional Flux Lines and Poles

For two dimensional magnetic fields, it is useful to define a coordinate axis with the real value of a complex function on the horizontal axis and the imaginary value on the vertical axis. Using this coordinate system, vector and scalar equipotentials can be plotted for various values of the function $F = C_n z^n$ for different values of the index, n . These plots reveal a great deal about the ideal magnetic field pattern and the shapes of the ideal poles resulting in the field patterns.

Vector and Scalar Equipotentials

The vector and scalar equipotentials are the curves in the $z = x + iy$ plane of the functions $C_n z^n = A + iV$ for constant values of the potentials A and V . The convention used in the mathematics of two dimensional fields is the family of vector equipotentials represents flux lines. The family of scalar equipotentials are orthogonal to the vector equipotentials, define boundary conditions for the vector potentials and can represent possible pole shapes. The combined families of equipotentials are curvilinear squares and are analogous to families of electrical voltage equipotential lines and current flow lines.

The plots resulting from the computation of the equipotentials represent ideal magnetic patterns and are different in small details from real magnetic patterns and those computed using Poisson or other two-dimensional magnet modeling programs. These differences are due to non-ideal boundary conditions and the finite permeability of iron. The potential plots provide useful information about the ideal generic multipole pole shapes and resulting magnetic flux pattern.

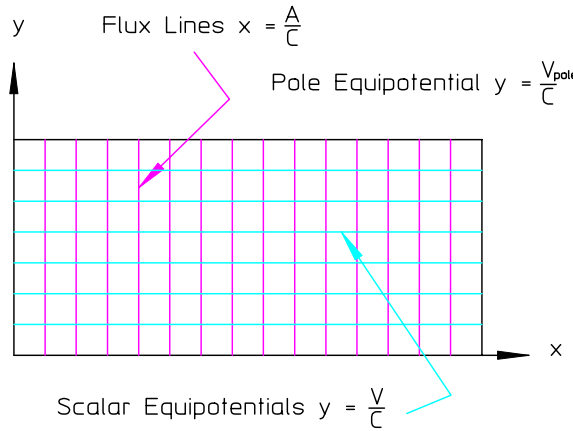


Figure 1 Dipole Vector and Scalar Potentials

n=1, the Dipole Magnet

The ideal dipole is characterized by the complex function with $n = 1$;

$$F = C_1 z = C_1 (x + iy) = A + iV.$$

If C is real, $A = \operatorname{Re} F = C_1 x$ and $V = \operatorname{Im} F = C_1 y$. Therefore, the equations for the equipotentials are,

$$x = \frac{A}{C_1} : \text{Vector Equipotentials} \quad (2.20)$$

$$y = \frac{V}{C_1} : \text{Scalar Equipotentials.} \quad (2.21)$$

The vector and scalar equipotentials for a dipole are illustrated in fig. 1.

n=2, the Quadrupole Magnet

The ideal quadrupole is characterized by the complex function with $n = 2$.

$$F = C_2 z^2 = C_2 (x + iy)^2 = C_2 (x^2 - y^2 + i2xy) = A + iV.$$

If C_2 is real, $A = \operatorname{Re} F = C_2 (x^2 - y^2)$ and $V = \operatorname{Im} F = 2C_2 xy$. The equations for the equipotentials are,

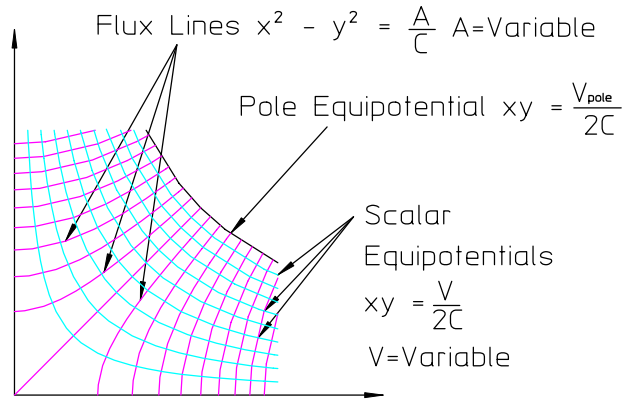


Figure 2 Quadrupole Vector and Scalar Potentials

$$x^2 - y^2 = \frac{A}{C_2} : \text{Vector Equipotentials} \quad (2.22)$$

$$xy = \frac{V}{2C_2} : \text{Scalar Equipotentials.} \quad (2.23)$$

The vector and scalar equipotentials for a quadrupole are illustrated in fig. 2.

n=3, the Sextupole Magnet

The ideal sextupole, characterized by the complex function with $n = 3$;

$$\begin{aligned} F &= A + iV = C_3 z^3 = C_3 (x + iy)^3 \\ &= C_3 (x^3 - 3xy^2) + iC_3 (3x^2y - y^3) = A + iV \end{aligned}$$

If C_3 is real, $A = \operatorname{Re} F = C_3 (x^3 - 3xy^2)$ and $V = \operatorname{Im} F = C_3 (3x^2y - y^3)$. The Cartesian equations for the equipotentials are,

$$x^3 - 3xy^2 = \frac{A}{C_3} : \text{Vector Equipotential,} \quad (2.24)$$

$$3x^2y - y^3 = \frac{V}{C_3} : \text{Scalar Equipotential.} \quad (2.25)$$

The Sextupole in Polar Coordinates For the sextupole example, polar coordinates are introduced, which are useful in understanding conformal mapping techniques. In polar coordinates;

$$F = C_3 z^3 = C_3 (|z| e^{i\theta})^3 = C_3 (|z|^3 e^{i3\theta}) = C_3 |z|^3 (\cos 3\theta + i \sin 3\theta) = A + iV$$

If C_3 is real, $A = \operatorname{Re} F = C_3 |z|^3 \cos 3\theta$ and $V = \operatorname{Im} F = C_3 |z|^3 \sin 3\theta$. Then

$$|z|_{\text{Vector Potential}} = \left(\frac{A}{C_3 \cos 3\theta} \right)^{\frac{1}{3}} \text{ and } |z|_{\text{Scalar Potential}} = \left(\frac{V}{C_3 \sin 3\theta} \right)^{\frac{1}{3}}.$$

Parametric equations for the vector and scalar equipotentials, written in the (r, θ) coordinate system are;

$$\begin{aligned} x_{\text{Vector Potential}} &= |z|_{\text{Vector Potential}} \cos \theta = \left(\frac{A}{C_3 \cos 3\theta} \right)^{\frac{1}{3}} \cos \theta \\ y_{\text{Vector Potential}} &= |z|_{\text{Vector Potential}} \sin \theta = \left(\frac{A}{C_3 \cos 3\theta} \right)^{\frac{1}{3}} \sin \theta \\ x_{\text{Scalar Potential}} &= |z|_{\text{Scalar Potential}} \cos \theta = \left(\frac{V}{C_3 \sin 3\theta} \right)^{\frac{1}{3}} \cos \theta \\ y_{\text{Scalar Potential}} &= |z|_{\text{Scalar Potential}} \sin \theta = \left(\frac{V}{C_3 \sin 3\theta} \right)^{\frac{1}{3}} \sin \theta. \end{aligned} \quad (2.26)$$

The vector and scalar equipotentials for a sextupole are illustrated in fig. 3.

Real and Skew Magnets

Magnets are described as real when the magnetic fields are vertical along the horizontal centerline ($B_x = 0$ and $B_y \neq 0$ for $y = 0$). Real magnets are characterized by $C = \text{real}$. Magnets are described as skew when the fields are horizontal along the horizontal centerline ($B_x \neq 0$ and $B_y = 0$ for $y = 0$). The skew magnet conditions are met for all three of the previous examples when $C = \text{imaginary}$. The skew magnet equipotentials of the three illustrated examples are rotated by $\frac{\pi}{2}$ for the dipole, $\frac{\pi}{4}$ for the quadrupole and $\frac{\pi}{6}$ for the sextupole.

2.7.3 Pole Contours

The previous section describes the scalar potentials and suggests that a scalar equipotential can be selected as a boundary condition for defining the field for different magnet types. The boundary is the profile of the iron pole of a magnet. The expressions for the ideal pole geometries for various magnet types can be generated using the information available from the different expressions for the scalar potential surfaces.

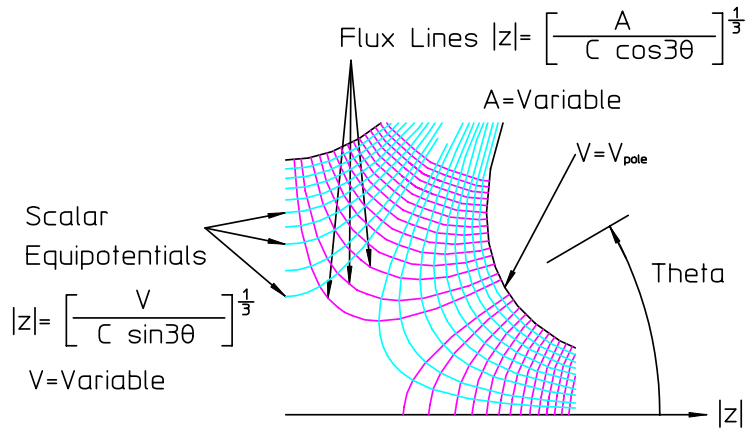


Figure 3 Sextupole Vector and Scalar Potentials

n=1, Dipole Magnet Pole

The real dipole field is generated by the boundary condition placing the surface of the magnet pole at a scalar equipotential line. Using eq. (2.21) and assigning the dipole half gap, h , as the argument, the equation for the dipole pole is

$$y = h. \quad (2.27)$$

n=2, Quadrupole Magnet Pole

The real quadrupole field is generated by the boundary condition where the magnet pole is located at the scalar equipotential hyperbola. Using eq. (2.23) and assigning the square of the quadrupole radius, h^2 , as the argument, the equation for the quadrupole pole with pole radius, h , is

$$xy = \frac{h^2}{2}. \quad (2.28)$$

n=3, Sextupole Magnet Pole

The real sextupole field is generated by the boundary condition where the magnet pole is located at the scalar cubic equipotential hyperbola. Using eqs. (2.25) and (2.26) and assigning the cube of the sextupole radius, h^3 , as the argument, the equation for the sextupole pole with pole radius, h , is

$$3xy^2 - y^3 = h^3 \quad (2.29)$$

$$\text{and in polar coordinates, } |z| = \sqrt{x^2 + y^2} = \frac{h}{\sqrt[3]{\sin 3\theta}}. \quad (2.30)$$

2.7.4 Complex Extrapolation

The desired two-dimensional field distribution for a magnet is specified and one is occasionally asked to design the pole contour which will produce this field. Complicated magnets have been specified which have combined up to three different magnet fields. A simple example of a field often specified in accelerator systems is presented in order to describe the process of complex extrapolation.

Gradient Magnet

A magnet with increasing use in lattices requiring efficient use of the ring perimeter is the combined function magnet. The gradient magnet combines bending and vertical focusing, thus conserving lattice space. This is important since the cost of an accelerator facility increases with the size of the machine. A gradient magnet field is non zero at its center and changes linearly along the horizontal axis. The required pole contour for this type of magnet can be derived from the field requirements and the desired aperture. The gradient magnet requirements are given as the field at its center, B_0 , its gradient, B' , and gap half height, h , at its transverse center, $x = 0$. The field distribution is expressed by the function

$$B_y = -B_0 - B'x.$$

Using eq. (2.15) to derive an expression for the scalar potential generating the required field

$$\begin{aligned} B_y &= -B_0 - B'x = -\frac{\partial V}{\partial y} \\ V &= \int (B_0 + B'x) dy = (B_0 + B'x) y \\ y &= \frac{V}{B_0 + B'x}. \end{aligned}$$

Since the field is B_0 at $x = 0$, where $y = h$, $V = (B_0 + B'x)y = B_0h$. Substituting, the equation for the pole is given by

$$y_{\text{Gradient Magnet}} = \frac{B_0h}{B_0 + B'x}. \quad (2.31)$$

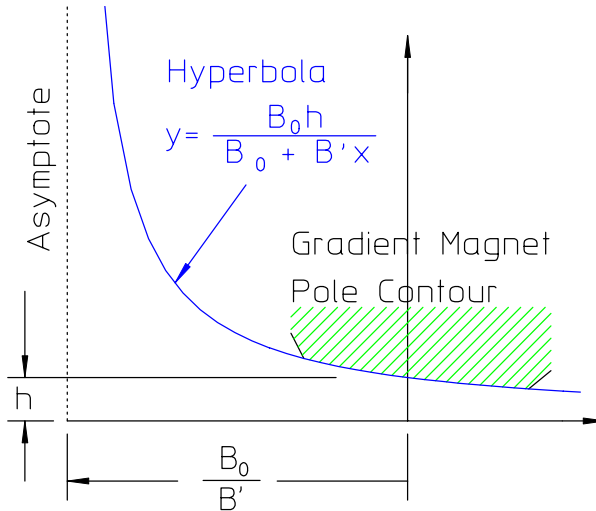


Figure 4 Gradient Magnet Pole as Part of a Quadrupole Pole

Fig. 4 illustrates the gradient magnet pole as part of the ideal hyperbola computed using the requirements. The ideal hyperbola with asymptotes at $y = 0$ and $x = -\frac{B_0}{B'}$ is the pole of a very large quadrupole.

2.8 Magnetic Fields Using the Function of the Complex Variable

In a previous section (2.18), it was shown that the expression, $B^* = B_x - iB_y = iF'(z)$, can be used to characterize the distribution of the magnetic fields and poles when the function, F , of a complex variable is written in terms of the vector and scalar potentials, A and V . Examples were presented for the dipole, quadrupole and sextupole magnets. In this section, the same expression is used to compute the magnetic field components directly from the function of the complex variable $F = C_n z^n$ and describe the characteristics of these same magnets. Using the expression for B^* ,

$$\begin{aligned} B^* &= B_x - iB_y = iF'(z), \\ B_x - iB_y &= i \frac{\partial}{\partial z} C_n z^n = i n C_n z^{n-1}. \end{aligned} \quad (2.32)$$

2.8.1 $n=1$, the Dipole Magnet

For the dipole

$$B_1^* = B_{1x} - iB_{1y} = i \frac{\partial}{\partial z} C_1 z = iC_1.$$

Equating the real and imaginary parts of the above expression

$$\begin{aligned} B_{1x} &= 0 \\ B_{1y} &= -C_1. \end{aligned}$$

Therefore, the fields in a dipole are constant.

2.8.2 $n=2$, the Quadrupole Magnet

For the quadrupole

$$B_2^* = B_{2x} - iB_{2y} = i \frac{\partial}{\partial z} C_2 z^2 = i2C_2 z = i2C_2 (x + iy) = -2C_2 y + i2C_2 x.$$

Equating the real and imaginary parts of the above expression,

$$\begin{aligned} B_{2x} &= -2C_2 y \\ B_{2y} &= -2C_2 x. \end{aligned}$$

The fields in a quadrupole are linearly distributed.

2.8.3 $n=3$, the Sextupole Magnet

For the sextupole

$$\begin{aligned} B_3^* &= B_{3x} - iB_{3y} = i \frac{\partial}{\partial z} C_3 z^3 = i3C_3 z^2 = i3C_3 (x + iy)^2 \\ &= i3C_3 (x^2 - y^2 + i2xy) = -6C_3 xy + i3C_3 (x^2 - y^2). \end{aligned}$$

Equating the real and imaginary parts of the above expression,

$$\begin{aligned} B_{3x} &= -6C_3 xy \\ B_{3y} &= 3C_3 (x^2 - y^2). \end{aligned}$$

The fields in a sextupole are quadratically distributed.

The Sextupole in Polar Coordinates

The expressions for the sextupole in polar coordinates are

$$\begin{aligned} B_3^* &= B_{3x} - iB_{3y} = i \frac{\partial}{\partial z} C_3 z^n = i3C_3 z^2 = i3C_3 |z|^2 e^{i2\theta} \\ &= i3C_3 |z|^2 (\cos 2\theta + i \sin 2\theta) = -3C_3 |z|^2 \sin 2\theta + i3C_3 |z|^2 \cos 2\theta. \end{aligned}$$

Equating the real and imaginary parts of the above expression,

$$\begin{aligned} B_{3x} &= -3C_3 |z|^2 \sin 2\theta \\ B_{3y} &= -3C_3 |z|^2 \cos 2\theta. \end{aligned}$$

The radial component of the sextupole field is

$$\begin{aligned} B_{3r} &= B_{3x} \cos \theta + B_{3y} \sin \theta, \\ &= -3C_3 |z|^2 (\sin 2\theta \cos \theta + \cos 2\theta \sin \theta), \\ &= -3C_3 |z|^2 \sin 3\theta. \end{aligned}$$

Real and Skew Magnets

Again, as in the previous section, the field components for skew magnets can be computed by substituting an imaginary value for C_n .

2.9 Multipole Errors

In this section, the concept of error multipoles is introduced. The multipole errors are divided among allowed or systematic multipole errors and random multipole errors. Symmetry conditions allow the existence of certain errors while forbidding others. Thus, the identification of certain errors can be ascribed to fabrication and/or assembly errors and are considered random while others can be ascribed to the limitations of the ability to optimize and perfect a pole design. The following chapter discusses the optimization process for various multipole magnets. A later chapter discusses the sources of the random or nonsystematic errors and quantifies the mechanical fabrication and/or assembly errors producing these errors.

2.9.1 The Error Spectrum

Since the function $F = C_n z^n$ satisfies Laplace's equation, then the Taylor's expansion of this function, $F = \sum C_n z^n$, must also satisfy Laplace's equation. A perfect multipole magnet is characterized by a single integer index. In general, a real magnet is characterized by a spectrum of harmonics including error terms due to the pole design, fabrication and/or assembly errors. Fields are conventionally characterized by the complex function

$$F = C_N z^N + \sum_{n \neq N} C_n z^n, \quad (2.33)$$

where N is the index of the fundamental (desired) field and $\sum_{n \neq N} C_n z^n$ represents the spectrum of error (undesired) terms where C_n is, in general, a complex number.

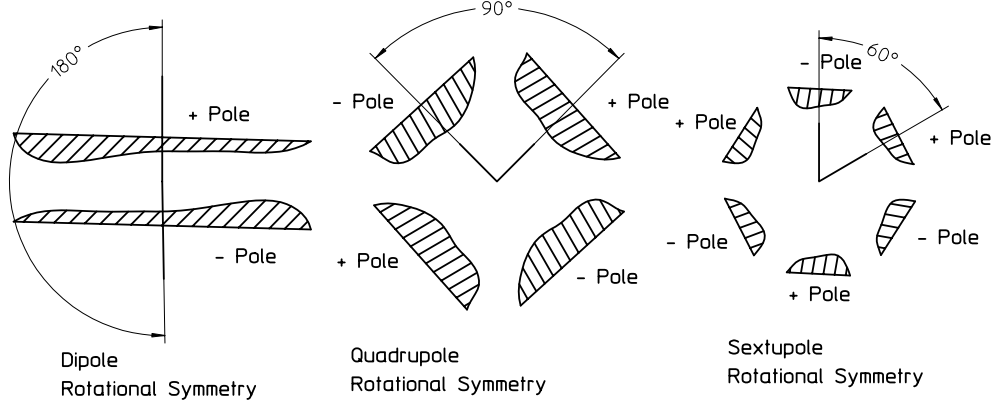


Figure 5 Pole Symmetry Conditions

2.9.2 “Allowed” or Systematic Multipole Errors

The undesired error multipoles ($n \neq N$) are divided among allowed or systematic multipole errors and random multipole errors. The systematic errors are those subject to symmetry and polarity constraints. These constraints require the errors to repeat and change polarities at angles spaced at angular intervals of π/N , where N is the index of the fundamental field. The symmetry constraints are

$$F_n\left(\theta + \frac{\pi}{N}\right) = -F_n(\theta).$$

Fig. 5 illustrates the angular rotation of the poles for a dipole, quadrupole and sextupole. In this figure, the illustrated poles are not symmetrical about their respective centerlines. This is to emphasize that rotational symmetry of the N poles and not mirror symmetry is assumed.

Consider the function of the complex variable, $F = \sum C_n z^n$. Written in polar coordinates

$$\begin{aligned} F(\theta) &= \sum C_n z^n = \sum C_n |z|^n e^{in\theta} = \sum C_n |z|^n (\cos n\theta + i \sin n\theta) \\ F\left(\theta + \frac{\pi}{N}\right) &= \sum C_n |z|^n \left[\cos\left(n\theta + \frac{\pi}{N}\right) + i \sin\left(n\theta + \frac{\pi}{N}\right) \right]. \end{aligned}$$

The symmetry conditions require

$$\cos\left(n\theta + \frac{\pi}{N}\right) + i \sin\left(n\theta + \frac{\pi}{N}\right) = -\cos n\theta - i \sin n\theta$$

Equating the real and imaginary terms and rewriting we obtain,

$$\begin{aligned}\cos\left(n\theta + \frac{\pi}{N}\right) &= -\cos n\theta \\ \cos n\theta \cos \frac{n\pi}{N} - \sin n\theta \sin \frac{n\pi}{N} &= -\cos n\theta\end{aligned}$$

$$\begin{aligned}\sin\left(n\theta + \frac{\pi}{N}\right) &= -\sin n\theta \\ \sin n\theta \cos \frac{n\pi}{N} + \cos n\theta \sin \frac{n\pi}{N} &= -\sin n\theta.\end{aligned}$$

These conditions can only be satisfied if

$$\begin{aligned}\sin \frac{n\pi}{N} &= 0 \implies \frac{n}{N} = 1, 2, 3, 4, \dots, \text{all integers} \\ \cos \frac{n\pi}{N} &= -1 \implies \frac{n}{N} = 1, 3, 5, 7, \dots, \text{all odd integers.}\end{aligned}$$

The more restrictive condition is $\frac{n}{N} = \text{all odd integers}$ and is rewritten as

$$n_{\text{allowed}} = N(2m+1), \quad (2.34)$$

where m is any positive integer including zero.

Sytematic or “Allowed” Multipole Phases

In general, the coefficients of the allowed multipoles $C_{N(2m+1)}$ = Complex Numbers. However, if in addition to the rotational symmetry, the poles are symmetric about their respective centerlines, $C_{N(2m+1)}$ = Real Numbers. (See problem 2.3 at the end of this chapter on page 56 and its solution at the end of this text.)

Allowed Dipole Multipole Errors

The allowed dipole multipole errors are $n_{\text{dipole}} = 3, 5, 7, 9, \dots$

Allowed Quadrupole Multipole Errors

The allowed quadrupole multipole errors are $n_{\text{quadrupole}} = 6, 10, 14, 18, \dots$

Allowed Sextupole Multipole Errors

The allowed sextupole multipole errors are $n_{\text{sextupole}} = 9, 15, 21, 27, \dots$

2.9.3 Multipole Field Errors

One is normally interested in the field errors rather than errors in the potential functions. The expression for the error fields normalized to the fundamental is;

$$B_n^* = iF'(z) = i \frac{d}{dz} C_n z^n = i n C_n z^{n-1} \quad B_N^* = i N C_N z^{N-1} \quad (2.35)$$

$$\frac{B_n^*}{B_N^*} = \frac{n}{N} \frac{C_n}{C_N} z^{n-N}. \quad (2.36)$$

The expression for the amplitudes of these errors normalized to the desired fundamental field amplitude can be computed as a function of radius.

$$\left| \frac{B_n^*}{B_N^*} \right|_r = \frac{n}{N} \left| \frac{C_n}{C_N} \right| r^{n-N}. \quad (2.37)$$

Finally, if one measures the normalized error spectrum at a give radius r_0 , the same spectrum can be computed at a different radius, r .

$$\left| \frac{B_n^*}{B_N^*} \right|_r = \left| \frac{B_n^*}{B_N^*} \right|_{r_0} \left(\frac{r}{r_0} \right)^{n-N}. \quad (2.38)$$

2.10 Simple Conformal Maps

The previous sections suggest that the characteristics of the different magnet types are mathematically related. Conformal mapping takes advantage of the similarities in the expressions for the various magnet types and allows the transformation of one type of magnet into another. Thus, one can extend the knowledge about the field distribution and uniformity of one type of magnet and map the boundary conditions which produce the distribution and uniformity into an entirely different magnet and predict the magnetic field characteristics of the mapped magnet. In this section, simple algorithms for mapping ideal multipole magnets into an ideal dipole geometry and reversing the mapping from dipole to multipole magnets are developed. These algorithms are used in the following chapter to extend canonical design rules associated with high quality dipole design to multipole magnets with equally high quality.

In the following discussions, two sets of coordinates are used; $z = x + iy$, the coordinates in the multipole space and $u = w + iv$, the coordinate system in the dipole space. For the multipole map to dipole space, Cartesian coordinate calculations are employed. For the reverse map from the dipole to the multipole space, polar coordinate calculations are employed.

2.10.1 Mapping Functions

The function of the complex variable, $F = C_n z^n = C_n |z|^n e^{in\theta}$, where C_n is real, yielded potential functions for $n = 1, 2$ and 3 , for the dipole, quadrupole and sextupole, respectively. The poles, selected from a scalar equipotential, are asymptotic to $\theta = 0$ and π for $n = 1$, asymptotic to $\theta = 0$ and $\frac{\pi}{2}$ for $n = 2$ and asymptotic to $\theta = 0$ and $\frac{\pi}{3}$ for $n = 3$. This suggests that a function which maps the multipole magnet into a dipole magnet should have the form, $w = \frac{z^n}{h^{n-1}}$. (The term in the denominator uses the aperture raised to a power such that the coordinate in the dipole space, w , remains linear.) The form of this function is suggested since, in polar coordinates for $z^n = |z| e^{in\theta}$, the angle domain is multiplied by n . Thus, the quadrupole angle domain, $0 \leq \theta \leq \frac{\pi}{2}$, is mapped into $0 \leq \phi = 2\theta \leq \pi$ and the sextupole angle domain, $0 \leq \theta \leq \frac{\pi}{3}$, is mapped into $0 \leq \phi = 3\theta \leq \pi$, where $0 \leq \phi \leq \pi$ is the angle domain of the dipole. (The multipole angle, θ , domain is mapped into the dipole angle domain, ϕ .)

2.10.2 Quadrupole to Dipole Map

The function describing the conformal map from the quadrupole to dipole space is

$$w = u + iv = \frac{z^2}{h} = \frac{(x + iy)^2}{h} = \frac{x^2 - y^2}{h} + i \frac{2xy}{h}. \quad (2.39)$$

Equating the real and imaginary parts, the coordinates of the quadrupole mapped into the dipole space are

$$u = \frac{x^2 - y^2}{h} \quad \text{and} \quad v = \frac{2xy}{h}. \quad (2.40)$$

Substituting the expression describing the quadrupole ideal pole contour, $xy = \frac{h^2}{2}$, $v = \frac{2xy}{h} = \frac{2h^2}{2h} = h$, a constant. The ideal quadrupole is mapped into the (u, v) coordinate space where $v = h = \text{constant}$, an ideal dipole.

2.10.3 Dipole to Quadrupole Map

For the dipole to quadrupole conformal map, using the pole coordinate form for the function

$$\begin{aligned} w &= |w| e^{i\phi} = \frac{z^2}{h} = \frac{(|z| e^{i\theta})^2}{h} = \frac{|z|^2}{h} e^{i2\theta} \\ |z| &= \sqrt{h |w|} \quad \text{and} \quad \theta = \frac{\phi}{2} \quad \text{and} \quad |w| = \sqrt{u^2 + v^2} \end{aligned} \quad (2.41)$$

$$x = |z| \cos \theta = \sqrt{h |w|} \cos \frac{\phi}{2} = \sqrt{h |w|} \sqrt{\frac{1 + \cos \phi}{2}} = \sqrt{h |w|} \frac{1 + \cos \phi}{2} \quad (2.41)$$

$$y = |z| \sin \theta = \sqrt{h |w|} \sin \frac{\phi}{2} = \sqrt{h |w|} \sqrt{\frac{1 - \cos \phi}{2}} = \sqrt{h |w|} \frac{1 - \cos \phi}{2}. \quad (2.42)$$

The expressions $\cos \phi = \frac{u}{|w|}$, then $\frac{1+\cos \phi}{2} = \frac{|w|+u}{2|w|}$ and $\frac{1-\cos \phi}{2} = \frac{|w|-u}{2|w|}$ are substituted.

The algorithms mapping the dipole $w = u + iv$ coordinates to the quadrupole, $z = x + iv$ coordinates are simplified and given by

$$x = \sqrt{\frac{h}{2} (|w| + u)} \quad \text{and} \quad y = \sqrt{\frac{h}{2} (|w| - u)}. \quad (2.43)$$

2.10.4 Sextupole to Dipole Map

The function describing the conformal map from the quadrupole to dipole space is $w = \frac{z^3}{h^2}$. Applying this map in Cartesian coordinates;

$$w = u + iv = \frac{z^3}{h^2} = \frac{(x + iy)^3}{h^2} = \frac{x^3 - 3xy^2}{h^2} - i \frac{y^3 - 3x^2y}{h^2}.$$

Equating the real and imaginary parts, the coordinates of the sextupole mapped into the dipole space are

$$u = \frac{x^3 - 3xy^2}{h^2} \quad \text{and} \quad v = -\frac{y^3 - 3x^2y}{h^2}. \quad (2.44)$$

Substituting eq. (2.29) which describes the sextupole ideal pole contour $3x^2y - y^3 = h^3$, then $v = \frac{h^3}{h^2} = h$, a constant. The ideal quadrupole is mapped into the (u, v) coordinate space where $u = h = \text{constant}$, an ideal dipole.

2.10.5 Dipole to Sextupole Map

For the dipole to sextupole conformal map, using the polar form for the coordinates

$$\begin{aligned} w &= |w| e^{i\phi} = \frac{z^3}{h^2} = \frac{(|z| e^{i\theta})^3}{h^2} = \frac{|z|^3}{h^2} e^{i3\theta} \\ |z| &= \sqrt[3]{h^2 |w|} \text{ and } \theta = \frac{\phi}{3} \text{ where } |w| = \sqrt{u^2 + v^2} \text{ and } \phi = \tan^{-1} \frac{v}{u}. \end{aligned}$$

The algorithms mapping the dipole $w = u + iv$ coordinates to the sextupole, $z = x + iv$ coordinates are given by

$$x = |z| \cos \theta = \sqrt[3]{h^2 |w|} \cos \frac{\phi}{3} \quad \text{and} \quad y = |z| \sin \theta = \sqrt[3]{h^2 |w|} \sin \frac{\phi}{3}. \quad (2.45)$$

2.10.6 Gradient Magnet to Dipole Map

Fig. 4 shows the gradient magnet pole as part of the ideal hyperbola computed using the gradient magnet requirements. The hyperbola has a horizontal asymptote at $y = 0$ and a vertical asymptote at $x = -\frac{B_0}{B'}$ and magnet aperture, h , at $x = 0$. It is convenient to introduce a displaced coordinate system $X = x + \frac{B_0}{B'}$, which has an origin at the vertical axis. The equation for the gradient magnet pole contour is given by eq. (2.31) ;

$$\begin{aligned} y(x) &= \frac{B_0 h}{B_0 + B' x} \\ y(X) &= Y = \frac{B_0 h}{B_0 + B' \left(X - \frac{B_0}{B'} \right)} = \frac{B_0 h}{B' X}. \end{aligned}$$

The equation for the hyperbola in the (X, Y) coordinate system then becomes $XY = \frac{H^2}{2} = \frac{B_0 h}{B'}$ where the radius of the quadrupole is given by $H = \sqrt{\frac{2B_0 h}{B'}}$. Performing the quadrupole to dipole map described earlier

$$\begin{aligned} w &= u + iv = \frac{Z^2}{H} = \frac{(X + iY)^2}{H} = \frac{X^2 - Y^2}{H} + i \frac{2XY}{H} \\ u &= \frac{\left(x + \frac{B_0}{B'} \right)^2 - y^2}{\sqrt{\frac{2B_0 h}{B'}}} \quad v = \frac{2XY}{H} = H = \sqrt{\frac{2B_0 h}{B'}}. \end{aligned} \quad (2.46)$$

Again, it is easy to see that this is an expression for an ideal dipole since $v = H$, a constant.

2.10.7 Dipole to Gradient Magnet Map

Using the results of the dipole to quadrupole transformation algorithms given in eq. (2.43);

$$X = x + \frac{B_0}{B'} = \sqrt{\frac{H}{2} (|w| + u)} \quad \text{and} \quad Y = y = \sqrt{\frac{H}{2} (|w| - u)}, \quad (2.47)$$

$$\text{where } H = \sqrt{\frac{2B_0 h}{B'}}, \text{ the radius of the displaced hyperbola.} \quad (2.48)$$

2.11 Chapter Closure

The differential equations required to characterize two dimensional magnet fields can be derived from Maxwell's general three-dimensional magnet equation. Using a

function of the complex variable, $z = x + iy$, the two-dimensional Poisson and Laplace equations can be derived from the three-dimensional expressions. The solution of the Laplace equation (the homogeneous form of the Poisson equation) characterizes the magnetic field in regions where current sources and permeable material are absent. Both two-dimensional magnetic fields and three-dimensional magnetic field integrals can be characterized by solutions of the two-dimensional Laplace equation. These solutions are relevant since charged beam interaction occurs in magnet gaps where conditions for the application of Laplace equation are satisfied. It is shown that all analytic functions of the complex variable $z = x + iy$, satisfy the Laplace equation. In particular, two forms of the solution, $F = A + iV$ and $F = Cz^n$, are discussed. The two dimensional magnetic field components can be computed by the same function, $B^* = B_x - iB_y = iF'(z)$, using either form of the function. The conventions used to interpret the two parts of the function, $F = A + iV$, the vector and scalar potentials, are discussed. Evaluation of the the vector and scalar potentials for the function, $F = C_n z^n$, for various values of the integer, n , provides mathematical expressions describing the magnetic flux distribution and the boundary conditions for different ideal multipole magnets. Since the function, $F = C_n z^n$, satisfies the Laplace equation, the Taylor expansion of this function, $F = \sum C_n z^n$, is also a solution of the differential equation. This form introduces the concept of the fundamental field and the spectrum of error multipoles. Application of symmetry conditions result in general rules concerning the allowed or systematic multipole errors associated with each fundamental field.

The final section of the chapter uses the similarity among the different functions defining the dipole, quadrupole and sextupole magnet types to develop simple conformal mapping algorithms. These algorithms are used in subsequent chapters as a powerful tool for the generalization of canonical pole tip design rules. The algorithms are also useful to map previously developed successful pole contours from one magnet geometry to another.

2.12 Problems

Problem 2.1 (Solution)

What is the equation for the ideal hyperbolic pole contour for a quadrupole with a pole radius of 35 mm? What is the equation for the ideal pole contour for a skew quadrupole with a pole radius of 35 mm?

Problem 2.2

What is the equation for the pole contour for a combined function magnet with central field $B_0 = 1.2\text{Tesla}$, gradient $B' = 3.5 \frac{T}{m}$ and half aperture $h = 25\text{mm}$? Draw the pole contour for a 100 mm wide pole. The gradient magnet pole is a portion of a much larger quadrupole hyperbolic pole. What is the quadrupole pole radius? What is the half gap for the dipole field mapped from this quadrupole?

Problem 2.3 (Solution)

Show that for poles symmetrical about their centerlines, the coefficients for the “allowed” error multipole functions of a complex variable are real and not complex. (Difficult but illustrative problem.)

Chapter 3

POLE TIP DESIGN

Perfect magnets can be built if the boundary conditions described in the previous chapter were practical. The imaginary parts of the function, $C_n z^n$, define ideal boundary conditions for different magnet types. These boundary conditions require a dipole with an infinitely wide flat pole and a quadrupole hyperbolic pole or sextupole cubic hyperbolic pole whose edges extend infinitely toward their asymptotes. These conditions are not practical in real magnets. Real magnets require finite poles whose edges result in imperfect boundary conditions yielding imperfect fields. Two dimensional design of the pole contour for various magnet types to satisfy field quality requirements is a crucial part of magnet design. Understanding of tools useful to visualize the field and to design the poles resulting in magnets with acceptable uniformity is an important part of magnet design.

This chapter introduces methods of understanding the field distribution in simple dipole magnets without having to understand the mathematics. An analog tool, useful for visualizing the field and suggesting means of improving field uniformity given practical non-ideal boundary conditions, is described. An example of the application of this model for the design conductor dominated magnet is presented to demonstrate the power of this tool.

Some canonical rules for the selection of the width of dipole magnet poles to satisfy field uniformity criteria are introduced. The methods of conformal mapping, introduced in the previous chapter, are exploited to extend the dipole rules to quadrupoles and gradient magnets. The effort of developing similar sextupole rules is left as an excercise for the reader.

3.1 Understanding the Dipole Magnet

Because of its simplicity, the dipole magnet is the easiest magnet to understand and visualize. Its ideal field is uniform, resulting in parallel, evenly spaced vector and scalar equipotential lines.

3.1.1 *The Orthogonal Analog Model*

A method for approximating the two-dimensional vector and scalar potentials is to use the orthogonal analog model. This method was originally described and named by Klaus Halbach[5], and provides a means for mapping scalar and vector equipotential

functions in a magnet gap when the iron and coil geometry are determined. This method can be used without having to understand the mathematics of the potential functions. Briefly, the principles of the orthogonal analog model are:

- Flow lines are analogous to the scalar equi-potentials.
 - Flow lines are drawn from the + to - coils.
 - Iron boundaries are impervious to the flow lines.
- Flux lines are analogous to the vector equi-potentials.
 - Flux lines are normal to the Flow lines.
 - Flux lines end and are approximately normal to iron boundaries.
- The combination of the family of flow lines and flux lines describe a set of curvilinear squares.

The Window-Frame Dipole Magnet

The window frame dipole magnet is one whose aperture is rectangular and whose coils are distributed uniformly in the vertical gap. It is conceptually the simplest dipole geometry. Physically, the coils for this magnet are difficult to wind. It requires a saddle coil to provide room for the charged beam particle orbit. Winding the coils for this geometry requires a table with two axes of rotation. Fig. 1 illustrates this geometry.

Results of the application of the principles of the Orthogonal Analog Model to this magnet geometry are shown in fig. 2. Using the principles of the model, it can be seen that the field is uniform over the entire magnet gap and extends to the edge of the coil as long as the current distribution is uniform.

A Conductor Dominated Dipole Magnet

Another example illustrating the principles of the orthogonal analog model is presented to demonstrate the power of this visual tool. The problem illustrated in Fig. 3 is to place conductor filaments along the inside radius of a circular iron yoke in a manner which will result in a uniform dipole field. The desired field is described by a series of uniformly spaced vertical flux lines. The orthogonal analog model rules require the flow lines to be uniformly spaced lines, perpendicular to the flux lines, originating in a positive current filament and ending in a negative current filament. It is then easy to place the conductor filaments at the ends of the flow lines. A later chapter, analyzing this same geometry, will show that the current distribution is a cosine current density distribution (see page 121).

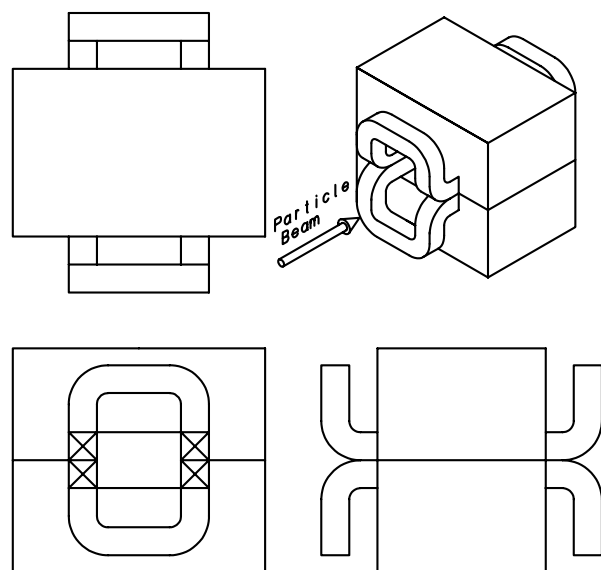


Figure 1 Window Frame Dipole

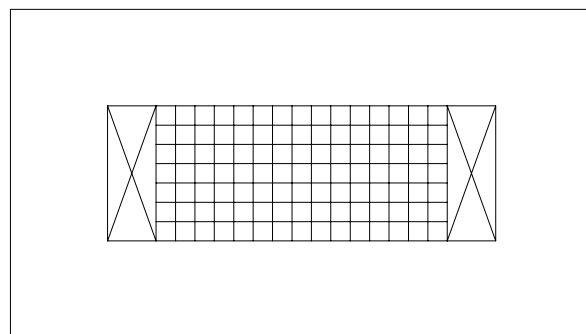


Figure 2 Window Frame Dipole

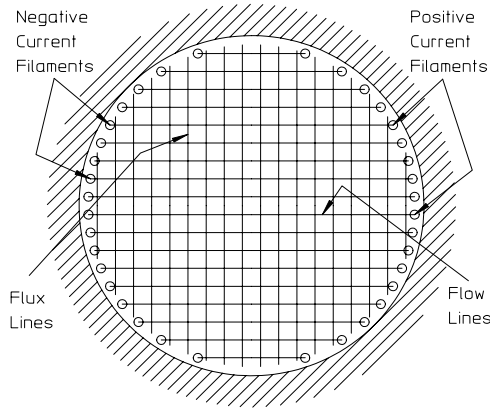


Figure 3 Conductor Dominated Field Distribution

3.1.2 The Orthogonal Analog Model and the Quadrupole

The orthogonal analog model is less useful for understanding the quadrupole magnet than for the dipole magnet since the ideal hyperbolic vector and scalar equipotential lines are quadratic hyperbolae. These contours are more complex than the uniform straight lines for an ideal dipole. Thus, the ideal contours for a uniform quadrupole field are more difficult to visualize. The mathematical conformal mapping algorithms developed in the last chapter are useful for designing a quadrupole magnet whose field quality corresponds to the uniformity of a window-frame dipole. The following example describing the means of designing a septum quadrupole demonstrates this technique.

The Septum Quadrupole

Colliders typically intersect high energy particle beams travelling in opposite directions crossing at narrow angles. In order to maximize the number of collisions, the two beams must be tightly focused with final focus lenses longitudinally close to the interaction point. Because of the small crossing angles between the two colliding beams, the particle beams are transversely very close to each other. Therefore, a quadrupole is required where the coil and a portion of the yoke are limited to a small lateral space between the colliding beams. A septum quadrupole is required for this application where the pole width is narrow and the coil is restricted to a small septum space between the intersecting beam spaces. Generally, the field quality of a quadrupole magnet can be improved by extending the pole edges towards their ideal asymptotes. Because of the space constraints, a septum quadrupole cannot take advantage of this design principle. A high quality quadrupole can be designed by using knowledge acquired about the performance of a uniform field dipole. The window frame dipole magnet and the results of mapping the geometry of this high

quality dipole to the quadrupole space are shown in fig 4.

The conformal mapping steps using eqs. (2.41) and (2.42), developed in the previous chapter for mapping a dipole to a quadrupole are described below:

- Consider the window frame dipole aperture with the centers of the separate conductors as illustrated.
 - The aperture is bounded by the half gap, H , and the half width, W .
- The ideal conductor placement for the window frame dipole requires uniform vertical spacing of their centers. The edge of the coil package is at the edge of the square aperture with $u = H$. The conductor centers locations are given by

$$(u_n, v_n) = \begin{pmatrix} H + H/6, H/6 \\ H + H/6, H/2 \\ H + H/6, 5H/6 \\ H + H/2, H/6 \\ H + H/2, H/2 \\ H + H/2, 5H/6 \end{pmatrix}.$$

- The iron inner boundary of the window frame dipole is mapped into the quadrupole space:

$$\text{Pole } x = \sqrt{\frac{h}{2}(|w| + u)}, \quad 0 \leq u \leq \frac{5H}{3} \quad v = H$$

$$\text{Side } u = \frac{5H}{3}, \quad 0 \leq v \leq H$$

$$x = \sqrt{\frac{h}{2}(|w| + u)} \quad \text{and} \quad y = \sqrt{\frac{h}{2}(|w| - u)}$$

$$x_{pole} = \sqrt{\frac{H}{2}(\sqrt{u^2 + H^2} + u)} \quad \text{for } 0 \leq u \leq \frac{5H}{3}$$

$$y_{pole} = \sqrt{\frac{H}{2}(\sqrt{u^2 + H^2} - u)}$$

$$x_{side} = \sqrt{\frac{H}{2} \left(\sqrt{\left(\frac{5H}{3}\right)^2 + v^2} + \frac{5H}{3} \right)} \quad \text{for } 0 \leq v \leq H$$

$$y_{side} = \sqrt{\frac{H}{2} \left(\sqrt{\left(\frac{5H}{3}\right)^2 + v^2} - \frac{5H}{3} \right)}$$

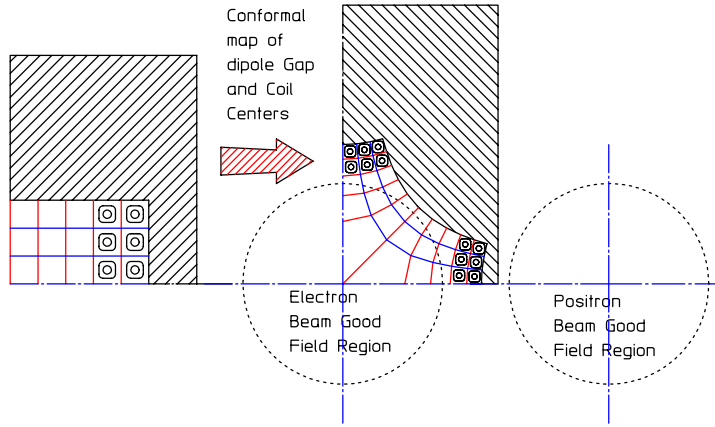


Figure 4 Window Frame Magnet and Mapped Septum Quadrupole

- The centers of the conductors are mapped into the quadrupole space. Note in fig. 4 that the separate conductors are centered in the curvilinear squares defined by the scalar and vector equipotentials for both the window frame dipole and the septum quadrupole.
 - The conductor shape does not have to be mapped since the current acts as point sources at the conductor centers:

$$x_n = \sqrt{\frac{H}{2} \left(\sqrt{u_n^2 + v_n^2} + u_n \right)} \quad \text{and} \quad y_n = \sqrt{\frac{H}{2} \left(\sqrt{u_n^2 + v_n^2} - u_n \right)}.$$

- The mapping for a septum quadrupole often results in small conductors spaced at close intervals. Often, in order to achieve the required quadrupole gradient, the current density is high, resulting in high power and difficulty in designing the hydraulic cooling circuits (see the discussion on page 128).

3.1.3 The “H” Dipole Geometry

The H-dipole geometry is one whose aperture is approximated by an H (see fig. 5). Its coils are installed in the vertical legs of the H-opening in the magnet yoke and the horizontal leg constitutes the magnet aperture. Most dipoles are built using this approximate configuration since the coils are easily wound in a single plane using a single axis winding fixture. The flat coil configuration is called a pancake coil. Fig. 6 illustrates the H-dipole configuration. Since the coils and the pole edges provide imperfect boundary conditions for a uniform dipole field, design work is required to improve the size of the aperture in which the field is uniform.

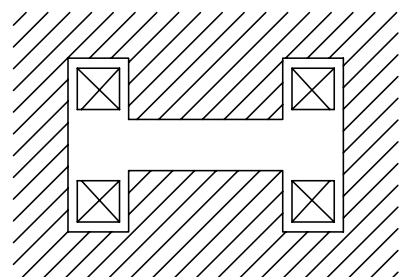


Figure 5 H-dipole aperture

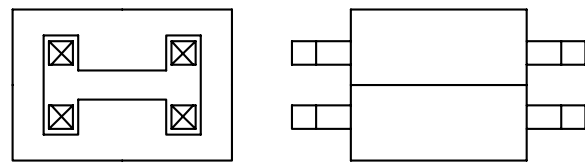
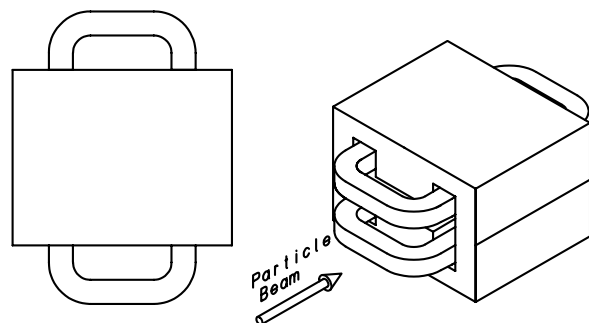


Figure 6 H-dipole

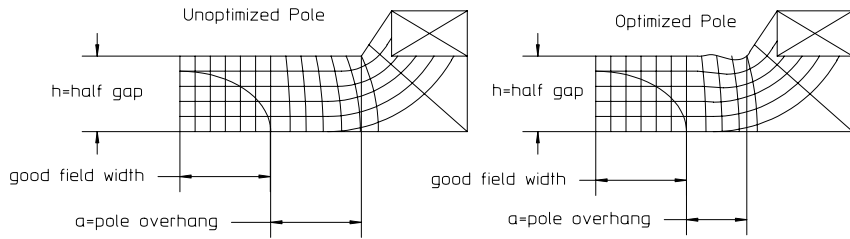


Figure 7 Orthogonal Analog Model of Unoptimized and Optimized H-Dipole

The orthogonal analog model, applied to two varieties of the H-dipole, is illustrated in fig. 7. The nomenclature describes the shape of the aperture where the coil is installed in the legs of the H and the gap is the horizontal leg of this configuration. This configuration is preferred over the window frame geometry because of the simpler flat pancake coil configuration.

Optimized and Unoptimized Pole Contours

Fig 7 describes an unoptimized and optimized pole contour. An unoptimized pole contour is flat all the way to the pole edge. An optimized pole contour is one with bumps near the pole edge to shape the field and increase the width of the uniform field region at the transverse center of the magnet.

For the unoptimized pole contour, the transition of the flow lines from the curved paths near the coil to a horizontal line near the center of the magnet is gradual. Thus, the uniform field region is limited to a small fraction of the pole width. In addition, the flow and flux lines crowd the sharp corner of the pole. This suggests that the field quality can be improved by adding smooth bumps near the edge of the pole, causing the flow lines to squeeze through a narrower gap and causing them to transition earlier to horizontal lines. This increases the fraction of the aperture with uniform field distribution. The smooth bumps also reduce the crowding of the flow and flux lines near the pole corner, reducing the saturation of the iron in this region.

3.1.4 H-Magnet Uniformity

The field uniformity in the required good field region of a dipole can be improved by adding excess pole beyond the edge of the good field region. This excess pole overhang extends the region of the ideal boundary conditions for a uniform dipole field. The excess pole beyond the edge of the required good field region is illustrated in fig. 7, labeled a , the pole overhang.

The canonical expressions[5] summarized in this section are used to estimate the amount of pole overhang required to achieve a desired field quality, or to estimate the field uniformity given the size of the pole overhang for both unoptimized and optimized pole contours. An unoptimized pole contour is a flat dipole pole. An

optimized pole contour is a dipole pole whose edges have been shaped to improve the field uniformity at the center of the aperture. The expressions for estimating the field uniformity or for the excess pole width to achieve a desired uniformity, given by eqs. (3.2) to (3.5), are approximate, but have been used successfully to estimate the required dipole pole width to satisfy field uniformity requirements. Successful application depends on the boundary conditions (the location of coils and pole edges) and the effort invested in the pole optimization process.

Dimensionless Pole Overhang Factor

In the following dimensionless expressions, x is the pole overhang normalized to the magnet half gap, h .

$$x = \frac{a}{h}. \quad (3.1)$$

Optimized Pole

The expressions for the potential field quality and the pole overhang required to achieve a specified field quality for an optimized pole are given in eqs. (3.2) and (3.3).

$$\left(\frac{\Delta B}{B} \right)_{optimized} = \frac{1}{100} \exp [-7.17(x - 0.39)] \quad (3.2)$$

$$x_{optimized} = \frac{a}{h} = -0.14 \ln \frac{\Delta B}{B} - 0.25 \quad (3.3)$$

Unoptimized Pole

The expressions for the potential field quality and the pole overhang required to achieve a specified field quality for an unoptimized pole are given in eqs. (3.4) and (3.5).

$$\left(\frac{\Delta B}{B} \right)_{unoptimized} = \frac{1}{100} \exp [-2.77(x - 0.75)] \quad (3.4)$$

$$x_{unoptimized} = \frac{a}{h} = -0.36 \ln \frac{\Delta B}{B} - 0.90 \quad (3.5)$$

Graph

These expressions are more easily used when the functions are graphed as shown in fig. 8.

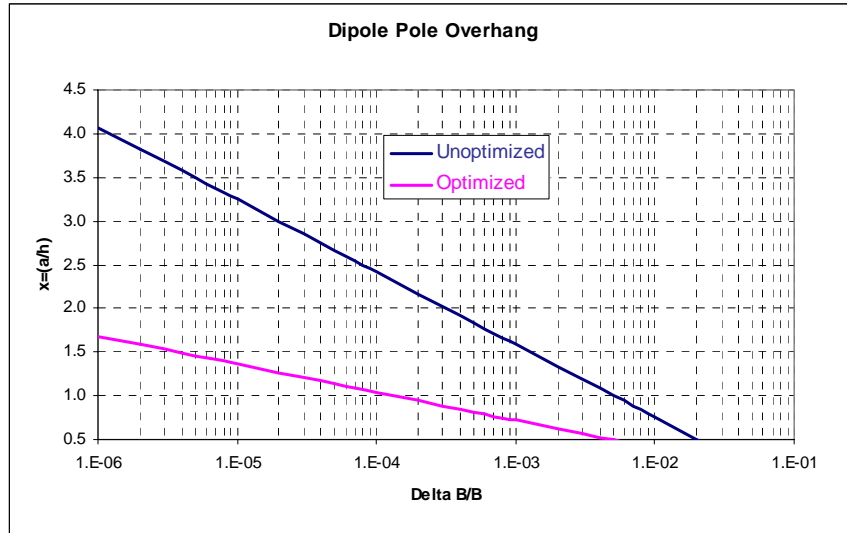


Figure 8 Pole Overhang for Required Field Uniformity

Dipole Optimization

The process of optimizing a dipole magnet pole contour is an iterative process requiring the use of a two dimensional magnet analysis code. An example of the process is described in more detail in a later chapter. Briefly, the process consists of the following steps:

1. Select a series of bumps (usually three) at and near the edge of a pole.
 - (a) Each bump shape is defined with a series of x and y coordinates with the y coordinates scalar fractions of a height parameter, H_n for each bump, where n is an index for the number of bumps. Most successful optimizations employ at least three bumps using three H_n 's for the optimization.
 - (b) The bumps overlap, so that the final pole shape is the sum of the bumps.
2. Each bump height parameter H_n , is varied and the magnet code is run and a performance function is measured. This performance function can be one of several computable factors.
 - (a) The first few of the allowed multipole errors and/or the square root of the sum of the squares of the multipole errors.
 - (b) The square root of the sum of the squares of the error fields at different positions at the boundary of the required good field region.
3. Compute the derivatives of the performance functions with respect to the height parameters.

4. Compute the H_n 's which minimizes the performance function.
5. Compute the bump shapes using 80% of the computed H_n 's and run the magnet code.
 - (a) Selection of 80% rather than the full value uses an under-relaxation method to ensure that the iterative process for this nonlinear relationship does not diverge or oscillate.
6. Using the new pole contour as a baseline, repeat steps 2 to 5 until the performance function is sufficiently small.

The steps described above are tedious. With some patience, pole tip optimization can be achieved for simple dipole geometries. Dipole pole tip optimization had previously been incorporated in the original UNIX version of the POISSON family of codes as a program called MIRT. However, this optimization program was not translated for the Windows version of the family of codes.

3.2 Understanding the Quadrupole Magnet

3.2.1 Quadrupole Uniformity

The expressions and graphs developed in the previous section provide tools for estimating the dipole pole width required for a magnet with a specified field uniformity. The mathematics of conformal mapping developed in Chapter 2 are employed to extend the knowledge about the design and performance of dipoles to quadrupoles.

Fig. 9 illustrates a quadrupole pole with pole radius h and required good field region defined by the radius, r_0 . It is useful to develop expressions for the location of the pole cutoff point, (x_c, y_c) , satisfying the requirement $\frac{\Delta B}{B} \leq$ a specified value within a region bounded by the radius of the good field region, r_0 . The quadrupole pole cutoff coordinate is analogous to the dipole pole edge. The location of this pole cutoff has important design implications. It affects the saturation characteristics of the magnet since the iron at the edge of the quadrupole pole is the first part of the pole to exhibit saturation effects as magnet excitation is increased. Also, it determines the width of the gap between adjacent poles and thus the width of the coil that can be installed for a two piece quadrupole. (The field quality advantages of a two piece quadrupole over a four piece quadrupole will be discussed in a later chapter).

Conformal Map

The expression for the function which conformally maps the quadrupole space to the dipole space is given in eqs. (2.39) and (2.40), $w = \frac{z^2}{h}$. Using this expression, the quadrupole good field radius, $|r_0|$, maps into the dipole good field radius $|w_0| = \frac{|r_0|^2}{h}$. The dipole pole illustration corresponding to the quadrupole pole illustration is shown in fig. 10.

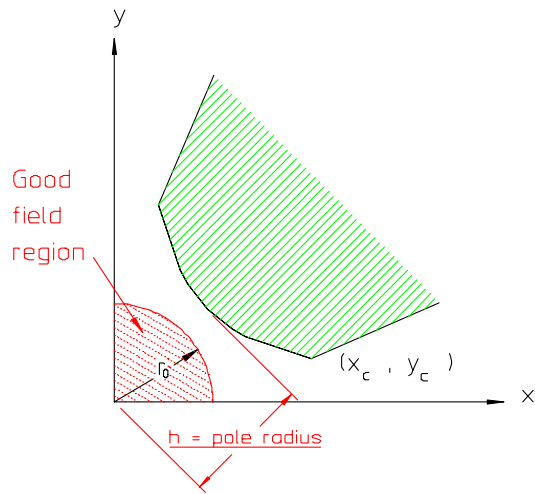


Figure 9 Quadrupole Pole Width

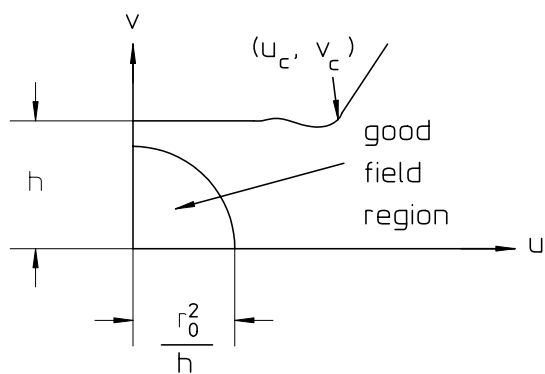


Figure 10 Mapped Dipole

For the dipole, the coordinates of the pole corner are given by $(u_c, v_c) = \left(\frac{r_0^2}{h} + a, h\right)$, where a can be computed using eqs. (3.2) and (3.3) or eqs. (3.4) and (3.5).

Using the shorthand version of these equations, $a = h[x_{optimized}]$ or $a = h[x_{unoptimized}]$, and $\rho_0 = \frac{r_0}{h}$ is a normalized good field radius, the normalized coordinate of the dipole pole corner is

$$\left(\frac{u_c}{h}, \frac{v_c}{h}\right) = \left(\rho_0^2 + \begin{bmatrix} x_{optimized} \\ x_{unoptimized} \end{bmatrix}, 1\right)$$

where $\begin{bmatrix} x_{optimized} \\ x_{unoptimized} \end{bmatrix} = \begin{bmatrix} -0.14 \ln \frac{\Delta B}{B} - 0.25 \\ -0.36 \ln \frac{\Delta B}{B} - 0.90 \end{bmatrix}$.

The expressions to map the dipole into the quadrupole are given by eqs. (2.41) and (2.42) and can be rewritten in the normalized form

$$\frac{x}{h} = \sqrt{\frac{1}{2} \left(\frac{|w|}{h} + \frac{u}{h} \right)} \quad \text{and} \quad \frac{y}{h} = \sqrt{\frac{1}{2} \left(\frac{|w|}{h} - \frac{u}{h} \right)}.$$

Since $\frac{|w|}{h} = \sqrt{\left(\frac{u}{h}\right)^2 + \left(\frac{v}{h}\right)^2}$ a final expression for the normalized coordinates of the quadrupole corner $\left(\frac{x_c}{h}, \frac{y_c}{h}\right)$ are

$$\frac{x_c}{h} = \sqrt{\frac{1}{2} \left(\sqrt{\left(\rho_0^2 + \begin{bmatrix} x_{optimized} \\ x_{unoptimized} \end{bmatrix}\right)^2} + 1 \right)} \quad (3.6)$$

$$\text{and } \frac{y_c}{h} = \sqrt{\frac{1}{2} \left(\sqrt{\left(\rho_0^2 + \begin{bmatrix} x_{optimized} \\ x_{unoptimized} \end{bmatrix}\right)^2} + 1 \right)} \quad (3.7)$$

The equations are graphed in a variety of formats. The normalized corner coordinates are shown in figs. 11 and 12. The expressions are graphed for both the optimized and unoptimized pole to illustrate the advantages of pole optimization. The quality at various good field radii are computed since the beam typically occupies different fractions of the aperture. Since the field for the quadrupole varies with the radius; $\frac{B_c}{B_{pole}} = \frac{|w_c|}{h} = \sqrt{\left(\frac{x_c}{h}\right)^2 + \left(\frac{y_c}{h}\right)^2}$, the flux density at the corner of the pole as a multiple of the flux density at the center of the pole tip can be computed and is illustrated in fig. 13.

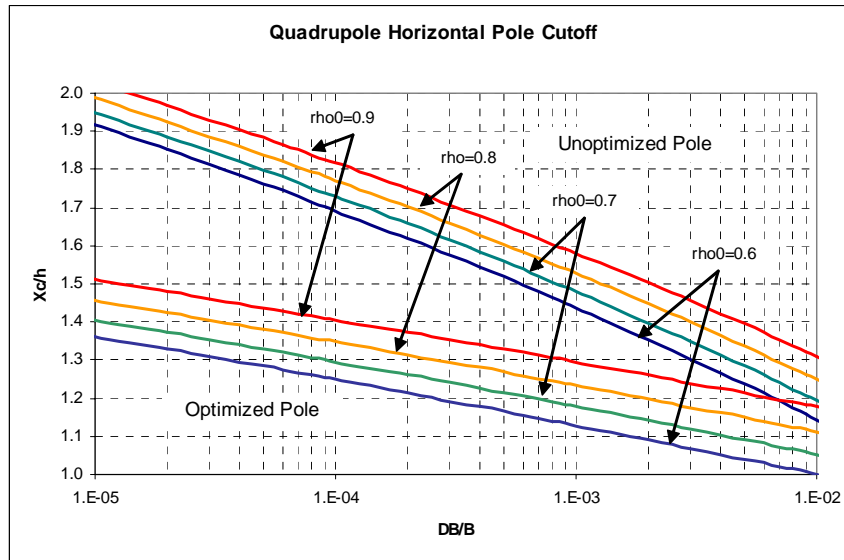


Figure 11 Horizontal Pole Cutoff

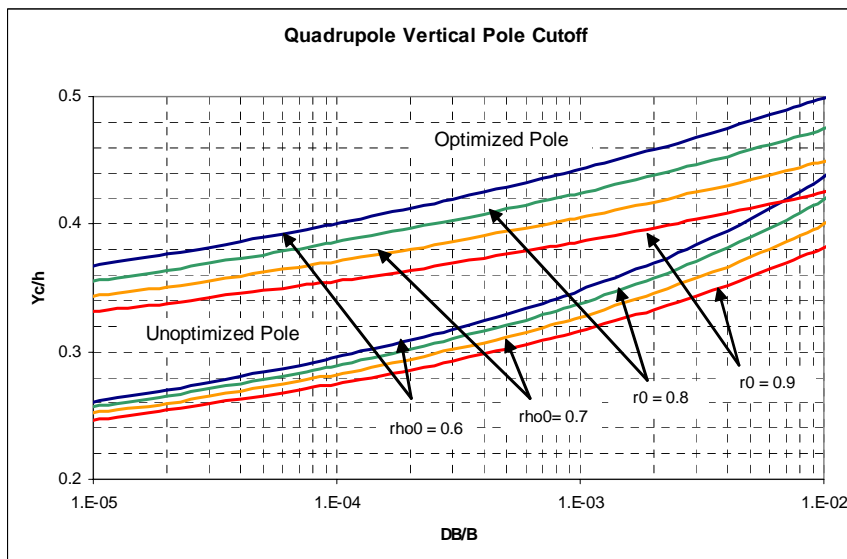


Figure 12 Vertical Pole Cutoff

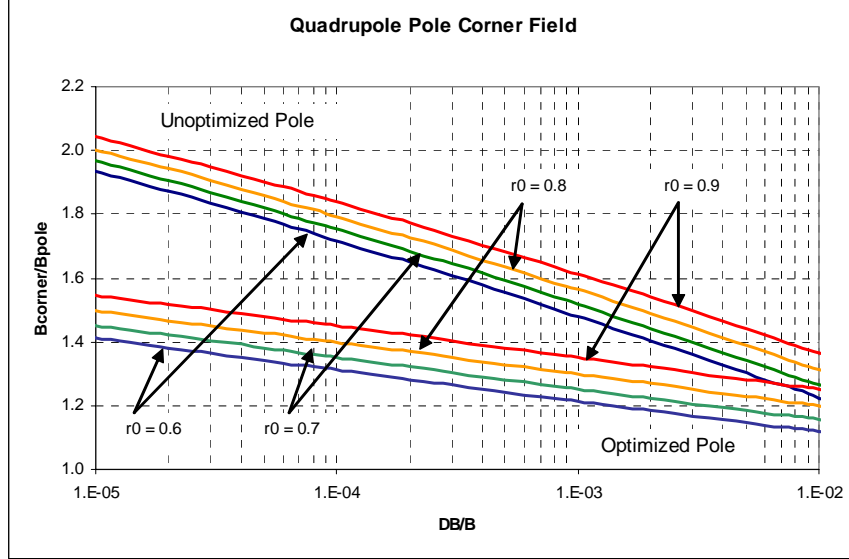


Figure 13 Pole Corner Field Ratio

3.3 Understanding the Gradient Magnet

3.3.1 Gradient Magnet Uniformity

Since gradient magnets are increasingly used in compact accelerators, similar relationships are derived allowing the calculation of the coordinates of the two edges of a gradient magnet pole with respect to the required good field region. As shown in an earlier chapter, the gradient magnet pole can be regarded as the edge of the pole of a very large quadrupole. In order to determine the coordinates of an ideal gradient magnet pole and its edges, the specified requirements for the magnet need to be known. These input variables are the central field, B_0 , the Gradient, B' , the vertical half gap at the magnet center, h , the half-width of the good field region, $|x_{GFR}|$, and the allowed normalized field error within the good field region, $\frac{\Delta B}{B}$. The gradient magnet pole is illustrated in fig. 14. Since the X coordinate is shifted and since the equation of the hyperbola is $XY = \frac{H^2}{2}$,

$$X = x + \frac{B_0}{B'} \quad \text{and} \quad Y = \frac{H^2}{2X} \quad \text{where } H = \sqrt{\frac{2B_0h}{B'}}.$$

Normalized to the quadrupole aperture,

$$\frac{X}{H} = \frac{x}{H} + \frac{B_0}{HB'} \quad \text{and} \quad Y = \frac{H}{2X}.$$

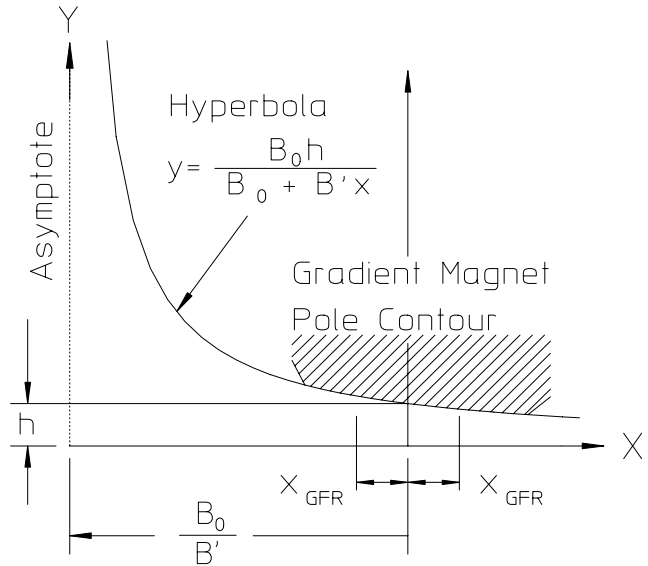


Figure 14 Gradient Magnet Pole in (X,Y) Coordinate System

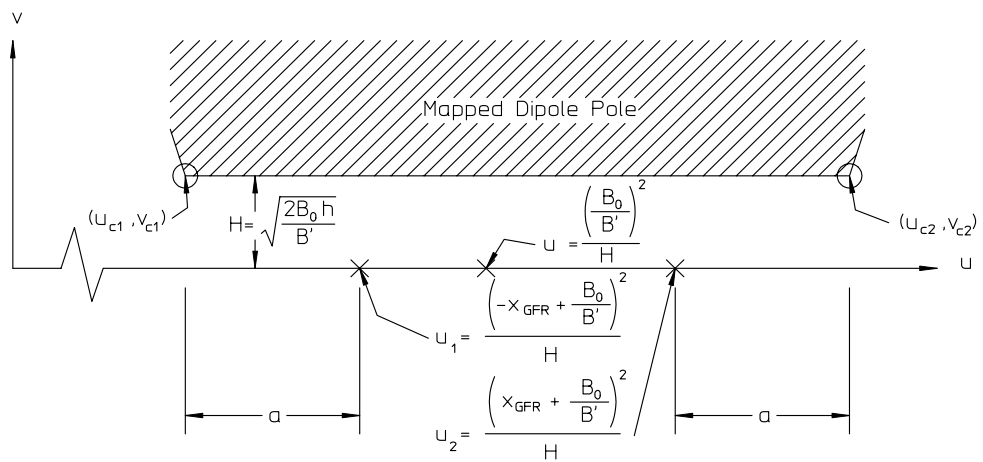


Figure 15 Mapped Dipole

The expressions derived in Chapter 1, $u = \frac{X^2 - Y^2}{H}$, for the conformal map of the dipole space to the quadrupole space are used. These expressions are normalized to the quadrupole “radius”, H , so that the unitless expressions can be used. The u coordinates of the left edge and right edge of the dipole, shown in fig. 15, u_1 and u_2 are;

$$\begin{aligned} u_1 &= \frac{X_{1 GFR}^2}{H} = \frac{\left(-x_{GFR} + \frac{B_0}{B'}\right)^2}{H} \\ u_2 &= \frac{X_{2 GFR}^2}{H} = \frac{\left(x_{GFR} + \frac{B_0}{B'}\right)^2}{H} \end{aligned}$$

and the coordinates of the pole edges are;

$$\begin{aligned} u_{c1} &= \frac{X_{1 GFR}^2}{H} - a = \frac{\left(-x_{GFR} + \frac{B_0}{B'}\right)^2}{H} - a \quad v_{c1} = H, \\ u_{c2} &= \frac{X_{2 GFR}^2}{H} + a = \frac{\left(x_{GFR} + \frac{B_0}{B'}\right)^2}{H} + a \quad v_{c2} = H, \\ \text{where } a &= H \begin{bmatrix} x_{optimized} \text{ or} \\ x_{unoptimized} \end{bmatrix}, \end{aligned}$$

where $x_{optimized}$ and $x_{unoptimized}$ are given by eqs. (3.3) and (3.5).

Written using normalized unitless coordinates.

$$\begin{aligned} \frac{u_{c1}}{H} &= \left(-\frac{x_{GFR}}{H} + \frac{B_0}{HB'}\right)^2 - \begin{bmatrix} x_{optimized} \text{ or} \\ x_{unoptimized} \end{bmatrix} \quad \frac{v_{c1}}{H} = 1 \\ \frac{u_{c2}}{H} &= \left(\frac{x_{GFR}}{H} + \frac{B_0}{HB'}\right)^2 + \begin{bmatrix} x_{optimized} \text{ or} \\ x_{unoptimized} \end{bmatrix} \quad \frac{v_{c2}}{H} = 1. \end{aligned}$$

$$\frac{|w|}{H} = \sqrt{\left(\frac{u}{H}\right)^2 + \left(\frac{v}{H}\right)^2} = \sqrt{\left(\frac{u}{H}\right)^2 + 1}.$$

$$\frac{|w_{c1}|}{H} = \sqrt{\left\{ \left(-\frac{x_{GFR}}{H} + \frac{B_0}{HB'} \right)^2 - \begin{bmatrix} x_{optimized} \\ x_{unoptimized} \end{bmatrix} \right\}^2 + 1}$$

$$\frac{|w_{c2}|}{H} = \sqrt{\left\{ \left(\frac{x_{GFR}}{H} + \frac{B_0}{HB'} \right)^2 + \begin{bmatrix} x_{optimized} \\ x_{unoptimized} \end{bmatrix} \right\}^2 + 1}.$$

Substituting using eqs. (2.41 and 2.42) for the conformal map from the dipole to the quadrupole space developed in the last chapter where $H = \sqrt{\frac{2B_0h}{B'}}$ is the quadrupole aperture radius;

$$X = x + \frac{B_0}{B'} = \sqrt{\frac{H}{2}(|w| + u)}, \quad Y = y = \sqrt{\frac{H}{2}(|w| - u)} \quad (3.8)$$

$$x_{c1} = -\frac{B_0}{B'} + \sqrt{\frac{H}{2}(|w_{c1}| + u_{c1})}, \quad y_{c1} = \sqrt{\frac{H}{2}(|w_{c1}| - u_{c1})}$$

$$x_{c2} = -\frac{B_0}{B'} + \sqrt{\frac{H}{2}(|w_{c2}| + u_{c2})}, \quad y_{c2} = \sqrt{\frac{H}{2}(|w_{c2}| - u_{c1})} \quad (3.9)$$

These equations are difficult to deal with and visualize. Therefore, a spreadsheet has been prepared to perform the calculations and compute and plot the pole contour and its edges given the required parameters, B_0 , B' , h , x_{GFR} , and $\frac{\Delta B}{B}$, which are input in the yellow cells in the spreadsheet. The green cells in the spreadsheet are computed values. (The indicated colors are not shown in this text but can be found in the Excel® spreadsheet.) Graphical results are updated in the spreadsheet illustrating the ideal hyperbolic gradient magnet pole and points on the edges required to achieve the required uniformity for a optimized and unoptimized pole. This spreadsheet is included in the CD attached to this publication. A sample page of the spreadsheet is shown in fig. 16.

3.4 Mapping an Existing Gradient Magnet Design

The previous section describes the means for applying the canonical rules for selecting an H type dipole pole width and applying these rules to the preliminary design of a gradient magnet pole contour. (The following discussion assumes that the magnet engineer/designer has elected to optimize the pole contour to minimize the pole width.) At some point, a great deal of effort is spent in developing a final pole contour with the required pole width and several bumps on each pole edge satisfying the requirements for a specific machine. b_0 (the central field), b' (the gradient), h (the

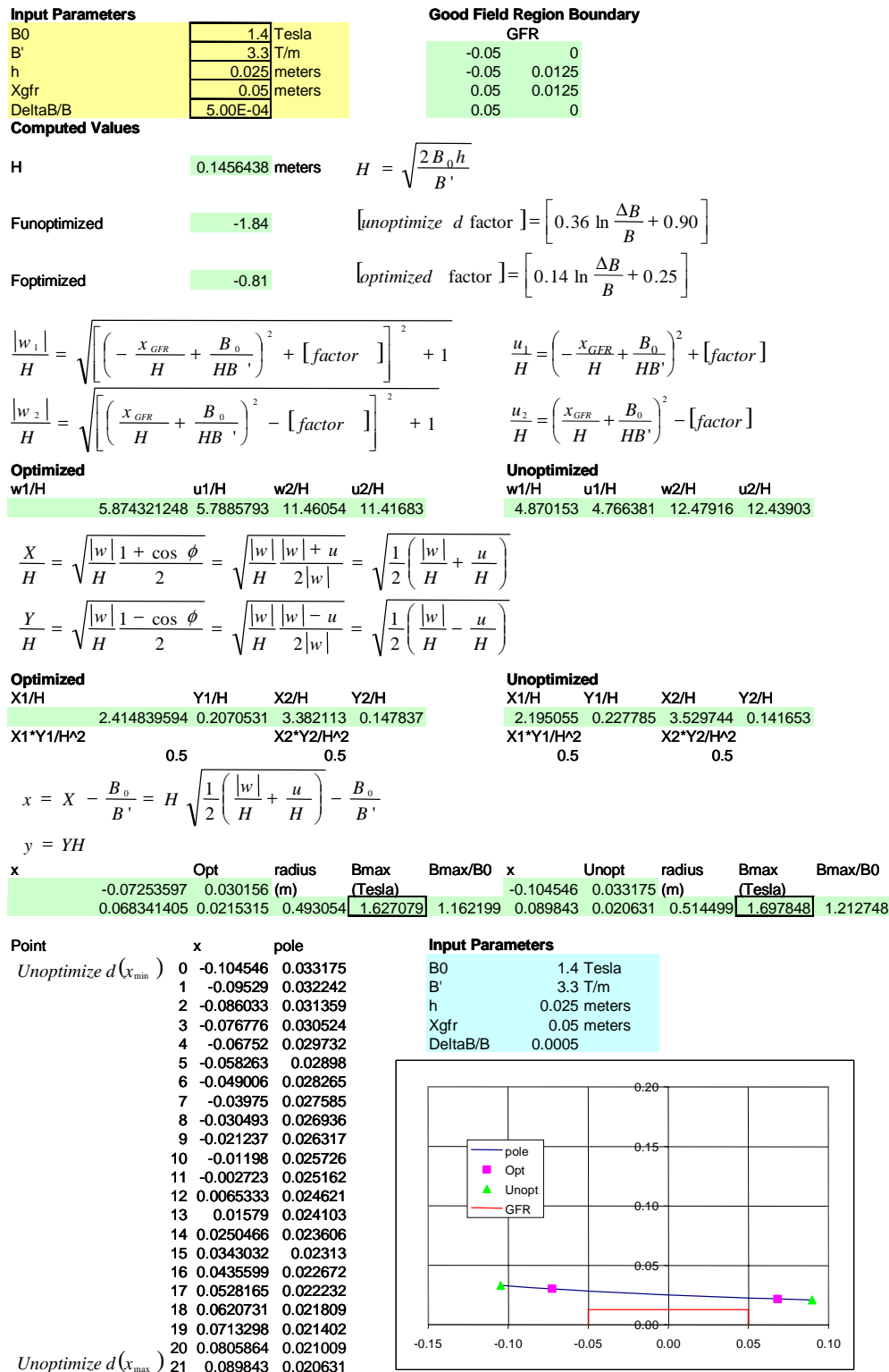


Figure 16 Gradient Magnet Edge Calculation Spreadsheet

aperture at the pole center), x_{gfr} (the half width of the good field region) and $\frac{\Delta B}{B}$ (the field uniformity) are the typical gradient two-dimensional magnet parameters required for a particular machine resulting in a set of optimized pole coordinates, (x_i, y_i) , where i is typically a large number representing the selection of many points on a pole contour. The optimized pole contour satisfies the field quality requirements, $\frac{\Delta B}{B}$, in the required good field region, $-x_{gfr} \leq x \leq +x_{gfr}$. (In this description, lower case letters are used to indicate the various parameters for a baseline design. One exception is for $\frac{\Delta B}{B}$. The field quality, $\frac{\Delta B}{B}$, is considered a generic requirement and assumed, in the following example, to be applied uniformly to all magnets.)

In this section, a process is described where a baseline pole contour, (x_i, y_i) , optimized originally for one application, is mapped to generate the pole contour coordinates, (X_j, Y_j) , where (in general) $j > i$, to satisfy entirely different design requirements (except for the uniformity) for another application. These requirements for the new application are listed as B_0 , B' , h_2 , X_{gfr} . (h_2 is lower case for the new contour. Capital H is reserved for the quadrupole aperture of the gradient magnet pole.) Much of the description of the mapping algorithm is graphically represented. Briefly, the process consists of the following steps.

1. Map the baseline gradient magnet pole into the dipole space.
2. Map the unoptimized new gradient magnet pole into the dipole space.
3. Scale the dipole map of the baseline pole so that it has the same gap as the mapped new gradient magnet pole.
4. Shift the transverse center of the scaled baseline dipole so that the new $\frac{B_0}{B}$ ratio is achieved.
5. Add (or subtract) from the center of the scaled and shifted dipole so that the new good field region is satisfied.
6. Map the mapped, scaled, shifted and center added (or subtracted) dipole back into quadrupole space.

The process is rather involved. However, the results are reasonably simple and elegant. The derivations can be skipped by the reader not specifically interested in the subject and one can simply use the algorithms presented at the end of this section. If a gradient magnet is required for a particular project, employing the mapping techniques described in this section can save a great deal of time. In addition, measurements from magnets mapped from an old design verifies that field quality can be successfully duplicated.

3.4.1 Baseline Optimized Pole

The design parameters for the baseline pole are $b_0 = 1.4 \text{ T}$, $b' = 3.6 \frac{T}{m}$, $h_1 = 0.035 \text{ m}$, $x_{gfr} = \pm 0.03 \text{ m}$, $\frac{\Delta B}{B} \leq 5 \times 10^{-4}$. The baseline optimized pole is shown in fig.17.

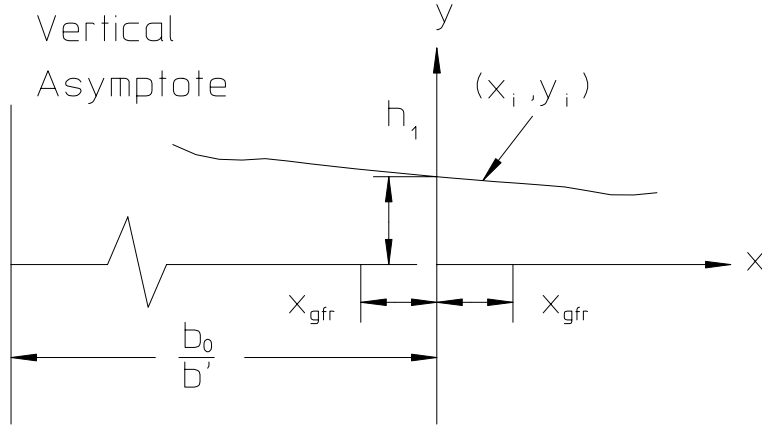


Figure 17 Baseline Gradient Magnet Pole

3.4.2 New **Unoptimized** Pole

The usual change in the specifications for a new magnet (and the parameters used for this example) is for a lower gradient, smaller half gap and a wider good field region. The design parameters for the new pole are $B_0 = 1.4 \text{ T}$, $B' = 3.3 \frac{\text{T}}{\text{m}}$, $h_2 = 0.020 \text{ m}$, $x_{gfr} = \pm 0.06 \text{ m}$, $\frac{\Delta B}{B} \leq 5 \times 10^{-4}$. The new unoptimized pole is shown in fig. 18.

3.4.3 Baseline Mapped Pole

The pole in the quadrupole $z = x+iy$ plane is mapped into the dipole $w = u+iv$ plane after the coordinate translation to the $X = x + \frac{b_0}{b'}$ is made. Using the expressions for the mapped dipole coordinates, $u = \frac{(X^2 - Y^2)}{H}$ and $v = \frac{XY}{H}$, the dipole coordinates of the baseline pole can be computed. The expressions for the mapped dipole pole and the edges of the good field region from the original optimized pole contour are

$$\begin{aligned} u_i &= \frac{\left(x_i + \frac{b_0}{b'}\right)^2 - y_i^2}{H_2}, \quad v_i = \frac{2XY}{H_1} = \frac{2\left(x_i + \frac{b_0}{b'}\right)y_i}{H_1}, \quad H_1 = \sqrt{\frac{2b_0h_1}{b'}} \\ u_1 &= \frac{\left(-x_{gfr} + \frac{b_0}{b'}\right)^2}{H_1}, \quad u_0 = \frac{\left(\frac{b_0}{b'}\right)^2}{H_1}, \quad u_2 = \frac{\left(+x_{gfr} + \frac{b_0}{b'}\right)^2}{H_1}. \end{aligned} \quad (3.10)$$

3.4.4 New Mapped Unoptimized Pole

Using the same mapping equation employed in the last section, the dipole coordinates of the new unoptimized pole and the edges of the new good field region are

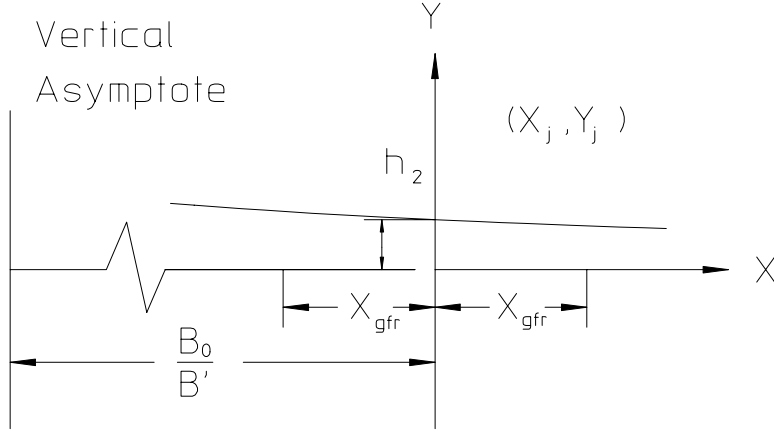


Figure 18 New Unoptimized Pole

$$\begin{aligned}
 U_i &= \frac{\left(X_i + \frac{B_0}{B'}\right)^2 - Y_i^2}{H_2}, \quad V_i = \frac{2XY}{H_2} = H_2, \quad H_2 = \sqrt{\frac{2B_0h_2}{B'}}, \\
 U_1 &= \frac{\left(-X_{gfr} + \frac{B_0}{B'}\right)^2}{H_2}, \quad U_0 = \frac{\left(\frac{B_0}{B'}\right)^2}{H_2}, \quad U_2 = \frac{\left(+X_{gfr} + \frac{B_0}{B'}\right)^2}{H_2}.
 \end{aligned}$$

The results of mapping both the baseline and the new unoptimized poles are shown in fig. 19.

3.4.5 Scaling and Shifting

If the optimized gradient magnet pole is to have the desired properties, the mapped optimized pole must be scaled so that the desired dipole gap is achieved. The good field boundaries and the centers are also scaled. (In this section, the capital U and V will be used for the final coordinates.) The expressions for the scaling are

$$U_{i-scaled} = \frac{H_2}{H_1} u_i, \quad V_{i-scaled} = \frac{H_2}{H_1} v_i.$$

Once the desired dipole gap is achieved, the center of the pole must be shifted

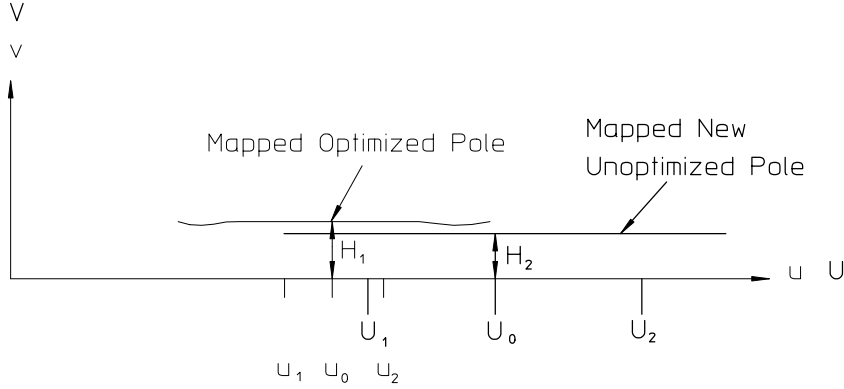


Figure 19 Baseline and New Unoptimized Pole

to achieve the proper central field gradient ratio. The expressions for the shift are

$$\begin{aligned} U_{i-scaled-shifted} &= \frac{H_2}{H_1} u_i + \left(U_0 - \frac{H_2}{H_1} u_0 \right) \\ V_{i-scaled-shifted} &= \frac{H_2}{H_1} v_i. \end{aligned}$$

The expressions for the scaled and shifted edges of the good field region are

$$\begin{aligned} U_{1-scaled-shifted} &= \frac{H_2}{H_1} u_1 + \left(U_0 - \frac{H_2}{H_1} u_0 \right), \\ &= \frac{H_2}{H_1} (u_1 - u_0) + U_0 \\ U_{2-scaled-shifted} &= \frac{H_2}{H_1} (u_2 - u_0) + U_0 \end{aligned}$$

3.4.6 Center Expansion

The scaled and shifted dipole contour, shown in fig. 20, has a good field region substantially narrower than the desired good field region for the new pole. Prior to mapping the contour into the quadrupole space, it is necessary to expand the center of the constant aperture dipole by the differences in the good field region to the left and to the right of the magnet center. The expressions for the expanded dipole

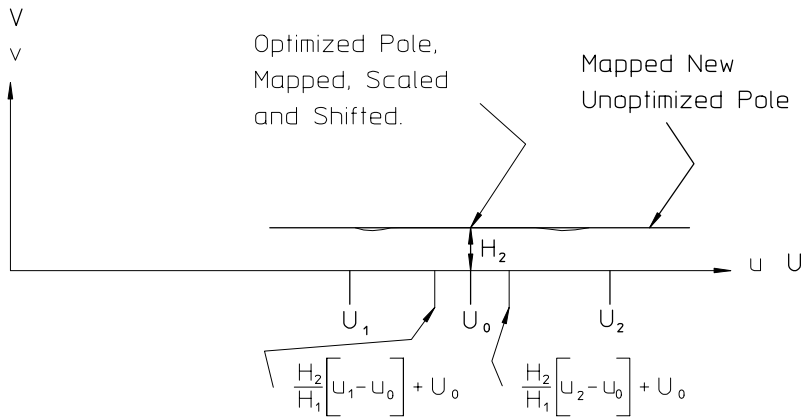


Figure 20 Mapped Dipole, Scaled and Shifted

coordinates are

$$\begin{aligned}
 U \begin{pmatrix} \text{i-scaled} \\ \text{shifted} \\ \text{left expanded} \end{pmatrix} &= \frac{H_2}{H_1} u_i + \left(U_0 - \frac{H_2}{H_1} u_0 \right) - \left[\frac{H_2}{H_1} (u_1 - u_0) + U_0 - U_1 \right] \\
 U \begin{pmatrix} \text{i-scaled} \\ \text{shifted} \\ \text{left expanded} \end{pmatrix} &= \frac{H_2}{H_1} (u_i - u_1) + U_1
 \end{aligned} \tag{3.11}$$

$$U \begin{pmatrix} \text{i-scaled} \\ \text{shifted} \\ \text{right expanded} \end{pmatrix} = \frac{H_2}{H_1} u_i + \left(U_0 - \frac{H_2}{H_1} u_0 \right) + \left[U_2 - \left(\frac{H_2}{H_1} (u_2 - u_0) + U_0 \right) \right]$$

$$U \begin{pmatrix} \text{i-scaled} \\ \text{shifted} \\ \text{right expanded} \end{pmatrix} = \frac{H_2}{H_1} (u_i - u_2) + U_2 \tag{3.12}$$

$$V_{i-scaled-shifted} = \frac{H_2}{H_1} v_i. \tag{3.13}$$

The vertical coordinates remain the same. Expanding the left and right sides of the good field region

$$U \begin{pmatrix} \text{1-scaled} \\ \text{shifted} \\ \text{expanded} \end{pmatrix} = \frac{H_2}{H_1} (u_1 - u_0) + U_0 - \left[\frac{H_2}{H_1} (u_1 - u_0) + U_0 - U_1 \right] = U_1$$

$$U \begin{pmatrix} \text{2-scaled} \\ \text{shifted} \\ \text{expanded} \end{pmatrix} = \frac{H_2}{H_1} (u_2 - u_0) + U_0 + \left[U_2 - \left(\frac{H_2}{H_1} (u_2 - u_0) + U_0 \right) \right] = U_2$$

the correct expressions for the required mapped good field regions are obtained.

3.4.7 Mapping Back into the Quadrupole Space

The final step in the process is mapping the dipole pole, derived from the existing optimized gradient magnet pole satisfying the initial requirements after it has been scaled, shifted and expanded, back into the quadrupole space. Eqs. (3.6), (3.6) and (3.6) are used and reviewed below;

$$X = x + \frac{B_0}{B'} = \sqrt{\frac{H}{2} (|W| + U)} \text{ and } Y = y = \sqrt{\frac{H}{2} (|W| - U)} \quad (3.14)$$

$$\text{where } H = H_2 = \sqrt{\frac{2B_0 h_2}{B'}} \quad (3.15)$$

$$U_{i-left} = \frac{H_2}{H_1} (u_i - u_1) + U_1 \quad U_{i-right} = \frac{H_2}{H_1} (u_i - u_1) + U_2 \quad (3.16)$$

$$V_i = \frac{H_2}{H_1} v_i \quad |W_i| = \sqrt{U_i^2 + V_i^2}. \quad (3.17)$$

In the above expressions, u_i and v_i are the left and right values of the mapped dipole coordinates computed for $x < 0$ and $x > 0$, respectively, from the original gradient magnet coordinates. The indices are changed in order to match the indices used in the mapped geometry. Additional points are needed at the center of the pole and are obtained by mapping a flat contour with aperture H_2 . The results of the mapping from one set of requirements to an entirely different set of requirements is illustrated in fig. 21.

3.5 Chapter Closure

This chapter begins by introducing the orthogonal analog model, a tool for visualizing the magnetic field potentials given the two-dimensional geometry of the magnet aperture and the coils. The utility of this tool is demonstrated by showing that a window frame magnet with coils uniformly spaced in the aperture can be conformally mapped to produce an almost perfectly linear quadrupole field. The conformal mapping tools, introduced in the previous chapter, are used to map the gap and individual conductors into quadrupole space supplying the boundary conditions so that

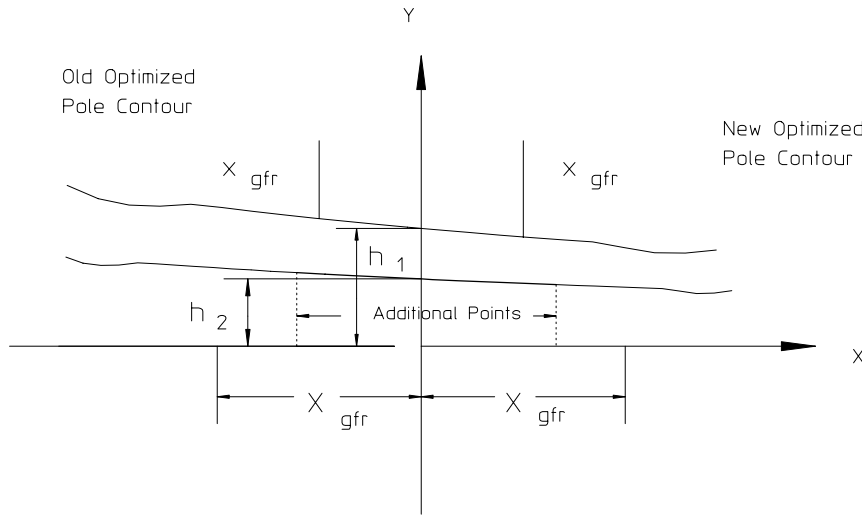


Figure 21 New Gradient Magnet Pole Mapped from an Old Optimized Pole

the potential functions are also mapped. The resulting quadrupole magnet achieves a nearly perfectly linear magnetic field distribution. This magnet is not without its difficulties. The mapping algorithms require the individual conductors to be placed precisely in their mapped locations which are not uniformly spaced, resulting in a challenging mechanical coil design. In addition, the current density required to achieve a practical gradient is high, resulting high power and a coil with many water circuits to dissipate the heat.

The window frame magnet with its inherently uniform field distribution is compared with the more commonly used H-magnet configuration. Application of the orthogonal analog model to the H-magnet suggests that uniform field is limited to the center of the pole. This configuration is used almost entirely in large accelerators since the coils can be economically wound as flat pancakes while the window frame magnets require more expensive saddle coils to provide room for beam tubes. Therefore, canonical rules have been developed which predict the field quality of flat and optimized poles or specify the pole width required to satisfy field quality requirements. Again, the orthogonal analog model can be used to estimate the size and shapes of the bumps at the pole edges to smooth out the flow lines and enhance (optimize) the field uniformity and reduce the flux concentration at the pole corners.

The conformal mapping algorithms, developed in the previous chapter, are exploited to extend the dipole rules for selecting the pole width to achieve a required field uniformity to quadrupole and gradient magnets. The graphs derived from the mapped expressions provide useful information regarding the preliminary designs of quadrupole and gradient magnet poles needed to achieve a desired field uniformity. The conformal mapping algorithms are exploited again, this time to take an existing

optimized gradient magnet pole, satisfying performance parameters for a single application, and map it into an entirely different geometry to achieve different performance parameters for a different application.

One can understand many families of magnets from his/her understanding of the simplest magnet geometry, the dipole. The dipole magnet is one which can be understood easily. The potential functions for the ideal dipole are straight and uniformly spaced and thus means of improving the fields are suggested instinctively. Therefore, the main task in pole tip design is to optimize a good dipole pole contour. Although the boundary conditions for the various magnet types (coil locations and angles at the pole edges) are not perfectly mapped, the pole contours for quadrupoles, sextupoles and gradient magnets can be mapped using the optimized dipole as a baseline. The field uniformity of the multipole magnets will nearly reproduce the performance of the baseline dipole.

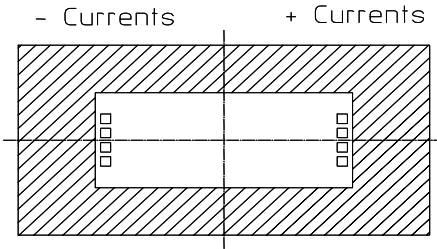


Figure 22 Orthogonal Analog Problem #1

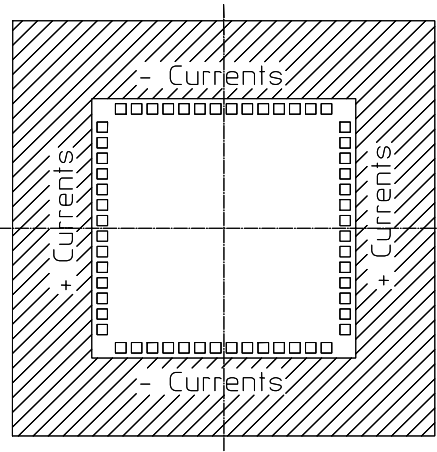


Figure 23 Orthogonal Analog Problem #2

3.6 Problems

Problem 3.1

Using the principles of the orthogonal analog model, plot the flow and flux lines for the illustrated dipole example shown in fig.(22). How would you characterize the field quality? What changes would you make either to the yoke design or the coil placement to improve the field quality?

Problem 3.2

Using the principles of the orthogonal analog model, plot the flow and flux lines for the illustrated magnet shown in fig. (23). Take advantage of the symmetry lines represented as the centerlines in the illustration.

From the flux line distribution, what type of magnet is this?

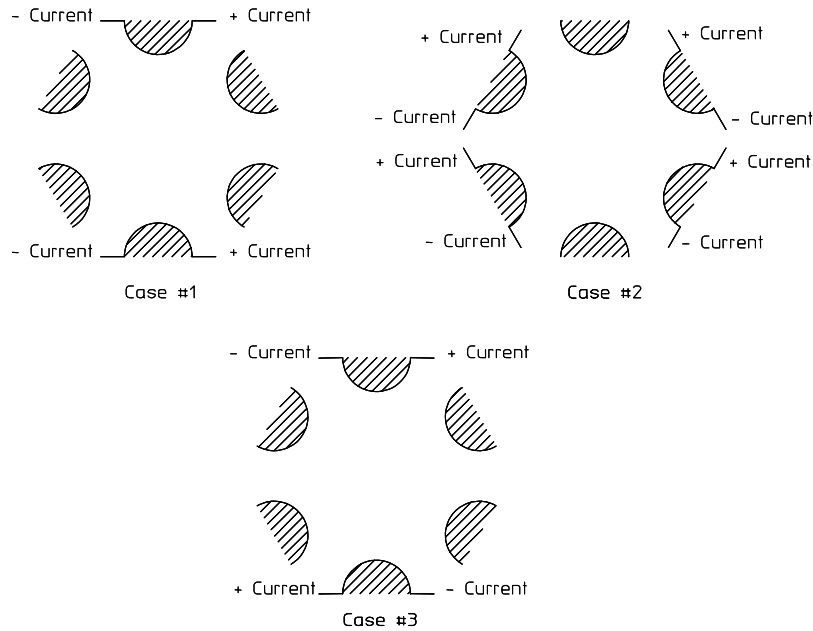


Figure 24 Sextupole Trim Configurations

Problem 3.3

For the sextupole yoke and the current distribution illustrated in fig. (24), use the principles of the orthogonal analog model to estimate the field distribution for the first of the three cases. What type of field is produced by case #1? For cases #2 and #3, determine the polarities indicated by the current directions and plot flux lines between the positive and negative (or neutral) poles. What type of fields are produced in cases #2 and #3?

Problem 3.4 (Solution)

For a 50 mm pole radius and a requiring $(\frac{\Delta B}{B})_{r=40mm} = 5 \times 10^{-4}$ and a gradient $B' = 12 \frac{T}{m}$, what is the maximum field on an unoptimized pole pole? What is the maximum field on an optimized pole? What is the maximum width of coil which can be installed in a two-piece quadrupole with an unoptimized pole? What is the maximum width of coil which can be installed in a two-piece quadrupole with an optimized pole? (Hint - Use the graphs - it's easier than computing.)

Chapter 4

PERTURBATIONS

4.1 Introduction

It was shown in a previous chapter that magnet fields can be characterized by a function of the complex variable written in the Taylor's series form, $F = \sum C_n z^n$.

In this chapter, formulae and tables in two papers by Dr. Klaus Halbach [6][7] are reproduced. Expressions and coefficients used to estimate the value of the change in the coefficients, ΔC_n , resulting from design assymtry or errors in mechanical, fabrication, assembly and/or excitation of magnet poles are summarized. The shorthand dimensionless expression $\frac{n}{N} \Delta C_n = \frac{n \Delta C_n}{N C_N} r_0^{n-N}$ is used to describe the ratio of the error field normalized to the fundamental field coefficient evaluated at the pole tip radius, r_0 . (The $\frac{n}{N}$ term is needed since the field ratios are ratios of the derivatives of the various terms, $C_n z^n$, and $\frac{d}{dz} C_n z^n = n C_n z^{n-1}$.) Constants for these normalized error fields due to various mechanical and excitation perturbations evaluated by Klaus Halbach are tabulated. These constants make it possible to compute the spectrum of normalized multipole errors due design assymetry and/or various mechanical, fabrication/assembly errors and pole excitation errors. Pole excitation errors, resulting from other factors rather than incorrect number of coil windings on a pole, are discussed and evaluated. Some of these excitation errors can result from differences in pole lengths and pole excitation differences in the scalar potential behind the coil due to mechanical assymetry. The error tables also list coefficients for $n = N$ and $n = N - 1$ so the expressions can be used to predict perturbations in excitation (the fundamental field) and the magnetic center displacement due to the mechanical and excitation errors.

The concept and the tools (the mathematical expressions) are extremely important since physics performance requirements are usually defined by the allowable maximum amplitude of the multipole error content of magnets, alignment specifications and required excitation precision. These physics requirements are defined by a spectrum of acceptable multipole errors, the spilloff multipole ($N - 1$) which characterizes the displacement of the magnetic center from the mechanical center and the fundamental field error, which affects the excitation and magnet to magnet reproducibility. Using the expressions and coefficients, it is possible to specify the fabrication/assembly tolerances which satisfy magnet physics requirements.

Finally, the expressions and the elements in the tables can be used to design trim coils which superimpose other desired fields in an existing magnet. Examples of trim windings on a sextupole yoke are presented.

4.2 Algorithms and Tables

Random multipole errors are introduced if the poles are improperly excited or assembly errors which displace poles are introduced. If these errors can be identified and measured, the resulting multipole content of the magnet can be predicted. The means for calculating these errors are summarized in two papers published by Klaus Halbach. The first paper describes the derivation of the relationships, the second computes and tabulates the coefficients used to calculate the multipole errors from the perturbations derived in the first paper. A portion of some selected tables of dimensionless coefficients are reproduced here and the algorithms for computing the field errors normalized to the fundamental at the pole tip radius are presented.

4.2.1 Quadrupole Pole Error Coefficients, $N=2$

The first table tabulates coefficients, x_n , for the computation of multipole fields, normalized to the fundamental field evaluated at the pole tip, for errors in the excitation, radial offset, azimuthal offset and pole rotation of individual poles for a quadrupole.

N=2, Quadrupole Individual Pole Coefficients				
n	$\frac{n}{N} \frac{\Delta C_n(j)}{i\varepsilon_j}$	$\frac{n}{N} \frac{\Delta C_n(rd)}{i\varepsilon_{rd}}$	$\frac{n}{N} \frac{\Delta C_n(az)}{\varepsilon_{az}}$	$\frac{n}{N} \frac{\Delta C_n(rot)}{\varepsilon_{rot}}$
1	1.99×10^{-1}	-4.25×10^{-1}	7.46×10^{-2}	1.76×10^{-1}
2	2.50×10^{-1}	-5.16×10^{-1}	2.14×10^{-1}	5.00×10^{-1}
3	1.57×10^{-1}	-2.88×10^{-1}	2.88×10^{-1}	6.60×10^{-1}
4	0	6.76×10^{-2}	2.31×10^{-1}	5.00×10^{-1}
5	-2.05×10^{-2}	1.08×10^{-1}	1.08×10^{-1}	1.91×10^{-1}
6	0	4.45×10^{-2}	2.87×10^{-2}	0
7	-1.61×10^{-2}	-1.04×10^{-2}	1.04×10^{-2}	-3.06×10^{-2}
8	0	1.28×10^{-2}	1.56×10^{-2}	0
9	-1.90×10^{-3}	1.25×10^{-2}	1.25×10^{-2}	7.53×10^{-3}
10	0	6.37×10^{-3}	5.81×10^{-3}	0
11	3.15×10^{-3}	-2.44×10^{-3}	2.44×10^{-3}	-3.62×10^{-3}
12	0	2.66×10^{-3}	2.79×10^{-3}	0
13	-2.45×10^{-4}	2.27×10^{-3}	2.27×10^{-3}	9.28×10^{-4}
14	0	1.26×10^{-3}	1.23×10^{-3}	0
15	6.69×10^{-4}	-5.55×10^{-4}	5.55×10^{-4}	-6.66×10^{-4}
16	0	5.76×10^{-4}	5.82×10^{-4}	0

4.2.2 Sextupole Pole Error Coefficients, $N=3$

The second table tabulates coefficients, x_n , for the computation of multipole fields, normalized to the fundamental evaluated at the pole tip, for errors in the excitation,

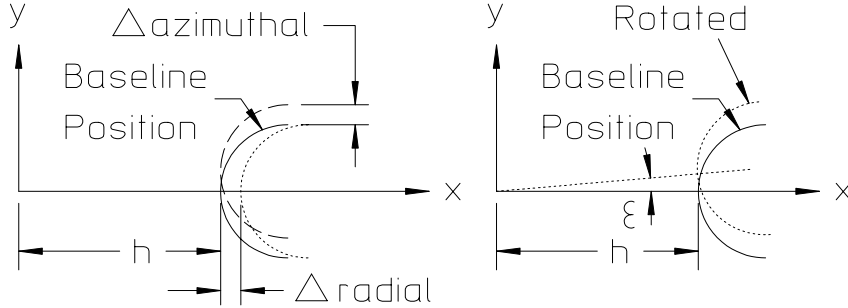


Figure 1 Individual Pole Mechanical Perturbations

radial offset, azimuthal offset and pole rotation of individual poles for a sextupole.

N=3, Sextupole Individual Pole Coefficients				
n	$\frac{n \Delta C_n(j)}{N i \varepsilon_j}$	$\frac{n \Delta C_n(rd)}{N i \varepsilon_{rd}}$	$\frac{n \Delta C_n(az)}{N \varepsilon_{az}}$	$\frac{n \Delta C_n(rot)}{N \varepsilon_{rot}}$
1	9.79×10^{-2}	-3.14×10^{-1}	5.09×10^{-2}	8.47×10^{-2}
2	1.56×10^{-1}	-4.95×10^{-1}	1.71×10^{-1}	2.84×10^{-1}
3	1.67×10^{-1}	-5.15×10^{-1}	3.03×10^{-1}	5.00×10^{-1}
4	1.33×10^{-1}	-3.90×10^{-1}	3.90×10^{-1}	6.39×10^{-1}
5	7.09×10^{-2}	-1.73×10^{-1}	3.97×10^{-1}	6.43×10^{-1}
6	0	6.55×10^{-2}	3.18×10^{-1}	5.00×10^{-1}
7	-1.34×10^{-2}	1.08×10^{-1}	1.95×10^{-1}	2.88×10^{-1}
8	-1.07×10^{-2}	9.03×10^{-2}	9.03×10^{-2}	1.08×10^{-1}
9	0	4.16×10^{-2}	2.51×10^{-2}	0
10	9.13×10^{-3}	-1.93×10^{-3}	1.90×10^{-3}	-3.38×10^{-2}
11	9.72×10^{-3}	-1.45×10^{-2}	5.49×10^{-3}	-2.05×10^{-2}
12	0	1.05×10^{-2}	1.31×10^{-2}	0
13	-1.01×10^{-3}	1.07×10^{-2}	1.36×10^{-2}	7.34×10^{-3}
14	-1.18×10^{-3}	9.85×10^{-3}	9.85×10^{-3}	5.82×10^{-3}
15	0	5.06×10^{-3}	4.56×10^{-3}	0

4.2.3 Computing Error Multipoles

The coefficients are computed for a pole whose baseline position is along the positive x-axis as shown in fig. 1.

Since the poles for normal multipole magnets are rotated an angle β from the horizontal axis, the fields relative to the horizontal coordinate axis for normal magnet poles located at angles, β , are calculated by an axis rotation $-n\beta$ for the individual poles at angle β . The error multipole normalized to the fundamental field evaluated

at the pole radius due to the errors of poles at an angle β from the positive x-axis is given by,

$$\left(\frac{B_n^*}{B_N^*} \right)_{@r=h} = \frac{n}{N} \Delta C_n e^{-in\beta}. \quad (4.1)$$

It is assumed that the fundamental field is real. Then, $B_{Nx} = 0$ and the expression can be rewritten;

$$\left(\frac{B_{nx} - iB_{ny}}{-iB_{Ny}} \right)_{@r=h} = \frac{n}{N} \Delta C_n e^{-in\beta},$$

or removing the imaginary term from the denominator,

$$\left(\frac{B_{ny} + iB_{nx}}{B_{Ny}} \right)_{@r=h} = \frac{n}{N} \Delta C_n e^{-in\beta}. \quad (4.2)$$

The expressions for the n^{th} normalized error multipole components due to a combination of all the perturbations of the pole located at angle β using the tabulated coefficients, are

$$\begin{aligned} \left(\frac{B_{ny} + iB_{nx}}{B_{Ny}} \right)_{@r=h} &= (i\varepsilon_j x_j + i\varepsilon_{rd} x_{rd} + \varepsilon_{az} x_{az} + \varepsilon_{rot} x_{rot}) e^{-in\beta}, \\ &= (i\varepsilon_j x_j + i\varepsilon_{rd} x_{rd} + \varepsilon_{az} x_{az} + \varepsilon_{rot} x_{rot}) (\cos n\beta - i \sin n\beta), \end{aligned} \quad (4.3)$$

where the x 's are the tabulated coefficients and the first two terms are multiplied by the $i \times$ the normalized mechanical and excitation errors and the last two terms are multiplied by the real error term. The real and skew error components can be computed by equating the real and imaginary parts of the expression and result in the skew and real multipole errors. All the mechanical and excitation errors are dimensionless and given by

$$\varepsilon_j = \frac{\Delta J}{J} \quad \varepsilon_{rd} = \frac{\Delta x}{h} \quad \varepsilon_{az} = \frac{\Delta y}{h} \quad \varepsilon_{rot} = \Delta \text{Angle (radians)}, \quad (4.4)$$

where ε_j is the expression for the excitation error, ΔJ , normalized to the nominal pole excitation, Δx and Δy are the horizontal and vertical offsets of the unrotated pole, normalized to the pole radius, h , and ε_{rot} is the rotation error (in radians) of the

individual poles about the center of the magnet. In general, the computation of the errors requires the characterization of the alignment and excitation errors of all the magnet poles with respect to a datum coordinate system. Thus, the expression for the n^{th} multipole error due to the mechanical alignment errors and excitation errors of all poles for a multipole magnet is,

$$\left(\frac{B_{ny} + iB_{nx}}{B_{Ny}} \right)_{@r=h} = \sum_{k=1}^N (i\varepsilon_{j,k}x_j + i\varepsilon_{rd,k}x_{rd} + \varepsilon_{az,k}x_{az} + \varepsilon_{rot,k}x_{rot}) (\cos n\beta_k - i \sin n\beta_k), \quad (4.5)$$

where $N = 4$ and $\beta_k = \frac{\pi}{4}, \frac{3\pi}{4}, \frac{5\pi}{4}$ and $\frac{7\pi}{4}$, for $k = 1, 2, 3$ and 4 for a quadrupole.

For the sextupole, $N = 6$ and $\beta_k = \frac{\pi}{6}, \frac{\pi}{2}, \frac{5\pi}{6}, \frac{7\pi}{6}, \frac{3\pi}{2}$, and $\frac{11\pi}{6}$, for $k = 1, 2, 3, 4, 5$ and 6 .

Using the expressions, one can compute the multipole spectrum resulting from excitation, fabrication and assembly errors provided that all the errors for each of the yoke segments can be accurately measured or identified. (The excitation error can result from mechanical errors in the length of individual poles, normalized to the nominal pole length as well as coil fabrication errors.) The computations for the effects of alignment and excitation errors for individual poles is tedious, complex and requires many terms. For a multipole with individual yoke pieces for each pole, the expression for multipole errors may contain 4^N terms for each multipole error, where N is the number of segments making up a single yoke assembly. (There are 4 degrees of freedom from each segment and for 4 quadrupole segments, the number of possible permutations is $4 \times 4 \times 4 \times 4$.) In addition, since both real and skew terms must be computed, the expression requires the computation of 2×4^N terms. This type of computation is seldom performed or needed. A more practical example of the use of this tool is presented in the discussion of a two piece quadrupole.

4.3 Two Piece Quadrupole

If the quadrupole yoke construction can be simplified so that the assembly is kinematic and fabrication or design errors can be predicted and/or measured, the algorithms for predicting the various multipole errors can be simplified. The obvious simplification is the reduction of the number of yoke segments to the smallest possible number satisfying assembly constraints. Assembly constraints include the requirement to provide room to install coils and vacuum chambers. A quadrupole yoke assembled from two pieces, each piece having two poles is such a simplification.

- The mechanical assembly errors can be limited to three degrees of freedom, $\Delta x, \Delta y$ and ε_{rot} errors of one half of the yoke with respect to the other.
- Errors can be predicted for assymetric designs forced by physics constraints.

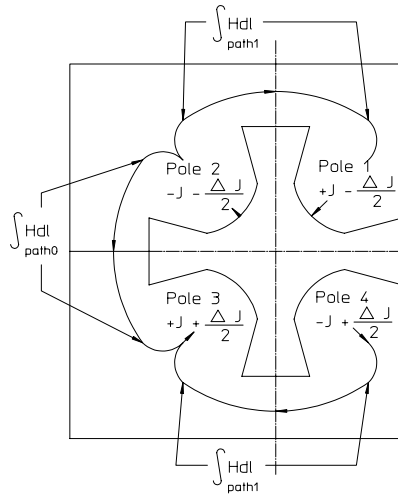


Figure 2 Assymmetric Quadrupole

- Mechanical fabrication errors can be limited to the differences in the lengths of each yoke segment.

In order to provide examples of the computations which the student can follow, the entries for a table coefficients for errors due to two cases are derived. The two examples selected are two dimensional yoke assymetry and fabrication errors which result in differences in the lengths of the two core segments. Table entries (derived in the cited references using similar techniques) are presented and not derived for the kinematic assembly errors, Δx , Δy and ε_{rot} .

4.3.1 Magnet Assymetry

Some of the concepts and formulations used in this section rely on the material covered more fully in the next chapter on pages 114 to 116. If unfamiliar with these concepts, this material may be reviewed by the student before proceeding with this section.

The first derived example assumes the magnet design is assymetric about the vertical centerline of the four poles. For synchrotron light electron accelerators, one side of the magnets must have room for the vacuum chamber housing the photon light generated by upstream bend magnets, wigglers or undulators. Because of this requirement, quadrupoles are occasionally constructed assymmetrically, causing the bases of the poles (the area behind the coils) to be at different scalar potentials. This is due to the differences in the lengths of the reluctance path through the iron. This is equivalent to reducing the current at two poles nearest the opening. The condition is illustrated in fig. 2.

The affect of this assymetry can be estimated by making a two dimensional magnetostatic calculation for the assymmetric condition and computing the difference

in the scalar potential on the top and bottom of the structure,

$$\Delta A = \Delta I = \int_{path1} H \cdot dl = \frac{1}{\mu_0} \int_{path1} \frac{B}{\mu} \cdot dl.$$

This is equivalent to reducing the magnitude of the excitation currents at the positive pole #1 and the negative pole #4. The effect on the multipole content can be computed using the tables for the individual poles and computing

$$|\varepsilon_a| = \frac{\int_{path1} H \cdot dl}{I}$$

(where ε_a signifies the error due to assymetry) for the two poles. Since the $\int_{path1} H \cdot dl$ has the effect of reducing the positive current at pole #1 and increasing the negative current at pole #2, the signs of the errors are both negative for poles #1 and #2. Moreover, in order to preserve computational symmetry, the errors are distributed to all four poles. The signs of the errors are both positive for poles #3 and #4. The perturbations are distributed with appropriate signs to each of the four poles. The values of the individual multipole errors from this error are computed using the expression;

$$\begin{aligned} \left(\frac{B_{ny} + iB_{nx}}{B_{Ny}} \right)_{@r=h} &= -i\frac{\varepsilon_a}{2}x_j e^{-in\frac{\pi}{4}} - i\frac{\varepsilon_a}{2}x_j e^{-in\frac{3\pi}{4}} + i\frac{\varepsilon_a}{2}x_j e^{-in\frac{5\pi}{4}} + i\frac{\varepsilon_a}{2}x_j e^{-in\frac{7\pi}{4}}, \\ &= i\frac{\varepsilon_a}{2}x_j \begin{pmatrix} -\cos n\frac{\pi}{4} + i\sin n\frac{\pi}{4} - \cos n\frac{3\pi}{4} + i\sin n\frac{3\pi}{4} \\ +\cos n\frac{5\pi}{4} - i\sin n\frac{5\pi}{4} + \cos n\frac{7\pi}{4} - i\sin n\frac{7\pi}{4} \end{pmatrix}, \\ &= \frac{\varepsilon_a}{2}x_j \begin{pmatrix} -i\cos n\frac{\pi}{4} - \sin n\frac{\pi}{4} - i\cos n\frac{3\pi}{4} - \sin n\frac{3\pi}{4} \\ +i\cos n\frac{5\pi}{4} + \sin n\frac{5\pi}{4} + i\cos n\frac{7\pi}{4} + \sin n\frac{7\pi}{4} \end{pmatrix}. \end{aligned}$$

Equating the real and imaginary parts of the expression

$$\begin{aligned} \left(\frac{B_{ny}}{B_{Ny}} \right)_{@r=h} &= \frac{\varepsilon_a}{2}x_j \left(-\sin n\frac{\pi}{4} - \sin n\frac{3\pi}{4} + \sin n\frac{5\pi}{4} + \sin n\frac{7\pi}{4} \right), \\ &= \varepsilon_a x_j \frac{Factor1}{2}, \\ \left(\frac{B_{nx}}{B_{Ny}} \right)_{@r=h} &= \frac{\varepsilon_a}{2}x_j \left(-\cos n\frac{\pi}{4} - \cos n\frac{3\pi}{4} + \cos n\frac{5\pi}{4} + \cos n\frac{7\pi}{4} \right), \\ &= \varepsilon_a x_j \frac{Factor2}{2}. \end{aligned}$$

In the following table, $\frac{\text{Factor1}}{2}$ is finite for all the odd indices. $\frac{\text{Factor2}}{2} = 0$ for all the even indices. Therefore, $\left(\frac{B_{ny}}{B_{Ny}}\right)_{@r=h}$ have only odd indices and $\left(\frac{B_{nx}}{B_{Ny}}\right)_{@r=h} = 0$ and the denominator for the error coefficients is real. In the following table, the coefficients computed for the assymetry conditions are;

$$\frac{n}{N} \frac{\Delta C_n(\text{rot})}{\varepsilon_a} = x_j \left(\frac{\text{Factor1}}{2} + i \frac{\text{Factor2}}{2} \right).$$

Assymetry Calculations				
n	$\frac{n}{N} \frac{\Delta C_n(j)}{i\varepsilon_j}$	$\frac{\text{Factor1}}{2}$	$\frac{\text{Factor2}}{2}$	$\frac{n}{N} \frac{\Delta C_n(\text{assymetry})}{\varepsilon_a}$
1	1.99×10^{-1}	$-\sqrt{2}$	0	-2.83×10^{-1}
2	2.50×10^{-1}	0	0	0
3	1.57×10^{-1}	$-\sqrt{2}$	0	-2.22×10^{-1}
4	0	0	0	0
5	-2.05×10^{-2}	$\sqrt{2}$	0	-2.90×10^{-2}
6	0	0	0	0
7	-1.61×10^{-2}	$\sqrt{2}$	0	-2.28×10^{-2}
8	0	0	0	0
9	-1.90×10^{-3}	$-\sqrt{2}$	0	2.69×10^{-3}
10	0	0	0	0
11	3.15×10^{-3}	$-\sqrt{2}$	0	-4.45×10^{-3}
12	0	0	0	0
13	-2.45×10^{-4}	$\sqrt{2}$	0	-3.46×10^{-4}
14	0	0	0	0
15	6.69×10^{-4}	$\sqrt{2}$	0	9.46×10^{-4}
16	0	0	0	0

From this table, it can be seen that the results of an assymetric quadrupole is to introduce real odd harmonic errors. These errors include the dipole ($n = 1$) error which displaces the magnetic center horizontally from the mechanical center of the quadrupole.

4.3.2 Differences in Lengths of the Upper and Lower Halves

The second derived example assumes the two halves of the magnets are different lengths. This is equivalent to increasing the integrated excitation of the two upper poles and decreasing the integrated excitation of the two lower poles. Since the polarities of the poles alternate, a positive current is added to positive pole #1, a negative current is added to the negative pole #2. Since the bottom two poles are shortened, a negative current is added to the positive pole #3 and a positive current

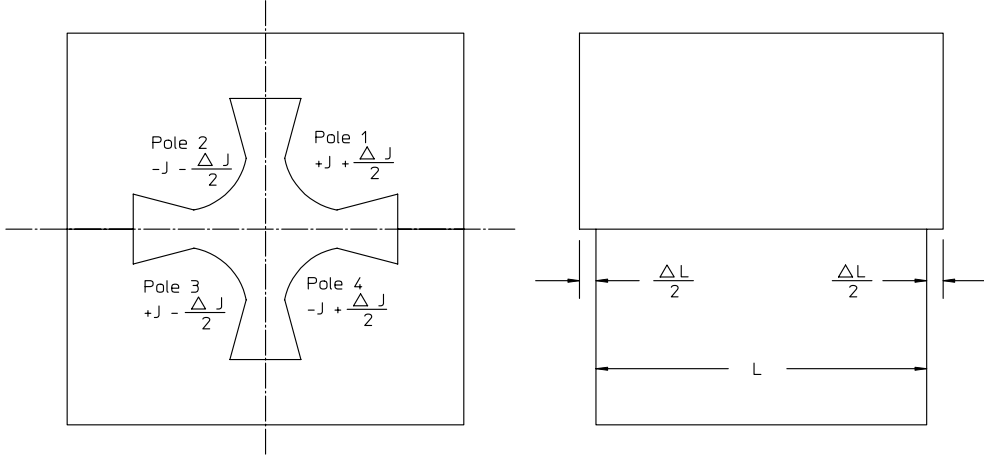


Figure 3 Differences in the Upper and Lower Half Lengths of a Two Piece Quadrupole

is added to the negative pole #4. The affect of this difference in length is computed assuming that $\varepsilon_j = \frac{\Delta L}{L}$ and assigning the proper sign for this error to each pole. These errors need to be distributed to all four poles so half the errors are assigned to each pole. The signs of the errors are both positive for poles #1 and #4 and both negative for poles #2 and #3. The condition is illustrated in fig. 3.

The values of the individual multipole errors from this error are computed using the expression,

$$\begin{aligned}
 \left(\frac{B_{ny} + iB_{nx}}{B_{Ny}} \right)_{@r=h} &= +i\frac{\varepsilon_l}{2}x_j e^{-in\frac{\pi}{4}} - i\frac{\varepsilon_l}{2}x_j e^{-in\frac{3\pi}{4}} - i\frac{\varepsilon_l}{2}x_j e^{-in\frac{5\pi}{4}} + i\frac{\varepsilon_l}{2}x_j e^{-in\frac{7\pi}{4}}, \\
 &= i\frac{\varepsilon_l}{2}x_j \begin{pmatrix} \cos n\frac{\pi}{4} - i \sin n\frac{\pi}{4} & -\cos n\frac{3\pi}{4} + i \sin n\frac{3\pi}{4} \\ -\cos n\frac{5\pi}{4} + i \sin n\frac{5\pi}{4} & \cos n\frac{7\pi}{4} - i \sin n\frac{7\pi}{4} \end{pmatrix}, \\
 &= \frac{\varepsilon_l}{2}x_j \begin{pmatrix} i \cos n\frac{\pi}{4} + \sin n\frac{\pi}{4} & -i \cos n\frac{3\pi}{4} - \sin n\frac{3\pi}{4} \\ -i \cos n\frac{5\pi}{4} - \sin n\frac{5\pi}{4} & i \cos n\frac{7\pi}{4} + \sin n\frac{7\pi}{4} \end{pmatrix}.
 \end{aligned}$$

Equating the real and imaginary parts of the expression,

$$\begin{aligned}
\left(\frac{B_{ny}}{B_{Ny}} \right)_{@r=h} &= \frac{\varepsilon_l}{2} x_j \left(\sin n \frac{\pi}{4} - \sin n \frac{3\pi}{4} - \sin n \frac{5\pi}{4} + \sin n \frac{7\pi}{4} \right) \\
&= \varepsilon_l x_j \frac{Factor3}{2}, \\
\left(\frac{B_{nx}}{B_{Ny}} \right)_{@r=h} &= \frac{\varepsilon_l}{2} x_j \left(\cos n \frac{\pi}{4} - \cos n \frac{3\pi}{4} - \cos n \frac{5\pi}{4} + \cos n \frac{7\pi}{4} \right), \\
&= \varepsilon_l x_j \frac{Factor4}{2}.
\end{aligned}$$

In the following table, $\frac{Factor3}{2} = 0$ for all the indices. $\frac{Factor4}{2}$ is finite for all the odd indices. Therefore, $\left(\frac{B_{ny}}{B_{Ny}} \right)_{@r=h} = 0$ and $\left(\frac{B_{nx}}{B_{Ny}} \right)_{@r=h}$ has finite values only for odd indices and the denominator for the error coefficients is imaginary. In the following table, the computed coefficients are;

$$\frac{n}{N} \frac{\Delta C_n (length)}{\varepsilon_l} = x_j \left(\frac{Factor3}{2} + i \frac{Factor4}{2} \right).$$

Since only $\frac{Factor4}{2}$ has finite values, the error coefficient is written

$$\frac{n}{N} \frac{\Delta C_n (length)}{i\varepsilon_l} = x_j \frac{Factor4}{2}.$$

Unequal Length Calculations				
n	$\frac{n}{N} \frac{\Delta C_n(j)}{i\varepsilon_j}$	Factor3	Factor4	$\frac{n}{N} \frac{\Delta C_n(\text{length})}{i\varepsilon_l}$
1	1.99×10^{-1}	0	$\sqrt{2}$	2.83×10^{-1}
2	2.50×10^{-1}	0	0	0
3	1.57×10^{-1}	0	$-\sqrt{2}$	-2.22×10^{-1}
4	0	0	0	0
5	-2.05×10^{-2}	0	$-\sqrt{2}$	2.90×10^{-2}
6	0	0	0	0
7	-1.61×10^{-2}	0	$\sqrt{2}$	-2.28×10^{-2}
8	0	0	0	0
9	-1.90×10^{-3}	0	$\sqrt{2}$	2.69×10^{-3}
10	0	0	0	0
11	3.15×10^{-3}	0	$-\sqrt{2}$	-4.45×10^{-3}
12	0	0	0	0
13	-2.45×10^{-4}	0	$-\sqrt{2}$	3.46×10^{-4}
14	0	0	0	0
15	6.69×10^{-4}	0	$\sqrt{2}$	9.46×10^{-4}
16	0	0	0	0

From this table, it can be seen that the results of a quadrupole with unequal half lengths is to introduce skew odd harmonic errors. These errors include the dipole error which displaces the magnetic center vertically from the mechanical center of the quadrupole.

4.3.3 Sorting

Although the previous section addresses the errors associated with mechanical fabrication errors resulting in different lengths of the two halves of a quadrupole yoke, similar errors can result from another fabrication practice. If the iron used in fabricating the two halves of the magnet are fabricated from iron with different chemistry or iron that is annealed differently, the fields in the two halves of the magnet, although excited with identical coils, can have different magnetic fields due to different saturation characteristics. This practice may result in the skew multipole errors with odd indices which change as the magnet excitation is increased. This potential source of error can be eliminated by using laminated iron for assembling the core segments and dividing (sorting) the laminations among the two core halves to ensure top to bottom material property symmetry. The lamination sorting practice can also enhance the magnet to magnet excitation reproducibility if the laminations stamped from different batches of iron sheet are divided among all the parts of all the magnets of the same family.

4.3.4 Two Piece Quadrupole Errors

The coefficients for the computation of multipole fields, normalized to the fundamental at the pole tip, for errors due to horizontal displacement, vertical displacement and rotation of the upper half of a two piece quadrupole with respect to the location of the lower half of a two piece quadrupole were computed in references[6][7] assuming that the poles are displaced or rotated symmetrically. These coefficients are computed assuming that the upper two poles are moved or rotated half the distance or angle in one direction and the lower two poles are moved or rotated half the distance or angle in the opposite direction. The effects on the error multipoles are characterized by the computed coefficients for the two piece quadrupole. The coefficients, x_n , tabulated for the two piece quadrupole are included in the following table along with the coefficients derived in the previous two sections.

The field errors using the tabulated coefficients are computed using the expression;

$$\left(\frac{B_{ny} + iB_{nx}}{B_{Ny}} \right)_{@r=h} = i\Delta_x x_x + \Delta_y x_y + \varepsilon_{rot} x_{rot} + \varepsilon_a x_a + i\varepsilon_l x_l \quad (4.6)$$

where,

$$\begin{aligned} x_x &= \frac{n}{N} \frac{\Delta C_n(x)}{i\Delta_x}, & x_y &= \frac{n}{N} \frac{\Delta C_n(y)}{\Delta_y}, & x_{rot} &= \frac{n}{N} \frac{\Delta C_n(rot)}{\varepsilon_{rot}}, \\ x_a &= \frac{n}{N} \frac{\Delta C_n(x)}{\varepsilon_a} \quad \text{and} \quad x_l &= \frac{n}{N} \frac{\Delta C_n(rot)}{i\varepsilon_l}, \end{aligned} \quad (4.7)$$

and,

$$\begin{aligned} \Delta_x &= \frac{\Delta x}{h}, & \Delta_y &= \frac{\Delta y}{h}, & \varepsilon_{rot} &= \text{rotation (radians)}, \\ |\varepsilon_a| &= \frac{\int H \cdot dl}{I} \quad \text{and} \quad \varepsilon_l &= \frac{\Delta L}{L}. \end{aligned} \quad (4.8)$$

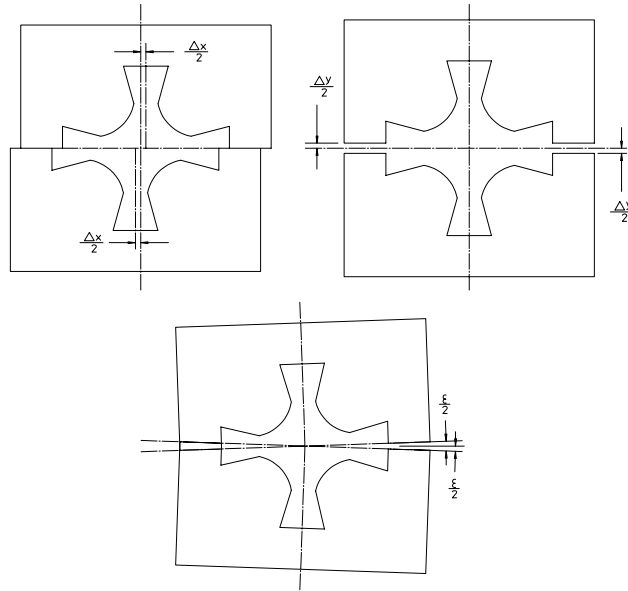


Figure 4 Quadrupole Horizontal, Vertical and Rotational Displacements

Two Piece Quadrupole Coefficients

$N = 2$					
n	$\frac{n}{N} \frac{\Delta C_n(x)}{i\Delta_x}$	$\frac{n}{N} \frac{\Delta C_n(y)}{\Delta_y}$	$\frac{n}{N} \frac{\Delta C_n(\text{rot})}{\varepsilon_{\text{rot}}}$	$\frac{n}{N} \frac{\Delta C_n(a)}{\varepsilon_a}$	$\frac{n}{N} \frac{\Delta C_n(l)}{i\varepsilon_l}$
1	0	0	2.49×10^{-1}	-2.83×10^{-1}	2.83×10^{-1}
2	3.02×10^{-1}	-7.30×10^{-1}	0	0	0
3	0	0	-9.33×10^{-1}	-2.22×10^{-1}	-2.22×10^{-1}
4	-9.56×10^{-2}	-3.27×10^{-1}	0	0	0
5	0	0	-2.70×10^{-1}	-2.90×10^{-2}	2.90×10^{-2}
6	-4.06×10^{-2}	-6.29×10^{-2}	0	0	0
7	0	0	-4.33×10^{-2}	-2.28×10^{-2}	-2.28×10^{-2}
8	1.81×10^{-2}	2.20×10^{-2}	0	0	0
9	0	0	1.06×10^{-2}	2.69×10^{-3}	2.69×10^{-3}
10	8.22×10^{-3}	9.01×10^{-3}	0	0	0
11	0	0	5.12×10^{-3}	-4.45×10^{-3}	-4.45×10^{-3}
12	-3.77×10^{-3}	-3.94×10^{-3}	0	0	0
13	0	0	-1.31×10^{-3}	-3.46×10^{-4}	3.46×10^{-4}
14	-1.74×10^{-3}	-1.78×10^{-3}	0	0	0
15	0	0	-9.41×10^{-4}	9.46×10^{-4}	9.46×10^{-4}
16	8.14×10^{-4}	8.23×10^{-4}	0	0	0

The displacements are illustrated in fig. 4.

4.3.5 Tolerances (*Examples of Computations*)

Given physics requirements, the mechanical fabrication and assembly tolerances can be calculated. In addition, if an assymetric design is selected, the minimum size of the yoke leading to saturation effects can be estimated. For the two piece quadrupole assembly, the tolerances are measureable and can be realistically defined. (This is not so easily accomplished for a four piece quadrupole.)

In the following sections, typical physics specifications for quadrupole magnets are used and the mechanical tolerances and limits on the two dimensional design are computed. These examples are presented to illustrate that realistic fabrication and assembly tolerances can be assigned based on physics specifications for magnets. All the following examples require the use of the tabulated coefficients for the quadrupole. Where a constant appears in the expressions used to compute the allowable assembly errors, these constants can be found as entries in the quadrupole ($N = 2$) table for two piece magnets shown on page (99).

4.3.6 Alignment Error

The example quadrupole has a 35 mm pole radius quadrupole and requires alignment of the magnetic center within $\pm 250 \mu m$ of its ideal position. In this example, the limits of the optical alignment system is $\pm 150 \mu m$, requiring the magnetic center to coincide with the mechanical center within $\pm 100 \mu m = \pm 0.1 mm$. The displacements of the quadrupole magnetic center depends on the dipole field at the mechanical center of the magnet and is given by;

$$|\Delta x| = h \left| \frac{B_{1y}}{B_2} \right| \quad \text{and} \quad |\Delta y| = h \left| \frac{B_{1x}}{B_2} \right|. \quad (4.9)$$

Rotation

The mechanical motion of a two piece quadrupole which results in a dipole field is the relative rotation of the upper half of the magnet relative to the lower half. This motion results in an error component of field, B_{1y} . The computation for this rotation tolerance is;

$$\begin{aligned} |\Delta x| &= h \left| \frac{B_{1y}}{B_2} \right|_h = h \varepsilon_{rot} x_{rot1} \leq \pm 0.1 mm, \\ \varepsilon_{rot} &\leq \pm \frac{0.1 mm}{35 mm \times 0.249} = \pm 0.0115 radians = \pm 11.5 mrad. \end{aligned}$$

Assymetry

If an assymetric magnet design is selected, the size of the yoke connecting two adjacent horizontal poles determines the losses, $\int_{path1} H \cdot dl$. Thus, if one selects a yoke whose

magnet efficiency is characterized by the value η , then,

$$\int_{pole} H \cdot dl + \int_{path1} H \cdot dl + \int_{pole} H \cdot dl = (1 - \eta) I.$$

(Magnet efficiency is explained more fully in the following chapter on page 116.) In particular, for a typical design;

$$\int_{path1} H \cdot dl \approx \left(\frac{1 - \eta}{2} \right) I,$$

since much of the losses due to saturation occurs at the root of the pole. Therefore, the error due to asymmetry can be written;

$$\varepsilon_a = \frac{\int_{path1} H \cdot dl}{I} = \frac{1 - \eta}{2}. \quad (4.10)$$

The computation for the magnet efficiency is;

$$\begin{aligned} |\Delta x| &= h \left| \frac{B_{1y}}{B_2} \right|_h = h \varepsilon_a x_{a1} \leq 0.1 \text{ mm}, \\ \varepsilon_a &= \frac{1 - \eta}{2} \leq \pm \frac{0.1 \text{ mm}}{35 \text{ mm} \times 0.283} = 0.0101, \\ 1 - \eta &\leq 0.0202 \\ \eta &\geq 1 - .02 = 0.98 = 98\%. \end{aligned}$$

Enough iron has to be supplied so that the losses in the iron yoke is $\leq 2\%$.

Yoke Length Difference

Suppose the 35 mm quadrupole core length is 200 mm. The computation for the length error is

$$\begin{aligned} |\Delta y| &= h \left| \frac{B_{1x}}{B_2} \right|_h = h \varepsilon_l x_{l1} \leq \pm 0.1 \text{ mm}, \\ \varepsilon_{rl} &= \frac{\Delta L}{L} \leq \pm \frac{0.1 \text{ mm}}{35 \text{ mm} \times 0.283} = \pm 0.0101, \\ \Delta L &\leq \pm 0.0101L = \pm 0.0101 \times 200 \text{ mm}, \\ \Delta L &\leq \pm 2 \text{ mm}. \end{aligned}$$

4.3.7 Excitation Error

Suppose the specification for a collection of the example 35 mm pole radius quadrupoles requires all magnet to have the identical gradient at a given current to $\leq 1 \times 10^{-3}$. This is a common requirement for magnet connected in series using a single power supply. Even for magnets using separate power supplies, this repeatability requirements allows the use of a common algorithm to compute the current required to achieve a given gradient for each of the magnets.

Since the even multipole errors are due to displacements of the upper half of the magnet relative to the lower half, the expression for the quadrupole errors are;

$$\left| \frac{\Delta B_2}{B_2} \right|_h = \begin{pmatrix} \Delta_x x_x = \frac{\Delta x}{h} x_{x2} \leq \pm 0.001 \\ \Delta_y x_y = \frac{\Delta y}{h} x_{y2} \leq \pm 0.001 \end{pmatrix},$$

$$\Delta x \leq \pm 0.001 \frac{35 \text{ mm}}{0.302} = \pm 0.116 \text{ mm},$$

$$\Delta y \leq \pm 0.001 \frac{35 \text{ mm}}{0.730} = \pm 0.048 \text{ mm}.$$

4.3.8 Random Multipole Error

The most important random multipole errors are those with the lowest indices. This is because the errors vary as r^{n-2} for the quadrupole. Thus, the sextupole error reduces linearly and the octopole error reduces quadratically with the radius. It is seldom necessary to define fabrication or assembly tolerances based on the multipole error specifications for indices > 4 .

Sextupole Error

The specification for the amplitude of a random multipole requires that its amplitude evaluated at the good field radius (gfr) . $\left| \frac{B_n}{B_N} \right|_{gfr} \leq 2 \times 10^{-4}$. Since

$$\left| \frac{B_n}{B_N} \right|_r = \left| \frac{B_n}{B_N} \right|_h \left(\frac{r}{h} \right)^{n-N},$$

the expression for the alignment tolerance to limit the amplitude of the sextupole (the largest) error field can be written;

$$\left| \frac{B_n}{B_N} \right|_r = \left| \frac{B_n}{B_N} \right|_h \left(\frac{r}{h} \right)^{n-N} \leq 2 \times 10^{-4},$$

$$\varepsilon_{rot} x_{rot} \left(\frac{r}{h} \right)^{3-2} = \varepsilon_{rot} x_{rot} \frac{r}{h} \leq 2 \times 10^{-4}.$$

Suppose the good field radius is 80% of the pole radius. The expression for Δrot can be rewritten;

$$\begin{aligned}\varepsilon_{rot} x_{rot3} \times 0.8 &\leq 2 \times 10^{-4}, \\ \varepsilon_{rot} &\leq \frac{2 \times 10^{-4}}{0.8 \times 0.933} = 0.0003 \text{ radians} = 0.3 \text{ mrad.}\end{aligned}$$

Octopole Error

The expression for the alignment tolerance to limit the amplitude of the octopole (the second largest error field can also be written;

$$\begin{aligned}\left| \frac{B_n}{B_N} \right|_r &= \left| \frac{B_n}{B_N} \right|_h \left(\frac{r}{h} \right)^{n-N} \leq 2 \times 10^{-4}, \\ \Delta_y x_y \left(\frac{r}{h} \right)^{4-2} &= \frac{\Delta y}{h} x_y \left(\frac{r}{h} \right)^2 \leq 2 \times 10^{-4}, \\ &= \frac{\Delta y}{h} x_y \times 0.8^2 \leq 2 \times 10^{-4}, \\ \Delta y &\leq \frac{2 \times 10^{-4} \times 35 \text{ mm}}{0.64 \times 0.327} = 0.033 \text{ mm.}\end{aligned}$$

These example show that, for the typical physics requirements, the quadrupole assembly tolerances are quite stringent (a few tens of microns and a few hundreds of microradians).

The assymetry and length errors for the two piece quadrupole also result in odd harmonics. However, the most difficult specification is usually reflected in the largest value of the coefficient. Since the coefficients x_a and x_l are smaller than x_{rot} and x_y , the tolerances for the assymetry and length errors are not calculated.

Orthogonality

Close inspection of the distribution of the table of coefficients on page 99 for the two piece quadrupole reveals that many of the errors are orthogonal.

- Δx assembly errors result in skew (imaginary) error multipoles with even indices.
- Δy assembly errors result in real error multipoles with even indices.
- ε_{rot} , relative rotation errors, result in real error multipoles with odd indices.
- ε_a , assymmetric designs, result in real error multipoles with odd indices.
- ε_l , length errors, result in skew (imaginary) error multipoles with odd indices.

Thus, it is possible to isolate the causes of the random multipole errors by close inspection of magnetic measurement data and to correct them. In addition, since the errors for assymetric design and rotation of the two halves are not orthogonal, one can devise means of correcting some errors due to assymetric design by intentionally introducing a rotation error among the two magnet halves. In general, the strategy selected is to compute the pole rotation required to compensate for the sextupole field ($n = 3$) and compute or measure the center offset (the dipole field). Compensation for this offset can be achieved by installing the magnet with a small transverse misalignment.

4.4 Sextupole Trim Windings

Particle accelerator lattice designs are usually compact. Selection of compact lattices result from efforts to reduce construction and operating costs. Facility costs are proportional to the building area housing the accelerator and vary with the square of the lattice ring radius. The costs of magnet power supplies vary with the required power ($\propto I^2$). These costs as well as operating power costs vary quadratically with dipole magnet half gaps, as h^4 for quadrupole pole tip radius and as h^6 for sextupole pole tip radius. Magnet gaps can increase with distance between magnets and thus with the lattice size. (Maintaining the same magnet gap with increasing drift space requires higher focusing element excitation and more power.) In addition to the power supply costs, the costs of magnet power distribution (cabling) and power supply operating costs and cooling system costs increase with lattice size. Because of desires to minimize construction and operating costs, the longitudinal distances between adjacent magnets is kept as small as possible. Consequently, adequate longitudinal space for separate corrector magnets is often either overlooked or intentionally eliminated. Because of this, separate correctors are eliminated and corrector trim windings are incorporated in other magnets. Compact accelerator lattices often include sextupole magnets with one, two or a combination of all three horizontal steering, vertical steering and/or skew quadrupole trim windings. In this section, the current perturbation coefficients for the sextupole magnet individual poles are used to compute the required excitation as well as the multipole error content of the various trim fields incorporated in a sextupole yoke.

4.4.1 Orthogonality

Since the sextupole yoke is primarily designed to supply sextupole field, a desired feature of trim fields is orthogonality to the sextupole field. That is, the excitation of a trim field should not alter the primary sextupole field. The windings for the horizontal steering trim field requires a turns ratio among the windings for the six coils which nulls the sextupole field. The four coils required to excite the vertical steering and the two coils for the skew quadrupole fields are naturally orthogonal to the sextupole field. For this reason expressions for the horizontal trim field and the coefficients for its error multipole spectrum are derived as a further example of the

perturbation computations. The expressions and coefficients for the vertical steering and skew quadrupole trims are merely presented and tabulated.

4.4.2 Horizontal Steering Trim

The horizontal steering trim is achieved by exciting all six poles. The excitation pattern orthogonal to the sextupole field requires currents, $+\Delta J$, $+2\Delta J$, $+\Delta J - \Delta J$, $-2\Delta J$ and $-\Delta J$ for the poles at $\beta = \frac{\pi}{6}$, $\frac{\pi}{2}$, $\frac{5\pi}{6}$, $\frac{7\pi}{6}$, $\frac{3\pi}{2}$ and $\frac{11\pi}{6}$, respectively. Letting $|\varepsilon_j| = \frac{\Delta J}{J}$, the expression for the error fields can be written

$$\begin{aligned} \left(\frac{B_{ny} + iB_{nx}}{B_{Ny}} \right)_{@r=h} &= +i\varepsilon_j x_j e^{-in\frac{\pi}{6}} + i2\varepsilon_j x_j e^{-in\frac{3\pi}{2}} + i\varepsilon_j x_j e^{-in\frac{5\pi}{6}} \\ &\quad -i\varepsilon_j x_j e^{-in\frac{7\pi}{6}} - i2\varepsilon_j x_j e^{-in\frac{3\pi}{2}} - i\varepsilon_j x_j e^{-in\frac{11\pi}{6}}, \\ &= i\varepsilon_j x_j \begin{pmatrix} \cos n\frac{\pi}{6} - i \sin n\frac{\pi}{6} + 2 \cos n\frac{\pi}{2} - i2 \sin n\frac{\pi}{2} \\ + \cos n\frac{5\pi}{6} - i \sin n\frac{5\pi}{6} - \cos n\frac{7\pi}{6} + i \sin n\frac{7\pi}{6} \\ -2 \cos n\frac{3\pi}{2} + i2 \sin n\frac{3\pi}{2} - \cos n\frac{11\pi}{6} + i \sin n\frac{11\pi}{6} \end{pmatrix}. \end{aligned}$$

Equating the real and imaginary terms

$$\begin{aligned} \left(\frac{B_{ny}}{B_{Ny}} \right)_{@r=h} &= \varepsilon_j x_j \begin{pmatrix} \sin n\frac{\pi}{6} + 2 \sin n\frac{\pi}{2} + \sin n\frac{5\pi}{6} \\ - \sin n\frac{7\pi}{6} - 2 \sin n\frac{3\pi}{2} - \sin n\frac{11\pi}{6} \end{pmatrix}, \\ \left(\frac{B_{nx}}{B_{Nx}} \right)_{@r=h} &= \varepsilon_j x_j \begin{pmatrix} \cos n\frac{\pi}{6} + 2 \cos n\frac{\pi}{2} + \cos n\frac{5\pi}{6} \\ - \cos n\frac{7\pi}{6} - 2 \cos n\frac{3\pi}{2} - \cos n\frac{11\pi}{6} \end{pmatrix}, \end{aligned}$$

and the fields can be written

$$\frac{n}{N} \frac{\Delta C_n(H_{trim})}{\varepsilon_l} = x_j (Factor5 + iFactor6).$$

Sextupole Yoke - Horizontal Trim Coefficients				
n	$\frac{n}{N} \frac{\Delta C_n(j)}{i\varepsilon_j}$	Factor5	Factor6	$\frac{n}{N} \frac{\Delta C_n(H_{trim})}{\varepsilon_{H \text{ trim}}}$
1	9.79×10^{-2}	6	0	0.5874
2	1.56×10^{-1}	0	0	0
3	1.67×10^{-1}	0	0	0
4	1.33×10^{-1}	0	0	0
5	7.09×10^{-2}	6	0	0.4254
6	0	0	0	0
7	-1.34×10^{-2}	-6	0	0.0804
8	-1.07×10^{-2}	0	0	0
9	0	0	0	0
10	9.13×10^{-3}	0	0	0
11	9.72×10^{-3}	-6	0	-0.0583
12	0	0	0	0
13	-1.01×10^{-3}	6	0	-0.0061
14	-1.18×10^{-3}	0	0	0
15	0	0	0	0

From this table, it can be seen that the first multipole error for this configuration is the ($n = 5$), decapole field error.

4.4.3 Vertical Steering and Skew Quadrupole Trim

In the same manner, vertical steering trim is achieved by exciting four of the six poles. The excitation pattern for the vertical steering trim orthogonal to the sextupole field requires currents, $+\Delta J$, $-\Delta J$, $-\Delta J$ and $+\Delta J$ for the poles at $\beta = \frac{\pi}{6}$, $\frac{5\pi}{6}$, $\frac{7\pi}{6}$ and $\frac{11\pi}{6}$, respectively.

Skew quadrupole trim is achieved by exciting two of the six poles. The excitation pattern for the skew quadrupole trim orthogonal to the sextupole field requires currents, $+\Delta J$ and $+\Delta J$ for the poles at $\beta = \frac{\pi}{2}$ and $\frac{3\pi}{2}$, respectively.

Letting $|\varepsilon_j| = \frac{\Delta J}{J}$, the coefficients for the error fields are computed. The following table consolidates the coefficients for all three of the trim configurations.

n	$\frac{n}{N} \frac{\Delta C_n(H_{trim})}{\varepsilon_{H \text{ trim}}}$	$\frac{n}{N} \frac{\Delta C_n(V_{trim})}{i\varepsilon_{V \text{ trim}}}$	$\frac{n}{N} \frac{\Delta C_n(SQ_{trim})}{i\varepsilon_{SQ \text{ trim}}}$
1	0.5874	0.3391	0
2	0	0	-0.3120
3	0	0	0
4	0	0	0.2660
5	0.4254	-0.2456	0
6	0	0	0
7	0.0804	0.0464	0
8	0	0	-0.0214
9	0	0	0
10	0	0	-0.0183
11	-0.0583	0.0337	0
12	0	0	0
13	-0.0061	-0.0035	0
14	0	0	0.0024
15	0	0	0

We note in the table, that all three configurations have a zero entry for the sextupole ($n = 3$) coefficient. The coil configurations have the desired orthogonality to the sextupole field and excitation of the trim coils does not excite a sextupole field. From this table, it can be seen that the first multipole error for horizontal steering configuration is the ($n = 5$) decapole field error, for the vertical steering configuration is the ($n = 5$) skew decapole field error, and for the skew quadrupole configuration, the ($n = 4$) skew octopole field error.

The coil excitations and locations for all three trim configurations are illustrated in fig. 5.

Sextupole Trim Multipole Spectra

The table reveals that the trim configurations result in poor field quality. If the first allowed multipole is normalized to the fundamental fields at the pole radius, the ratio, $\left| \frac{B_5}{B_1} \right| = 0.72$ describe the normalized amplitudes of the first error multipole for both the horizontal and vertical steering configurations evaluated at the pole tip. The ratio $\left| \frac{B_4}{B_2} \right| = 0.85$ describes the normalized amplitude of the first error multipole at the pole radius for the skew quadrupole configuration. However, for the sextupole magnet, the good field radius is typically $\leq 60\%$ of the pole radius, h . Recalling the relationship of the amplitudes of the normalized multipole with the radius;

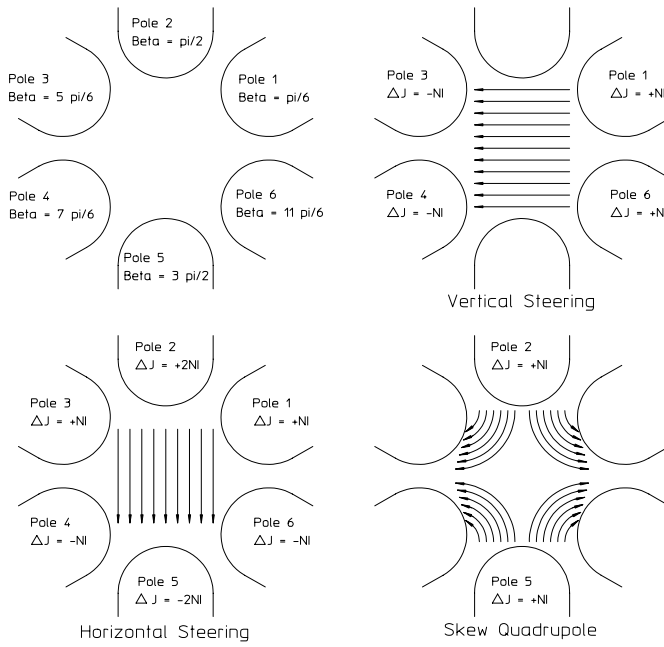


Figure 5 Sextupole Trims

$$\begin{aligned} \left| \frac{B_n}{B_N} \right|_r &= \left| \frac{B_n}{B_N} \right|_h \left(\frac{r}{h} \right)^{n-N}, \\ \left| \frac{B_5}{B_1} \right|_{0.6h} &= 0.72 \times 0.6^4 = 0.093, \\ \left| \frac{B_4}{B_2} \right|_{0.6h} &= 0.85 \times 0.6^2 = 0.306. \end{aligned}$$

4.4.4 Trim Excitations

From the table

$$\begin{aligned} \left| \frac{n}{N} \frac{\Delta C_n(H_{trim})}{\varepsilon_{H \text{ trim}}} \right| &= 0.5874 = \frac{B_1}{B_3 \varepsilon_{H \text{ trim}}}, \\ \left| \frac{n}{N} \frac{\Delta C_n(V_{trim})}{\varepsilon_{V \text{ trim}}} \right| &= 0.3391 = \frac{B_1}{B_3 \varepsilon_{V \text{ trim}}}, \\ \left| \frac{n}{N} \frac{\Delta C_n(SQ_{trim})}{\varepsilon_{SQ \text{ trim}}} \right| &= 0.3120 = \frac{B_2}{B_3 \varepsilon_{SQ \text{ trim}}}. \end{aligned}$$

Solving and using the definitions for the normalized excitations;

$$\begin{aligned}\varepsilon_{H \ trim} &= \frac{NI_{H \ trim}}{NI_3} = \frac{B_1}{0.5874B_3}, \\ \varepsilon_{V \ trim} &= \frac{NI_{V \ trim}}{NI_3} = \frac{B_1}{0.3391B_3}, \\ \varepsilon_{SQ \ trim} &= \frac{NI_{SQ \ trim}}{NI_3} = \frac{B_2}{0.3120B_3},\end{aligned}$$

or;

$$\begin{aligned}NI_{H \ trim} &= \frac{B_{1h}NI_3}{0.5874B_3}, \\ NI_{V \ trim} &= \frac{B_{1v}NI_3}{0.3391B_3}, \\ NI_{SQ \ trim} &= \frac{B_2NI_3}{0.3120B_3}.\end{aligned}$$

Writing the expressions for some of the terms;

$$NI_3 = \frac{B''h^3}{6\mu_0}, \quad B_3 = \frac{B''h^2}{2} \quad \text{and} \quad B_2 = B'h,$$

and substituting, we finally get the expressions for the required coil excitations;

$$NI_{H \ trim} = \frac{B_{1h}}{0.5874} \frac{B''h^3}{6\mu_0} \times \frac{2}{B''h^2} = \frac{B_{1h}h}{1.7622\mu_0}, \quad (4.11)$$

$$NI_{V \ trim} = \frac{B_{1v}}{0.3391} \frac{B''h^3}{6\mu_0} \times \frac{2}{B''h^2} = \frac{B_{1v}h}{1.0173\mu_0}, \quad (4.12)$$

$$NI_{SQ \ trim} = \frac{B'_{SQ}h}{0.3120B_3} \frac{B''h^3}{6\mu_0} \times \frac{2}{B''h^2} = \frac{B'_{SQ}h^2}{0.9360\mu_0}. \quad (4.13)$$

4.5 Chapter Closure

For engineers/designers defining the fabrication tolerances and specifications for accelerator magnets, this is one of the most important chapters in this publication. This chapter illustrates that magnet performance, as specified by physics constraints for field quality, magnet to magnet reproducibility and alignment, can be translated into fabrication and assembly requirements and tolerances. It also illustrates means of incorporating trim magnets into yokes designed for other required fields, conserving space and eventually reducing the cost of new accelerator facilities.

Means of calculating separate error multipole components due to fabrication, assembly and excitation errors are reviewed. Exploitation of the algorithms and the tabulated coefficients result in powerful tools for the estimation of the displacement of the magnetic center, the changes in the fundamental field and selected components of the multipole spectrum due to fabrication and assembly errors for two piece quadrupole magnets. Because of the orthogonality of the various multipole types, magnetic measurements can isolate fabrication or assembly errors and suggest means of correcting them. Reversing the process, examples of calculations using these tools to determine fabrication and assembly tolerances ensuring achieving adequate quadrupole performance are presented. The examples include calculations of tolerances using typical physics specifications. The examples can be used as templates for identifying tolerances based on the physics requirements for quadrupoles required for other projects. Identification of these tolerances can provide guidance ensuring that high fabrication costs due to unrealistic fabrication and assembly tolerances are avoided. The tools also provide guidance for the design of asymmetric quadrupole magnets forced by certain accelerator operating constraints.

The algorithms and perturbation tables are further exploited to provide formulae for the design of and estimation of the multipole spectrum for various trim fields incorporated in a sextupole yoke. These trim configurations are useful in congested accelerator lattices where room for separate correctors can result in high project costs.

4.6 Problems

Problem 4.1 (Solution)

Assume a quadrupole with an aperture radius $h = 50 \text{ mm}$, whose length is $l = 50 \text{ cm}$. Suppose one half of the magnet core is longer than the other half by $\Delta l = 5 \text{ mm}$. What is the magnitude of the first error harmonic, $n = 3$, at the desired good field radius $r_0 = 40 \text{ mm}$?

Problem 4.1a (Solution) By how much has the magnetic center shifted with respect to the mechanical center?

Problem 4.1b (Solution) For an assymetric magnet whose efficiency $\eta = 98\% = 0.98$, What is the magnitude of the first harmonic, $n = 3$, at the desired good field radius $r_0 = 40 \text{ mm}$? By how much has the magnetic center shifted with respect to the mechanical center?

Problem 4.2

A sextupole magnet requires trim coils to supply horizontal steering, vertical steering and skew quadrupole fields. Assume that the sextupole aperture radius is $h = 45 \text{ mm}$. What is the amplitude and the error multipole index of the ratio of the first allowed multipole error to the fundamental $\left| \frac{B_n}{B_N} \right|_{r_0}$ when $r_0 = 35 \text{ mm}$. for each of the corrector modes? Specify whether they are real or imaginary.

Problem 4.3

The angular alignment tolerance for an $h = 35 \text{ mm}$. quadrupole is $\Delta\theta = 0.5 \text{ mrad}$. Assume that the magnet can be perfectly aligned with respect to its mechanical horizontal datum. What is the shear displacement tolerance required for the assembly of one half of a quadrupole with respect to the other half of the quadrupole to achieve a maximum rotational error of 0.5 mrad ? (Hint-the angular rotation of the field is the ratio $\frac{B_{2x}}{B_{2y}}$.)

Chapter 5

MAGNETIC EXCITATION AND COIL DESIGN

5.1 Introduction

Stoke's theorem is applied to Maxwell's general magnet equations to convert the two dimensional differential form of the equation to an integral form. The integral form is used to develop the expressions for magnet excitation for different magnet types. Examples are presented to demonstrate that the magnitude of fringe fields in selected geometries can be estimated using the integral form of the excitation equation. Additional examples demonstrate that the distribution of conductors for current dominated magnets can be described.

The integral expressions are used to compute the required current in real coils to achieve a desired magnet excitation. The relationships between the current density parameter and the power dissipated in a magnet are developed. Canonical values of some of the variables in the expressions for the magnet power dissipation are suggested.

Expressions useful in the design of water cooled coils are developed. These include expressions for computing flow velocity, volume flow and water temperature rise. Typical values of some design parameters are listed. The expressions of the cooling parameters as a function of the selected dimensions (water passage diameter and number of water circuits) are developed. These expressions are useful for understanding the sensitivities of these parameters which changes in the coil water circuit and conductor cooling channel dimensions.

5.2 Maxwell's Inhomogeneous Equation

In a previous chapter, Maxwell's differential magnet equation was written in terms of the magnetic field as

$$\vec{\nabla} \times \vec{B} = \mu\mu_0 \vec{J}, \quad (5.1)$$

where \vec{J} is the current density vector. This equation is written more conveniently in terms of the magnetic field intensity,

$$\vec{\nabla} \times \vec{H} = \vec{J}, \quad (5.2)$$

where $\vec{H} = \frac{\vec{B}}{\mu\mu_0}$. Applying Stoke's theorem,, the differential form can be written in integral form

$$\begin{aligned} \oint \vec{H} \cdot d\vec{l} &= \int_S (\vec{\nabla} \times \vec{H}) \cdot d\vec{S}. \quad \text{Therefore,} \\ \oint \vec{H} \cdot d\vec{l} &= \int_S (\vec{\nabla} \times \vec{H}) \cdot d\vec{S} = \int_S \vec{J} \cdot d\vec{S}. \end{aligned} \quad (5.3)$$

Written in terms of the magnetic field and in two dimensions,

$$\oint \frac{\vec{B}}{\mu\mu_0} \cdot d\vec{l} = \int_S J_z \cdot dS = NI, \quad (5.4)$$

$$\text{or } \oint \vec{H} \cdot d\vec{l} = NI, \quad (5.5)$$

where $\vec{B} = B_x \hat{i} + B_y \hat{j}$, $\vec{H} = H_x \hat{i} + H_y \hat{j}$ and $d\vec{l} = dx \hat{i} + dy \hat{j}$ and \hat{i} and \hat{j} are unit vectors in the x and y directions, respectively. In the eq. (5.4), μ is the relative permeability which is equal to one for vacuum and is a nonlinear function of field amplitude in iron and other permeable material. The \cdot indicates an inner product (a scalar quantity) where $(\vec{B} \text{ or } \vec{H}) \cdot d\vec{l} = |B| \text{ or } |H| |dl| \cos \theta$ and θ is the angle between the two vectors. The surface integral is performed in the area bounded by the line integral path.

5.2.1 Continuity

An earlier chapter used one of Maxwell's magnet equations to establish the continuity of $B \perp$, the perpendicular B vector, across an iron/air boundary (see page 33). Since we used Stoke's theorem to write the integral form of the Maxwell's inhomogeneous equation, $\oint \frac{\vec{B}}{\mu\mu_0} \cdot d\vec{l} = NI$, it is convenient to develop the concepts that establish the continuity of $H \parallel$, the parallel H vector, across an iron/air boundary which encloses no current sources in this chapter.

Consider the closed rectangular path shown in fig. 1 through the iron and the air enclosing the region where $NI = 0$. Eq. (5.4) can be rewritten

$$\oint \frac{\vec{B}}{\mu\mu_0} \cdot d\vec{l} = 0 = \int_{path1} \vec{H}_{iron} \cdot d\vec{l} + \int_{path2} \vec{H}_{air} \cdot d\vec{l}.$$

Since, for the illustrated path $L_{iron} = L_{air}$, $H_{iron} \parallel L_{iron}$ and $H_{air} \parallel L_{air}$, the expression can be rewritten

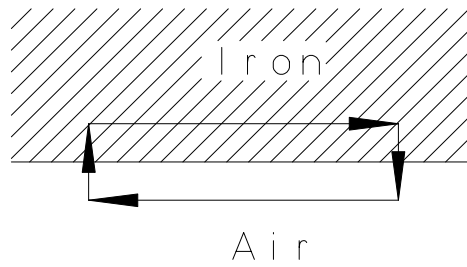


Figure 1 Integral of Hdl at the iron/air Boundary

$$\begin{aligned} H_{iron}L + H_{air}L &= 0 \rightarrow H_{iron} = -H_{air} \\ \text{and } |H_{iron}| &= |H_{air}| \end{aligned} \quad (5.6)$$

This relationship becomes important when considering the magnitude of fringe fields and methods for shielding in regions where magnetic fields are undesirable.

5.3 Magnet Excitations

The excitation current to achieve a required magnetic field can be computed for different field distributions using the integral form of Maxwell's equation. Since the permeability in iron is large for unsaturated yokes, $\oint_{iron} \frac{\vec{B}}{\mu\mu_0} \cdot d\vec{l} \ll \oint_{gap} \frac{\vec{B}}{\mu_0} \cdot d\vec{l}$ and the excitation current is dominated by the field in the magnet gap. Magnet efficiency, a convenient concept for the comparison of the required current to drive the field in the gap and through the iron is introduced.

5.3.1 Magnet Efficiency

The concept of magnet efficiency is introduced in the beginning of this section and will be used for the expressions for each of the specific magnet types. The magnet efficiency is an expression used to divide the excitation current among the current required to excite the desired field and the current required to complete the excitation through the remaining magnetic circuit. The desired field is the field in the magnet gap, where the charged particle is bent, focussed or corrected for chromatic aberration. The excitation through the remaining circuit is the current required to drive the magnetic flux through the yoke. In eq. (5.4), the line integral is taken through the gap region of the magnet where the relative permeability, $\mu = 1$ and the yoke, normally made from steel or iron where $\mu \approx 1000$. Thus, eq. (5.4) can be rewritten

as

$$\begin{aligned} NI &= \oint \frac{\vec{B}}{\mu\mu_0} \cdot d\vec{l} = \oint_{gap} \frac{\vec{B}}{\mu_0} \cdot d\vec{l} + \oint_{yoke} \frac{\vec{B}}{\mu\mu_0} \cdot d\vec{l}, \\ &= NI_{gap} + NI_{yoke}, \end{aligned}$$

and the magnet efficiency is defined as

$$\text{Efficiency} = \eta = \frac{NI_{gap}}{NI_{gap} + NI_{yoke}}. \quad (5.7)$$

Normally, the integrated path length through the yoke is $\approx 10 \times$ the path length through the gap. For a well designed magnet, the yoke is sized so that the average relative permeability at the yoke field level, $\mu \approx 1000$ along the integrated path length and

$$\eta = \frac{NI_{gap}}{NI_{gap} + NI_{gap} \times \frac{10}{1000}} \approx 0.99 = 99\%.$$

5.3.2 Dipole Magnets

Four varieties of dipole magnet are described in this section. The first is a conventional H-dipole magnet. The remaining types are included in this discussion to illustrate certain design principals. The current carrying and Lambertson septa magnets are used for beam injection into and extraction out of an accelerator. The cosine wound coil is a dipole whose field distribution is determined by the location of individual conductors and is a distribution approximated in superconducting magnets.

The H-Dipole Magnet

Fig. 2 illustrates the integration path through a conventional H-dipole magnet.

The integration is taken through three different paths,

$$\begin{aligned} \oint \frac{\vec{B}}{\mu\mu_0} \cdot d\vec{l} &= \oint_{Path1} \frac{\vec{B}}{\mu\mu_0} \cdot d\vec{l} + \oint_{Path2} \frac{\vec{B}}{\mu\mu_0} \cdot d\vec{l} + \oint_{Path3} \frac{\vec{B}}{\mu\mu_0} \cdot d\vec{l}, \\ &= \frac{Bh}{\mu_0} + \frac{B_{iron}L_{iron}}{\mu_{iron}\mu_0} + 0 \quad (\mu_{air} = 1 \text{ and } B \perp Path_3). \end{aligned}$$

$B_{iron} \approx B$, $L_{iron} \gtrsim 10h$ and $\mu_{iron} \gtrsim 1000$. Therefore, $\frac{B_{iron}L_{iron}}{\mu_{iron}\mu_0} \approx 0.01 \times \frac{Bh}{\mu_0}$.

Since $\int_S J_z dS = NI$, the integral equation can be rewritten;

$$NI_{dipole} = \frac{Bh}{\eta\mu_0}, \quad (5.8)$$

where the magnet efficiency, η , is expressed in eq. (5.7).

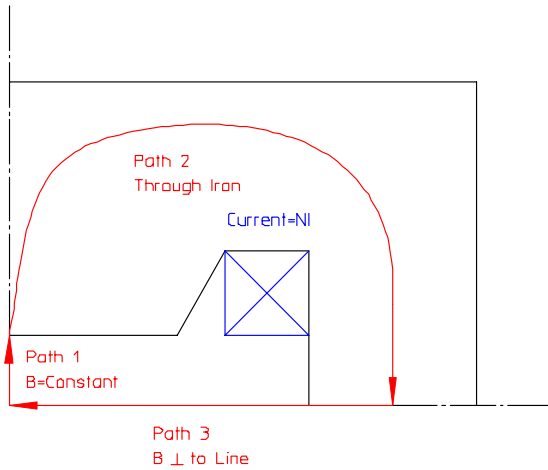


Figure 2 Dipole Excitation

Current Carrying Septum Magnet

The current carrying septum magnet is used for beam injection and extraction. The injection magnet bends beam into the accelerator. The extraction magnet kicks the beam out of the accelerator. This injection/extraction magnet is called a septum since a physical object (the septum) separates the high field region from an ideally zero field region. Normally, during injection and/or extraction, the accelerator circulating beam is displaced from its orbit in the center of the beam pipe by a series of bump magnets. For injection, the circulating beam is displaced as close to the septum as possible. This places the orbit of the injected beam parallel and transversely close to the circulating beam so that the injected beam can be incorporated with the circulating beam by beam damping. For extraction, the circulating beam is displaced across the septum and bent out of the closed synchrotron orbit.

The bump magnets, described in the first chapter, are rapidly pulsed so that the circulating beam is perturbed during one, or at most a few orbits. Since the bump magnets are generously spaced along the circulating beam, the fields can be relatively small and the rapid pulse can be produced with power supplies with high but achievable voltages. Septum magnets are occasionally pulsed. However, the majority of septum magnets are operated in the persistent mode. Typically, the layout of the injection line requires a relatively large bend angle for the septum magnet. The fields and the volume of the aperture are large. Therefore, a septum magnet stored energy is sizeable, resulting in a fairly high inductance. The voltages required to pulse the septum magnet to the required field can be prohibitive (see discussion on inductance in Chapter 7 on page 191). In order to minimize the perturbation of the septum magnet on the circulating beam, the primary goal for septum magnet, excited

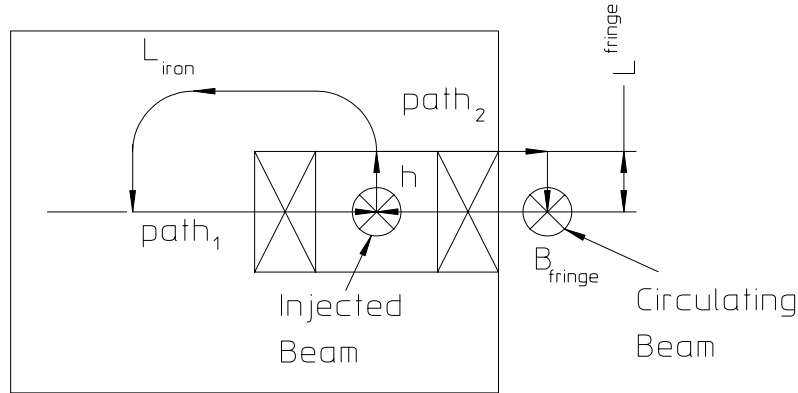


Figure 3 Current Carrying Septum Magnet

continuously during accelerator operation, is to minimize the effect on the circulating beam by achieving a low external fringe field in the region of the circulating beam. A septum magnet geometry is illustrated in fig. 3.

If the coil current is given by NI , eq. (5.4) can be used to describe the magnetic reluctance along a path through the yoke. The expression is given by;

$$\int_{gap} \frac{B}{\mu_0} dl + \int_{iron} \frac{B}{\mu\mu_0} dl + \int_{path1} \frac{B}{\mu\mu_0} dl = NI,$$

$$\frac{B_{gap}h}{\mu_0} + \frac{B_{iron}L_{iron}}{\mu\mu_0} + 0 (B_{path1} \perp path1) = NI.$$

The expression along a second path (path₂) which includes the path through the fringe field is,

$$\int_{gap} \frac{B}{\mu_0} dl + \int_{path2} \frac{B}{\mu\mu_0} dl + \int_{Fringe} \frac{B}{\mu_0} dl = NI,$$

$$\frac{B_{gap}h}{\mu_0} + 0 (B_{path2} \perp path2) + \frac{B_{fringe}}{\mu_0} L_{fringe} = NI.$$

Therefore, noting that $L_{fringe} \approx h$, and equating both expressions since the value of the closed integrals are NI , we get, finally,

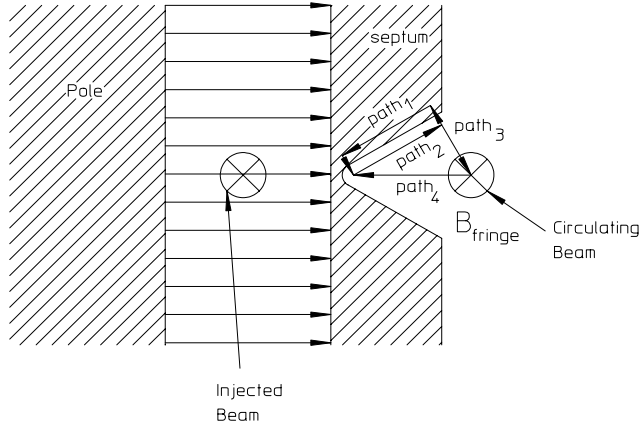


Figure 4 Lambertson Septum Fringe Field

$$\begin{aligned} \frac{B_{fringe}}{\mu_0} L_{fringe} &= \frac{B_{fringe}}{\mu_0} h = \frac{B_{iron} L_{iron}}{\mu \mu_0}, \\ \text{or } B_{fringe} &\approx \frac{B_{iron} L_{iron}}{\mu h}. \end{aligned} \quad (5.9)$$

The final expression demonstrates that the magnitude of the fringe field is determined by the design of the yoke. A high field in the yoke as a result of too little iron or low iron permeability results in large fringe fields.

Lambertson Septum Magnet

The Lambertson Septum Magnet serves the same purpose as the current carrying septum. The primary difference is that the fields are horizontal for vertical injection/extraction into/from an accelerator. Again, as in the case of the current carrying septum, the primary design goal is to minimize the effect on the circulating beam by achieving a low external field in the region of the circulating beam. In this case, the fringe field is horizontal, resulting in a vertical perturbation in the circulating beam. The Lambertson Septum magnet and the integration paths used in the following calculations are illustrated in fig. 4.

Using the expression (5.6) since no currents are enclosed and noting that $H = \frac{B}{\mu \mu_0}$,

$$\int_{path1} \frac{B_{iron}}{\mu \mu_0} dl + \int_{path2} \frac{B_{air}}{\mu_0} dl = 0.$$

In this expression, the contribution to the $\int H \cdot dl$ along the paths connecting paths 1 and 2 are essentially zero. This is because the paths are short and the fields are essentially perpendicular to the path direction. Also, since $path1 = path2$,

$$\frac{B_{iron}}{\mu} \approx B_{air}.$$

Taking the integral $\int_{path2-3-4} Hdl = 0$ (no current sources are enclosed), $\int_{path2} \frac{B}{\mu_0} dl + \int_{path3} \frac{B}{\mu_0} dl + \int_{path4} \frac{B}{\mu_0} dl = 0$. In this expression, the contribution to the $\int Hdl$ from $\int_{path3} \frac{B}{\mu_0} dl \approx 0$ since the fields are nearly perpendicular to the path3 direction. Also, since $path4 < path2$, we get finally,

$$B_{fringe} \approx \left| \frac{path2}{path4} \right| \frac{B_{iron}}{\mu}. \quad (5.10)$$

This last relationship reveals that it is important that the septum be fabricated using material with high permeability at the field level expected in the septum. Also, the angle of the septum cut must be carefully selected since $B_{iron} \cos(\frac{angle}{2}) \approx B_{septum}$. The fringe field magnitude can be estimated using the final expression;

$$B_{fringe} \approx \frac{1}{\mu} \left| \frac{path2}{path4} \right| \frac{B_{septum}}{\cos\left(\frac{angle}{2}\right)}.$$

Cosine Current Distribution Dipole Magnet

An earlier chapter, covering the principles of the Orthogonal Analog Model, described a dipole magnet whose field uniformity is determined by the distribution of the current along the inner circular surface of an iron yoke (see page 60). This geometry is illustrated in fig. 5.

Eq. (5.4) can be used to describe the current distribution along the path described in the illustration. The expression is given by

$$\begin{aligned} |Current|_0^\theta &= \int_{gap} \frac{B}{\mu_0} dl + \int_{iron} \frac{B_{iron}}{\mu_{iron}\mu_0} dl + \int_{path3} \frac{B}{\mu\mu_0} dl =, \\ &= \frac{B_{gap}R \sin \theta}{\mu_0} + 0 \left(\frac{B_{iron}}{\mu_{iron}} \ll B_{gap} \right) + 0 \ (B_{path1} \perp path3), \\ &\approx \frac{B_{gap}R \sin \theta}{\mu_0}. \end{aligned}$$

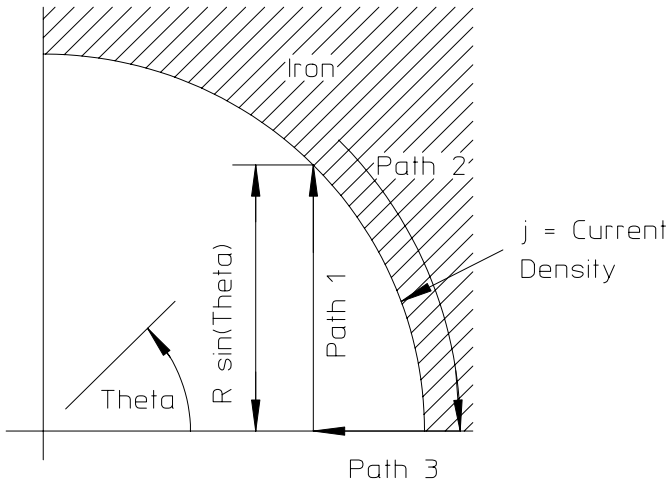


Figure 5 Cosine Distributed Current Density

where $|Current|_0^\theta$ is the total current along path₂. But, $|Current|_0^\theta = \int_0^\theta jt(\theta) Rd\theta$ where $j(\theta)$ is the linear current density distribution. Integrating the uniform field along the indicated path and applying eq. (5.4)

$$\int_0^\theta j(\theta) Rd\theta \approx \frac{B_{gap}R \sin \theta}{\mu_0}.$$

Differentiating both sides of the equation with respect to the angle, we obtain

$$j(\theta) R \approx \frac{B_{gap}R \cos \theta}{\mu_0},$$

Solving, $j(\theta) \approx \frac{B_{gap}}{\mu_0} \cos \theta,$ (5.11)

showing that, for a uniform current density, a cosine distribution of the coil configuration is required to obtain a uniform field in this geometry.

The total current in the illustrated upper quadrant of the magnet is given by

$$\begin{aligned} NI &= \int_0^{\frac{\pi}{2}} j(\theta) Rd\theta = \int_0^{\frac{\pi}{2}} \frac{RB_{gap}}{\mu_0} \cos \theta d\theta, \\ &= \frac{RB_{gap}}{\mu_0} \left(\sin \frac{\pi}{2} - \sin 0 \right) = \frac{RB_{gap}}{\mu_0}, \end{aligned}$$

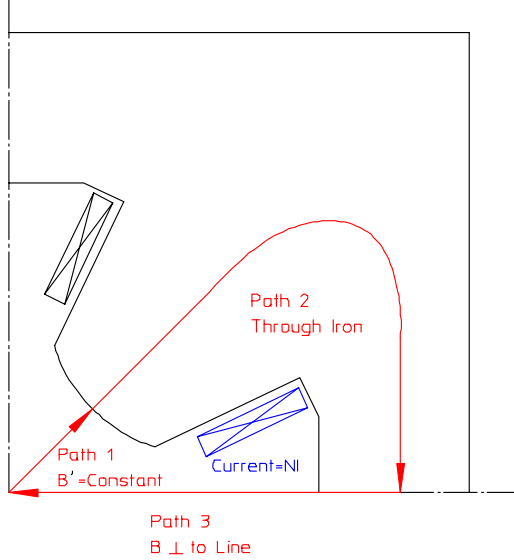


Figure 6 Quadrupole Excitation

where NI is the total current in the upper coil of the magnet geometry (for the upper pole).

5.3.3 Quadrupole Magnet

Fig. 6 illustrates the integration path through a quadrupole magnet.

$$\oint \frac{\vec{B}}{\mu\mu_0} \cdot d\vec{l} = \oint_{Path1} \frac{\vec{B}}{\mu_0} \cdot d\vec{l} + \oint_{Path2} \frac{\vec{B}}{\mu\mu_0} \cdot d\vec{l} + \oint_{Path3} \frac{\vec{B}}{\mu\mu_0} \cdot d\vec{l}.$$

For a quadrupole magnet, the gradient, $B' = \text{Constant}$ and $B = B'l$. Therefore,

$$\oint_{Path1} \frac{\vec{B}}{\mu_0} \cdot d\vec{l} = \int_0^h \frac{B'l}{\mu_0} dl = \frac{B'h^2}{2\mu_0}.$$

$B_{iron} \approx B'h$, $L_{iron} \gtrsim 10h$ and $\mu_{iron} \gtrsim 1000$. Therefore, $\frac{B_{iron}L_{iron}}{\mu_{iron}\mu_0} \approx 0.01 \times \frac{B'h^2}{\mu_0}$. Again, since the field along path3 is perpendicular to the path, $\oint_{Path3} \vec{B} \cdot d\vec{l} = 0$ and the expression for the required quadrupole excitation is

$$NI_{quadrupole} = \frac{B'h^2}{2\eta\mu_0}. \quad (5.12)$$

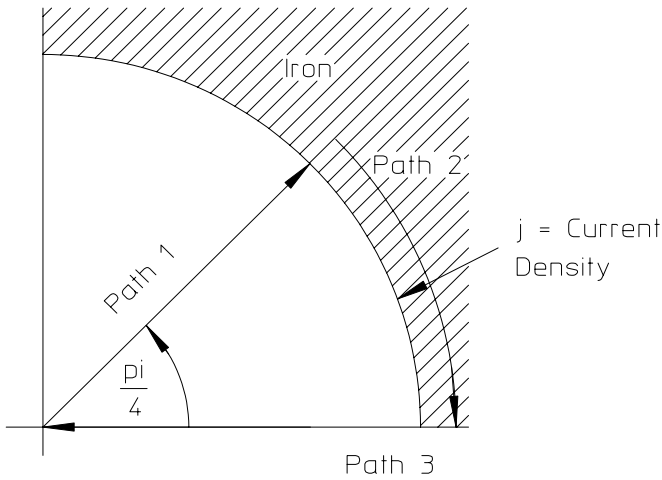


Figure 7 Cosine Current Quadrupole Magnet

where $\eta < 1$ is defined as the magnet efficiency and $\frac{1}{\eta} \approx 1.01$.

Cosine Current Distribution Quadrupole Magnet

A previous section described a cosine current distribution dipole magnet (see page 120). Fig. 7 illustrates an equivalent quadrupole magnet.

The principles of conformal mapping are employed to show that a similar geometry can produce a quadrupole field. The polar forms of the z quadrupole coordinates and the w dipole coordinates are given by;

$$z = |z| e^{i\theta}, \quad w = |w| e^{i\phi}.$$

The expression for the conformal map from the quadrupole to the dipole coordinates are,

$$\begin{aligned} w &= \frac{z^2}{R}, \\ \text{or } |w| e^{i\phi} &= \frac{|z|^2}{R} e^{i2\theta}. \end{aligned}$$

This mapping expression requires the angle 2θ in the quadrupole domain to be mapped from ϕ . Therefore, the linear current density distribution is,

$$j \propto \cos 2\theta.$$

Eq. (5.4) is used again to describe the current distribution along the path described in the illustration. The expression is given by;

$$\begin{aligned} |Current|_0^\theta &= \int_{path1} \frac{B}{\mu_0} dl + \int_{iron} \frac{B_{iron}}{\mu_{iron}\mu_0} dl + \int_{path3} \frac{B}{\mu\mu_0} dl, \\ |Current|_0^\theta &= \int_{path1} \frac{B}{\mu_0} dl + 0 \left(\frac{B_{iron}}{\mu_{iron}} \ll B_{gap} \right) + 0 \left(B_{path1} \perp path3 \right), \\ |Current|_0^\theta &\approx \int_{path1} \frac{B}{\mu_0} dl. \end{aligned}$$

From the previous section, $\oint_{Path1} \frac{\vec{B}}{\mu_0} \cdot d\vec{l} = \int_0^R \frac{B' l}{\mu_0} dl = \frac{B' R^2}{2\mu_0}$. The total current integrated from $0 \leq \theta \leq \frac{\pi}{4}$ is

$$\begin{aligned} NI &= \int_0^{\frac{\pi}{4}} R j_0 \cos 2\theta d\theta \\ &= \frac{R j_0}{2} |\sin 2\theta|_0^{\frac{\pi}{4}} = \frac{R j_0}{2}. \end{aligned}$$

Equating

$$\begin{aligned} \frac{R j_0}{2} &= \frac{B' R^2}{2\mu_0}, \\ j_0 &= \frac{B' R}{\mu_0}, \\ \text{and finally } j &= j_0 \cos 2\theta = \frac{B' R}{\mu_0} \cos 2\theta. \end{aligned}$$

5.3.4 Sextupole Magnet

Fig. 8 illustrates the integration path through a sextupole magnet.

For a sextupole magnet, the field is parabolic and the second derivative of the field, $B'' = \frac{d^2 B}{dr^2}$ is a constant. Thus,

$$\begin{aligned} B'(r) &= \int_0^r B'' dr = B'' r, \\ B(r) &= \int_0^r B'(r) dr = \int_0^r B'' r dr = \frac{B'' r^2}{2}. \end{aligned}$$

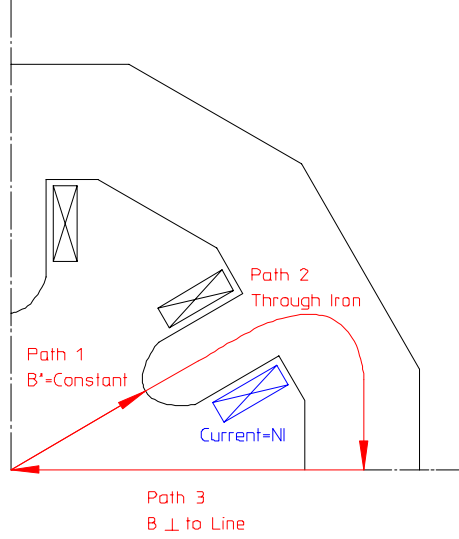


Figure 8 Sextupole Excitation

Therefore,

$$\oint_{Path1} \frac{\vec{B}}{\mu_0} \cdot d\vec{l} = \int_0^h \frac{B'' r^2}{2\mu_0} dr = \frac{B'' h^3}{6\mu_0},$$

$$B_{iron} \approx \frac{B'' h^2}{2}, L_{iron} \gtrsim 10h \text{ and } \mu_{iron} \gtrsim 1000.$$

Therefore, $\frac{B_{iron} L_{iron}}{\mu_{iron} \mu_0} \approx 0.01 \times \frac{B'' h^3}{2\mu_0}$. Again, since the field along path 3 is perpendicular to the path, $\oint_{Path3} \vec{B} \cdot d\vec{l} = 0$ and the expression for the required sextupole excitation is

$$NI_{sextupole} = \frac{B' h^3}{6\eta\mu_0}, \quad (5.13)$$

where $\eta < 1$ is defined as the magnet efficiency and $\frac{1}{\eta} \approx 1.01$ for a well designed yoke.

5.4 Coil Design

Magnet design begins by defining two-dimensional magnet cross sections satisfying magnet excitation and field-quality requirements. Magnet lengths are specified to satisfy beam bending, focusing and chromatic correction requirements for dipoles,

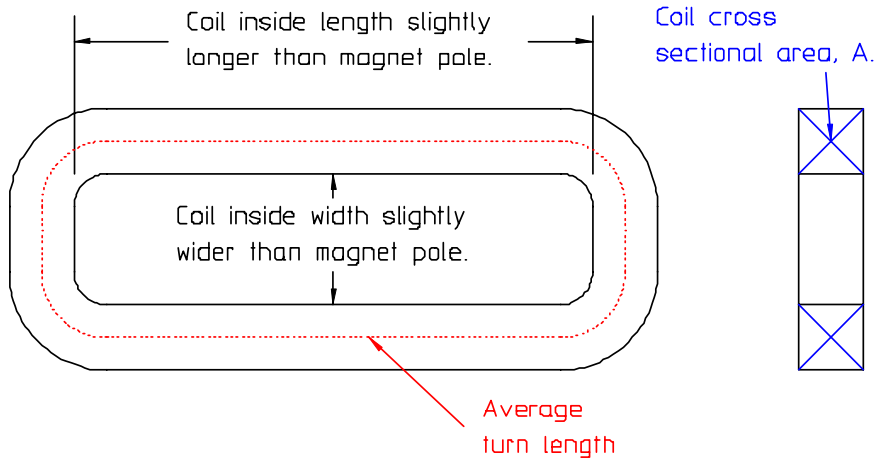


Figure 9 Pancake Coil

quadrupoles and sextupoles, respectively. These general shapes are useful for accelerator and/or beamline layouts, but provide little information regarding the impact of proposed designs on other subsystems. The magnet engineer/designer needs to fully specify the power supply and power dissipation requirements for proposed magnet designs so that the scale of these subsystems can be developed for project proposals. The specifications need to be developed without having to fully carry out detailed magnet designs. In this section, expressions for the approximate power and cooling requirements for various magnet designs are developed using only the physics requirements for magnets and one design parameter, the current density,

$$j = \frac{\text{Current}}{\text{Conductor Area}}. \quad (5.14)$$

Consider the typical flat pancake style coil illustrated in fig. 9.

5.4.1 Coil Power

The power dissipated in the coil is given by

$$\begin{aligned} P &= I^2 R, \\ \text{where } R &= \frac{\rho L}{a}. \end{aligned} \quad (5.15)$$

In these expressions

$$\begin{aligned} \rho &= \text{resistivity } (\Omega m), \\ (\text{for copper, } \rho &\approx 1.86 \times 10^{-8} \Omega m \text{ at } T = 40^\circ C), \\ L &= \text{Coil Length} = Nl_{ave}, \end{aligned}$$

where

$$\begin{aligned} N &= \text{Number of Turns,} \\ \text{and } l_{ave} &= \text{Average Turn Length.} \end{aligned}$$

The gross coil area can be expressed as a function of the individual conductor areas as

$$Na = fA,$$

where

$$\begin{aligned} A &= \text{Coil Gross Area,} \\ \text{and } f &= \text{packing fraction} = \frac{\text{Net Conductor Area}}{\text{Gross Coil Area}} \end{aligned}$$

Substituting into the expression for the resistance

$$R = \frac{\rho N l_{ave}}{\frac{fA}{N}} = \frac{\rho N^2 l_{ave}}{fA}.$$

and the expression for the power becomes

$$P = I^2 R = \frac{\rho (NI)^2 l_{ave}}{fA}.$$

But $\frac{NI}{fA} = \frac{NI}{Na} = \frac{I}{a} = j$, the current density. Therefore

$$P = \rho NI j l_{ave}.$$

The required excitation for dipoles, quadrupoles and sextupoles are

$$NI_{dipole} = \frac{Bh}{\eta\mu_0}, \quad NI_{quad} = \frac{B'h^2}{2\eta\mu_0}, \quad \text{and} \quad NI_{sext} = \frac{B''h^3}{6\eta\mu_0},$$

respectively.

The dipole has two coils per magnet. The quadrupole has four coils per magnet. The sextupole has six coils per magnet. Therefore, the total power dissipated per magnet is given by

$$P_{dipole} = 2\rho \frac{Bh}{\eta\mu_0} jl_{ave}, \quad (5.16)$$

$$P_{quad} = 2\rho \frac{B'h^2}{\eta\mu_0} jl_{ave}, \quad (5.17)$$

$$P_{sext} = \rho \frac{B''h^3}{\eta\mu_0} jl_{ave}. \quad (5.18)$$

These expressions can be modified for magnets with more than one coil per pole.

Note that the expressions for the magnet power include only the conductor resistivity, ρ , magnet gap, h , the magnet field parameters, B , B' and B'' , current density, j , magnet efficiency, η , the permeability for vacuum, μ_0 , and the average coil turn length, l_{ave} . In addition, for most magnets, $2.5 L_{magnet} \lesssim l_{ave} \lesssim 3 L_{magnet}$. Thus, the magnet power can be accurately estimated knowing only the magnet physics requirements without having to select the conductor size or the number of turns. In addition, if one uses the MKS system of units, the expressions compute the power directly in Watts. An example is given for the expression for the dipole power.

$$\begin{aligned} P_{dipole} &= 2\rho \frac{Bh}{\eta\mu_0} jl_{ave}, \\ P_{dipole} &= \Omega m \frac{\frac{T}{Amp} \frac{m}{Amp}}{\frac{T}{Amp} \frac{m^2}{Amp}} Amps \\ P_{dipole} &= \Omega Amps^2 = Watts. \end{aligned}$$

Current and Voltage

Since the power can be expressed as the product of the voltage and current, the power can be divided among the current and the voltage. Thus, selection of a coil design with many turns reduces the current and increases the voltage. This is desirable for individually controlled magnets with single power supplies since the cost of cabling and the voltage drop through the power distribution system is minimized. Normally, power distribution cables are convectively cooled and are limited to $\leq \frac{1.5 \text{ Amps}}{\text{mm}^2}$, resulting in large, expensive cables if the magnet power is divided using a high current and low voltage magnet design. Quadrupole and sextupole magnets in a synchrotron are normally low current high voltage magnets using coils with many turns.

A magnet requiring high current will require the installation of heavy cable. The selection of a coil design with fewer turns reduces the voltage and increases the current. This is desirable for many magnet in series using a single power supply. Dipole and gradient magnet in a synchrotron are often connected in series and normally require low voltage high current magnets using coils with fewer turns.

Canonical Values

In using the expressions for estimating the power, knowledge about the canonical values of some of the constants is useful. These values allow one to estimate the cross sectional size of the coils and make rough layouts of the magnet for accelerator lattices.

- Normally, a good value for the current density is $j = \frac{10 \text{ Amps}}{\text{mm}^2} = \frac{10^{-5} \text{ Amps}}{\text{m}^2}$ for water cooled coils.
 - This value usually results in simple coil designs with sufficient conductor circuit length for simple coils with adequate cooling and acceptable number of water circuits.
- The value of the packing fraction is typically $f \approx 0.5$ for small conductors. This value may be higher for large conductors carrying currents $\geq 500 \text{ Amps}$.
 - This value is useful for estimating the gross coil cross section and provides allowances for the insulation, coolant channel as well as the radius at the corners of the conductor.
- The magnet efficiency for a well designed yoke is $\eta \gtrsim 98\% = 0.98$.
- In general, the average conductor length per turn is $l_{ave} \lesssim 3L_{mag}$ where L_{mag} is the magnet core length.

5.5 Coil Cooling

In order to avoid magnets requiring coils with large cross sections, the magnet coils are normally water cooled. This requires the use of conductors with cooling channels (hollow conductors). In this section, expressions for the water flow in coils divided into a number of water circuits and the temperature rise in these coils are developed. The choice of the number of water circuits depends on the selection of the size of the water channel through the conductor and the available water pressure in an accelerator facility. The design of water cooled coils normally requires several iterations. The sensitivity of the various cooling system parameters to the several design dimensions is developed so that intelligent dimensional choices can be made and the number of design iterations reduced.

5.5.1 Pressure Drop

The following section summarizes expressions summarized in an engineering design data sheet used for the calculation of pressure drops through smooth pipes and tubes[8]. The expression for the pressure drop through a water circuit is given by

$$\Delta p = f \frac{l}{d} \frac{\delta v^2}{2}, \quad (5.19)$$

where

- f = friction factor
- l, d = water circuit length and diameter, respectively
- δ = water mass density
- v = water velocity

Friction Factor

The friction factor depends on the non-dimensional Reynolds number, $Re = \frac{vd}{\nu}$, where ν = kinematic viscosity of the water. The value of the Reynolds number (Re) determines the flow regime for the fluid. For laminar flow, $Re < 2000$, and $f = \frac{64}{Re}$. For turbulent flow, $Re > 4000$, the expression for the friction factor is transcendental and must normally be solved iteratively. The transitional flow regime for $2000 < Re < 4000$ is usually avoided since flow and pressure drop are difficult to predict.

The transcendental friction factor equation for turbulent flow is

$$\frac{1}{\sqrt{f}} = -2 \log_{10} \left(\frac{\epsilon}{3.7d} + \frac{2.51}{Re \sqrt{f}} \right), \quad (5.20)$$

where ϵ is the surface roughness of the cooling channel expressed in the same dimensions as the hole diameter, d . Fluid flow textbooks list the surface roughness of smooth copper tubes as $\epsilon = 5 \times 10^{-6} \text{ ft.} \approx 1.5 \times 10^{-3} \text{ mm.}$

5.5.2 Flow Velocity

Since the expression for flow velocity using eq. (5.19) and the transcendental equation for the friction factor, eq. (5.20), requires computation of the Reynolds number, a function of the flow velocity, the calculation of the final flow has been calculated by iteration in the past. With some manipulation of the expressions, a direct solution for the water flow velocity through a water passage with diameter, d , and length, l , can be found. Solving for the flow velocity, using eq. (5.19)

$$v = \sqrt{\frac{2\Delta p}{\delta f} \frac{d}{l}}.$$

The expression for the Reynolds number can then be written;

$$\text{Re} = \frac{vd}{\nu} = \frac{d}{\nu} \sqrt{\frac{2\Delta p}{\delta f} \frac{d}{l}}.$$

Substituting into the expression for the friction factor;

$$\begin{aligned} \frac{1}{\sqrt{f}} &= -2 \log_{10} \left(\frac{\epsilon}{3.7d} + \frac{2.51}{d \sqrt{\frac{2\Delta P}{\delta f} \frac{d}{l}}} \sqrt{f} \right) \\ &= -2 \log_{10} \left(\frac{\epsilon}{3.7d} + \frac{2.51}{d \sqrt{\frac{2\Delta p}{\delta} \frac{d}{l}}} \right). \end{aligned}$$

In this final form, the friction factor term is eliminated from the right side of the equation.

The expression for the flow velocity can finally be rewritten;

$$\begin{aligned} v &= \sqrt{\frac{2\Delta P}{\delta f} \frac{d}{l}} = \frac{1}{\sqrt{f}} \sqrt{\frac{2\Delta p}{\delta} \frac{d}{l}}, \\ &= -2 \sqrt{\frac{2\Delta p}{\delta} \frac{d}{l}} \log_{10} \left(\frac{\epsilon}{3.7d} + \frac{2.51}{d \sqrt{\frac{2\Delta p}{\delta} \frac{d}{l}}} \right). \end{aligned} \quad (5.21)$$

5.5.3 Units

Before going too far, it is important to clarify the units used in the calculations. Most of the world uses the MKS system of units. The US uses the more arcane English units. Therefore, the following calculations are made so that either system of units can be used and to demonstrate that, using the correct conversion factors, the expressions yield consistent results.

Pressure Drop

The expression for the pressure drop, given by eq. (5.19), is

$$\Delta p = f \frac{l}{d} \frac{\delta v^2}{2},$$

where the friction factor, f , and the ratio of the length and diameter of the water circuit, $\frac{l}{d}$, are unitless. Therefore, we concentrate on the terms which result in the units for pressure;

$$\Delta p \propto \delta v^2,$$

where the mass density of water is expressed in $\delta \left(\frac{Kg}{m^3} \right)$ and flow velocity is expressed in $v \left(\frac{m}{sec} \right)$. The units for pressure drop in the MKS system are

$$\begin{aligned} \Delta p &\propto \delta v^2, \\ &\propto \frac{Kg}{m^3} \times \frac{m^2}{sec^2}, \\ &\propto \frac{Kg - m}{sec^2} \times \frac{1}{m^2} = \frac{Newton}{m^2} = Pa. \end{aligned}$$

In the English system of units, the force density (weight) for water is given in units $\delta g \left(\frac{lb_f}{ft^3} \right)$ and flow velocity is expressed in $v \left(\frac{ft}{sec} \right)$. The units for gravity acceleration is, $g \left(\frac{ft}{sec^2} \right)$. The units for pressure drop in the English units is;

$$\begin{aligned} \Delta p &\propto \frac{\delta g}{g} v^2, \\ &\propto \frac{lb_f}{ft^3} \times \frac{1}{ft} \times \frac{ft^2}{sec^2}, \\ &\propto \frac{lb_f}{ft^2}. \end{aligned}$$

In the US, this pressure unit is converted to pounds per square inch (psi) = $\left(\frac{lb_f}{in^2} \right)$ by multiplying by the factor, $\frac{ft^2}{144 in^2}$.

Velocity

The expression for velocity is given by

$$v = \sqrt{\frac{2\Delta p}{\delta f} \frac{d}{l}},$$

where the friction factor, f , and the ratio of the length and diameter of the water circuit, $\frac{l}{d}$, are unitless. The units for pressure are given by $\Delta P (Pa) = \Delta P \left(\frac{\text{Newtons}}{m^2} \right)$. The units for velocity are given by;

$$\begin{aligned} v &\propto \sqrt{\frac{\Delta p}{\delta}}, \\ &\propto \sqrt{\frac{\frac{\text{Newtons}}{m^2}}{\frac{Kg}{m^3}}} = \sqrt{\frac{Kg \frac{m}{\text{sec}^2}}{\frac{m^2}{Kg}}} \\ &\propto \sqrt{\frac{m^2}{\text{sec}^2}} = \frac{m}{\text{sec}}. \end{aligned}$$

In English units, assuming that the pressure is converted to $\frac{lb_f}{ft^2}$, the units for velocity are given by

$$\begin{aligned} v &\propto \sqrt{\frac{\Delta p}{\delta}} = \sqrt{\frac{\Delta p}{\delta_{\text{weight}}}} = \sqrt{\frac{g\Delta p}{\delta_{\text{weight}}}}, \\ &\propto \sqrt{\frac{\frac{lb_f}{ft^2} \times \frac{ft}{\text{sec}^2}}{\frac{lb_f}{ft^3}}}, \\ &\propto \sqrt{\frac{ft^2}{\text{sec}^2}} = \frac{ft}{\text{sec}}. \end{aligned}$$

Pressure Conversion Factor The conversion for pressure from English to MKS units is,

$$\Delta p (Pa) = 6.895 \times 10^3 \Delta p (psi).$$

Flow Through the Conductor Coolant Passage

Once the flow velocity through the cooling circuit is computed, the volume flow rate can be computed. The flow passages through most conductors are circular holes with diameter d . Most conductor vendors describe conductor dimensions in mm. The expression for the coolant volume flow rate through a circular conductor coolant passage is given by

$$q = vA = v \frac{\pi d^2}{4}.$$

If the diameter is expressed in mm and the flow velocity in $\frac{m}{sec}$, the units must be adjusted for convenient volume flow units. The volume flow rate is rewritten as

$$\begin{aligned} q &= vA = v \left(\frac{m}{sec} \right) \frac{\pi d^2}{4} (mm^2) \times \frac{m^2}{10^6 mm^2} \times \frac{10^3 liters}{m^3} \\ q \left(\frac{liters}{sec} \right) &= 10^{-3} v \left(\frac{m}{sec} \right) \frac{\pi [d(mm)]^2}{4}. \end{aligned} \quad (5.22)$$

Flow Conversion Factor The conversion for flow from MKS to English units is derived in the following expression;

$$\begin{aligned} q \left(\frac{liters}{sec} \right) &= 10^{-3} v \left(\frac{m}{sec} \right) \frac{\pi [d(mm)]^2}{4} \\ q \left(\frac{liters}{sec} \right) \times \frac{gal}{3.875 liters} \times \frac{60 sec}{min} &= 10^{-3} v \left(\frac{m}{sec} \right) \frac{\pi [d(mm)]^2}{4} \times \frac{60}{3.875} \\ q (gpm) &= 1.548 \times 10^{-2} v \left(\frac{m}{sec} \right) \frac{\pi [d(mm)]^2}{4} \end{aligned} \quad (5.23)$$

Convenient Values

- A convenient unit for pressure used everywhere is $1 atm = 14.7 psi = 101352 Pa = 0.101 MPa$ (Mega Pascals).
 - Pressure drops across magnet cooling manifolds are typically $\Delta p \approx 10 atm$. If this value is to be selected at a “green field site”, selection of a lower value for facility construction may result in complex (and expensive) magnet coil systems.
- Flow velocity should be high enough so that the flow is fully turbulent, $Re \gtrsim 4000$. (See the next section.)

- Flow velocity $v \leq 4 \frac{m}{sec}$ to avoid flow vibration and erosion of the conductor coolant passage.
- The surface roughness for “smooth” tubes has been estimated as $\epsilon = 5 \times 10^{-6} ft = 1.5 \times 10^{-6} m = 1.5 \times 10^{-3} mm$.
- An acceptable coil temperature rise which protects the coil epoxy encapsulation from damage is $\Delta T \lesssim 30^\circ C$.
- For synchrotron radiation accelerators where beam stability depends on temperature stability, $\Delta T \lesssim 15^\circ C$.

Reynolds Number

The unitless factor, the Reynolds number, is given by $Re = \frac{vd}{\nu}$, where ν is the kinematic viscosity. ν is expressed in English units in Kreith[9]. The values are converted to MKS units in the following table.

Temperature		Kinematic Viscosity	
$^{\circ}F$	$^{\circ}C$	$\frac{ft^2}{sec}$	$\frac{m^2}{sec}$
60	15.4	1.22×10^{-5}	1.13×10^{-6}
70	21	1.06×10^{-5}	9.85×10^{-7}
80	26.6	0.93×10^{-5}	8.64×10^{-7}
90	32.1	0.825×10^{-5}	7.66×10^{-7}
100	37.7	0.740×10^{-5}	6.87×10^{-7}

Normally, the temperature in the water flow passage increases along the length of the conductor. Computations using the variation of the kinematic viscosity along the flow passage is unnecessarily complicated since it requires several iterations. For the sake of design of the coil system, a simpler and conservative approach is taken by assuming that the kinematic viscosity is constant and equal to the maximum value expected over the cooling water temperature range. Thus, one may assume a constant low water temperature and select $\nu = 1.13 \times 10^{-6} \frac{m^2}{sec}$ over the entire length of the conductor. The water in the conductor will heat up and the average temperature and the kinematic viscosity will decrease, increasing the flow. The more conservative approach will result in the computation of the minimum flow and the worst possible case scenario for the water (and coil) temperature rise.

5.5.4 Coil Cooling

The assumption is made that at high Reynolds numbers (turbulent flow), the heat transfer through the thin fluid film separating the conductor surface and the bulk fluid flow is high (a good assumption). Thus, the temperature at the inner surface of the conductor cooling channel is nearly the same as the water temperature. Moreover, because of the high thermal conductivity of the conductor, the entire conductor cross

section temperature is approximately equal to the cooling channel surface temperature. With these assumptions, it is only necessary to compute the maximum exit temperature of the coolant flow to estimate the maximum coil temperature. Since magnet conductors are normally cooled by water, water properties are used in the following expressions.

The heat (electrical power) absorbed by water flowing across a heated surface is given by

$$P = \dot{m} c_p \Delta T,$$

where \dot{m} = mass flow rate = $\delta_{water} q$, c_p = heat capacity and ΔT = Temperature change. In the expression, q = volume flow rate and δ_{water} = water mass density. The expression for the heat absorbed by water can be rewritten and solved for the volume flow rate resulting in the expression

$$q = \frac{P}{\delta_{water} c_p \Delta T}. \quad (5.24)$$

The properties of water required for the expression are;

$$\begin{aligned} \delta_{water} &= \frac{1.0 \text{ kg}}{\text{liter}} \\ c_p &= \frac{1.0 \text{ BTU}}{\text{lbm}^\circ F} = 4.187 \frac{\text{kjoules}}{\text{Kg}^\circ C} = 4.187 \frac{\text{kW sec}}{\text{Kg}^\circ C} = 1.9 \frac{\text{kW sec}}{\text{lbm}^\circ C}. \end{aligned}$$

Substituting into the equation for the required flow;

$$\begin{aligned} q &= \frac{P}{\delta_{water} c_p \Delta T} \\ q &= \frac{P (\text{kW})}{\frac{1.0 \text{ Kg}}{\text{liter}} \times 4.187 \frac{\text{kW sec}}{\text{Kg}^\circ C} \times \Delta T (\text{ }^\circ C)} \\ q \left(\frac{\text{liters}}{\text{sec}} \right) &= 0.2388 \frac{P (\text{kW})}{\Delta T (\text{ }^\circ C)}. \end{aligned} \quad (5.25)$$

Since flow is measured in $gpm = \frac{\text{gal}}{\text{min}}$ in the US, the units are converted in the following expression in the same manner used in a previous section;

$$\begin{aligned} q \left(\frac{\text{liters}}{\text{sec}} \right) \times \frac{\text{gal}}{3.875 \text{ liters}} \times \frac{60 \text{ sec}}{\text{min}} &= 0.2388 \frac{P (\text{kW})}{\Delta T (\text{ }^\circ C)} \times \frac{60}{3.875} \\ q (gpm) &= 3.7 \frac{P (\text{kW})}{\Delta T (\text{ }^\circ C)}. \end{aligned} \quad (5.26)$$

5.5.5 Calculations

The computation of the expressions for all the flow quantities, expressed by all the equations from (5.19) to (5.26) is tedious. One must substitute the values of the constants which express the properties of the coolant into the expressions. Also, a roughness value for the surface property of the inside of the coolant passage with the proper units must be used in the expression for the friction factor. The required input parameters are tabulated in a sample set of parameters. The appropriate units for the calculations in the English and MKS units are listed. In some cases, the English units are the same as the MKS units.

Quantities	English Units	MKS Units
Input Information		
Hole Diameter (d)	(ft)	(m)
Roughness (ε)	$(5 \times 10^{-6} \text{ m})$	$(1.5 \times 10^{-3} \text{ mm})$
Conductor Length (L)	(ft)	(m)
Coil Power (P)	(kW)	(kW)
Available Pressure Drop, Δp	$\left(\text{psi} = \frac{\text{lb}_f}{\text{in}^2} \right)$	$\left(\text{Pa} = \frac{\text{N}}{\text{m}^2} \right)$
Water Properties		
Mass Water Density	$= \frac{62.4 \frac{\text{lb}_f}{\text{ft}^3}}{g = 32.2 \frac{\text{ft}}{\text{sec}^2}}$	$= \frac{1 \text{ kg}}{\text{liters}}$
Water Heat Capacity	$= 1.9 \frac{\text{kW sec}}{\text{lbm}^\circ\text{C}}$	$= 4.19 \frac{\text{kW sec}}{\text{kg}^\circ\text{C}}$
H_2O Kinematic Viscosity (@60°F)	$= 1.216 \times 10^{-5} \frac{\text{ft}^2}{\text{sec}}$	$= 1.13 \times 10^{-6} \frac{\text{m}^2}{\text{sec}}$
Calculated Values		
Friction Factor, f	(No Units)	(No Units)
Flow Velocity, v	$\left(\frac{\text{ft}}{\text{sec}} \right)$	$\left(\frac{\text{m}}{\text{sec}} \right)$
Volume Flow, q	$\left(\text{gpm} = \frac{\text{US gal}}{\text{min}} \right)$	$\left(\frac{\text{liters}}{\text{sec}} \right)$
Temperature Rise, ΔT	(°C)	(°C)

In order to reduce the drudgery of the hydraulic calculations, a spreadsheet was prepared, automating the required calculation, which can be used to compute the relevant expressions by substituting the appropriate input information for any specific coil design. This spreadsheet is written on the CD attached to this publication. A sample page of the spreadsheet is presented in fig. 10 in English units and in fig. 11 in MKS units. The graphical outputs from the spreadsheets are presented in figs. 12 and 13 for the US and MKS units, respectively.

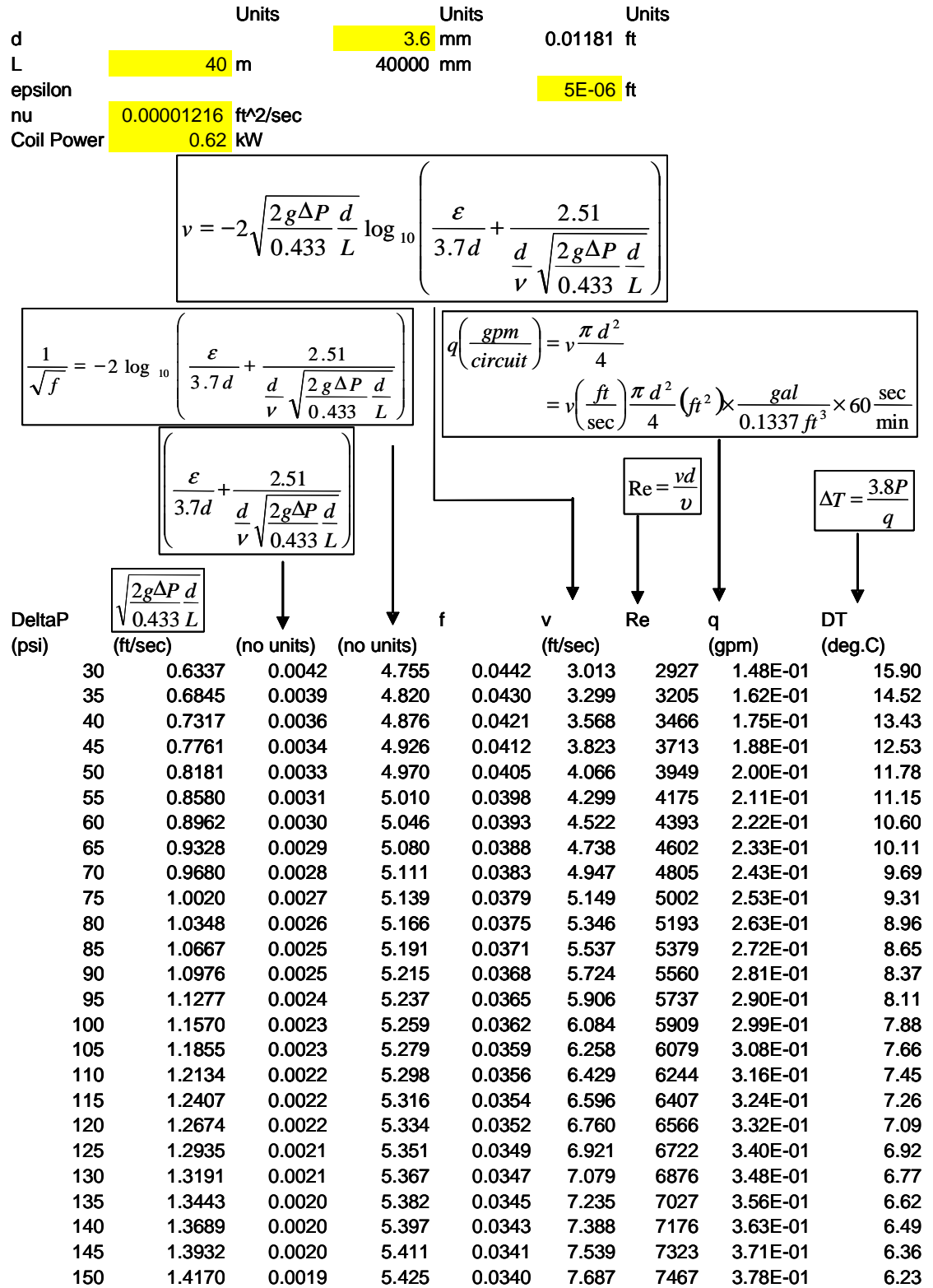


Figure 10 Flow Calculations Using US Units

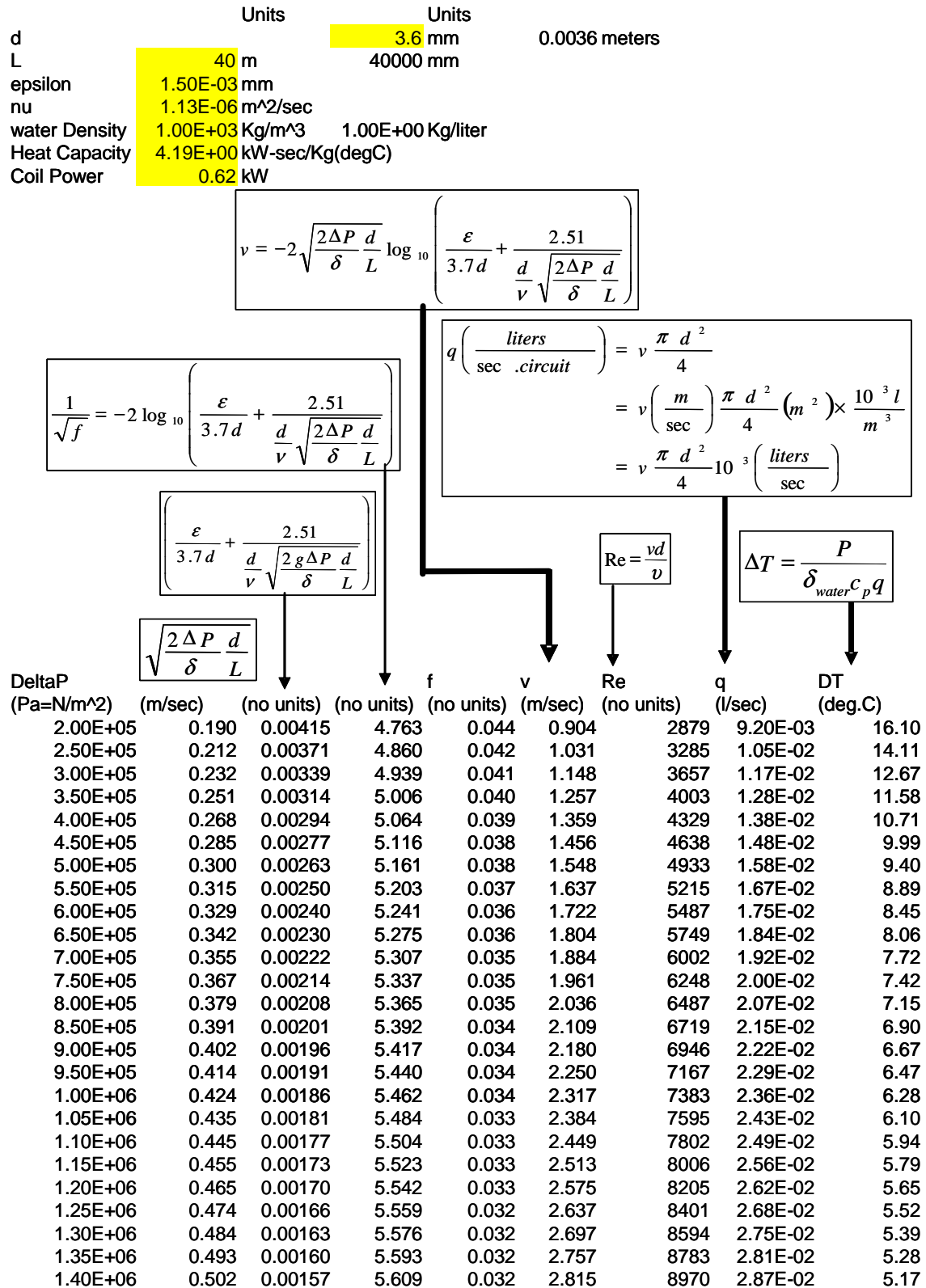


Figure 11 Flow Calculations Using MKS Units

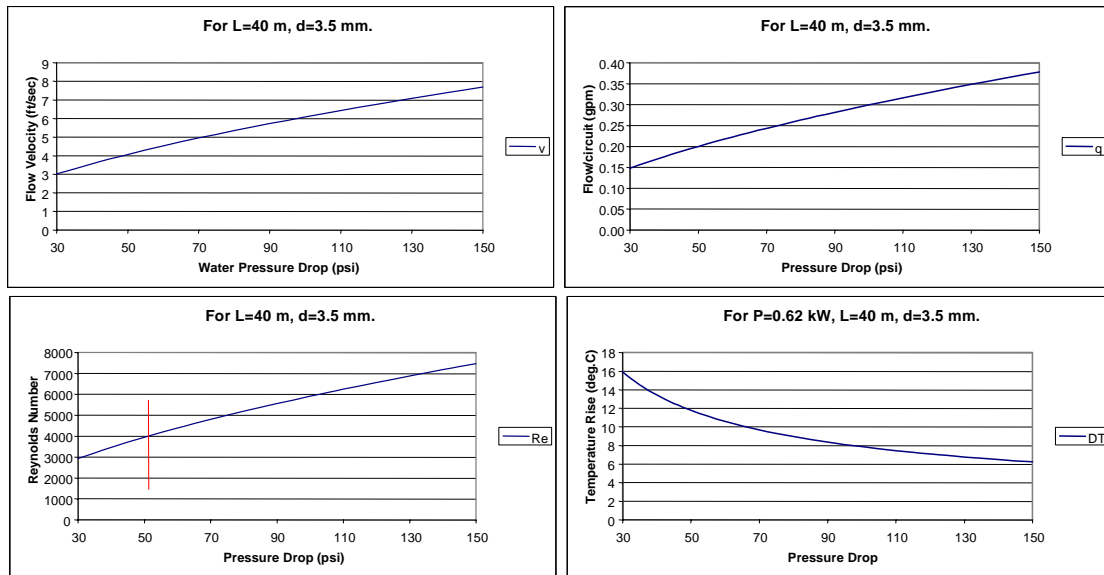


Figure 12 Graphical Relationships Using English Units

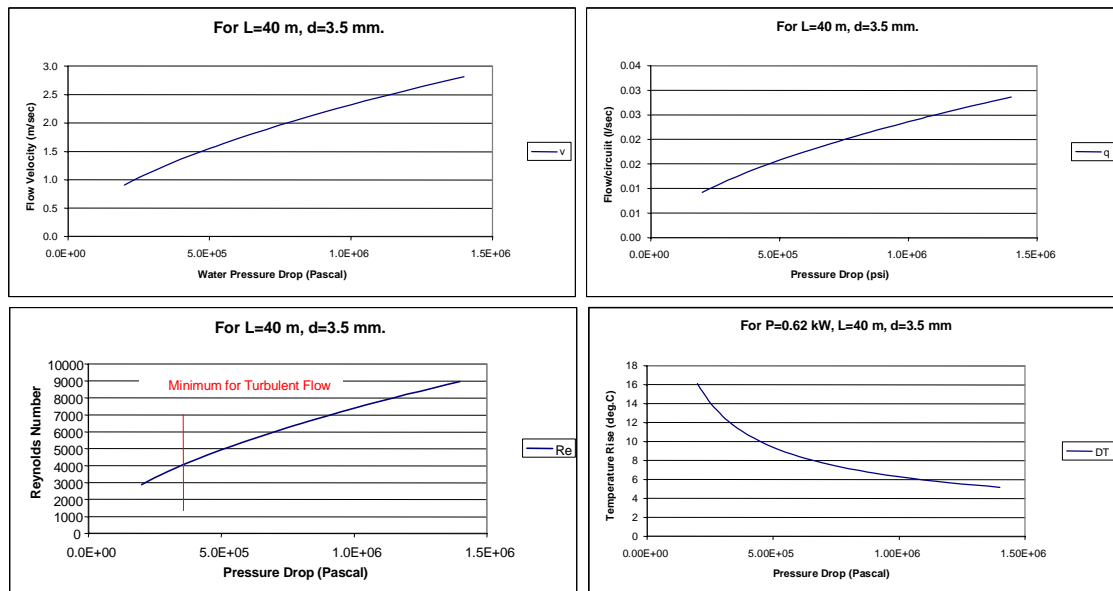


Figure 13 Graphical Relationships Using MKS Units

5.5.6 Sensitivities

The design of cooling circuits for magnets is often an iterative exercise. One may start with a simple case selecting a conductor with a given diameter hole and proposing a design requiring a single water circuit per coil. Preliminary calculation may result in findings that the water flow needed to limit the coil temperature rise to a reasonable value requires more water pressure than is available in the facility. On the other hand, one may find that the required water pressure for the proposed design is far less than the available pressure. Therefore, one can simplify and/or improve the magnet design by either combining the water circuits of several coils and connecting them in series or reducing the size of the coolant hole so that more area is available to carry the electrical current and reduce the total voltage or power. In any case, it is desirable to understand the sensitivities of the critical performance factors to selected parameters so that the results can be estimated prior to repeating the tedious flow and cooling calculations. In the following sections, it is assumed that the friction factor, f , is nearly constant (a good assumption).

Number of Water Circuits

The expression for the required flow is determined by the selection of the maximum allowable temperature and the computed magnet power at the required magnet excitation and given by;

$$q \left(\frac{\text{liters}}{\text{sec}} \right) = 0.2388 \frac{P (\text{kW})}{\Delta T (\text{°C})}.$$

The total flow can be divided among several circuits each of which dissipates a portion of the magnet power. The pressure drop is roughly proportional to the length of the water circuit. The length of the water circuit is expressed as;

$$l = \frac{K N l_{ave}}{N_w},$$

where K is the number of coils per magnet and $K = 2, 4$ and 6 for a dipole, quadrupole and sextupole, respectively. $N = \frac{\text{Turns}}{\text{coil}}$ and N_w is the number of water circuits per magnet. In general, $K = N_w$ for magnets with one water circuit per coil. The flow per water circuit is $\frac{q}{N_w}$ and the velocity is proportional to the flow per circuit.

Therefore, since

$$\begin{aligned}\Delta p &= f \frac{l}{d} \frac{\delta v^2}{2} \propto lv^2, \text{ and } v \propto \frac{q}{N_w}, \\ \Delta p &\propto lv^2 = \frac{KNl_{ave}}{N_w} \times \left(\frac{q}{N_w}\right)^2, \\ \text{or } \Delta p &\propto \left(\frac{1}{N_w}\right)^3.\end{aligned}\quad (5.27)$$

Thus, for instance, doubling the number of water circuits reduces the pressure drop to provide the required flow by a factor of eight.

Diameter of the Cooling Channel

Using the expression for the pressure drop, the proportionality can be expressed as

$$\Delta p \propto \frac{v^2}{d}.$$

But the volume flow rate $\dot{q} = Av = \frac{\pi d^2}{4}v$, and thus $v \propto \frac{1}{d^2}$. Substituting;

$$\Delta p \propto \frac{v^2}{d} \propto \frac{1}{d} \left(\frac{1}{d^2}\right)^2 = \frac{1}{d^5}. \quad (5.28)$$

It can be seen that increasing the cooling channel by a small factor can reduce the required pressure drop tremendously. Thus asking a conductor vendor to slightly alter a standard design and fabricate a new die set can result in major benefits. Conversely, the effect of small mechanical fabrication errors, systematically reducing the cooling channel diameter by a small amount, can have major consequences. Thus, when specifying the diameter of the tooling channel, the dimensions should be $+Δd$, -0 . It is important to carefully define the mechanical fabrication tolerances for conductors.

5.6 Chapter Closure

Using Stoke's Theorem to convert Maxwell's general differential equation to an integral form, generalized expressions for the required electrical excitation for various magnet types are developed. A few examples of different magnet geometries are illustrated to develop relationships for a current carrying septum, a Lambertson septum and conductor dominated geometries. It is shown that expressions for estimating the magnitude of the fringe fields in septum magnets can be developed from the integral relationships. It is also shown that the current distribution for a high

quality dipole and quadrupole can be computed for magnet geometries where fields are dominated by the distribution of the conductors. The examples of the current dominated magnet types are academic examples since, if substituting real magnet requirements, it will be quickly evident that the required current densities are far larger than practical to achieve reasonable fields with reasonable geometries. The examples are useful since they are the first step in developing the coil locations for superconducting dipole and quadrupole magnets whose coils are divided into blocks of conductors spaced to approximate a cosine current density distribution.

Manipulation of the expressions for the required magnet excitations result in expressions for the estimation of magnet power requiring only information about the physics requirements for the magnet and the selection of one design parameter, the current density, j . Using canonical values for the design parameters, one can estimate the cross section of magnets and estimate the requirements for power and power distribution.

Detailed mechanical design of the magnet coil eventually requires selection of the number of turns per coil and the conductor size. These involve consideration of the coil cooling and the availability of cooling water pressure at a facility. Expressions for the computation of water flow are presented. These expressions can be used to analyze the hydraulic performance of detailed designs for magnet coils.

Since the first design seldom satisfies thermal and hydraulic constraints, sensitivities of flow parameters to the selection of the number of water circuits and the diameter of the cooling channel are developed. These hydraulic sensitivity relations show that, although a first design iteration may exceed desired values by a wide margin, changes in the topology of the hydraulic circuit or small changes in the diameter of the hydraulic cooling channel can quickly bring the parameters within limits imposed by the facility infrastructure. Typical values of some of the design parameters are listed. These provide starting points for real designs developed from physics requirements and typical constraints of materials and facilities.

This chapter is an introduction to practical engineering design of magnets. This chapter, along with the chapter on perturbations, can be exploited to translate the magnet mathematics covered in the earlier chapters to develop engineering designs, translated into mechanical fabrication drawings and specifications for electro-magnetic devices ultimately used in particle accelerators and beam transport systems.

5.7 Problems

Problem 5.1

Assuming a dipole with a halfgap, $h = 20 \text{ mm}$ requiring a field $B = 1.3 \text{ Tesla}$, estimate the required gross size of the coil assuming a coil packing fraction of 50% and a magnet efficiency $\eta = 98\%$. Use the “canonical” current density, $j = 10 \frac{\text{Amps}}{\text{mm}^2}$. Assume the dipole length of 0.5 meters with an average turn length of 1.2 meters. Estimate the magnet power dissipation assuming $\rho = 1.86 \times 10^{-8} \Omega \text{ m}$.

Problem 5.2

Assuming a quadrupole with a pole radius, $h = 35 \text{ mm}$ and a poletip field $B = 0.6 \text{ Tesla}$, estimate the required gross size of the coil assuming a coil packing fraction of 50% and a magnet efficiency $\eta = 98\%$. Use the “canonical” current density $j = 10 \frac{\text{Amps}}{\text{mm}^2}$. Assume the quadrupole length of 0.2 meters with an average turn length of 0.5 meters. Estimate the magnet power dissipation assuming $\rho = 1.86 \times 10^{-8} \Omega \text{ m}$.

Problem 5.3 (Solution)

Assuming a sextupole with a pole radius, $h = 45 \text{ mm}$ and a poletip field $B = 0.3 \text{ Tesla}$, estimate the required gross size of the coil assuming a coil packing fraction of 50% and a magnet efficiency $\eta = 98\%$. Use the “canonical” current density $j = 10 \frac{\text{Amps}}{\text{mm}^2}$. Assume that the sextupole is 20 cm. long requiring a copper coil with an average turn length of 50 cm. Estimate the required magnet power assuming $\rho = 1.86 \times 10^{-8} \Omega \text{ m}$.

Problem 5.4 (Solution)

For problem 5.3, assume selection of standard Outukumpu[®] conductor #6881 illustrated in fig. 14. The cross sectional area for this conductor is $A = 20.323 \text{ mm}^2$. Based on this area and using the “canonical” current density $j = \frac{10 \text{ Amps}}{\text{mm}^2}$. the coil can be designed for $I = 200 \text{ Amps}$. Suppose we select a 20 turn coil (two rows of ten turns each) and assume a 200 Amp power supply, providing a 10% margin over the physics requirement for this magnet. Recompute the power and perform the hydraulic calculations. Assume the facility can provide a pressure across the water manifolds of approximately 10 atmospheres.

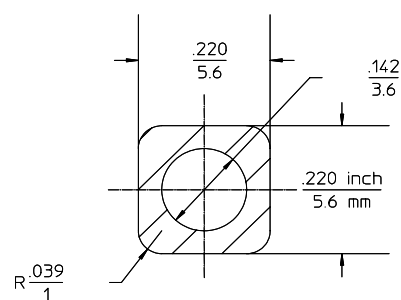


Figure 14 Standard 5.6 mm. Square Copper Conductor

Chapter 6

POISSON

Fabrication of a three dimensional magnet begins with the two dimensional design. The effort to design a two dimensional magnet requires the determination of the pole contour to achieve a specified field amplitude and uniformity using the non-ideal boundary conditions determined by the excitation, physical size and location of the coils and the physical boundaries of the steel yoke. The design process involves defining a baseline pole contour, analyzing its performance, improving the contour by adjusting its shape, reanalyzing and repeating the process until the desired two dimensional field amplitude and uniformity are achieved. Since the magnetic behavior of steel is nonlinear, the calculations must be performed iteratively, adjusting the nonlinear magnetic properties of the steel at the calculated field amplitude at each iteration.

A two dimensional analysis tool is required to carry out the difficult and tedious analysis requiring point by point calculation of the entire two dimensional field distribution. Poisson and Pandira are two computer codes which carry out this calculation. They both solve the Poisson's equation (page 36) on a two dimensional grid generated by defining the boundaries of the coil, yoke and pole. The two codes differ only in the algorithms used to solve the huge number of nonlinear finite element equations generated at an array of two dimensional points in the magnet cross section. Poisson uses an iterative under-relaxation method to invert the matrix and solve the array of nonlinear equations. Pandira takes advantage of the nearly diagonal structure of the coefficient matrix and successively approximates the solution by inverting the smaller matrix blocks along the diagonal making up the elements of the larger matrix. (The few nonzero off diagonal elements coupling the larger blocks are initially ignored.) The inverted matrix solution is used to adjust the nonlinear iron properties and the process is repeated. Poisson and Pandira are the solver codes in a family of magnetostatic codes originally written and developed by Klaus Halbach and Ron Holsinger[10] at LBNL [11] in Berkeley. These codes were originally written in Fortran, converted to UNIX[®] and finally ported to operate under MicroSoft Windows[®].

The Windows[®] version of Poisson and Pandira, as well as their descendants which solve electrostatic and RF problems, are maintained by a US Department of Energy (DOE) supported Los Alamos National Laboratory[12] program and admin-

stered by a group headed by James Billen[13]. This family of codes is grouped as the Poisson and SuperFish[©] family. Since the codes were written, developed and maintained by government funded programs, they are public domain and provided cost free for any user. Instructions for downloading and installing the family of codes and supporting help documents can be obtained by email to James H. Billen <jbillen@lanl.gov>.

Many commercial codes have been written to solve two dimensional magnetostatic problems. Most of the codes are subsets of more general three dimensional codes. Initially, the three dimensional codes were difficult to operate and required a long learning curve. The commercial vendors have lately developed sophisticated user interfaces resulting in much more user friendly three dimensional codes and their two dimensional counterparts. In some cases, three dimensional computer aided design (CAD) databases can be used as inputs for meshing of the three dimensional space. Baseline tests of the three dimensional codes have been performed and reported by various laboratories. It is very difficult to evaluate the accuracy of the three dimensional codes because of the difficulty in making accurate and detailed maps of measured field vectors for comparison with computed values. In general, two dimensional codes provide more accurate results than three dimensional codes. This is because they more accurately characterize the tangential H field at the iron/air interface than the three dimensional codes.

Commercial two dimensional codes have improved their user interfaces and presentation formats. Improvements in the Poisson family of codes, since they are not driven by competitive economics, is steady but substantially slower.

The primary advantage of the Poisson family of codes is its familiarity and use of the language of magnet theory. Results are presented as edited lists of the vector potentials and field component values in specified line or rectangular regions. Vector potential values can be interpolated around arcs defining the good field region. These quantities are then Fourier analyzed and the field harmonics evaluated at the radius of the arc are computed from the coefficients of the vector potential Fourier series. The vector potentials edited around larger radius arcs, incorporating portions of the pole, can also be used to define the boundary conditions for the solution of the field distribution in a more limited region of the two dimensional magnet cross-section. This technique can be used to limit the size of the mesh and provide a finer mesh for defining the important pole tip configurations. The Poisson code also provides internal algorithms so that the nonlinear iron properties are properly scaled during conformal mapping. This allows for Poisson calculations to be made in conformally mapped geometries, correctly modelling the iron properties from the original geometry. Examples are presented using the vector potential boundary conditions in conformally mapped configurations.

Since the Poisson family of codes is familiar to the author (and many users at other laboratories), it is the code of choice for the description in this text of the detailed computer calculations required to develop the two dimensional magnet

cross section design. The design and analysis of the two dimensional magnet cross-section is the first step in evolving a fabricated magnet meeting the physics needs of accelerator and beam transport magnets.

6.1 Elements of the Family of Codes

Only the subset of the Poisson and SuperFish[©] family of code elements used in magnetostatic calculations are listed and described. Four main components are of interest to the magnet designer.

1. Automesh.exe

- (a) Automesh is an automatic mesh generator. It takes the (x, y) coordinates of the boundaries of the coil and yoke written in a text file and generates the (k, l) coordinates of the boundaries and interpolates the (k, l) coordinates of the space in the gap and the area surrounding the magnet, the points in the iron yoke and the points in the conductors.
- (b) Automesh defines boundary conditions, defines the type of iron used in the calculation and can choose whether the problem is two dimensional or three dimensional rotationally symmetric.
- (c) Automesh input parameters are provided to define the boundaries for the edit of computed quantities and define the radius and the multipole indices allowed by the symmetry conditions of particular magnet types (see page 50) for harmonic analysis of the vector potential and the field.

2. Poisson.exe

- (a) Poisson solves the series of finite element equations using the boundary conditions, limits, coordinates and iron properties generated by Automesh and generates an edit file which summarizes the calculated values (the desired solutions) and (if requested) the harmonic field values.

3. Pandira.exe

- (a) Pandira duplicates the function of Poisson but uses a different algorithm for achieving the solution of the finite element equations. In general, the solution algorithm is faster and more robust than the under relaxation algorithm employed by Poisson and can occasionally achieve converged results when Poisson cannot.

4. Wfsplot.exe

- (a) Wfsplot is a graphics package which can display the geometry, the mesh structure and the flux plot. It can be run after the Automesh routine to display the geometry to help the user ensure that the geometry has been input correctly. It is also useful to determine whether the mesh density is appropriate for defining the geometry when many points are required in a local area with complicated geometry. After solving a problem using Poisson or Pandira, Wfsplot displays the vector equipotential curves, whose density is proportional to the flux density. An icon on the display can be moved to display the components and the magnitude of the flux density at the location of the icon.

6.2 Documentation

The Poisson and SuperFish family of codes is fully documented with a set of Word[©] documents supplied with an index and links to the subject selected in the index. The documentation describes all the ProbCons (Problem Constants) and the variable names used to describe the input quantities required for the AutoMesh program. The ProbCons can be input using names as well as subscripted constants. Sample problems are provided as examples which can be used as templates for the generation of files for different geometries. Because the primary LANL interest are RF problems, most of the documented examples are in this area. Because of this, example magnet analysis problems are presented in this chapter that illustrate different features of different magnet types and different features of the magnet codes.

6.3 Problem Flow

The generation of files and the flow of the computations is schematically represented in fig. 1.

1. The designer writes a text file describing the boundary conditions, the geometry and desired output format for the solution of the two dimensional magnet problem.
2. Automesh is run using this text file as input.
 - (a) Automesh generates a temporary file with the same name as the text file appended with the designation .T35. This designation is a remnant of the old Fortran version of the code where Automesh and Poisson wrote a file to a reserved magnetic tape identified as Tape35.
 - (b) Filename.T35 is the source file for running either Poisson or Pandira or Wfsplot. When Wfsplot is run using the source file before running Poisson or Pandira, the graphical output presents a scaled outline of the input geometry. The pulldown menu allows displaying the geometry with or without the mesh.

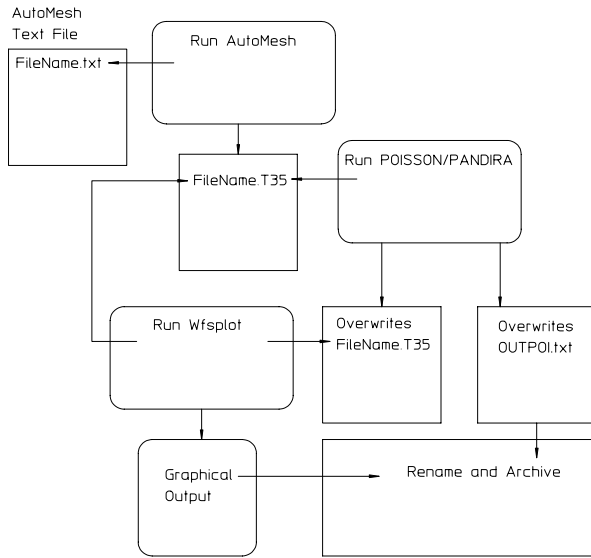


Figure 1 Poisson Calculation Flow Diagram

3. Poisson or Pandira is executed.
 - (a) Filename.T35 must be designated as the source for the input data to Poisson or Pandira. If Automesh.exe is run just before Poisson or Pandira is run, the last .T35 file written is used and Filename.T35 does not have to be designated.
 - (b) Poisson or Pandira overwrites Filename.T35 after its execution.
 - (c) The overwritten Filename.T35 is the source file for running Wfsplot. When Wfsplot is run using the source file after completion of the Poisson or Pandira calculations, the graphical output presents a plot of vector equipotentials superimposed on the scaled outline of the input geometry. The pulldown menu allows displaying the geometry with or without the mesh. The graphical output can be stored in a variety of formats to include in documentation or for archiving.
 - (d) During execution, Poisson or Pandira overwrites files OUTPOI.txt or OUTPAN.txt. These are text files which record the progress of the program while converging, review the BH relations of the selected steel used in the computation, tabulate the vector potential, field and field gradient distribution in the area specified by the input text file and summarize the Fourier coefficients of the solution (if requested in the input text file). Selected portions of this file can be copied and pasted into archival documents or pasted into a spreadsheet for later analysis. These files can be renamed

```

Simple Dipole
To test VP boundary conditions

$reg mat=1, kprob=0, mode=0,conv=.1,
kmax=100, lmax=75,
icylin=0,
xminf=0, xmaxf=25,ktop=11
yminf=0, ymaxf=10,ltop=5
ktype=121,nptc=31, nterm=14,rint=20,
rnorm=25, angle=90, anglz=0
ienergy=1,
nbsup=0, nbslo=1, nbsrt=0, nbslf=0$

```

Figure 2 Sample Boundary Conditions AutoMesh Dataset

for archiving since later execution of Poisson or Pandira overwrites these files.

6.4 AutoMesh

All the labor required to define and set up a problem for Poisson or Pandira is in writing a text file which is executed by AutoMesh. Examples of the text files written for various magnet geometries are presented to highlight the nomenclature and variables.

6.4.1 Boundary Conditions and Constraints

The example of the first part of the text file illustrated in fig. 2 is for a simple dipole.

1. The first two lines in the text file are the title and descriptors for the problem. These two lines will be copied in the output file OUTPOI.txt or OUTPAN.txt.
 - (a) Comment lines can follow which provide more detailed information. Each comment line must be started with a !. All characters on a line following the ! sign are ignored by the program.
2. The first section of the input file defines the boundary conditions and the calculation and output edit constraints. This section is delineated with a starting \$reg or @reg and ended with a \$ or @ and defines the following;
 - (a) (mat=1) - The region defining the problem boundary is an air region. The regions which are read later are superimposed on this air region.
 - (b) (kprob=0) - The problem is a Poisson or Pandira problem. Other values are used for electrostatic or RF problems.

- (c) (mode=0) - The generic 1010 steel finite permeability table is used for the nonlinear BH properties of the steel.
- (d) (conv=0.1) - The physical dimensions for the input coordinates is mm. (conv=1 is cm and conv=2.54 is inches.)
- (e) The range of the horizontal and vertical axes are determined by the first region in the text file. In the example shown in fig. 3, the physical boundaries are defined by the limits $0 \leq x \leq 150 \text{ mm}$ and $0 \leq y \leq 100 \text{ mm}$. The range of the horizontal and vertical mesh points are determined by the values (kmax=50) and (lmax=50). In the example, the unmodified mesh densities are given by

$$\frac{150 \text{ mm}}{50 \text{ mesh points}} = \frac{3 \text{ mm}}{\text{horizontal mesh}}$$

and

$$\frac{100 \text{ mm}}{50 \text{ mesh points}} = \frac{2 \text{ mm}}{\text{vertical mesh}}.$$

- (f) (xreg1=20, kreg1=20, yreg1=20, lreg1=20) - If more detail is required in specified regions, both the horizontal and vertical regions can be subdivided with different densities of mesh points. These variables define a higher mesh density in the horizontal region, $0 \leq x \leq 20 \text{ mm}$ divided into $0 \leq k \leq 20$ mesh points, and a higher density in the vertical region, $0 \leq y \leq 20 \text{ mm}$ divided into $0 \leq l \leq 20$ mesh points, a mesh density of 1 mm per horizontal mesh. The remainder of the horizontal space has a mesh density

$$\frac{150 \text{ mm} - 20 \text{ mm}}{30 \text{ mesh points}} = \frac{4.33 \text{ mm}}{\text{horizontal mesh}}$$

and the remainder of the vertical space has a mesh density

$$\frac{100 \text{ mm} - 20 \text{ mm}}{30 \text{ mesh points}} = \frac{2.67 \text{ mm}}{\text{horizontal mesh}}.$$

- i. The horizontal and vertical regions can be divided into an arbitrary number of subregions by defining the variables xregn, kregn, yregn and lregn where n is an integer in the expressions. The mesh density in these subregions is

$$\begin{aligned} \text{XSubregion Density} &= \frac{xregn - xregn_{-1}}{kregn - kregn_{-1}} \\ \text{YSubregion Density} &= \frac{yregn - yregn_{-1}}{lregn - lregn_{-1}}. \end{aligned}$$

- (g) (icylin=0) - The dimensions are given in Cartesian coordinates.

- i. (icylin=1) The coordinates are for a three dimensional solid using cylindrical coordinates. ($x=\text{radius}$, $y=z$) coordinates.
- (h) (xminf=0, xmaxf=25, ktop=11) - The horizontal range of the output edit of the calculated values is $0 \leq x \leq 25 \text{ mm}$. The number of increments for the edit is 11. For these range of variables, the calculated vector potential, field and field gradient are tabulated at $k_{top} - 1 = 10$ increments of 2.5 mm in the horizontal direction.
- (i) (yminf=0, ymaxf=10, ltop=5) - The vertical range of the output edit of the calculated values is $0 \leq y \leq 10 \text{ mm}$. The number of increments for the edit is $l_{top} - 1 = 4$. For these range of variables, the calculated vector potential, field and field gradient are tabulated at 4 equal increments of 2.5 mm in the vertical direction.
- (j) (ktype=121, nptc=31, nterm=14, rint=20, rnorm=25, angle=90, anglz=0) - If these variable inputs are given, the Fourier coefficients of the vector potential and the field components are computed from the vector potentials.
 - i. (ktype= n , $\Delta n_{\text{allowed}}$, boundary) - $n = \text{field index} = 1$ (dipole), $\Delta n_{\text{allowed}} = \text{multipole increment} = 2$, $n_{\text{allowed}} = n + \Delta n_{\text{allowed}}$. boundary = 1 means the flux lines are perpendicular to the horizontal axis. boundary = 0 means the flux lines are tangent to the horizontal axis.
 - ii. (ktype=121) is for a normal (non skew) dipole with allowed multipoles = 1, 3, 5,
 - iii. (ktype=120) is for a skew dipole with allowed multipoles = 1, 3, 5,
 - iv. (ktype=241) is for a normal (non skew) quadrupole with allowed multipoles = 2, 6, 10,
- (k) (nterm=14) - Fourteen multipole terms are computed. A number this large is seldom needed.
- (l) (nptc=31, rint=20, rnorm=25, angle=90, anglz=0) - The vector potential values edited on a rint=20 mm arc from angle starting at anglz=0 degrees and ending at anglz+angle=90 degrees divided into nptc=(31-1) = 3° angular increments. The calculated values are renormalized at rnorm=25 mm radius.
 - i. Evaluation of the vector potentials for Fourier analysis must be made at least two mesh points away from any iron boundary (rint=20 mm). This is because the vector potential solution has a discontinuity at the iron boundary and the field is interpolated from the vector potential nearest two neighboring mesh points surrounding the designated points for the harmonic analysis. Often, however, the vector potential and field values are desired at a larger radius. The values are extrapolated to rnorm=25 mm radius.

- A. An exception to the mapping of the vector potential through the steel boundary is given in a later section in this chapter. The exception uses the vector potential as the boundary values for calculating the field distribution in a limited portion of the full magnet.
- (m) (ienergy=1) - The stored energy in $\frac{\text{joules}}{\text{cm}}$ for the two dimensional cross section is computed when ienergy=1. If ienergy=0, this calculation is not made. The total magnet stored energy is computed by multiplying this factor by the magnet length and the number of segments in which the full magnet is divided to take advantage of symmetry. The stored energy is useful in calculating the inductance of the magnet.
- (n) (nbsup=0, nbslo=1, nbsrt=0, nbslf=0) - The boundary conditions for the problem are defined. *nbsup*, *nbslo*, *nbsrt* and *nbslf* refer to the *upper*, *lower*, *right* and *left* boundaries, respectively. *nbsxx*=0 and *nbsxx*=1 are for a Dirichlet (flux parallel) and Neumann (flux normal) boundary conditions, respectively.

6.4.2 Geometry

The geometry portion of the dataset for a simple dipole is illustrated in fig. 3. Some of the features and rules governing the format of the geometry filetype are listed below. Since conv=0.1 was selected in the definition portion of the filetype, all the input dimensions are in mm.

1. It is useful to insert a comment line starting with a ! describing each geometric shape.
2. The line defining each geometric point starts with a \$po or @po and ends with a \$ or @.
3. The regions can be closed, open or can be defined by a point.
 - (a) The first and last entries defining a closed region must be identical.
4. The first area is an air region bounded by the points in the first group of coordinates in fig. 3 and defines a two dimensional area on which the coils and yoke are superimposed. This region can describe any arbitrary closed space.
5. The second area is bounded by the points in the second group of coordinates in fig. 3 and defines a two dimensional rectangular area of the coil.
 - (a) The first line defining this region, (\$reg mat=1 cur=-2000\$) signifies a new region, with mat=1 (meaning air) with a total current of -2000 Amperes.

- i. A negative value for the current was selected since, in this example, it results in a positive vertical field on the horizontal centerline.
 - ii. The current is uniformly distributed over the geometric shape.
 - iii. The remaining five points define the boundaries of the rectangular coil area with the fifth coordinate identical with the first coordinate, closing the rectangular area.
- (b) The coil can be defined by any number of points.
- i. A single conductor is defined by a single coordinate point.
 - ii. A line current is defined by two coordinate points.
 - iii. More than two coordinate points can be used to define a line current, or if the first and last coordinates are equal, a coil defined by the area of the closed coordinates.
6. The third area is bounded by the points in the third group of coordinates in fig. 3 and defines a two dimensional boundaries of the yoke.
- (a) The first line defining this region, (`$reg mat=2$`) signifies a new region, with $\text{mat}=2$ (meaning finite nonlinear permeability steel).
 - (b) The remaining points define the coordinates of the closed area describing the shape of the two dimensional yoke.
7. New areas are superimposed over the previous meshed points. Therefore, if a hole is desired in the iron, a new region following the third group of coordinates defining the closed boundary of a hole with $\text{mat}=1$ will superimpose a hole in the iron.

6.4.3 Setting Up and Testing the Geometry

The process of setting up the geometry can be very difficult without graphical presentation of the digital data (the coordinates). A useful technique found by the author was to take advantage of the graphical capabilities of a spreadsheet. The spreadsheet has the added advantage that coordinate points can be added, deleted and/or modified and the graphical output will immediately reflect the results of the changes. The graphical output quickly verifies if areas overlap or fail to fall within the problem boundary. A simple concatenate instruction can then be used to convert the coordinates into the text form required by Automesh. The series of text lines can then be copied and pasted into the input text file. This process is illustrated in fig. 4.

```

!first region is air (mat=1), defines
the problem limits.
$po x=0, y=0$
$po x=150, y=0$
$po x=150, y=100$
$po x=0, y=100
$po x=0, y=0

!Coil
$reg mat=1 cur=-200000
$po x=55, y=25
$po x=75, y=25
$po x=75, y=45
$po x=55, y=45
$po x=55, y=25

!Iron Yoke
$reg mat=2
$po x=0, y=25
$po x=40, y=25
$po x=50, y=50
$po x=80, y=50
$po x=80, y=0
$po x=120, y=0
$po x=120, y=80
$po x=0, y=80
$po x=0, y=25

```

Figure 3 Geometry Dataset for a Simple Dipole

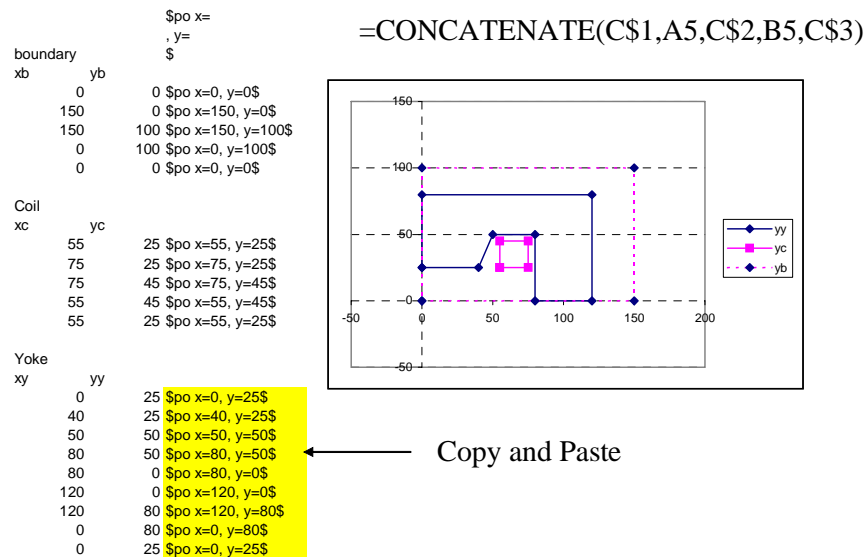


Figure 4 Setting Up the Geometry in a Spreadsheet

6.5 Symmetries

The previous example of a simple dipole took advantage of the symmetries of the design and divided the problem so that the geometry was defined only in the first quadrant of the Cartesian coordinate system. It is seldom necessary, in fact it is undesirable, to include the symmetric regions of the magnet. In the previous example, the number of mesh points can be increased from $k \times l = 50 \times 50 = 2500$ to 2 or 4 times this number, depending on whether half or the whole magnet is analyzed. This results in the program having to invert a much larger matrix to achieve a solution. A second, more crucial reason that it is undesirable to include the symmetric regions of the magnet is computational. The solving algorithms used in Poisson and Pandira find it difficult to converge on a solution when the mesh is symmetric. This is because the solutions oscillate by attempting to balance about points which are symmetrically located with respect to centerlines. The convergence factors appear to be asymptotically approaching a small value as the number of iterations increase, but suddenly appear to grow again. This cycling repeats until the limit of the number of iterations is reached, resulting in an un converged and incorrect solution.

6.5.1 Example - Collins or Figure Eight Quadrupole

Some geometries are inherently assymmetric. A commonly used example of an assymmetric two piece quadrupole is a Collins or figure eight geometry with very narrow vertical legs and a wider horizontal leg carrying most of the flux between the horizontal poles. A conventional quadrupole is symmetric about a line at $\frac{\pi}{4}$, with equal width vertical and horizontal legs. This geometry can be completely and accurately characterized by calculation of the field distribution for the angular region, $0 \leq \theta \leq \frac{\pi}{4}$. Despite the assymetry of the Collins or figure eight geometry, two dimensional magnet calculations achieve very accurate results if the calculations were carried out as if the geometry were symmetric. The second Poisson/Pandira example is a symmetric quadrupole. An example of the input file for the Automesh program for an assymmetric quadrupole, treated as if it were symmetric, is presented.

Boundary and Constraints Dataset

The text entries (shown in fig. 5) are very similar to the entries for the simple dipole. Some noteable differences are listed.

1. The x and y mesh regions are subdivided into xreg1, xreg2, yreg1 and yreg2 to achieve a higher mesh density in the pole region of the magnet. The pole can be optimized and characterized by many densely spaced coordinates.
2. (ktype=241) - This indicates a quadrupole with harmonic indices spaced at $\Delta n = 4$ values ($n = 2, 6, 10, \dots$). Again, the last integer 1 indicates flux normal to the horizontal axis. This overwrites the equivalent ktype=4 line.

```

• $reg mat=1, kprob=0, mode=0,conv=.1
• xmin=0, xreg1=50.0, xreg2=235, xmax=301.65,
•           kreg1=60, kreg2=200, kmax=220,
•           ymin=0.0, yreg1=30.0, yreg2=108, ymax=301.65,
•           lreg1=40, lreg2=120, lmax=220,
•           icylin=0,
•           xminf=0, xmaxf=230,
•           yminf=0, ymaxf=0,
•           ktype=4,
•           nbsup=0, nbslo=1, nbsrt=0, nbslf=1,
•           ktype=241,nptc=46 nterm=14,rint=30, rnorm=32.5, angle=45, anglz=0$
•           !first region is air (mat=1)
•           !problem type is poisson
•           $po x=0.0, y=0.0$
•           $po x=301.65, y=0.0$
•           $po x=301.65, y=301.65$
•           $po x=0.0, y=0.0$

```

Figure 5 Quadrupole Boundary Condition and Computation Boundary Textfile

3. (nptc=46, angle=45, anglz=0) - The vector potential edit is performed on an arc with $0 \leq \theta \leq 45^\circ$ at $(nptc - 1) \Delta\theta = 1^\circ$ steps.
4. The four points limiting the boundary of the problem are the closed coordinates of a triangular area.

Geometry Dataset

The pole contour for the sample quadrupole, $xy = \frac{35^2}{2}$, is an ideal hyperbola with a 35 mm pole radius. The quadrupole geometry along with the solution flux plot derived from the POISSON calculation is illustrated in fig. 6. The POISSON analysis indicated that the field quality for this pole geometry does not satisfy the physics multipole error content requirements. A later section in this chapter describes the means of optimizing the pole contour to achieve the required field quality.

6.5.2 Coil Geometry

The dataset for the coils is illustrated in fig. 7. Some of the Physics considerations for the unusual coil design is described before listing some of the meshing practices.

Beam Based Alignment In this example, the coil is divided among two rectangular blocks. The second, small block, is added as a trim coil operated at low alternating currents to perform beam based alignment. A misaligned beam through a quadrupole will steer the beam. A small alternating current (AC) can be added

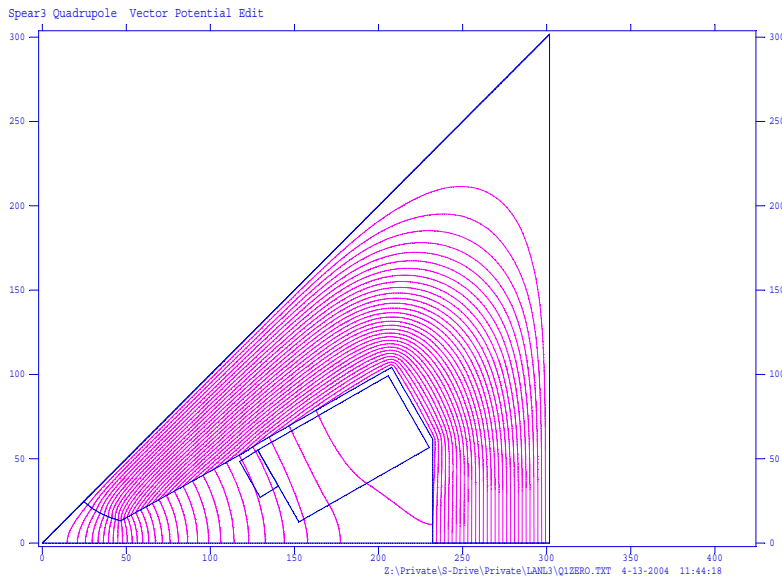


Figure 6 Symmetric Quadrupole Flux Plot

during accelerator commissioning to determine whether the charged particle beam is centered in the quadrupole aperture. If the beam is misaligned, signals at downstream beam position monitors (BPM's) with the frequency of the alternating trim coil current will identify beam misalignment through that particular magnet. Correctors, located in front of the quadrupole, can then be used to steer the beam through the quadrupole until the signal amplitude at the beam position electrode is minimized or nulled. The matrix of steering magnet currents can be developed by individually conducting the beam based alignment excercise through all the quadrupoles in the lattice.

Trim coils are added to quadrupoles grouped in a family connected in electrical series. A small AC power supplies can be connected to each set of trim coils. This allows the discrimination among the individual magnets in a power supply string.

For magnets with individual power supplies, the trim coil can be omitted and beam based alignment can be performed by making changes in the main power supply currents. Because it is often difficult to resolve the small BPM signals when the currents are changed slowly, some individually powered quadrupoles are supplied with trim coils so that the BPM signals can be amplified using a frequency analyzer tuned to the frequency of the trim coil power supply.

Meshing Practices for Abutting Geometries In this example, the two coils abut, sharing the same boundary for a short distance. The mesh text file for the two abutting coils is illustrated in fig. 7. The following practices aids the Automesh routine to converge quickly on a mesh.

- \$reg mat=1 cur=10700\$
- \$po x=128.175, y=55.152\$
- \$po x=205.74, y=99.264\$
- \$po x=230.190, y=56.655\$
- \$po x=152.625, y=12.543\$
- **\$po x=140.4, y=33.848\$**
- \$po x=128.175, y=55.152\$

- \$reg mat=1 cur=135\$
- \$po x=117.380, y=48.379\$
- \$po x=128.175, y=55.152\$
- **\$po x=140.4, y=33.848\$**
- \$po x=129.605, y=27.075\$
- \$po x=117.380, y=48.379\$

Figure 7 Coil Package Coordinates

1. The large upper rectangular coil is defined using six, rather than five points. The additional point, the corner boundary point for the lower coil, is added along the common boundary of the two coils. The point sequence describes a clockwise path around the larger rectangular coil.
2. The small lower rectangular coil is defined using five points. The point sequence describes a counterclockwise path around the smaller rectangular coil.
 - (a) With these directions, the points along the common boundary of the two coils are interpolated in the same direction.
3. When more than two shapes abut, it is sometimes difficult to interpolate the common boundaries in the same direction. The meshing may require additional common points if the Automesh routine does not converge.

6.5.3 Yoke Geometry

The yoke is defined by a series of points describing the steel boundaries, including the hyperbolic pole contour, of a symmetric quadrupole. The computation approximates the geometry for an asymmetric quadrupole with unequal vertical and horizontal leg widths. The width of the vertical leg, in this example, is the average width of the vertical and horizontal legs.

Line Boundary

In this example, a final line region is added which describes a line and defines the boundary conditions on this line.

1. (\$reg ibound=0\$) - This line defines the boundary conditions.
 - (a) ibound=0 Dirichlet boundary, (flux parallel boundary).

```

$reg mat=2$
$po x=24.75, y=24.75 $
$po x=26, y=23.56 $
$po x=30, y=20.42 $
$po x=34, y=18.01 $
$po x=38, y=16.12 $
$po x=42, y=14.58 $
$po x=46, y=13.32 $
$po x=46.683, y=13.206$#
$po x=119.38, y=53.379$#
$po x=130.175, y=60.152$#
$po x=207.740, y=104.264$#
$po x=232.19, y=61.655$#
$po x=232.19, y=0.0$#
$po x=301.65, y=0.0$#
$po x=301.65, v=301.65$
$po x=24.75, v=24.75$

$reg ibound=0$
$po x=0., y=0.0$#
$po x=24.75, v=24.75$
$po x=301.65, v=301.65$

```

Figure 8 Quadrupole Yoke Dataset

- (b) ibound=1 Neumann boundary, (flux perpendicular boundary).
- 2. \$po x=24.75, y=24.75\$#
 - (a) This point is identical to the center coordinate of the quadrupole poletip.
- 3. \$po x=301.65, y=301.65\$#
 - (a) This point is identical to the upper right hand corner of the quadrupole yoke.

6.6 The Vector Potential Boundary Condition

Boundary conditions can be used to simplify the mesh. The vector potential can also provide the boundary conditions to perform Poisson calculations in conformally mapped geometries. The vector potential calculated from one case can be used as boundary conditions for another case. Several examples are presented.

6.6.1 Simple Dipole

A simple dipole consisting of a yoke and coil is illustrated in fig. 10. The text file used to create the mesh for this problem is reproduced as fig. 9

1. ktype=121, nptc=19, nterm=3, rint=58.95, rnorm=58.95, angle=90, anglz=0.

Simple Dipole

To test VP boundary conditions

```

$reg mat=1, kprob=0, mode=0,conv=.1,
xmin=0 ,xmax=150,
      kmax=100,
ymin=0, ymax=100,
      lmax=75,
icylin=0,
xminf=0, xmaxf=43,ktop=11
yminf=0, ymaxf=33.2,ltop=2
ktype=121,nptc=19 nterm=3,rint=58.95, rnorm=58.95, angle=90, anglz=0
ienergy=1,
nbsup=0, nbslo=1, nbsrt=0, nbslf=0$

!first region is air (mat=1), defines the problem limits.
$po x=0, y=0 $
$po x=150, y=0 $
$po x=150, y=100 $
$po x=0, y=100 $
$po x=0, y=0 $

!Coil
$reg mat=1 cur=-20000$
$po x=55, y=25$
$po x=75, y=25$
$po x=75, y=45$
$po x=55, y=45$
$po x=55, y=25$

!Iron Yoke
$reg mat=2$
$po x=0, y=25
$po x=40, y=25
$po x=45.16, y=37.89
$po x=50, y=50
$po x=80, y=50
$po x=80, y=0
$po x=120, y=0
$po x=120, y=95
$po x=0, y=95
$po x=0, y=25

```

Figure 9 Simple Dipole Mesh File

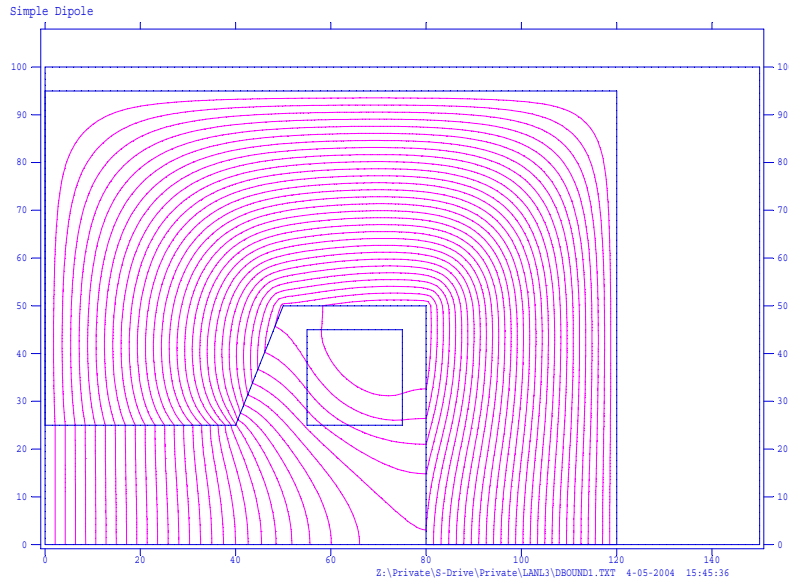


Figure 10 Simple Dipole with a Flat Pole

- (a) This line requests an edit of the vector potential at a radius of $r_{int}=58.95$ mm, normalized to the same radius $r_{norm}=58.95$ mm. The vector potentials are computed from $\text{anglz}=0$ degrees to $\text{angle}=90$ degrees and are computed at $nptc=19$ points (5° equal increments from 0° to 90° .). The 58.95 mm radius was selected since a 40° line from the origin intersects the sloping portion of the edge of the pole at a well defined point on the yoke, \$po x=45.16, y=37.89\$.

The flux plot from the Poisson calculations is illustrated in fig. 10.

The output from this computation (shown in fig. 11) lists the values of the vector potentials around a circular arc which intersects the steel pole.

6.6.2 The Simple Dipole with Vector Potential Boundary Conditions

The example of the simple dipole calculation limited to a small region surrounding the pole tip and the good field region is presented to demonstrate that computing the field distribution using vector potential boundary conditions accurately reproduces the field distribution computed from the full dipole geometry. This illustration also describes a means of simplifying the pole optimization process so that the magnet designer can focus his/her attention to the pole tip design. Fig. 12 illustrates the flux plot from a Poisson calculation for the simple dipole using the values of the vector potential computed from the output illustrated in fig. 11. This example illustrates a simple flat dipole pole whose field uniformity may not satisfy the required field uniformity for the desired dipole magnet. Since the mesh can be arbitrarily dense for this small region of the magnet, many more points than are necessary to describe

Harmonic analysis Interpolated points on an arc of radius = 58.95 centered at (XORG,YORG) = (0.0,0.0) K,L is nearest mesh point to physical coordinates X,Y.						
n	Angle	X	Y	K	L	Avector
1	0	58.95	0	40	1	-5.01E+04
2	5	58.7257	5.1378	40	5	-5.03E+04
3	10	58.0544	10.2366	40	8	-5.09E+04
4	15	56.9413	15.2574	39	12	-5.18E+04
5	20	55.3949	20.1621	38	16	-5.30E+04
6	25	53.4268	24.9133	36	19	-5.43E+04
7	30	51.0522	29.475	35	22	-5.54E+04
8	35	48.289	33.8123	33	26	-5.65E+04
9	40	45.1583	37.8923	31	29	-5.77E+04
10	45	41.6839	41.6839	29	32	-5.26E+04
11	50	37.8923	45.1583	26	34	-4.69E+04
12	55	33.8123	48.289	23	37	-4.07E+04
13	60	29.475	51.0522	21	38	-3.44E+04
14	65	24.9133	53.4268	18	40	-2.82E+04
15	70	20.1621	55.3949	15	42	-2.21E+04
16	75	15.2574	56.9413	11	43	-1.63E+04
17	80	10.2366	58.0544	8	44	-1.07E+04
18	85	5.1378	58.7257	5	44	-5.31E+03
19	90	0	58.95	1	44	-3.83E-11

Figure 11 Poisson Vector Potential Edit

the pole region for the full magnet can be used to describe the pole contour. The principles of the orthogonal analog model can be used to draw the approximate flow lines (not shown in the figure) which are orthogonal to the flux lines. With this visualization, it seems clear that bumps near the edge of the pole can squeeze the flow lines together, resulting in more vertical (and uniformly spaced) flux lines on the magnet centerline. The mesh file used for the calculation using the vector potential boundary conditions can be used to iterate the coordinates of the pole edge to develop the bumps and optimize the field. In the full geometry, bumps on the pole edge will slightly alter the vector potential distribution along the arc. Thus, the boundary condition using the vector potential boundary conditions for the unperturbed flat pole does not precisely reflect the altered boundary conditions. However, the changes are small and re-calculating the field distribution using the full geometry with the optimized pole will demonstrate that the field distribution changes are minor.

The Boundary

The portion of the mesh file defining the boundaries of the problem is illustrated in fig. 13. Part of the boundary is determined by the coordinates of the circular arc from the edit of the vector potential illustrated in fig. 11.

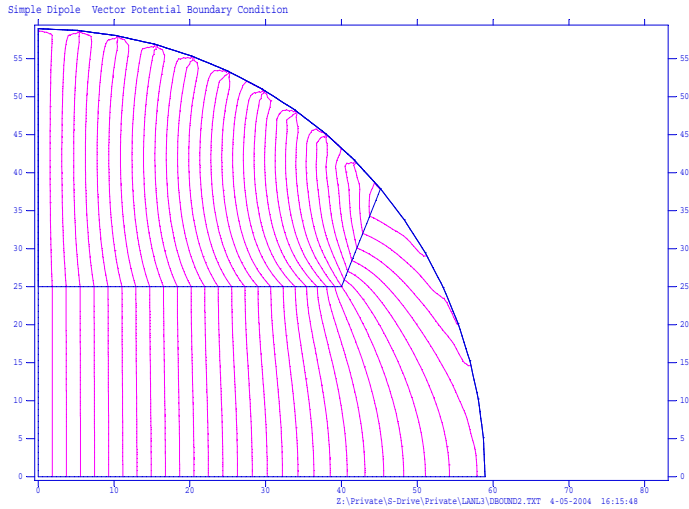


Figure 12 Simple Dipole Pole Region with Vector Potential Boundary Conditions

```

Simple Dipole Vector Potential Boundary Condition
To test VP boundary conditions

$reg mat=1, kprob=0, mode=0, conv=.1,
xmin=0, xmax=58.95,
kmax=100,
ymin=0, ymax=58.95,
lmax=75,
icylin=0,
xminf=0, xmaxf=43, ktop=11
yminf=0, ymaf=33.2, ltop=2
!ktype=121, ptc=19 nterm=3, rint=58.95, morm=58.95, angle=90, anglz=0
ienergy=1,
nbsup=0, nbslo=1, nbsrt=0, nbslf=0$

!first region is air (mat=1), defines the problem limits.
$po x=0,y=0$
$po x=58.95,y=0$
$po x=58.73,y=5.14
$po x=58.05,y=10.24
$po x=56.94,y=15.26
$po x=55.39,y=20.16
$po x=53.43,y=24.91
$po x=51.05,y=29.48
$po x=48.29,y=33.81
$po x=45.16,y=37.89
$po x=41.68,y=41.68
$po x=37.89,y=45.16
$po x=33.81,y=48.29
$po x=29.48,y=51.05
$po x=24.91,y=53.43
$po x=20.16,y=55.39
$po x=15.26,y=56.94
$po x=10.24,y=58.05
$po x=5.14,y=58.73
$po x=0,y=58.95
$po x=0,y=0

```

Figure 13 Boundary Mesh File

```

!Iron Yoke
$reg mat=2$
$po x=0,y=25$
$po x=40,y=25$
$po x=45.16,y=37.89$
$po x=41.68,y=41.68$
$po x=37.89,y=45.16
$po x=33.81,y=48.29
$po x=29.48,y=51.05
$po x=24.91,y=53.43
$po x=20.16,y=55.39
$po x=15.26,y=56.94
$po x=10.24,y=58.05
$po x=5.14,y=58.73
$po x=0,y=58.95
$po x=0,y=25

```

Figure 14 Iron Yoke Mesh File

The Iron Yoke

The mesh points for the iron yoke is illustrated in fig. 14. Note that many of the points are identical to the boundary points.

The Vector Potential Sources

The mesh coordinates for the vector potential sources (illustrated in fig. 15) are modelled as line sources using the `ibound=-1` special boundary conditions. The beginning and final coordinates of each line source are the Cartesian coordinates of the angular points around the 58.95 mm arc. The values of the potentials are the averages of the vector potential at the beginning and final coordinates of the line. These values are computed from the edit of the simple dipole vector potential map shown in fig. 11.

Results

Comparison of the results of the field calculations along the horizontal centerline of the simple dipole and the dipole using the vector potential boundary conditions is illustrated in fig. 16. The differences in the normalized values computed using the full geometry and the vector potential boundary, $\frac{\Delta B}{B}$, is ≤ 0.004 . It is possible to increase the accuracy of the boundary condition calculation if the radius of the vector potential boundary is increased and/or the density of line sources is increased.

6.6.3 The Vector Potential Boundary Condition for Optimizing the Quadrupole Pole

One of the most powerful techniques for pole tip design is to combine conformal mapping techniques with the use of vector potential boundary conditions for the optimization of a quadrupole pole. As described in earlier chapters, the required pole shape to achieve uniformity of a dipole field can be easily visualized from the flux plot. The flux lines for a high quality dipole are uniformly spaced and nearly vertical. To achieve this dipole uniformity, one needs to add bumps near the pole

```

!Vector Potential Lines
$reg mat=1, cur=-50237.7, ibound=-1 $      $reg mat=1, cur=-49759.85, ibound=-1 $
$po x=58.95,y=0$                            $po x=41.68,y=41.68$
$po x=58.73,y=5.14$                          $po x=37.89,y=45.16$

$reg mat=1, cur=-50609.25, ibound=-1 $      $reg mat=1, cur=-43807.15, ibound=-1 $
$po x=58.73,y=5.14$                          $po x=37.89,y=45.16$
$po x=58.05,y=10.24$                         $po x=33.81,y=48.29$

$reg mat=1, cur=-51335.95, ibound=-1 $      $reg mat=1, cur=-37566.55, ibound=-1 $
$po x=58.05,y=10.24$                         $po x=33.81,y=48.29$
$po x=56.94,y=15.26$                         $po x=29.48,y=51.05$

$reg mat=1, cur=-52378.3, ibound=-1 $       $reg mat=1, cur=-31284.35, ibound=-1 $
$po x=56.94,y=15.26$                         $po x=29.48,y=51.05$
$po x=55.39,y=20.16$                         $po x=24.91,y=53.43$

$reg mat=1, cur=-53642.55, ibound=-1 $       $reg mat=1, cur=-25136.4, ibound=-1 $
$po x=55.39,y=20.16$                         $po x=24.91,y=53.43$
$po x=53.43,y=24.91$                         $po x=20.16,y=55.39$

$reg mat=1, cur=-54873, ibound=-1 $          $reg mat=1, cur=-19206.65, ibound=-1 $
$po x=53.43,y=24.91$                         $po x=20.16,y=55.39$
$po x=51.05,y=29.48$                         $po x=15.26,y=56.94$

$reg mat=1, cur=-55966.1, ibound=-1 $        $reg mat=1, cur=-13509.55, ibound=-1 $
$po x=51.05,y=29.48$                         $po x=15.26,y=56.94$
$po x=48.29,y=33.81$                         $po x=10.24,y=58.05$

$reg mat=1, cur=-57123.85, ibound=-1 $       $reg mat=1, cur=-8014.79, ibound=-1 $
$po x=48.29,y=33.81$                         $po x=10.24,y=58.05$
$po x=45.16,y=37.89$                         $po x=5.14,y=58.73$

$reg mat=1, cur=-55188.9, ibound=-1 $        $reg mat=1, cur=-2655.49, ibound=-1 $
$po x=45.16,y=37.89$                         $po x=5.14,y=58.73$
$po x=41.68,y=41.68$                         $po x=0,y=58.95"

```

Figure 15 Vector Potential Line Sources

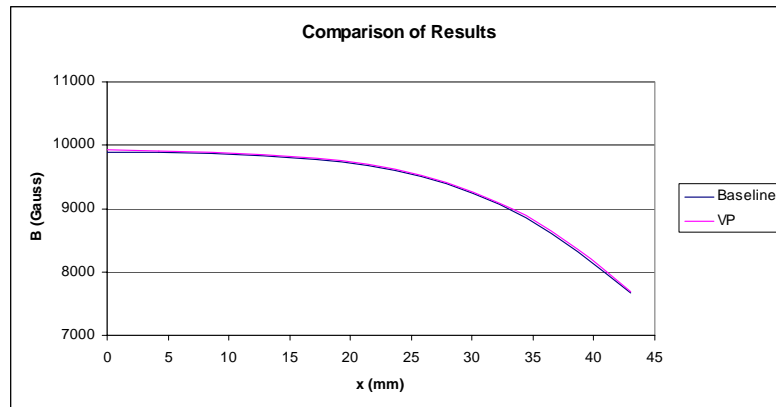


Figure 16 Comparison - Baseline Dipole and Vector Potential Boundary Calculations

edge of the flat baseline pole to “squeeze” the flow lines (see the section on the Orthogonal Analog Model) to achieve more uniformly spaced flux lines. In contrast, it is difficult to visualize and judge the uniformity of a quadrupole field whose flux lines are quadratic hyperbolae and whose spacing along the centerlines is linear rather than uniform. It is even more difficult to visualize the sizes and shapes of the bumps at the quadrupole pole edge to achieve this desired distribution of flux lines. Because of this difficulty, one can use the techniques of conformal mapping to convert the quadrupole pole into a dipole pole so that the design of the optimizing bumps can be performed in the more instinctively understood dipole space. The quadrupole example described in an earlier section of this chapter is used to illustrate the utility of using the vector potential boundary condition for conformally mapped geometries.

The process used to optimize a quadrupole pole contour for a given yoke shape are briefly described in the following steps. These steps are described more fully in the subsections following this description.

1. A text file is written to generate a mesh describing the boundaries of the yoke and coil configuration for the desired quadrupole two-dimensional cross section. The pole shape for the starting quadrupole calculation is an ideal hyperbola with pole shape described by $xy = \frac{h^2}{2}$, where h is the pole radius.
 - (a) The text file includes instructions for editing the vector potential at a radius which includes the pole tip and a segment of the pole. This radius should not include any of the coil.
 - i. The mesh is generated and the Poisson calculations are made.
 - (b) The text file is altered to include instructions for editing the vector potential at the radius defining the boundary of the desired good field region and computing the multipole field spectrum at this radius.
 - i. The mesh is regenerated and the Poisson calculations are rerun.
2. A text file including only the pole end coordinates and the edge of the pole is written. The vector potential distribution computed from the step 1-a-i POISSON run is used to define the boundary conditions for this more limited area of the full magnet cross section.
 - (a) The text file is written to include instructions for editing the vector potential at the radius defining the boundary of the desired good field region and computing the multipole field spectrum at this radius.
 - (b) The mesh is generated and Poisson calculations are made.
 - (c) The results of the Poisson calculation are compared with the results of the Poisson calculations from step 1-b-i.

3. A text file for the geometry described in step 2 conformally mapped into dipole space is written.
 - (a) The text file includes instructions for the vector potential edit and the computation of multipole errors at the mapped radius of the desired good field region.
 - (b) The mesh is generated and Poisson calculations are made. The multipole spectrum for this case are compared with the results from steps 2-c and 1-b-i. Since the geometry has been mapped into dipole space, the comparisons are $\left| \frac{B_n}{B_1} \right|_{\text{mapped radius}}$ (is it \approx) $\left| \frac{B_{2n}}{B_2} \right|_{\text{good field radius}}$.
4. The coordinates of bumps (up to three overlapping bumps can be defined) are added to the text file of the mapped dipole. The amplitudes of these bumps are parameterized using coefficients.
5. The values of the optimized coefficients are computed by iteratively running Poisson. A detailed description of this process is included in a subsection following this description.
 - (a) Poisson is run for the optimized pole contour in dipole space.
6. A text file is written with the pole geometry defined by the optimized dipole pole geometry conformally mapped into quadrupole space using the vector potential boundary conditions in the quadrupole space.
 - (a) Poisson is run for the optimized pole contour in quadrupole space.
7. The comparisons, $\left| \frac{B_n}{B_1} \right|_{\text{mapped radius}}$ and $\left| \frac{B_{2n}}{B_2} \right|_{\text{good field radius}}$, are made using the results of step 5-a and 6-a.
8. The text file used in step 1 (the full yoke geometry) is altered to include the optimized quadrupole pole contour used in step 6.
 - (a) The final Poisson run is made using the mesh generated from this text file and the comparison will show that $\left| \frac{B_n}{B_2} \right|_{\text{step 8}} \approx \left| \frac{B_n}{B_2} \right|_{\text{step 1}}$.

Mapping Algorithm

The Poisson algorithm mapping the multipole coordinates $z = x + iy$ to the dipole coordinates $w = u + iv$ is given by $w = \frac{z^n}{nh^{n-1}}$, ($w = \frac{z^2}{2h}$ for the quadrupole to dipole map and $w = \frac{z^3}{3h^2}$ for the sextupole to dipole map). This is different than the mapping function described in Chapter 2 and uses the convention written into Poisson. If h

is the quadrupole pole radius, the Poisson mapping algorithm results in the following expression for the dipole pole contour;

$$w = u + iv = \frac{z^2}{2h} = \frac{(x+iy)^2}{2h} = \frac{x^2-y^2}{2h} + i\frac{2xy}{2h} = \frac{x^2-y^2}{2h} + i\frac{xy}{h}, \quad (6.1)$$

$$u = \frac{x^2-y^2}{2h} \quad \text{and} \quad v = \frac{xy}{h}. \quad (6.2)$$

The equation for the quadrupole ideal hyperbolic pole contour with radius, $r = h$, is $xy = \frac{h^2}{2}$. Substituting

$$w = u + iv = \frac{x^2-y^2}{2h} + i\frac{h}{2},$$

an expression for a dipole with half gap $\frac{1}{2}$ of the quadrupole pole radius. (It is the full radius using the algorithm described in Chapter 2.) The reason for using this algorithm, rather than the one described in Chapter 2 is that the field amplitude at the center of the pole for the mapped dipole is made identical to the field amplitude at the center of the pole for the quadrupole and facilitates the mapping of the nonlinear steel permeability. The amplitudes of the fields at the centers of the quadrupole and dipole are computed using the following expressions;

$$\begin{aligned} NI &= \frac{B'h^2}{2\mu_0} \implies B_{Quadrupole} = B'h = \frac{2\mu_0 NI}{h}, \\ NI &= \frac{B\frac{h}{2}}{\mu_0} \implies B_{Dipole} = B = \frac{2\mu_0 NI}{h}. \end{aligned}$$

Poisson allows the finite element computation in the mapped geometry. The current densities in the coil are properly scaled and the mapped fields scaled to the quadrupole space are used to interpolate the appropriate relative permeability of the iron, μ . Despite these features, computing the field for the fully mapped quadrupole can be impractical. This is because the mapping algorithm, $w = \frac{z^2}{2h}$, maps the corner of the quadrupole yoke $|z_{corner}| >> h$ at an enormous distance from the origin compared to the pole radius, h . Thus, the area inside the pole radius is a small fraction of the area of the balance of the mapped quadrupole yoke. If, on the other hand, a larger radius h (not the pole radius), is used for the mapping function, the region of interest, the area defining the pole and inside the pole, becomes tiny compared to the remainder of the area required to define the mapped quadrupole yoke.

Using the vector potential as a boundary condition greatly reduces these scaling problems since the radius used to edit the vector potentials, which are ultimately

mapped into the dipole coordinate system, can be selected as a small multiple of the pole radius h . As in the dipole example, the entire quadrupole is analyzed and the vector potential distribution on an arbitrary circular arc boundary is computed. The results of an edit of the vector potentials distributed on a 71.03 mm arc are calculated for $0 \leq \theta \leq \frac{\pi}{4}$ at $\Delta\theta = 1^\circ$ increments. The 71.03 mm radius for the arc was chosen since a line at $\theta = 20^\circ$ intersects the pole edge at a fixed point which can be used as a boundary point for the pole. As in the previous dipole example, the mesh coordinates for the vector potential sources are modelled as line sources using the ibound=-1 special boundary conditions. The beginning and final coordinates of each line source are the Cartesian coordinates of the angular points around the 71.03 mm arc. The values of the potentials are the averages of the vector potential at the beginning and final coordinates of the line. These values, shown in fig. 17, are computed from the edit of the quadrupole calculation shown in fig. 6.

The flux plot resulting from the Poisson calculations using these boundary conditions is shown in fig. 18.

Mapping into Dipole Space

Using the $w = \frac{z^2}{2h}$ to map the quadrupole iron boundary to the dipole space, the mesh file for the dipole space is generated.

Using the $w = \frac{z^2}{2h}$ for determining the interpolation radius and the normalization radius in the dipole space, $|w| = \frac{|z|^2}{2h}$ where $|z_{interpolation}| = 30 \text{ mm}$, $|z_{normalization}| = 32.5 \text{ mm}$ and h (the pole radius) = 35 mm.

$$|w_{interpolation}| = \frac{|z_{interpolation}|^2}{2h} = \frac{30^2}{2 \times 35} = 12.857 \text{ mm},$$

$$\text{and } |w_{normalization}| = \frac{|z_{normalization}|^2}{2h} = \frac{32.5^2}{2 \times 35} = 15.089 \text{ mm}.$$

All the coordinate points illustrated in fig. 18 are conformally mapped to the $w = u + iv$ dipole coordinates by using the expressions;

$$u = \frac{x^2 - y^2}{2h}, \quad v = \frac{xy}{h}.$$

Only radial straight lines in the z space are mapped into straight lines in the w space. The straight line at the edge of the quadrupole pole maps into a line with a slight curvature in the dipole space.

Mapping the Iron Properties and Boundary Values

In addition, in order to map the iron permeability correctly, the first line of the iron region is defined by the line;

Interpolated points on an arc of radius = 71.03 centered at (XORG,YORG) = (0.0,0.0) K,L is nearest mesh point to physical coordinates X,Y.						
n	Angle	X	Y	K	L	Avector
1	0	71.03	0	76	1	4.07E+04
2	1	71.0192	1.2396	76	3	4.07E+04
3	2	70.9867	2.4789	76	4	4.07E+04
4	3	70.9327	3.7174	76	6	4.07E+04
5	4	70.857	4.9548	76	7	4.07E+04
6	5	70.7597	6.1907	76	9	4.08E+04
7	6	70.6409	7.4247	76	11	4.08E+04
8	7	70.5006	8.6564	76	12	4.08E+04
9	8	70.3387	9.8855	76	14	4.09E+04
10	9	70.1555	11.1115	76	16	4.09E+04
11	10	69.9509	12.3342	75	17	4.10E+04
12	11	69.725	13.5532	75	19	4.10E+04
13	12	69.4778	14.768	75	20	4.11E+04
14	13	69.2095	15.9783	75	22	4.11E+04
15	14	68.9201	17.1837	75	24	4.12E+04
16	15	68.6097	18.3839	74	25	4.13E+04
17	16	68.2784	19.5785	74	27	4.14E+04
18	17	67.9263	20.7672	74	28	4.14E+04
19	18	67.5535	21.9495	74	30	4.15E+04
20	19	67.1602	23.1251	73	31	4.16E+04
21	20	66.7464	24.2937	73	33	4.17E+04
22	21	66.3122	25.4549	73	34	4.02E+04
23	22	65.8579	26.6083	72	36	3.87E+04
24	23	65.3835	27.7536	72	38	3.71E+04
25	24	64.8891	28.8905	71	39	3.55E+04
26	25	64.375	30.0186	71	40	3.39E+04
27	26	63.8413	31.1375	70	41	3.23E+04
28	27	63.2882	32.2469	70	42	3.07E+04
29	28	62.7158	33.3466	70	44	2.91E+04
30	29	62.1242	34.436	69	45	2.74E+04
31	30	61.5138	35.515	69	46	2.58E+04
32	31	60.8846	36.5832	68	47	2.41E+04
33	32	60.2369	37.6402	68	48	2.24E+04
34	33	59.5708	38.6857	67	49	2.07E+04
35	34	58.8865	39.7195	67	50	1.90E+04
36	35	58.1844	40.7411	66	51	1.73E+04
37	36	57.4645	41.7504	66	52	1.56E+04
38	37	56.7271	42.7469	65	53	1.39E+04
39	38	55.9724	43.7304	65	54	1.22E+04
40	39	55.2007	44.7006	64	55	1.04E+04
41	40	54.4121	45.6572	64	56	8.70E+03
42	41	53.607	46.5999	63	57	6.96E+03
43	42	52.7856	47.5283	62	59	5.23E+03
44	43	51.9481	48.4423	61	59	3.49E+03
45	44	51.0947	49.3416	61	60	1.74E+03
46	45	50.2258	50.2258	60	61	4.40E-01

Figure 17 Vector Potential Distribution in the Quadrupole Evaluated at 71.03 mm radius

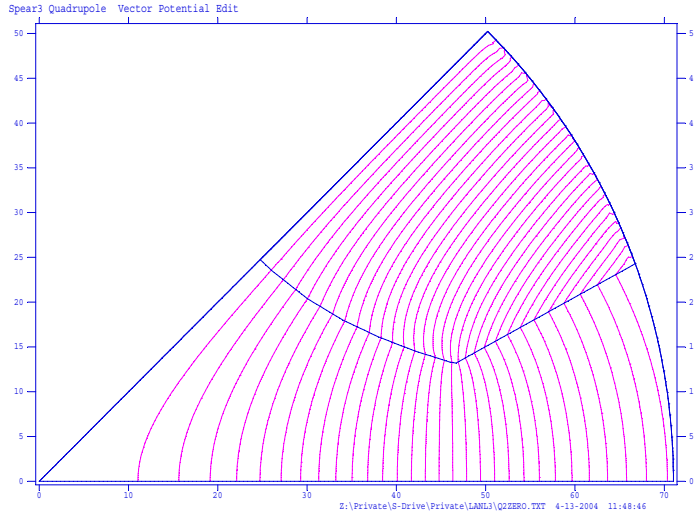


Figure 18 Hyperbolic Pole with Vector Potential Boundary

1. \$reg mat=2, map=2, rzero=35\$.

- (a) mat=2 indicates that the Poisson 1010 Steel default nonlinear steel properties are used.
- (b) map=2 uses the quadrupole to dipole scaling for the flux density in order to interpolate the relative permeability.
- (c) rzero=35; the mapping function is

$$w = \frac{z^{map}}{map \times rzero^{map-1}}. \quad (6.3)$$

The first line of the first vector potential boundary line is defined by;

1. \$reg mat=1, cur=40703.2, ibound=-1, map=1\$

- (a) map=1 restores the unmapped currents to their input values.
 - i. The average vector potentials between the ends of the line elements are not scaled when the geometry is mapped.
- (b) If map=2, the currents will be scaled.

The flux plot for the mapped, unoptimized quadrupole case is shown in fig. 19.

The results of the multipole analysis of the mapped dipole is compared with the multipole analysis of the quadrupole and is shown in fig.20.

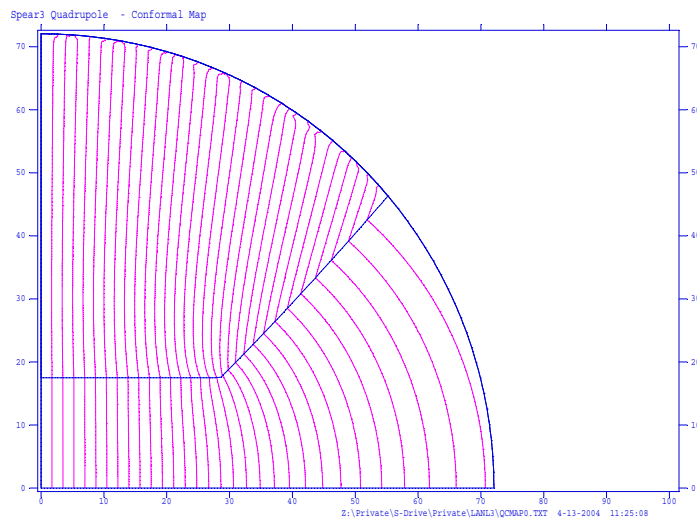


Figure 19 Baseline Mapped Quadrupole

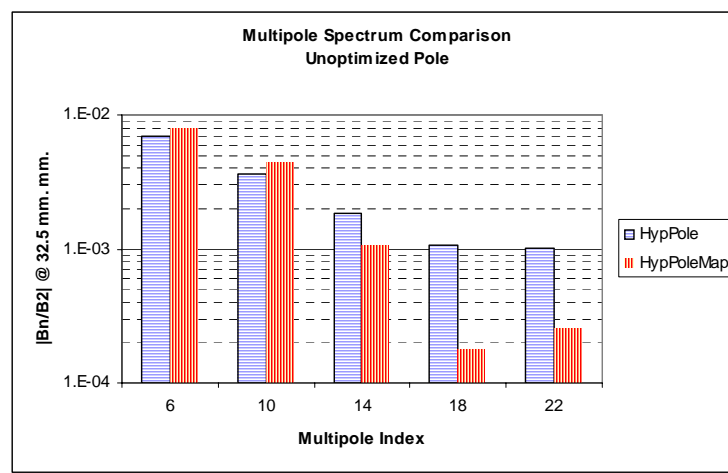


Figure 20 Multipole Spectrum for Baseline and Mapped Quadrupole

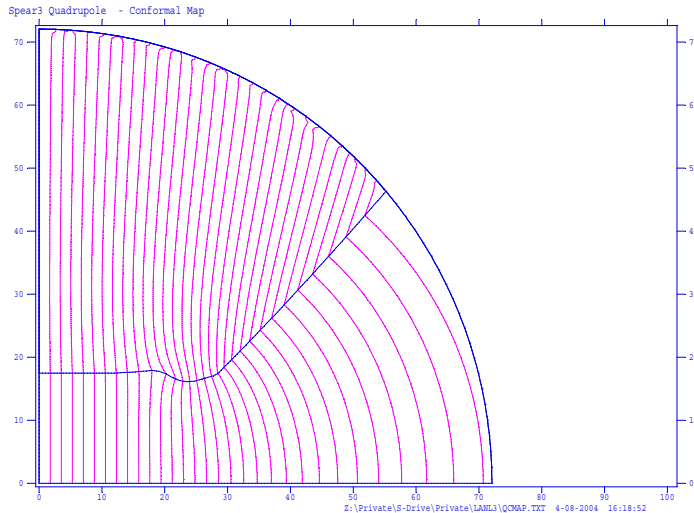


Figure 21 Optimized Quadrupole Pole (Dipole Map)

The graphed results (fig. 20) indicate that the multipole spectra for the unmapped (horizontally striped) and mapped (vertically striped) multipoles reproduce reasonably well (at least for the multipoles with lower indices, $n = 6, 10, \text{ and } 14$). The results also show that the multipole errors are large, approaching 1% errors for the $n = 6$ normalized multipole error. The flat pole contour badly needs optimizing.

Optimization of the Quadrupole Pole in Dipole Space

The process of optimizing the pole is iterative. It consists of selecting the x and y-coordinates of overlapping bumps (up to three), and scaling their amplitudes with coefficients. Poisson runs are made for different values of these coefficients. The results of various iterations are evaluated and compared until the field quality criteria are satisfied. The process of converging on an optimum set of coefficients is to calculate the changes of either selected multipoles or the rms amplitude of the field errors around an arc at the boundary of the required good field region (the quality parameter) as a function of the coefficients. These results of the different runs are used to compute a derivative of the quality parameter as a function of the coefficients. The derivatives are used to extrapolate the coefficient values to achieve some minimum value for the quality parameter.

The Poisson flux plot results of the pole optimization in the dipole space is illustrated in fig. 21. Note that the corner of the optimized pole contour has been rounded as a result of the bumps superimposed on the pole corner. This softened contour helps to avoid flux concentrations and results in fields which are more independent of the magnet excitation.

The flux plot resulting from the POISSON calculation for the optimized dipole

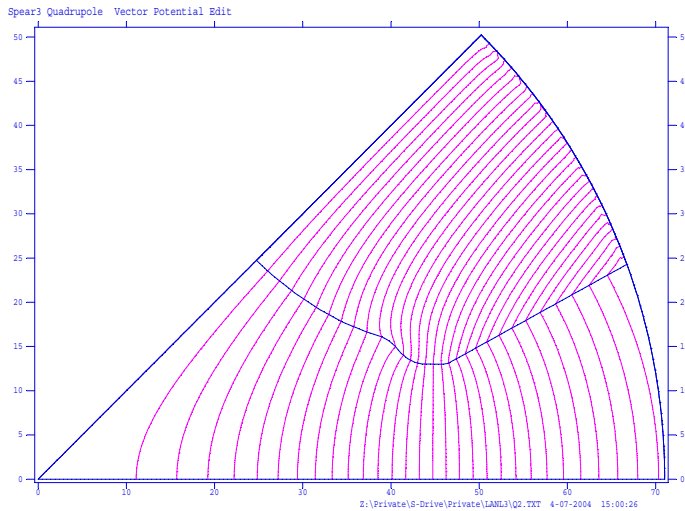


Figure 22 Quadrupole Poisson Calculations Using Vector Potential Boundary Conditions

geometry mapped back into quadrupole space is shown in fig. 22.

Multipole Spectrum Results

Results can be displayed in terms of the field errors or the amplitudes of the multipole errors. In the accelerator craft, it is often customary to specify requirements in terms of multipole errors since the orbit calculations use “k” values, related to the magnet multipole errors, to compute the beam orbits. The results of all the calculations described in this section, displayed as multipole errors normalized to the fundamental field at the pole tip, are summarized in fig. 23. Four sets of data summarize $\left| \frac{B_n}{B_2} \right|_{@32.5mm}$ for four different cases.

1. The diagonally striped bars describe the multipole spectrum for the unoptimized (hyperbolic) pole contour.
2. The horizontally striped bars describe the multipole spectrum for the optimized pole tip in the dipole space using the mapped vector potential boundary conditions.
3. The vertically striped bars describe the multipole spectrum for the optimized pole tip conformally mapped into the quadrupole space using the vector potential boundary conditions.
4. The solid bars describe the multipole spectrum for the optimized pole tip conformally mapped into the quadrupole space with the full yoke.

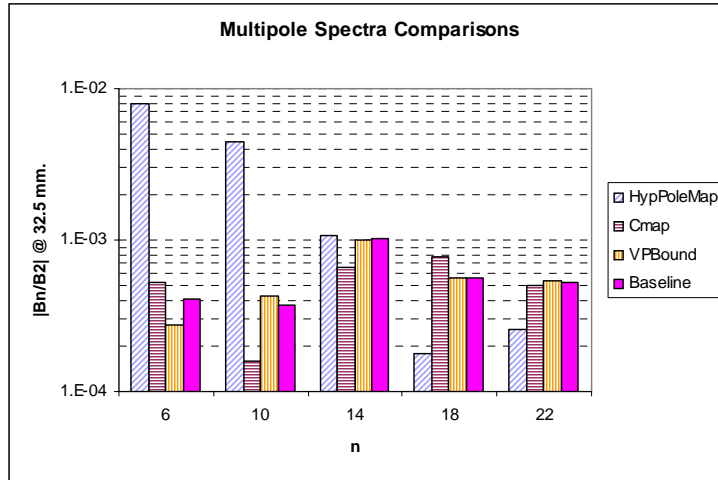


Figure 23 Summary Multipole Spectrum

The differences in the results of the last three cases are finite but small. This indicates that the conformal mapping and use of the different boundary conditions give substantially the same results.

Field Error Results

Comparisons showing the results of the pole optimization for the quadrupole and the dipole mapped from the quadrupole can also be displayed as errors from the desired field normalized by the desired field. These curves are generated from the error multipole coefficients. Because of the manner in which the fields are computed from differences of the distribution of the computed vector potential, the field edit presented by the output of Poisson calculations frequently display small discontinuities. These discontinuities are avoided by generating the field from the Taylor's series of the multipole coefficients. In many ways, this type of "analog" display is more meaningful to the engineer and/or designer shaping the pole bumps at the edge of the pole. For instance, in the dipole space, it is clear that one has to increase the amplitude of a bump near the edge of the pole to reduce the "sag" in the field. The improvement in the dipole field translates directly into improvement in the field from a quadrupole pole contour mapped from the optimized dipole. The results of the pole optimization for the dipole shown in figs. 19 and 21 are shown in fig. 24. The results of the pole optimization for the quadrupole shown in figs. 18 and 22 are shown in fig. 25.

6.6.4 Other Applications of the Vector Potential Boundary Conditions

Beam injection/extraction into/out of accelerators requires the use of septum magnets. Besides the amplitude of the field on one side of the septum, a primary requirement for these magnets is a low fringe field on the opposite side of the septum

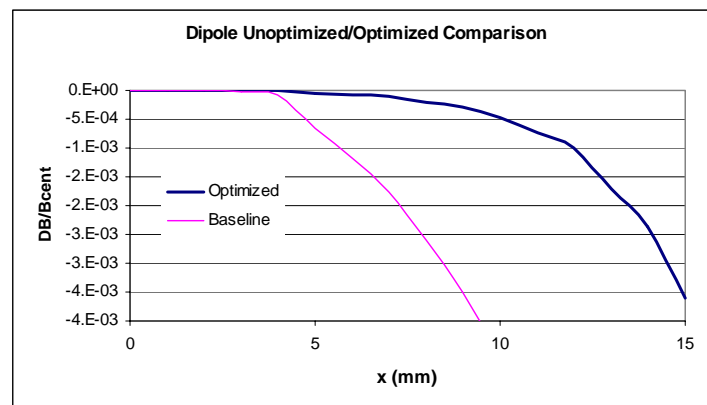


Figure 24 Dipole Optimization Results

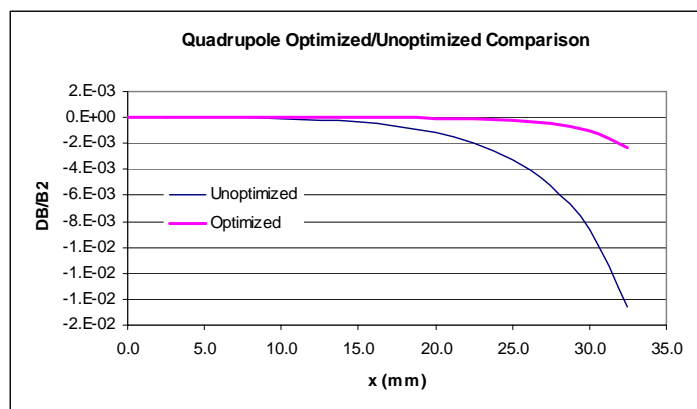


Figure 25 Quadrupole Mapped from Dipole Optimization Results

in the region of the circulating beam. The minimum amplitude of this fringe field is often limited by the finite permeability of the iron return yoke in the case of the current carrying septum.

Design of permeable shields is limited by the mesh density. This is because the space between the surface of the septum and the center of the circulating beam is small so that the injected beam can be merged as close as possible to the central orbit of the circulating beam. The shield must be placed in this limited space. The typical shield thickness and its spacing is small compared to the dimensions of the magnet. In order to define the shield geometry adequately, the mesh density external to the magnet must be increased over the density inside of the magnet. Accurate computation of the fringe field requires a high mesh density since the fields are computed by taking the differences among vector potentials at several neighboring mesh points to the location at which the field is calculated. If the mesh density is too coarse, the field calculations require using vector potentials at mesh points on the boundary of the shield where the function is discontinuous. Thus, the increased mesh density accommodates several mesh points in the thin shield and in the space between the shield and the coil and iron yoke.

Because of these difficulties, means of making accurate calculations and/or accurately characterizing the effect of shields needed to be developed. Calculations using the vector potential boundary conditions computed from the calculation of the fields in a septum magnet are a means of enhancing the accuracy of these calculations.

The Current Carrying Septum

The example in this section is the current carrying septum magnet. The current carrying septum is required to bend the injected beam into the accelerator ring. Besides the field in the gap, the primary requirement for this magnet is a low fringe field. A low fringe field minimizes the horizontal steering of the circulating beam.

The Poisson flux plot for the septum geometry is illustrated in fig. 26. The initial tries attempted to use the vector potential values at the boundary of the coil and iron yoke and the air region outside these regions. The comparison of the field distribution using these boundary values did not compare well with the field distribution using the entire magnet cross section. It is believed that the computations using the vector potentials at these points, where the transverse derivatives of the vector potentials is discontinuous, resulted in the disagreement of the two calculations. Therefore, the vector potential edit was performed inside the coil at $x = 22 \text{ mm}$. This boundary condition replaces the balance of the geometry for $x \geq 22 \text{ mm}$. The Poisson flux plot for the calculations in the limited region bounded by the vector potential is shown in fig. 27. The mesh density is increased in the area adjacent to the coil so that a 0.25 mm thick septum can be placed 0.25 mm from the surface of the coil. The flux plot for the POISSON calculation and the mesh for shielded

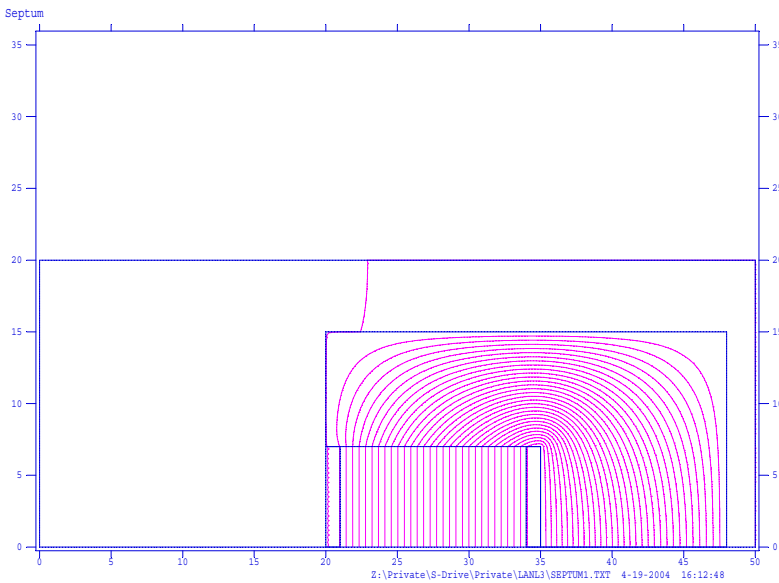


Figure 26 Current Carrying Septum

case is shown in fig. 28. Finally, the comparison of the flux density edits along the horizontal centerline adjacent to the coil is shown in fig. 29. The upper two curves compares the results of the full geometry and the vector potential boundary condition POISSON runs. The lower curve presents the flux plot for the case where a 0.25 mm thick setptum is placed 0.25 mm from the surface of the coil. The shield reduced the fringe field adjacent to the coil from 10 *Gauss* to < 0.5 *Gauss*.

6.7 Chapter Closure

This chapter is written to describe some of the features of the Poisson family of codes. These computer programs are used to set up, analyze and display the distribution of the magnetic field in two dimensional geometries. The separate elements of the codes and the flow of calculations is described. Several examples are presented to illustrate the various input parameters used to generate the lattice for the finite element calculations, define the boundary conditions, select the properties of the iron and determine the required computed output information and format. An example is given of a simple dipole geometry. The output of the Poisson calculations for the dipole is used to show that the size of the mesh can be substantially reduced by replacing the features of the magnetic geometry and coil excitation by vector potential boundary conditions, edited from text output of the calculation of the full geometry.

The Poisson calculations for a simple quadrupole with a generic hyperbolic pole contour is presented. This example illustrates the use of non-rectangular boundaries for a symmetric multipole magnet. The example is used to compute the distribution of the vector potential around a circular arc boundary. The vector potential

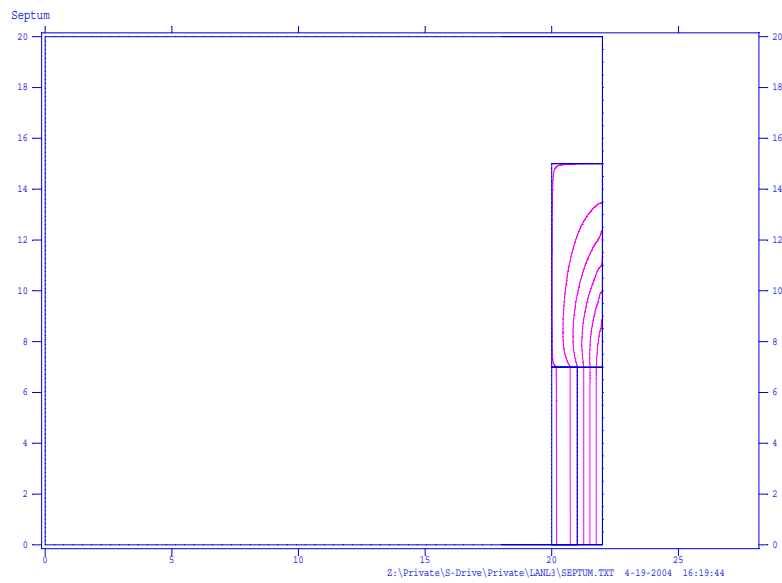


Figure 27 Current Carrying Septum with Vector Potential Boundaries

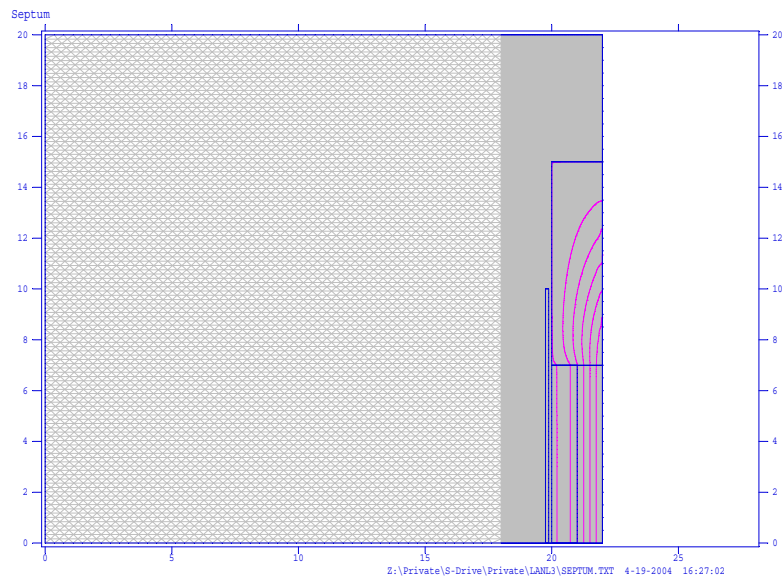


Figure 28 Current Carrying Septum - VP Boundary and Shield

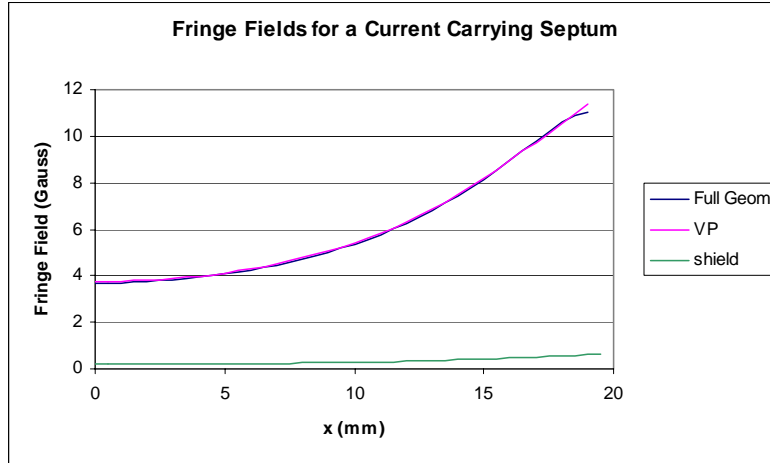


Figure 29 Results of POISSON Calculations

distribution is used in a further example to illustrate that size of the problem can be reduced by replacing a large portion of the geometry with the boundary values. These boundary values are further exploited by mapping the boundary values and the pole geometry into dipole space using the algorithm, $u = \frac{z^2}{2h}$. The mapping function ($map = n$) in Poisson is illustrated in the text file for generating the lattice to ensure that the iron properties are properly interpolated at the mapped field levels in dipole space. Using the vector potential boundary condition for the conformally mapped geometry is especially useful since the mapping algorithm creates a dipole geometry whose pole and good field region are small compared to the remainder of the mapped magnet. When the good field region is mapped in dipole space, it is shown that the normalized fields in dipole space, $\left(\frac{B_n}{B_1}\right)_{\text{mapped radius}}$, are approximately equal to the normalized fields in quadrupole space, $\left(\frac{B_{2n}}{B_2}\right)_{\text{radius}}$.

Since the behavior of the dipole magnet is easily visualized, the mapped pole contour in dipole space is optimized by introducing bumps at the edge of the pole. After several iterations, a pole geometry is determined satisfying some good field criteria within the good field region mapped in dipole space. This pole contour is mapped back into quadrupole space for analysis using the vector potential boundary conditions and the full quadrupole geometry. Again, the multipole spectra of the various cases are compared and shown to be approximately equal.

A final example is presented to calculate the fringe field in a current carrying septum. The vector potential map is used to replace much of the magnet geometry so that the mesh density can be increased in the fringe field region. This allows more accurate calculation of the fringe fields and also provides many more mesh points so that a very thin shield with very small spacing can be adequately defined for the finite element calculations.

The Poisson family of codes is only one of many codes available for magnet calculations. Commercial three dimensional codes with two dimensional components are available which perform well. The Poisson family of codes is discussed since it is widely used in the National Accelerator community.

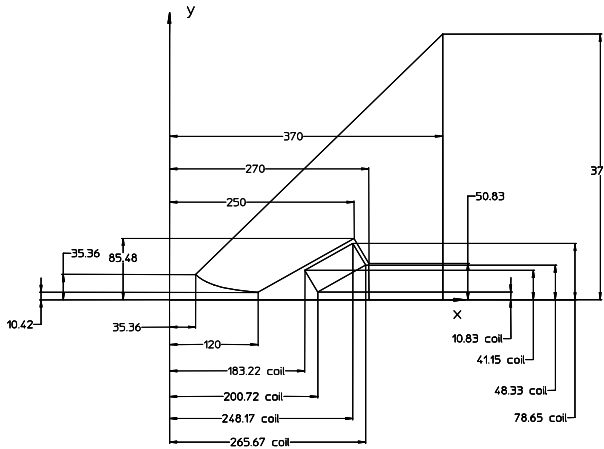


Figure 30 Problem Quadrupole

6.8 Problems

Problem 6.1

Fig. 30 illustrates the coordinates of the core and coil outline for a 50 mm. radius quadrupole. Compute the gradient required to achieve a magnetic field at the center of the poletip, $B_{pole} = 0.6T$. Using the eq. (5.12), estimate the current required to achieve this gradient. The estimate assumes magnet efficiency $\eta = 100\%$. Assume that the required good field region is $r_0 = 40 \text{ mm}$. Using the graph on page 70, estimate the field quality $(\frac{\Delta B}{B})_{r_0}$ inside the good field radius for the edge of the pole at $x = 120 \text{ mm}$.

Problem 6.1a Write a text file to generate a Poisson lattice for this geometry with pole contour defined by the expression $xy = \frac{h^2}{2}$ where $h = 50 \text{ mm}$. The text file should include the parameters required to perform a vector potential edit at the good field radius and compute the amplitudes of the multipole errors up to $n = 18$. Run POISSON and run WFSPLT.exe to verify the geometry and whether the flux distribution is as expected. Read the OUTPOI.txt file written by the computation. Determine whether the field quality achieved in the required good field region as determined by the amplitudes of the error multipoles agrees with the estimate made using the graph on page. 70.

Problem 6.1b Edit the POISSON lattice text file so that the vector potential edit is performed at $r = 180 \text{ mm}$. Select sufficiently small angle increments so that enough boundary points are available to run the geometry conformally mapped as a dipole. Rerun the lattice program and POISSON.

Problem 6.1c Compute all of the $w = u + iv$ coordinates of the dipole geometry conformally mapped from the quadrupole illustrated in fig. 30 using eq. (6.2). If all the coordinates are plotted in the w coordinate space, what can be said regarding the coordinates of the points remote from the pole contour? Can a practical lattice be generated using the conformally mapped coordinates?

Problem 6.1d Compute all of the $w = u + iv$ coordinates of the dipole geometry conformally mapped from the quadrupole illustrated in fig. 30 using eq. (6.2) for points $x^2 + y^2 \leq 180 \text{ mm}$. (Several points beyond the pole corner along the straight pole edge should be mapped. A straight line in the quadrupole space does NOT map to a straight line in the dipole space unless the straight line is radial with origin at the center.) Compute the w coordinates of the ends of the edit points from the OUTPOI.txt file written in Problem 4.1b at $r = 180 \text{ mm}$ in the z coordinate space and use the average vector potential values for line currents between the w coordinates of the conformally mapped circle. These currents are the boundary conditions along the circular boundary of the problem. Write a text file to generate a lattice for the dipole conformally mapped from the quadrupole. Include in the text file the parameters required to perform a vector potential edit at the mapped good field radius, w_0 , and compute the amplitudes of the multipole errors up to $n = 9$. Compare the amplitudes of the multipole fields from the mapped dipole calculation to the orginal quadrupole calculation. (The reverse process, mapping a dipole to a quadrupole, required to solve Problems 4.1b to 4.1d is illustrated in the section beginning at sec. 6.6.)

Problem 6.1e What is the pole overhang in the dipole space? What field uniformity is predicted in the good field region due to this overhang?

Problem 6.2

Problem 3.2 illustrated on page 84 served to illustrate the usefulness of the orthogonal analog model to visualize the field distribution in a magnet. For the illustrated square yoke geometry, simplify the discrete square conductors into a uniform line current and generate a Poisson lattice. The simplification should include only the upper quadrant of the problem for $0 \leq \theta \leq \frac{\pi}{2}$ using the horizontal and vertical centerlines as problem boundaries. (Should these boundaries be Neumann or Dirichlet boundaries?) Use arbitrary dimensions and evaluate the field distribution using Poisson for some arbitrary magnitude of the line currents. Run Wfsplot.exe from using the solution. What type of magnet is this?

Chapter 7

STORED ENERGY, MAGNETIC FORCES AND DYNAMIC EFFECTS

The concept of magnetic stored energy is introduced to formulate expressions for magnetic forces on poles and the inductance of iron dominated magnets. Forces on coils are computed by using the relation, $d\vec{F} = \vec{j} \times \vec{B}$, and integrating over the volume of the coil. Pole forces are computed by equating work required for an incremental pole motion with the increase in the stored energy. Inductance is computed from the stored energy. The inductance is important since, for pulsed or cycled magnets, the power supply voltage must be designed for the inductive load of the magnet as well as the resistive load of the coils. The discussion is limited to magnets which are cycled or pulsed at relatively slow rates (\geq a few msec.). For magnets which are operated at faster rates, transmission line issues are important where the filling time of the current in the conductors exciting the magnets require consideration of the velocity of the current front in the conductors.

Effects on the magnetic fields inside conductive metallic vacuum chambers, in the areas where the charged particle beams are bent, focused or corrected, due to time varying magnetic fields, are estimated. Algorithms describing the field attenuation and amplification are developed using simple one dimensional differential equations approximating these effects.

7.1 Force on Coils

Only the simplest geometry is considered here as an example to develop the relationships. Consider the window frame magnet illustrated in fig. 1.

The expression for the force due to a current density in a magnetic field is given by;

$$\vec{F} = \int \vec{j} \times \vec{B} dv. \quad (7.1)$$

In the figure, the magnet current is “into the page”, and the cross product gives the direction of force to the left.

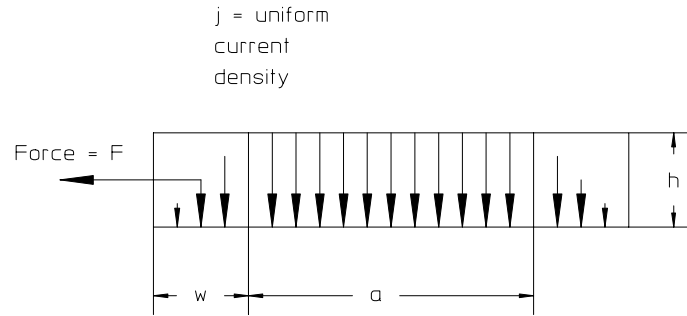


Figure 1 Window Frame Magnet with Uniform Current Density Coils

Since, for the window frame magnet;

$$\begin{aligned} NI &= \frac{Bh}{\mu_0} \quad \text{and} \quad j = \frac{NI}{wh}, \\ j &= \frac{Bh}{wh\mu_0}. \end{aligned}$$

The distribution of the magnetic field in the conductor is maximum at its inner edge, linearly decreasing to zero at its outer edge. The expression for the field distribution in the conductor is;

$$B(x) = \frac{Bx}{w}.$$

The \vec{j} and \vec{B} are perpendicular so the vector equation can be simplified to an expression for the magnitude of the force, given by;

$$|F| = \int_0^w j \times B(x) \times h \times l \times dx.$$

Substituting for j and $B(x)$, we get;

$$\begin{aligned} |F| &= \int_0^w \frac{Bh}{wh\mu_0} \times \frac{Bx}{w} \times h \times l \times dx, \\ &= \frac{B^2h}{w^2\mu_0} l \int_0^w x dx = \frac{B^2h}{w^2\mu_0} l \left[\frac{x^2}{2} \right]_0^w, \\ &= \frac{B^2h}{w^2\mu_0} l \frac{w^2}{2} = \frac{B^2h}{2\mu_0} l, \end{aligned}$$

or written in terms of pressure,

$$P = \frac{|F|}{Area} = \frac{|F|}{l \times h} = \frac{B^2}{2\mu_0}. \quad (7.2)$$

7.2 Force on a Pole

The relationship between stored energy and work is used to derive an expression for the forces on a pole. The magnetic stored energy in the volume of a constant field window frame magnet is given by;

$$\begin{aligned} U &= \frac{1}{2} \int BHdV = \frac{1}{2} B \frac{B}{\mu_0} a \times h \times l, \\ &= \frac{B^2}{2\mu_0} a \times h \times l. \end{aligned}$$

If we consider the work performed in pushing the pole up a distance h , the expression for the work is;

$$Work = Force \times h = P \times (a \times l) \times h,$$

where P , again, is the pressure.

Equating the $Work = U$,

$$\begin{aligned} P \times (a \times length) \times h &= U = \frac{B^2}{2\mu_0} a \times h \times l, \\ \text{or } P &= \frac{B^2}{2\mu_0}. \end{aligned} \quad (7.3)$$

We note that eqs. (7.2) and (7.3) are identical.

7.2.1 Units

Using the MKS system of units,

$$\begin{aligned} P &= \frac{B^2}{2\mu_0} = \frac{T^2}{T m} = \frac{T \text{ Amps}}{m} \\ &= \frac{\text{Webers}}{m^2} \frac{\text{Amps}}{m} = \frac{V \text{ sec}}{m^2} \frac{\text{Amps}}{m} = \frac{\text{Watt sec}}{m^3} \\ &= \frac{\text{Joules}}{m^3} = \frac{N m}{m^3} = \frac{N}{m^2} = \text{Pascals}. \end{aligned}$$

7.2.2 A Reference Point

It is useful to calculate the magnetic pressure at some baseline field so that one can make quick estimates. Computing the magnetic pressure at $B = 5 \text{ kG} = 0.5 \text{ Tesla}$,

$$\begin{aligned} P_{@0.5\text{Tesla}} &= \frac{B^2}{2\mu_0} \\ &= \frac{0.5^2}{2 \times 4\pi \times 10^{-7}} = 99,472 \frac{\text{N}}{\text{m}^2} \\ &= 99,472 \frac{\text{N}}{\text{m}^2} \times \frac{1 \text{ lb}_f}{4.448 \text{ N}} \times \frac{\text{m}^2}{39.37^2 \text{ in}^2} = 14.43 \frac{\text{lb}_f}{\text{in}^2} \\ &\approx 1 \text{ atmosphere and } P \propto B^2. \end{aligned}$$

7.3 Magnet Stored Energy

Computation of the magnet stored energy is often difficult and tedious. The field distribution is non-uniform in the gap and in the coils and the stored energy distribution in the magnet yoke depends on the permeability of the iron at the field. Stored energy computations in real two-dimensional magnet cross sections is best done by computer programs such as Poisson. Poisson will calculate the stored energy per unit length of the computed two dimensional field and express it in units of stored energy per cm. of length of the magnet.

Despite this difficulty, it is instructive to compute the stored energy with a simple example using a window frame magnet. The magnetic stored energy is given by $U = \frac{1}{2} \int BHdv$, $\frac{1}{2} \times$ the volume integral of the product of H and B in the magnet gap, coil and core. Consider the stored energy in the window frame magnet illustrated in fig. 1. Since the field is constant in the gap, the stored energy in the gap is;

$$U_{gap} = \frac{B^2}{2\mu_0} (V)_{gap}. \quad (7.4)$$

The field varies linearly across the width of the coil, therefore, the stored energy in each coil is

$$\begin{aligned} U_{coil} &= \frac{1}{2\mu_0} l \times h \times \int_0^w \frac{B^2 x^2}{w^2} dx, \\ &= \frac{B^2}{2\mu_0} l \times h \times \frac{w^3}{3w^2} = \frac{B^2}{2\mu_0} \frac{lhw}{3}, \\ U_{coil} &= \frac{B^2}{6\mu_0} (V)_{coil}. \end{aligned} \quad (7.5)$$

Assuming a well designed yoke, the field in the yoke is reasonably constant and is approximately B_{gap} . The stored energy in the yoke can then be approximated by the expression;

$$U_{yoke} = \frac{1}{2} \int BHdv = \frac{B^2}{2\mu\mu_0} (V)_{yoke}.$$

Adding the elements, the total stored energy in the magnet is given by;

$$\begin{aligned} U_{magnet} &= U_{gap} + 2U_{coil} + U_{yoke}, \\ &= \frac{B^2}{2\mu_0} \left((V)_{gap} + 2\frac{(V)_{coil}}{6} + \frac{1}{\mu} (V)_{yoke} \right). \end{aligned}$$

As shown in the section on Units, the units for $\frac{B^2}{2\mu_0}$ is $\frac{joules}{m^3}$ and, thus, the units for stored energy is joules.

7.3.1 Inductance

The inductance of a magnet is given by

$$L = \frac{2U}{I^2} \left(\frac{joules}{Amp^2} = henries \right) \quad (7.6)$$

The voltage in a ramped or cycled magnet is given by

$$V = RI + L \frac{dI}{dt}. \quad (7.7)$$

Substituting for the inductance,

$$V = RI + \frac{2U}{I^2} \frac{dI}{dt}.$$

Using the MKS system of units,

$$\begin{aligned} V &= \Omega \times Amps + \frac{Joules}{Amps^2} \frac{Amps}{sec} \\ &= Volts + \frac{Watt \ sec}{Amp \ sec} = Volts + Volts. \end{aligned}$$

Cycled Magnets

Suppose a sinusoidal current, $I = I_0 \sin \omega t$, is desired for the magnet excitation. The expression for the required power supply voltage is;

$$\begin{aligned} V &= RI + L \frac{dI}{dt}, \\ &= RI_0 \sin \omega t + L \omega I_0 \cos \omega t, \\ &= RI_0 \left(\sin \omega t + \frac{L\omega}{R} \cos \omega t \right), \\ &= RI_0 \sin(\omega t + \phi), \text{ where } \phi = \tan^{-1} \frac{L\omega}{R}. \end{aligned} \quad (7.8)$$

The power supply voltage must provide a sinusoidal excitation with a leading phase.

Pulsed Magnets

Suppose a linear current ramp, $I = \frac{I_0}{\Delta t} t$, is desired for the magnet excitation. The expression for the required power supply voltage is;

$$\begin{aligned} V &= RI + \frac{2U}{I^2} \frac{dI}{dt}, \\ &= RI_0 + \frac{2U}{I_0^2} \frac{I_0}{\Delta t} = RI_0 + \frac{2U}{I_0 \Delta t}, \\ &= RI_0 + \frac{2}{I_0 \Delta t} \times \frac{B^2}{2\mu_0} \left((V)_{gap} + \frac{(V)_{coil}}{3} + \frac{1}{\mu} (V)_{yoke} \right). \end{aligned}$$

Looking more closely at the term, $\frac{2}{I_0 \Delta t} \times \frac{B^2}{2\mu_0}$ for the example window frame dipole;

$$\frac{2}{I_0 \Delta t} \times \frac{B^2}{2\mu_0} = \frac{B^2}{I_0 \Delta t \mu_0}.$$

For most pulsed magnets, the resistive power in the coil operated at low duty cycle is unimportant. The coil volume is small compared to the gap volume and the current density, j , can be large. Moreover, the volume of the yoke is a few times the gap volume and when multiplied by $\frac{1}{\mu}$, a small number, the yoke volume term adds a negligible amount to the magnet inductance. The required excitation for the window frame dipole is $NI = \frac{Bh}{\mu_0} \Rightarrow I_0 = \frac{Bh}{N\mu_0}$. Making the indicated simplifications;

$$\begin{aligned}
V &\approx \frac{B^2}{I_0 \Delta t \mu_0} (V)_{gap} \approx \frac{B^2}{\frac{Bh}{N\mu_0} \Delta t \mu_0} l \times h \times a, \\
&\approx \frac{BN}{\Delta t} l \times a.
\end{aligned} \tag{7.9}$$

From this expression, the voltage relies on physics specifications, $\int B dl \approx B \times l$, the pulse length, Δt , and the aperture width and height of the magnet, h and a . The only design variable is the number of coil turns, N . Rapidly ramped magnets are often designed with a single turn coil to limit the power supply voltage. Again, analyzing the units,

$$\begin{aligned}
V &\approx \frac{BN}{\Delta t} l \times a = \frac{T m^2}{\text{sec}}, \\
&= \frac{\text{Webers} \times m^2}{m^2 \text{ sec}} = \frac{\text{Volt sec}}{\text{sec}} = \text{Volts}.
\end{aligned}$$

7.4 Eddy Currents

Eddy currents are currents excited by time varying magnetic fields. This is a broad area and the number of analytic solutions describing the distribution of eddy currents in complicated shapes is limited. This subject is important in particle accelerators since the charged particles circulate inside of electrically conductive metallic vacuum chambers. Eddy currents generated in these chambers will attenuate and distort the magnetic fields generated by an otherwise well designed accelerator magnet, alter the field or gradient uniformity and affect the orbit of charged particle beams. This subject is also important for magnet design since eddy currents can amplify the distribution of magnetic fields in a solid core magnet resulting in portions of the magnet yoke to operate on different legs of the material hysteresis curve. This behavior is equivalent to magnets in the same family being fabricated using iron or steel with different BH characteristics.

Computer codes capable of solving the complicated distribution of eddy currents in different chamber shapes imbedded in a time varying field are available. For the purposes of this text, it is not important to solve for specific complicated shapes and describe their behavior in a detailed manner. It is instructive, however, to describe the distribution of eddy currents and the attenuation and amplification effects in very simple cases. The cases reviewed in this section simplify the mathematics by considering the distribution of the field in one dimension. The real solutions are substantially more complex, but the one dimensional solutions give first order approximations of the two dimensional behavior of the magnetic fields under time varying conditions. The results of these simple calculations yield relationships which

describe the field attenuation and amplification in a general way and can be used to quantify the field perturbations due to the magnitude of various parameters. Although the mathematics are consistent, the cases don't describe the detailed behavior in a totally accurate manner. In order to obtain accurate results, employment of computer calculations using codes specifically set up for these problems is required. The sensitivities obtained from the simple mathematical computations are important since one can estimate the magnitude of the eddy currents and the resulting magnetic field perturbations before embarking on the significant effort of setting up and performing complex computer calculations. The following computations develop field attenuation relationships for three simple cases, a semi-infinite conductive horizontal plate and a pair of semi-infinite conductive vertical plates. These two cases are superimposed in order to develop field attenuation relationships for a two-dimensional simple rectangular vacuum chamber imbedded in a time varying magnetic field. The third case assumes that the magnet pole is constructed of thick laminations or is solid and shows that it is possible to amplify as well as attenuate the magnetic field and demonstrates that the time constant of the magnet can be severely altered. Again, it is important to emphasize that the mathematical rigor of these simple solutions is questionable since discontinuities of the otherwise smooth behavior of the time dependent magnetic field are introduced.

7.4.1 Field Attenuation due to Eddy Currents in a Semi-infinite Conductive Horizontal Plate

The simple case selected for description in this section (illustrated in fig. 2) describes the boundary conditions for solving for a one dimensional distribution of eddy currents and the attenuated field due to the presence of a conductive plate of finite width, $2b$, and thickness, t . (The solution of the differential equation summarized in this section is due to work performed by Glen Lambertson[14]). The eddy current field distribution in the plate is computed for a dipole magnet with a given half-gap, h , and a uniformly distributed cyclic time varying magnetic field, $B = B_0 e^{i\omega t}$ where $i = \sqrt{-1}$

The distribution of the eddy currents can be computed knowing that the distribution of voltage in an electrical circuit depends only on the time rate of change of the enclosed magnetic flux

$$V(x) = \frac{\partial \Phi}{\partial t} = \frac{\partial B}{\partial t} A = \frac{\partial B}{\partial t} L \int_0^x dx, \quad (7.10)$$

where L is the length of the plate in the z direction.

The current flowing in the plate can be described by

$$\begin{aligned} I(x) &= \frac{V(x)}{R} \\ &= \frac{\partial B}{\partial t} \frac{L}{R} \int_0^x dx, \end{aligned} \quad (7.11)$$

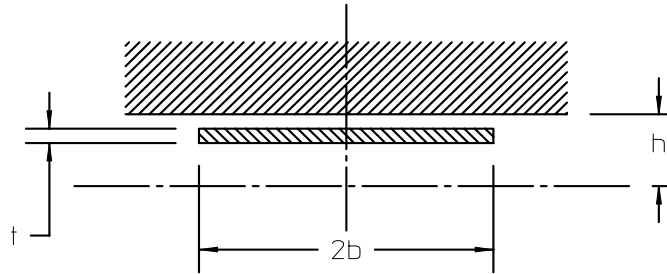


Figure 2 Eddy Current Field Attenuation due to Horizontal Plate

where

$$R = \frac{\rho L}{\text{Area}} = \frac{\rho L}{t dx}, \quad (7.12)$$

where ρ is the volume resistivity of the metal used in the plate. Introducing the current density $j(x)$ where $I(x) = j(x) dx$ and substituting the expression for resistance into eq. (7.11).

$$j(x) dx = \frac{\partial B t}{\partial t} \frac{dx}{\rho} \int_0^x dx. \quad (7.13)$$

Taking the integral form of the Poisson's equation, $\oint \vec{H} \cdot d\vec{l} = \int_{\text{Area}} j dA$ and assuming that the fields are vertical,

$$-H(0) h + H(x) h = \frac{-B(0) h + B(x) h}{\mu_0} = \int_0^x j(x) dx. \quad (7.14)$$

Substituting eq. (7.13) into (7.14)

$$\begin{aligned} \frac{-B(0) h + B(x) h}{\mu_0 \mu_0} &= \int_0^x j(x) dx \\ &= \frac{t}{\rho} \int_0^x \int_0^x \frac{\partial B}{\partial t} dx dx. \end{aligned}$$

Differentiating twice with respect to x , we get finally

$$\frac{\partial^2 B}{\partial x^2} = \frac{t \mu_0}{h \rho} \frac{\partial B}{\partial t}. \quad (7.15)$$

Assume that the magnetic field is given by $B(x, t) = B(x) e^{i\omega t}$. Substituting into eq. (7.15)

$$\begin{aligned} \frac{\partial^2 B(x)}{\partial x^2} e^{i\omega t} &= \frac{t \mu_0}{h \rho} B(x) \frac{\partial e^{i\omega t}}{\partial t} = \frac{t \mu_0}{h \rho} i\omega B(x) e^{i\omega t} \implies \\ \frac{\partial^2 B}{\partial x^2} &= \frac{i t \omega \mu_0}{h \rho} B. \end{aligned} \quad (7.16)$$

Eq. (7.16) is an expression in x only.

Skin Depth

At this point, we introduce a variable called the “skin depth”, δ , where

$$\begin{aligned} \delta &= \sqrt{\frac{2 \rho t}{\omega \mu_0 h}}, \\ \text{with units } &= \sqrt{\frac{\Omega m}{\sec^{-1} \frac{T m}{Amp}}} = \sqrt{\frac{\Omega m}{\sec^{-1} \frac{Webers m}{m^2 Amp}}}, \\ &= \sqrt{\frac{\Omega m m^2 Amp}{\sec^{-1} Volt \ sec \ m}} = \sqrt{m^2} = m \ (\text{length}). \end{aligned} \quad (7.17)$$

(The “classical” definition of the skin depth is independent of the ratio $\frac{t}{h}$.)

Substituting this variable, the differential equation for the distribution of the magnetic field on the magnet centerline is simplified to

$$\frac{\partial^2 B}{\partial x^2} = \frac{2 i}{\delta^2} B. \quad (7.18)$$

Solution to the Differential Equation

Eq. (7.18) has the general solution of a hyperbolic function. We limit our attention to the even (\cosh) function because of the symmetry of the field about $x = 0$.

$$B = A \cosh kx.$$

Substituting this expression into eq. (7.18),

$$\frac{\partial^2 B}{\partial x^2} = A k^2 \cosh kx = \frac{2i}{\delta^2} A \cosh kx.$$

Therefore,

$$k^2 = \frac{2i}{\delta^2} \quad (7.19)$$

and the distribution of the attenuated magnetic field on the dipole centerline is given by

$$B = A \cosh \frac{\sqrt{2i}}{\delta} x. \quad (7.20)$$

Assuming that the magnitude of the uniform unattenuated field is B_0 at the edge of the plate, $x = b$, the value of the constant is given by

$$B_0 = A \cosh \frac{\sqrt{2i}}{\delta} b \implies A = \frac{B_0}{\cosh \frac{\sqrt{2i}}{\delta} b}.$$

Therefore, the attenuated field under the conductive metallic plate is given by

$$B = \frac{B_0 \cosh \frac{\sqrt{2i}}{\delta} x}{\cosh \frac{\sqrt{2i}}{\delta} b}. \quad (7.21)$$

Expressions for Numerical Evaluation

For numerical evaluation of eq. (7.21), it can be shown that

$$\sqrt{2i} = 1 + i.$$

Substituting into eq. (7.21) and normalizing with respect to the external field

$$\frac{B}{B_0} = \frac{\cosh (1+i) \frac{x}{\delta}}{\cosh (1+i) \frac{b}{\delta}} \quad (7.22)$$

where

$$\cosh(1+i)\frac{x}{\delta} = \cosh\frac{x}{\delta}\cos\frac{x}{\delta} + i\sinh\frac{x}{\delta}\sin\frac{x}{\delta}$$

$$\text{and } \cosh(1+i)\frac{b}{\delta} = \cosh\frac{b}{\delta}\cos\frac{b}{\delta} + i\sinh\frac{b}{\delta}\sin\frac{b}{\delta}.$$

Attenuation at the Center of the Magnet

Since $\cosh(0) = 1$ and $\sin(0) = 0$, the minimum normalized attenuated field at the center of the magnet and the phase of the attenuation with respect to the driving field can be computed by evaluating eq. (7.22) at $x = 0$.

$$\left(\frac{B}{B_0}\right)_{x=0} = \frac{1}{\cosh(1+i)\frac{b}{\delta}}$$

$$= \frac{1}{\cosh\frac{b}{\delta}\cos\frac{b}{\delta} - i\sinh\frac{b}{\delta}\sin\frac{b}{\delta}} \quad (7.23)$$

$$\text{Therefore, } \left|\frac{B}{B_0}\right|_{x=0} = \frac{1}{\sqrt{\cosh^2\left(\frac{b}{\delta}\right)\cos^2\left(\frac{b}{\delta}\right) + \sinh^2\left(\frac{b}{\delta}\right)\sin^2\left(\frac{b}{\delta}\right)}} \quad (7.24)$$

$$\text{and the phase is } \Phi_{x=0} = \tan^{-1} \frac{-\sinh\frac{b}{\delta}\sin\frac{b}{\delta}}{\cosh\frac{b}{\delta}\cos\frac{b}{\delta}}. \quad (7.25)$$

Numerical Evaluation

In order to fully appreciate the effect of a conductive plate in the magnetic field, the expression for the field attenuation at the center of the magnet is numerically evaluated. The evaluation is made for a magnet with 10 mm. gap, with a 2 mm. thick metallic plate with a half width of 10 mm. The attenuation is compared for three different materials, stainless steel with $\rho_{ss} = 70 \times 10^{-8} \Omega m$, aluminum with $\rho_{al} = 3.3 \times 10^{-8} \Omega m$, and copper with $\rho_{cu} = 1.89 \times 10^{-8} \Omega m$. Graphing eq. 7.24 in fig. 3, one can see that the attenuation at the center of the magnet is large for a plate with material with higher conductivity.

If one carries out the numerical computation of the phase, one will find that an almost constant phase shift with π is computed for the range of selected frequencies.

7.4.2 Field Attenuation due to Eddy Currents in a Pair of Semi-infinite Conductive Vertical Plates

The solution of the field attenuation for a pair of semi-infinite vertical plates, illustrated in fig. 4, is given by the expressions developed in the previous section. Assume that the plate height is given by H and its thickness is t and are separated by a distance $2b$. The skin depth is given by

Figure 3 Field Attenuation at the Center of a Plate

$$\delta_v = \sqrt{\frac{2 \rho H}{\omega \mu_0 h}}, \quad (7.26)$$

and the attenuated field at the inside surface of the plate is

$$\frac{B}{B_0} = \frac{\cosh(1+i) \frac{b-t}{\delta_v}}{\cosh(1+i) \frac{b}{\delta_v}}. \quad (7.27)$$

The Vertical Plate as a Boundary Condition for Computing the Attenuation in a Closed Rectangular Chamber

The attenuation at the inside surface of vertical plates is useful since it provides the boundary condition for the evaluation of the attenuation in a closed rectangular chamber. However, if one numerically evaluates the attenuation at the inside surface of vertical plates, one finds that the attenuation is small for resistive material (stainless steel) and low frequencies (\leq a few Hz) and the difference between using

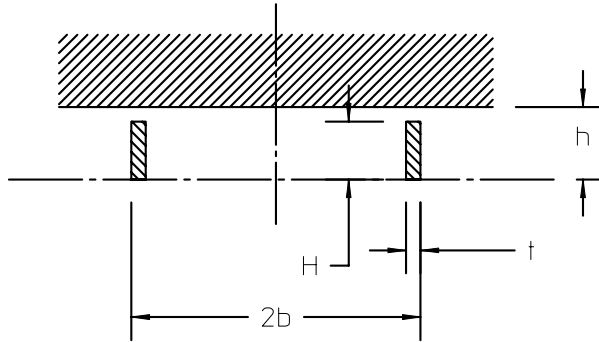


Figure 4 Eddy Current Field Attenuation due to Vertical Plates

the amplitude of the unattenuated field and the field value at the inside surface of the vertical plate is small. The attenuation in a closed rectangular chamber is dominated by the presence of the horizontal plate of the rectangular chamber and one can compute a good approximation by considering only the horizontal plate.

7.4.3 Field Attenuation due to Eddy Currents in a Closed Rectangular Chamber

Although the attenuation in a closed rectangular chamber is dominated by the presence of the horizontal plate, the more complete solution of a rectangular chamber is included for completeness. The solution of the field attenuation for a closed rectangular chamber, illustrated in fig. 5, is developed by the superposition of the two previous cases. From eq. (7.27) the attenuated field at the inside surface of the vertical portions of the chamber is given by

$$B_{b-t} = B_0 \frac{\cosh(1+i) \frac{b-t}{\delta_v}}{\cosh(1+i) \frac{b}{\delta_v}}. \quad (7.28)$$

where δ_v is given by eq. (7.26).

The attenuated field under the horizontal plate is given by

$$B = B_{b-t} \frac{\cosh(1+i) \frac{x}{\delta_h}}{\cosh(1+i) \frac{b-t}{\delta_h}} \quad (7.29)$$

where

$$\delta_h = \sqrt{\frac{2 \rho t}{\omega \mu_0 h}}. \quad (7.30)$$

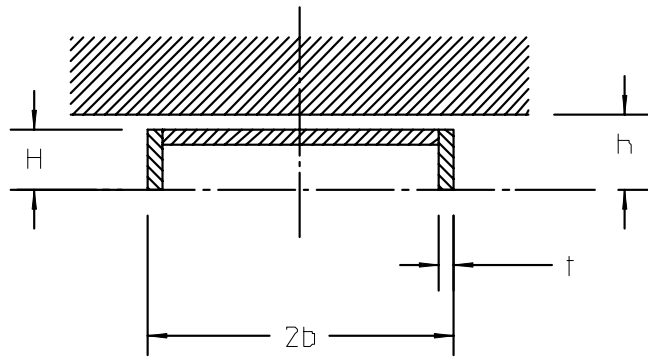


Figure 5 Eddy Current Attenuation in a Rectangular Chamber

Substituting eq. (7.28) into eq. (7.29) and normalizing to the external field amplitude, the expression for the attenuated field in a rectangular vacuum chamber for $x \leq b - t$ is

$$\frac{B}{B_0} = \frac{\cosh(1+i)\frac{b-t}{\delta_v}}{\cosh(1+i)\frac{b}{\delta_v}} \frac{\cosh(1+i)\frac{x}{\delta_h}}{\cosh(1+i)\frac{b-t}{\delta_h}}. \quad (7.31)$$

7.4.4 Field Amplification

In an accelerator, all the magnets of the same family are required to operate with identical fields or gradients when excited at the same current. This magnet reproducibility is crucial to the successful, reliable and reproducible operation of a synchrotron. Iron and steel properties, in addition to the mechanical fabrication errors, described in Chapter 4, can compromise reproducibility among magnets of the same family. Despite care in sorting material and fabrication and assembly, magnets made from material with nominally identical magnetic properties can fail to be reproducible. This lack of reproducibility is due to the material operating on different hysteresis curves for the same material. The operating curve for the magnet material depends on its history. Magnet steel taken to identical high fields will operate on identical curves. Therefore, before they are excited in the ring, magnets of the same family are excited at fields and/or gradients at least 10% higher than their maximum operating level. This procedure is called “conditioning” and is normally performed three times prior to exciting the magnet to its required field and/or gradient. Despite rigidly following conditioning requirements, individual magnets can occasionally be operated in a manner which can compromise the reproducible performance of an otherwise identical magnet. The operation leading to loss of magnet reproducibility is rapid field changes, generating eddy currents which amplify the field in portions of the magnet iron.

Eddy currents can amplify as well as attenuate magnetic fields. This is a problem for solid core magnets or magnets constructed using thick steel or iron slabs since the fields generated by eddy currents for changing magnetic fields can often cause the field level in the iron yoke to exceed the maximum conditioning field of the magnet. Portions of the edges of an iron pole can thus become saturated and operate on a different leg of the iron or steel hysteresis curve than during previous operation.

Crowbarring

Assume that the electrical properties of the dipole magnet can be described by its inductance, L , and its resistance, R . The current in a magnet is determined by eq. (7.7),

$$RI + L \frac{dI}{dt} = V,$$

where R and L are the resistance and inductance, respectively, of the magnet electrical circuit.

Crowbarring is the operation of a power supply when a steady voltage source is suddenly turned off. The voltage and the current as a function of time is illustrated in fig. 6. It is easily shown that, in a power supply circuit which includes a diode to allow the control current decay and avoid voltage spikes, the solution of the differential equation for current for the illustrated voltage step function for $t \geq 0$ is

$$I = \frac{V_0}{R} e^{-\frac{t}{\tau}}, \quad (7.32)$$

where $\tau = \frac{L}{R}$.

Affect of the Solid Core or Thick Steel Laminations

In the following section, an attempt is made to describe the spatial distribution of the magnetic field and its time behavior using a very simplified time dependent one dimensional (in space) differential equation. The behavior of the eddy currents and the magnetic fields it generates is, of course, far more complex than the mathematical treatment which follows. The solution of the simple differential equations lead to certain discontinuities which are not physically possible. The actual spatial distribution of the field and its time behavior is best computed using MAFIA© or other computer codes specially written for these complex time dependent problems. However, the solution to the simple differential equation and the use of boundary conditions to

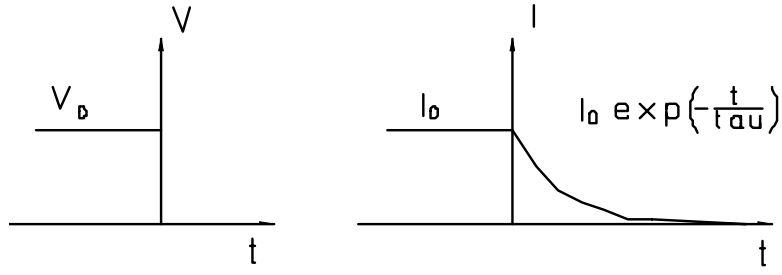


Figure 6 Voltage Crowbar

evaluate integration constants leads to analytic expressions which approximate the behavior of the time dependent fields due to eddy currents in permeable material for magnet yokes with certain dimensional and permeability parameters. These expressions are useful since they point out that field amplifications are possible and that the time response for the rapid field changes can be much longer than the time constant determined by the electrical parameters of the magnet.

Consider the dipole (or a thick lamination in the dipole) illustrated in fig. 7 operating at a uniform field, B_0 and suddenly losing power supply voltage so that the magnet current is behaves as described in eq. 7.32.

Consider the iron pole in half of the magnet whose length into the page is given by ℓ . The distribution of the eddy currents generated in the iron obey the same differential equation as describes the behavior of the magnet. In the following expression, the current in an incremental strip in the iron yoke or lamination is given by $I = j(x) H dx$.

$$dR_{iron} j(x) H dx + dL_{iron} \frac{d(j(x) H dx)}{dt} = V,$$

where
$$V = \frac{\partial}{\partial t} B_0 e^{-\frac{t}{\tau}} \int_0^x \ell dx$$

$$= -\frac{B_0}{\tau} e^{-\frac{t}{\tau}} \int_0^x \ell dx,$$

where H in this expression is the height of the pole and L_{iron} and R_{iron} are the inductance and resistance, respectively, of the iron yoke. Rewriting,

$$j(x) H dx + \frac{L_{iron}}{R_{iron}} \frac{d(j(x) H dx)}{dt} = \frac{B_0}{\tau} e^{-\frac{t}{\tau}} \int_0^x \frac{\ell}{dR_{iron}} dx. \quad (7.33)$$

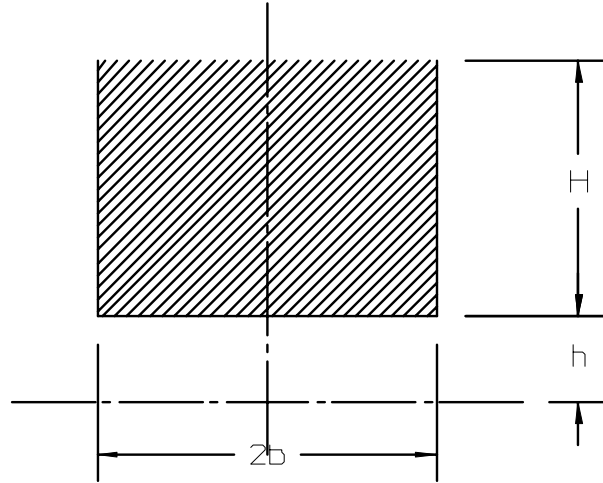


Figure 7 Solid Core Field Amplification

Inductance and Resistance Calculating the inductance using the stored energy for half the steel block,

$$\begin{aligned}
 L_{iron} &= \frac{2U}{I^2} \text{ where} \\
 U &= \text{Stored Energy} = \frac{B^2 \times \text{Volume}}{\mu \mu_0} \\
 &= \frac{B^2 \times \ell H b}{\mu \mu_0} \\
 \text{and } I_{iron} &= \frac{B H}{\mu \mu_0} \\
 \text{Therefore } L_{iron} &= \frac{2U}{I^2} = 2 \frac{\mu^2 \mu_0^2}{B^2 H^2} \frac{B^2 \times \ell H b}{\mu \mu_0} \\
 &= \frac{2 \mu \mu_0 \ell b}{H}.
 \end{aligned}$$

Calculating the resistance for half the steel block and the incremental resistance, dR_{iron} ,

$$\begin{aligned}
 dR_{iron} &= \frac{\rho_{iron} \ell}{H dx} \\
 dR_{iron} &= \frac{\rho_{iron} \ell}{H dx}.
 \end{aligned}$$

The total resistance for half the iron pole is

$$R_{iron} = \frac{\rho_{iron} \ell}{H b}$$

Then

$$\begin{aligned} \frac{L_{iron}}{R_{iron}} &= \frac{2 \mu \mu_0 \ell b}{H} \frac{H b}{\rho_{iron} \ell} \\ &= \frac{2 \mu \mu_0 b^2}{\rho_{iron}}. \end{aligned}$$

Using the MKS system of units, it can be shown that this expression has the units of time. Therefore, we define the time constant τ_2 by

$$\tau_2 = \frac{L_{iron}}{R_{iron}} = \frac{2 \mu \mu_0 b^2}{\rho_{iron}}. \quad (7.34)$$

Substituting into eq. (7.33),

$$\begin{aligned} j(x) H dx + \tau_2 \frac{d(j(x) H dx)}{dt} &= -\frac{B_0}{\tau} e^{-\frac{t}{\tau}} \int_0^x \frac{\ell}{dR_{iron}} dx, \\ &= -\frac{B_0}{\tau} e^{-\frac{t}{\tau}} \int_0^x \frac{\ell}{\frac{\rho_{iron} \ell}{H dx}} dx, \end{aligned}$$

Integrating,

$$\int_0^x j(x) H dx + \tau_2 \frac{d(\int_0^x j(x) H dx)}{dt} = -e^{-\frac{t}{\tau}} \frac{B_0 H}{\tau \rho_{iron}} \int_0^x \int_0^x dx dx. \quad (7.35)$$

Using the relationship, $\int_{Area} j(x) dA = \oint \frac{B}{\mu \mu_0} \cdot d\ell$

$$\int_0^x j(x) H dx = \frac{H}{\mu \mu_0} [B(0) - B(x, t)].$$

Substituting into eq. (7.35) and simplifying,

$$B(0) - B(x, t) + \tau_2 \frac{d(-B(0) - B(x, t))}{dt} = -\frac{B_0}{\tau} e^{-\frac{t}{\tau}} \frac{\mu \mu_0}{\rho_{iron}} \int_0^x \int_0^x dx dx$$

At this point, we make an assumption that $B(x, t)$ is separable function of x and t and can be written as $B(x) \theta(t)$.

Substituting and differentiating twice with respect to x and removing the negative sign.

$$\begin{aligned}\frac{d^2B}{dx^2}\theta + \tau_2 \frac{d^2B}{dx^2} \frac{d\theta}{dt} &= \frac{B_0}{\tau} e^{-\frac{t}{\tau}} \frac{\mu \mu_0}{\rho_{iron}}, \\ \frac{d^2B}{dx^2} \left(\theta + \tau_2 \frac{d\theta}{dt} \right) &= \frac{B_0}{\tau} e^{-\frac{t}{\tau}} \frac{\mu \mu_0}{\rho_{iron}}.\end{aligned}$$

From eq. (7.34), $\frac{2 \mu \mu_0 b^2}{\rho_{iron}} = \tau_2$. Therefore, substituting $\frac{\mu \mu_0}{\rho_{iron}} = \frac{\tau_2}{2b^2}$, the expression can be rewritten

$$\frac{d^2B}{dx^2} \left(\theta + \tau_2 \frac{d\theta}{dt} \right) = \frac{B_0 \tau_2}{2b^2 \tau} e^{-\frac{t}{\tau}},$$

or separating the variables,

$$\frac{\frac{d^2B}{dx^2}}{\frac{B_0}{2b^2}} = \frac{\frac{\tau_2}{\tau} e^{-\frac{t}{\tau}}}{\theta + \tau_2 \frac{d\theta}{dt}}. \quad (7.36)$$

Solution in the Space Domain Taking the left side of the separated differential eq. (7.36)

$$\frac{d^2B}{dx^2} = \frac{B_0}{2b^2}.$$

The differential equation has the solution

$$B = \frac{B_0 x^2}{4b^2}. \quad (7.37)$$

Solution in the Time Domain Taking the right side of the separated differential eq. (7.36)

$$\theta + \tau_2 \frac{d\theta}{dt} = \frac{\tau_2}{\tau} e^{-\frac{t}{\tau}}.$$

Taking the LaPlace transform of the differential equation in time

$$\begin{aligned}
\mathcal{L}\theta + \tau_2 [s\mathcal{L}\theta - \theta(0+)] &= \frac{\tau_2}{\tau} \frac{1}{s + \frac{1}{\tau}} \\
\mathcal{L}\theta &= \frac{\tau_2}{\tau} \frac{1}{(s + \frac{1}{\tau})(1 + \tau_2 s)} + \frac{\tau_2 \theta(0+)}{1 + \tau_2 s} \\
\mathcal{L}\theta &= \frac{1}{\tau(s + \frac{1}{\tau})(s + \frac{1}{\tau_2})} + \frac{\theta(0+)}{s + \frac{1}{\tau_2}}.
\end{aligned} \tag{7.38}$$

The inverse LaPlace transform for this expression is

$$\begin{aligned}
\theta(t) &= \frac{1}{\tau} \frac{\exp(-\frac{t}{\tau}) - \exp(-\frac{t}{\tau_2})}{\frac{1}{\tau_2} - \frac{1}{\tau}} + \theta(0+) \exp\left(-\frac{t}{\tau_2}\right) \\
\theta(t) &= \frac{\tau_2}{\tau_2 - \tau} \left[\exp\left(-\frac{t}{\tau_2}\right) - \exp\left(-\frac{t}{\tau}\right) \right] + \theta(0+) \exp\left(-\frac{t}{\tau_2}\right).
\end{aligned} \tag{7.39}$$

Combination of the Space and Time Domain The second term in eq. (7.39) is associated with the initial condition in the iron yoke. The field before the rapid decay of the field due to power supply loss is constant and is equal to B_0 . This, in combination of the solution of the spatial differential equation given by eq. (7.37) and the solution of the differential equation in the time domain, eq. (7.39), yields the final expression for the time dependent one dimensional magnetic field in the magnet pole (or thick lamination).

$$B(x, t) = \frac{B_0 x^2}{4b^2} \frac{\tau_2}{\tau_2 - \tau} \left[\exp\left(-\frac{t}{\tau_2}\right) - \exp\left(-\frac{t}{\tau}\right) \right] + B_0 \exp\left(-\frac{t}{\tau_2}\right),$$

and the maximum field at the pole edge (at $x = b$) is given by

$$B(b, t) = \frac{B_0}{4} \frac{\tau_2}{\tau_2 - \tau} \left[\exp\left(-\frac{t}{\tau_2}\right) - \exp\left(-\frac{t}{\tau}\right) \right] + B_0 \exp\left(-\frac{t}{\tau_2}\right).$$

The ratio of the maximum field in the yoke to the nominal field is given by

$$\frac{B_{\max}}{B_0} = \frac{\tau_2}{4(\tau_2 - \tau)} \left[\exp\left(-\frac{t}{\tau_2}\right) - \exp\left(-\frac{t}{\tau}\right) \right] + \exp\left(-\frac{t}{\tau_2}\right). \tag{7.40}$$

7.5 Chapter Closure

This chapter is added to develop some of the relationships associated with the magnet stored energy. Expressions for the magnetic forces on poles and on coils for simple magnet geometries are developed. The concept of stored energy allows one to compute the magnet inductance so that the power supply needs for pulsed and cycled magnets can be anticipated.

The area of dynamic magnet effects is much more extensive than can be covered completely in this chapter. Eddy currents, currents induced by time varying magnetic fields, can exclude fields from selected areas. This subject is important in rapidly cycled synchrotrons, often used as injectors for larger machines storing charged particle circulating beam operated in the persistent mode. The field perturbation caused by eddy currents in metallic vacuum chambers can distort and attenuate the otherwise uniform fields of the magnets in the regions of the accelerator where the charged particle beam reside. Eddy currents effects are also important in the area of corrector magnets which may have to operate at wide bandwidths through metallic vacuum chambers when used for rapid feedback of beam orbit errors in DC synchrotrons. They are also important in injection, where the circulating beam is momentarily (usually during one beam transit time around the ring) "bumped" near the injection septum to enhance damping into the circulating beam phase space. Detailed descriptions of eddy currents and their effects for complicated chamber shapes is a far broader subject than can be covered in this limited edition. Other texts are available covering this important subject. However, some simple cases are introduced so that analytic expressions can be developed. These analytic expressions are important since they describe, in a general way, the effect of chamber thickness and width as a fraction of the magnet gap and the chamber material conductivity on the attenuation and field distortion for a simple case.

Another area where eddy currents are important is the area of field amplification in the yoke of a magnet. Because of transient fields generated by rapid magnet excitation or rapid field decay due to power supply problems, large eddy currents generated in the iron or steel magnet yoke can locally amplify the maximum field in a magnet. This is an important effect since it can locally change the BH curve of portions of the magnet pole and cause local field perturbations or cause the magnet excitation at identical currents to differ before and after the transient.

The transient effects are approximated using simplified one-dimensional models. More detailed and precise calculations can be made using the many computer codes which are made available specifically to analyze these complicated problems. The algorithms developed using the simplifications can be useful to the magnet designer to make estimates of the magnitudes of the field perturbations and can provide guidance as to the sensitivities of these perturbations to magnet parameters and material properties.

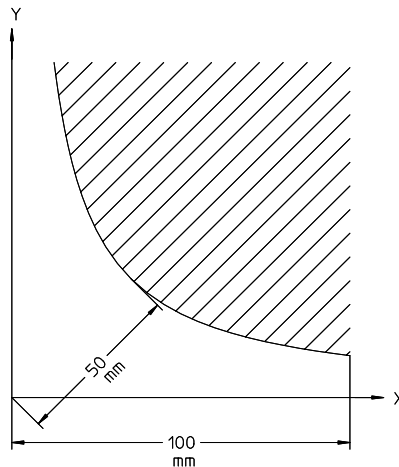


Figure 8 Quadrupole Pole Contour

7.6 Problems

Problem 7.1 (Solution)

Given a two piece quadrupole with a 50 mm. pole radius as shown in fig. with a gradient of $5 \frac{T}{m}$, what is the maximum magnetic field on the horizontal centerline directly beneath the edge of the pole?

Problem 7.1a (Solution) What is the maximum magnetic “pressure” on the magnet centerline beneath the edge of the pole?

Problem 7.1b (Solution) What is the “shape” of the magnetic pressure curve and its maximum amplitude?

Problem 7.1c (Solution) Integration of the magnetic pressure curve results in the force on the magnet per unit length. What is this force per length on the illustrated quadrupole? Assuming a magnet which is 300 mm. long, what is the total magnetic force between the upper half and the lower half of the quadrupole?

Problem 7.2

For a sextupole with 100 mm half width and 300 mm length with a sextupole gradient $B'' = 10 \frac{T}{m^2}$, what is the force between the upper half and the lower half of the magnet.

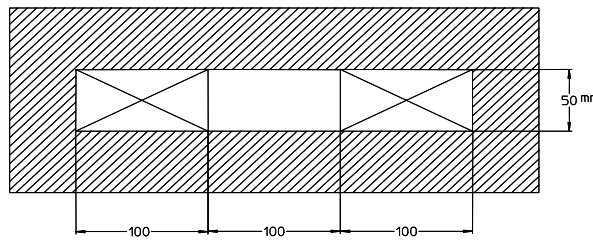


Figure 9 Window Frame Dipole Magnet

Problem 7.3

Assume a 0.5 meter long window frame dipole magnet with the configuration described by fig. 9. Suppose the coil has 40 turns and the magnet is designed to operate at 1000 Amps. The conductor is made with copper with a resistivity $\rho = 1.86 \times 10^{-8} \Omega m$ with cross sectional area 100 mm^2 and the average turn length is 1.3 meters.

Problem 7.3a (Solution) What is the field in the gap?

Problem 7.3b (Solution) What is the magnetic stored energy in the air gap?

Problem 7.3c (Solution) What is the magnetic stored energy in the coil?

Problem 7.3d (Solution) What is the approximate total magnetic stored energy in the magnet?

Problem 7.3e (Solution) What is the magnet inductance? What is the magnet resistance?

Problem 7.3f (Solution) Write the differential equation for the magnet voltage as a function of time varying magnet current. Assume that a sinusoidal current wave form $I(t) = I_{\max} \sin \omega t$ where $\omega = 1 \text{ Hz}$, and $I_{\max} = 1000 \text{ Amps}$ is required. Compute the voltage required to drive the magnet with this current. What are the maximum voltage amplitude and the phase difference between the current and voltage waveforms.

Problem 7.4 (Solution)

Consider a dipole with half gap $h = 25 \text{ mm}$ with a vacuum chamber whose horizontal surfaces has a thickness of $t = 3 \text{ mm}$ and halfwidth $b = 50 \text{ mm}$. Compute the ampli-

tude of the attenuated field in the center of the magnet as a function of frequency for a stainless steel ($\rho = 70 \times 10^{-8} \Omega m$) and aluminum chamber ($\rho = 3.3 \times 10^{-8} \Omega m$).

Chapter 8

MAGNETIC MEASUREMENTS

Magnetic measurements are used to characterize excitation and field quality. The location of the magnet center with respect to mechanical features of a quadrupole and sextupole can also be found using the results of magnetic measurements. Knowledge of these characteristics for different magnet types and individual magnets of each type is important for operation of high performance accelerators. Magnet excitation is the relationship of the field and/or field integral with power supply current. Characterization of the excitation behavior of each magnet provides information to ensure that each magnet in an accelerator lattice bends, focuses and trims the beam correctly and precisely. Field quality is the measure of the difference between the actual field and/or field integral and the desired field and/or field integral. The measured magnetic field is characterized by the amplitudes and phases of the fundamental field and the multipole error fields or their integrals. Field quality measurements are required to verify that individual amplitudes of the spectrum of error terms are small compared to the desired fundamental field and satisfy physics requirements. The relationship between the magnet axis and external mechanical features of the magnet need to be measured and characterized to ensure that each magnet is properly aligned. A multipole magnet whose axis does not coincide with the beam central axis will introduce unwanted steering or focusing.

Many magnetic measurement techniques are used. Among the different methods of measuring magnets are Hall probe maps, wire measurements and rotating coil measurements. In this chapter, the discussion is limited to the description of measurement of different magnet types using relatively slowly rotating coils (\leq a few Hz). The techniques have long and widespread usage and descriptions of this technique can be found in the literature. However, it is useful to summarize in this text, features of the measurement coil design, the rotating coil data acquisition system and algorithms to convert the electrical data to parameters describing the magnet performance.

Rotating coils have several advantages over other methods of measurement. It can reproducibly measure the integrated field, the multipole errors and the location of the magnetic axis in a simple and precise way. The biggest advantage of using this method is its simplicity, requiring far less measurement time than mapping methods or wire measurements. A single measurement can be completed in a few seconds. It also provides more information about the magnetic field (multipole content) than

flip coil techniques. The rotating coil measurements discussed in this chapter are different from earlier methods which relied on rapidly rotating coils, requiring data reduction by spectrum analysis of the output voltage signal. It also provides more information (the relative amplitudes of the skew and real components of multipole fields), enhancing the ability to isolate the sources of mechanical errors resulting in particular multipole errors. (Certain multipole error spectra are generated by mechanical assembly or fabrication errors violating symmetry conditions. See page 103.) The accuracy of the measurement is enhanced by the design of the rotating coil which can be wired to reject a large fraction of the fundamental field. In this compensated configuration, the small error multipole signals can be measured in the absence of a large signal from the fundamental field. When the measurement coil wiring does not include the windings which reject the fundamental, it is said to be uncompensated. The fabrication of the coil in an accurately machined housing allowing it to be supported using the magnet poles simplifies the mechanical design of the measurement system and allows measurements leading to the identification of the displacement of the magnet center from the magnet mechanical center.

The mathematical theory developed in the first chapter is used both to describe the measurements and to develop the algorithms to reduce the measured data. This chapter describes magnetic measurements using rotating coils operated in compensated and uncompensated configurations. It begins by developing the theory for a rotating coil with a single wire at a given radius. The development starts from the principle that the voltage generated in a loop of wire is equal to the time rate of change of magnetic flux intersecting the loop area and shows that the time integrated voltage signal from a rotating coil measures the line integral of the vector potential. A numerical example is given to demonstrate the difficulty of measuring the error field components and resolving the error multipoles with a single wire. This motivates the design of measurement coils wound with many wires whose configuration can be designed to isolate the small error field signals from the much larger fundamental field signal. The topology of a rotating coil data acquisition system is described, the algorithms for data reduction are developed and summarized and a format for the tabulated summary of the field distribution is suggested.

8.1 The Vector Potential

Consider a wire with sufficient length to span the entire field of the measured magnet. From the chapter on the mathematical theory, the three-dimensional field integral satisfies the same differential equations used to develop the two-dimensional fields. Therefore, the mathematical functions used to describe the two dimensional field can be extended to three dimensional field integrals providing the range of integration covers the span where the field is nonzero.

In order to understand magnetic measurements, it is only necessary to understand that the voltage generated in a closed loop of electrical conductor depends

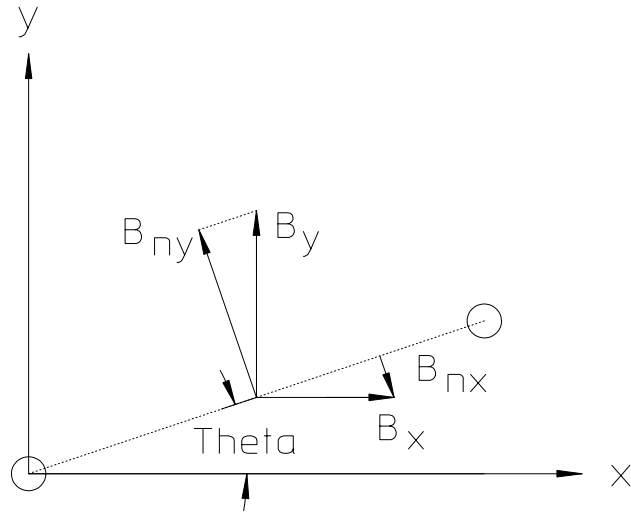


Figure 1

on the rate of change of magnetic flux intersecting that loop. The voltage generated in a rotating wire at radius s with the return at the center of rotation is given by

$$\begin{aligned} V &= \frac{d\Phi}{dt} \text{ where } \Phi \text{ is the total flux between the wires.} \\ \Phi &= L_{eff} \int B(s) ds \\ \frac{d\Phi}{dt} &= \frac{d\Phi}{ds} \frac{ds}{dt} = L_{eff} B(s) \frac{ds}{dt}. \end{aligned}$$

Therefore, $V = \frac{d\Phi}{dt} = L_{eff} B(s) \frac{ds}{dt}$ and the time integrated voltage for a wire with one filament at the origin and the other filament at radius r is $\int V dt = L_{eff} \int_0^r B(s) ds$.

Computing the field component normal to the plane of the wires and recalling that $B_x = \frac{\partial A}{\partial y}$ and $B_y = -\frac{\partial A}{\partial x}$, the expressions are simplified;

$$\begin{aligned} B(s) &= -B_{nx} + B_{ny}, \\ &= -B_x \sin \theta + B_y \cos \theta, \\ &= -\frac{\partial A}{\partial y} \frac{dy}{ds} - \frac{\partial A}{\partial x} \frac{dx}{ds} = -\frac{dA}{ds}. \end{aligned}$$

Therefore,

$$\int V dt = -L_{eff} \int B(s) ds = -L_{eff} \int dA = -L_{eff} A(\theta). \quad (8.1)$$

The integrated voltage from a rotating wire loop is the product of the magnet effective length and the vector potential at the wire radius.

8.1.1 Fourier Analysis

The time integrated voltage measured while the wire is rotated describes an analytic function of the angle θ which can be mathematically characterized as,

$$\int V dt = \sum_n (p_n \cos n\theta + q_n \sin n\theta), \quad (8.2)$$

a Fourier series expansion of the measurements whose coefficients p_n and q_n can be computed using any fast Fourier analysis routine.

Fourier Coefficients

Most data acquisition and data reduction software comes with a fast Fourier analysis routines included to digitally evaluate the coefficients from the measured data. However, it is useful to have the “classical” expression for the computation of the Fourier coefficients summarized in this section. The expressions for the coefficients,

$$\left. \begin{array}{l} p_n \\ q_n \end{array} \right\} = \frac{1}{\pi} \int_0^{2\pi} f(\theta) \begin{array}{l} \cos n\theta \\ \sin n\theta \end{array} d\theta, \quad (8.3)$$

can be found in any calculus text[15].

The Vector Potential from the Fourier Analysis

Since eq. (8.2) described the measurement as the integrated vector potential of the magnetic field, it is necessary to relate the Fourier coefficients of the measurements to the coefficients characterizing the components of the functions describing the magnetic field. The vector potential is the real part of an analytic function of a complex variable satisfying Laplace’s equation. Using the subscript n to represent the multipole components, $F_n(z) = C_n z^n$ where in general C_n is a complex constant and can be written in the polar form, $C_n = |C_n| e^{i\psi_n}$. The function is rewritten $F_n(z) = C_n z^n = |C_n| e^{i\psi_n} z^n$ where the vector potential and its line integral is evaluated as follows;

$$\begin{aligned} F_n(z) &= C_n z^n = |C_n| e^{i\psi_n} |z|^n e^{in\theta} = |C_n| |z|^n e^{i(n\theta + \psi_n)}, \\ &= |C_n| |z|^n [\cos(n\theta + \psi_n) + i \sin(n\theta + \psi_n)]. \\ A_n L_{eff} &= L_{eff} \operatorname{Re} F_n = L_{eff} |C_n| |z|^n \cos(n\theta + \psi_n). \end{aligned}$$

Therefore, substituting for $\cos(n\theta + \psi_n)$,

$$\left(\int V dt \right)_n = -L_{eff} A_n = -L_{eff} |C_n| |z|^n (\cos \psi_n \cos n\theta - \sin \psi_n \sin n\theta). \quad (8.4)$$

Equating the common coefficients among eqs. (8.2) and (8.4) and evaluating at the wire radius $|z| = r$

$$\begin{aligned} p_n &= -L_{eff} |C_n| r^n \cos \psi_n, \\ \text{and } q_n &= L_{eff} |C_n| r^n \sin \psi_n, \end{aligned}$$

and the phase angle ψ_n is;

$$\begin{aligned} \tan \psi_n &= \frac{\sin \psi_n}{\cos \psi_n} = \frac{\frac{q_n}{L_{eff} |C_n| r^n}}{\frac{p_n}{-L_{eff} |C_n| r^n}}, \\ \text{and } \psi_n &= -\arctan \frac{q_n}{p_n}. \end{aligned} \quad (8.5)$$

We get, finally, an expression for the amplitude of the integrated vector potential coefficients in terms of the Fourier coefficients,

$$L_{eff} |C_n| = \frac{\sqrt{p_n^2 + q_n^2}}{r^n}. \quad (8.6)$$

The Field as a Function of the Complex Variable

Having related the measurement results to the vector potential, it is now necessary to take the measured parameters and develop expressions for the magnetic field components. In an earlier section (see page 46), the components of the magnetic field are computed from $B^* = iF'(z)$. Using the more general expression for the function

of a complex variable described in the previous section and evaluating at the wire radius $|z| = r$;

$$\begin{aligned} B_n^* &= B_{nx} - iB_{ny} = iF'(z) = i \frac{d}{dz} |C_n| e^{i\psi_n} z^n = in |C_n| e^{i\psi_n} z^{n-1}, \\ &= in |C_n| e^{i\psi_n} |z|^{n-1} e^{i(n-1)\theta} = in |C_n| |z|^{n-1} e^{i[(n-1)\theta + \psi_n]}, \\ &= in |C_n| r^{n-1} \{\cos[(n-1)\theta + \psi_n] + i \sin[(n-1)\theta + \psi_n]\}, \\ &= n |C_n| r^{n-1} \{i \cos[(n-1)\theta + \psi_n] - \sin[(n-1)\theta + \psi_n]\}. \end{aligned}$$

Equating the real and imaginary parts of the expression,

$$\begin{aligned} B_{nx} &= n |C_n| r^{n-1} \operatorname{Re} \{i \cos[(n-1)\theta + \psi_n] - \sin[(n-1)\theta + \psi_n]\} \\ &= -n |C_n| r^{n-1} \sin[(n-1)\theta + \psi_n] \end{aligned} \quad (8.7)$$

$$\begin{aligned} B_{ny} &= -n |C_n| r^{n-1} \operatorname{Im} \{i \cos[(n-1)\theta + \psi_n] - \sin[(n-1)\theta + \psi_n]\} \\ &= -n |C_n| r^{n-1} \cos[(n-1)\theta + \psi_n] \end{aligned} \quad (8.8)$$

Substituting eqs. (8.5) and (8.6),

$$\begin{aligned} B_{nx} L_{eff} &= -n L_{eff} |C_n| r^{n-1} \sin[(n-1)\theta + \psi_n], \\ &= -\frac{n \sqrt{p_n^2 + q_n^2}}{r} \sin \left[(n-1)\theta - \arctan \frac{q_n}{p_n} \right]. \end{aligned} \quad (8.9)$$

$$\begin{aligned} B_{ny} L_{eff} &= n L_{eff} |C_n| r^{n-1} \cos[(n-1)\theta + \psi_n], \\ &= -\frac{n \sqrt{p_n^2 + q_n^2}}{r} \cos \left[(n-1)\theta - \arctan \frac{q_n}{p_n} \right]. \end{aligned} \quad (8.10)$$

$$|B_n L_{eff}| = \frac{n \sqrt{p_n^2 + q_n^2}}{r}. \quad (8.11)$$

8.2 Output Voltage

This section develops the expressions for estimating the voltage output from a rotating wire and gives an example, illustrating the signal size from measurements of a typical magnet with typical error multipole spectrum. From eq. (8.2), the expression for the amplitude of the time integrated signal from the rotating coil is $\int V dt = \sum_n (p_n \cos n\theta + q_n \sin n\theta)$. The output voltage is

$$\begin{aligned}
V &= \frac{d}{dt} \sum_n (p_n \cos n\theta + q_n \sin n\theta), \\
&= n \frac{d\theta}{dt} \sum_n (-p_n \sin n\theta + q_n \cos n\theta). \\
|V_n| &= n \frac{d\theta}{dt} \sqrt{p_n^2 + q_n^2} = r \frac{d\theta}{dt} |B_n L_{eff}|.
\end{aligned}$$

Assume that the measured fundamental field amplitude is about 1.0 T and the measured magnet effective length is 0.5 meters. Assume further that the magnet aperture is limited so that the maximum radius of the wire in the coil is 30 mm.=0.030 meters. As described in the introduction, the rotating coil data is taken at a relatively slow rotation rate, say $\frac{d\theta}{dt} = 3\text{Hz} = \frac{2\pi}{3\text{sec}}$.

The measurement output voltage is then;

$$\begin{aligned}
|V_N| &= r \frac{d\theta}{dt} |B_N L_{eff}| = 0.030m \times \frac{2\pi}{3\text{sec}} \times 1 \text{ Tesla} \times 0.5 \text{ meters} \\
&= 0.03142 \frac{Tm^2}{\text{sec}} = 0.03142 \frac{\text{Webers}}{\text{sec } m^2} m^2 = 0.03142 \frac{V \text{ sec}}{\text{sec}} \approx 0.03 V.
\end{aligned}$$

For a well designed and fabricated magnet, the error terms at the pole tip radius are $\leq 10^{-3}$ of the fundamental. Therefore, the voltage amplitude of the error multipole if the field could be measured at the pole tip radius is

$$|V_n| \lesssim 10^{-3} \times 0.03 V = 3 \times 10^{-5} V = 30 \mu V.$$

However, a measurement coil cannot measure the field at the pole tip radius. Most measurement coils are fabricated so that the wire at the outer radius is $< 80\%$ of the pole radius. From eq. (2.32),

$$B^* = B_x - iB_y = iF'(z) = i \frac{\partial}{\partial z} C_n z^n = i n C_n z^{n-1}.$$

Therefore, $|B_n| \propto r^{n-1}$. The first systematic multipole error (see page 50) for the dipole, quadrupole and sextupole are $n = 3, 6$ and 9 , respectively. Therefore, for a measurement coil with wire at 80% of the pole radius, the voltages from the first systematic multipole error are reduced to

$$\begin{aligned}
|V_3| &\lesssim 0.8^{3-1} \times 30 \mu V \approx 20 \mu V \text{ for the dipole error.} \\
|V_6| &\lesssim 0.8^{6-1} \times 30 \mu V \approx 10 \mu V \text{ for the quadrupole error.} \\
|V_9| &\lesssim 0.8^{9-1} \times 30 \mu V \approx 5 \mu V \text{ for the sextupole error.}
\end{aligned}$$

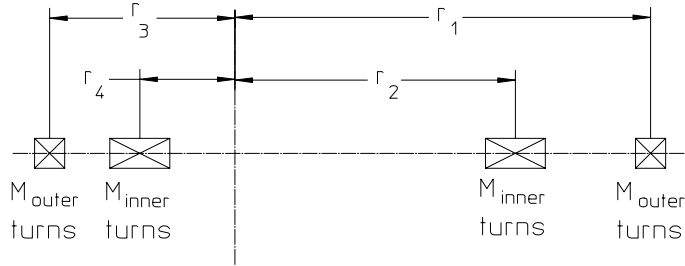


Figure 2 Compensated Coil

Signals this small are difficult to measure and resolve in the presence of electrical noise. Therefore, the typical coil is fabricated from multiple turns of wires, usually ≥ 100 . In addition, for a coil with a single set of windings, these error multipole signals must be resolved in the presence of the fundamental signal, whose amplitude, computed in the example, is approximately $30,000 \mu\text{V}$. Therefore, in addition to multiple wires in the measurement coil, a coil geometry is employed where measurements of the error fields can be made while rejecting the signal from the fundamental field.

8.3 The Compensated Coil

Because of the extremely small electrical signal from the error multipole components of magnets, some means of accurately measuring these quantities was needed. The means used in a compensated coil is to reject the large electrical signal from the fundamental field while measuring the error fields. The compensated coil is a coil consisting of two sets of windings which can be connected to measure the full field or the error multipoles. The full field is measured using the outer windings only in the uncompensated mode. The error multipole measurements are performed with the both windings connected in opposition so that the measurements are the differences in the integrated output signal from the two coils in the compensated mode. In the compensated mode, the coil is designed (in principal) to null the fundamental field allowing the full range of the data acquisition system to resolve the amplitudes of the error fields only. In reality, the coil in the compensated mode does not entirely null the fundamental field because of unavoidable mechanical errors in winding the two sets of coils. The following discussion develops the theory and summarizes the algorithms used to collect and reduce the measurement data.

Consider the compensated coil illustrated in fig. 2 with M_{outer} and M_{inner} turns. The integrated electrical signal from each of the coils are given by the following expression. The expressions include the measurement of the fundamental field.

$$\begin{aligned}
\left(\int V dt \right)_{outer \ coil} &= L_{eff} M_{outer} \sum_n |C_n| (r_1^n - r_3^n) \cos(n\theta + \psi_n) \\
\left(\int V dt \right)_{inner \ coil} &= L_{eff} M_{inner} \sum_n |C_n| (r_2^n - r_4^n) \cos(n\theta + \psi_n) \\
\left(\int V dt \right)_{compensated} &= L_{eff} \sum_n |C_n| [M_{outer} (r_1^n - r_3^n) - M_{inner} (r_2^n - r_4^n)] \cos(n\theta + \psi_n)
\end{aligned}$$

Defining the following parameters,

$$\beta_1 \triangleq \left| \frac{r_3}{r_1} \right|, \quad \beta_2 = \left| \frac{r_4}{r_2} \right|, \quad \rho = \frac{r_2}{r_1}, \quad \mu = \frac{M_{inner}}{M_{outer}}, \quad (8.12)$$

and substituting into the expression for the outer coil only and for both outer and inner coils,

$$\begin{aligned}
\left(\int V dt \right)_{uncomp.} &= L_{eff} M_{outer} \sum_n |C_n| r_1^n [1 - (-\beta_1)^n] \cos(n\theta + \psi_n) \\
\left(\int V dt \right)_{comp.} &= L_{eff} M_{outer} \sum_n |C_n| r_1^n \begin{bmatrix} \{1 - (-\beta_1)^n\} \\ -\mu \rho^n \{1 - (-\beta_2)^n\} \end{bmatrix} \cos(n\theta + \psi_n)
\end{aligned}$$

Defining the following terms,

$$\text{Uncompensated Sensitivity } S_N = 1 - (-\beta_1)^n, \quad (8.13)$$

$$\text{Compensated Sensitivity } s_n = 1 - (-\beta_1)^n - \mu \rho^n (1 - (-\beta_2)^n), \quad (8.14)$$

the expressions for the integrated voltages can be simplified as

$$\left(\int V dt \right)_{uncomp.} = L_{eff} M_{outer} \sum_n |C_n| r_1^n S_N \cos(n\theta + \psi_n) \quad (8.15)$$

$$\text{and } \left(\int V dt \right)_{comp.} = L_{eff} M_{outer} \sum_n |C_n| r_1^n s_n \cos(n\theta + \psi_n) \quad (8.16)$$

8.3.1 The Quadrupole Coil

To null the quadrupole ($n = 2$ fundamental) and dipole ($n = 1$) fields in the compensated coil configuration,

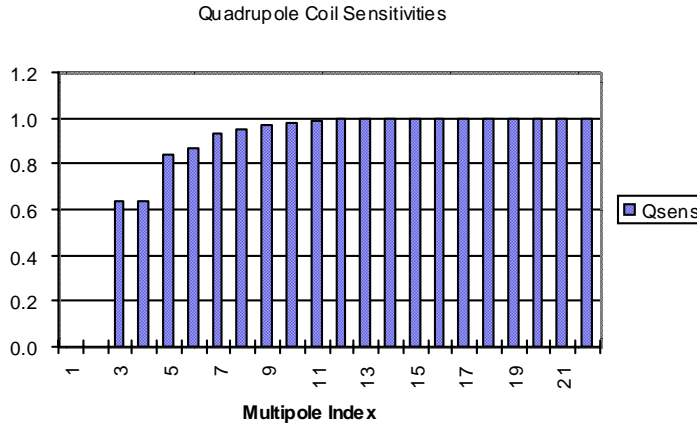


Figure 3 Quadrupole Coil Compensated Sensitivities

$$\begin{aligned} s_2 &= 1 - (-\beta_1)^2 - \mu\rho^2 (1 - (-\beta_2)^2) = 0, \\ s_1 &= 1 - (-\beta_1) - \mu\rho (1 - (-\beta_2)) = 0. \end{aligned}$$

These conditions can be satisfied for a variety of conditions. However, for convenience, the turns ratio, μ , and the ratio of the major radii of the outer and inner coils, ρ , are selected arbitrarily. The set of parameters for which $s_1 = s_2 = 0$ are

$$\beta_1 = 0.5, \quad \beta_2 = 0.2, \quad \rho = 0.625, \quad \mu = 2. \quad (8.17)$$

8.3.2 The Dipole Coil

The same coil used to measure the quadrupole can be used to measure the dipole magnet. In principle, a symmetric dipole magnet should not have even multipoles ($n = 2, 4, 6, 10, \dots$). Therefore, the zero sensitivity for the quadrupole field in the compensated configuration is not important. However, the quadrupole field (if it exists) can be measured with the coil configured in the uncompensated configuration.

8.3.3 The Sextupole Coil

To null the sextupole ($n = 3$ fundamental) and quadrupole ($n = 2$) fields in the compensated coil configuration,

$$\begin{aligned} s_3 &= 1 - (-\beta_1)^3 - \mu\rho^3 (1 - (-\beta_2)^3) = 0, \\ s_2 &= 1 - (-\beta_1)^2 - \mu\rho^2 (1 - (-\beta_2)^2) = 0. \end{aligned}$$

These conditions can be satisfied for a variety of conditions. One of many solutions for which $s_1 = s_2 = 0$ are

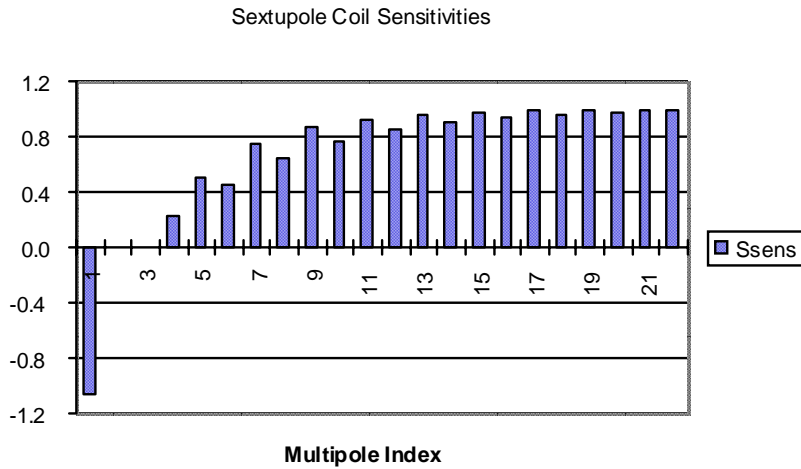


Figure 4 Sextupole Coil Compensated Sensitivities

$$\beta_1 = 0.79139, \quad \beta_2 = 0.83234, \quad \rho = 0.77987, \quad \mu = 2. \quad (8.18)$$

8.4 “Spiltdown” and Magnetic Center

In the previous discussions describing the configurations of the compensated quadrupole and sextupole measurement coils, the coil constants were selected to null both the fundamental field and the error field whose indices are one below the fundamental field. The error field with index $n = N - 1$ reflects the displacement of the magnetic center for the magnet whose index is $N = 2$ for the quadrupole and $N = 1$ for the sextupole. Nulling this “spiltdown” field results in compensated measurements insensitive to misalignment of the measurement coil with respect to the magnetic center of the measured magnet.

In this section, the mathematics that describe the magnetic centers of multipole magnets are developed. “Spiltdown” is a term used to describe the phenomenon observed when rotating coil measurements are performed with a coil whose axis is displaced by a constant amount $\Delta z = \Delta x + i\Delta y$ with respect to the magnetic center of a multipole magnet. (This phenomenon excludes dipole magnets whose field is constant and thus does not have a center.) The pheonomenon is called spiltdown since the off center measurements appear to generate a field whose index is one below the index of the fundamental signal. Although compensated coils are designed to null the apparent fields generated by off axis rotating coils, spiltdown can be measured with the uncompensated coil and is useful to locate the center of a magnet and provide information for magnet alignment.

The largest measurement signal for a magnet are generated by the fundamental field. The function of a complex variable for the fundamental field is given by $F = C_N z^N$. If the measurement coil is misaligned with respect to the magnet center, the equation for the fundamental field becomes

$$F = C_N (z + \Delta z)^N = C_N (z^N + N z^{N-1} \Delta z + N(N-1) z^{N-2} \Delta z^2 + \dots).$$

In this expression, Δz is a small constant displacement and Δz^n with ($n > 1$) is considered a higher order term. Therefore;

$$F \approx C_N (z^N + N z^{N-1} \Delta z). \quad (8.19)$$

The size of this signal can be large if $\frac{\Delta z}{r}$, the displacement normalized to the measurement coil outer radius, is large. Thus, if the coil axis rotating center displacement is 1% of the measurement coil radius, the spilloff signal is ($N \times 1$) % of the fundamental field signal.

Quadrupole Spilloff

For a quadrupole ($N = 2$) the expression for the fundamental field becomes

$$F \approx C_2 (z^2 + 2z\Delta z),$$

and appears to be a function of the complex variable z describing both a quadrupole, $F = C_2 z^2$, and a dipole, $F = (2C_2 \Delta z) z$. (The power of z is the multipole index.)

Sextupole Spilloff

For a sextupole ($N = 3$) the expression for the fundamental field becomes;

$$F \approx C_3 (z^3 + 3z^2 \Delta z)$$

and appears to be a function of the complex variable z describing both a sextupole, $F = C_3 z^3$, and a quadrupole, $F = (3C_3 \Delta z) z^2$.

8.4.1 Quadrupole Magnetic Center

For various reasons associated with errors in mechanical yoke fabrication and assembly, the magnet center may not coincide with the mechanical center of the four poles. The section on page 224 discusses the spilloff effect of a shift in the center of the magnet on the multipole spectrum. The same formulae can be used to develop an

expression which takes the measured data from the rotating coil to compute the displacement of the magnetic center of the quadrupole with respect to the measurement coil rotational axis. If the fabricated measurement coil and the sleeve centering the coil in the magnet gap are precisely fabricated so that the installed measurement coil axis coincides with the magnet mechanical center, the measurement data can be used to compute the displacement of the magnetic center with respect to the magnet mechanical center. The spilldown expression written for the quadrupole is

$$\begin{aligned} F &\approx C_2(z^2 + 2z\Delta z), \\ &\approx C_2[z^2 + 2z(\Delta x + i\Delta y)], \end{aligned}$$

and

$$\begin{aligned} B^* &= B_x - iB_y = iF' = iC_2[2z + 2(\Delta x + i\Delta y)] \\ &= i2C_2z + i2C_2(\Delta x + i\Delta y) \end{aligned}$$

The magnetic field appears to consist of a dipole term and a quadrupole term;

$$\begin{aligned} B_{1x} - iB_{1y} &= i2C_2(\Delta x + i\Delta y) \\ \frac{B_{1x} - iB_{1y}}{2C_2} &= i(\Delta x + i\Delta y) \\ \frac{B_{1x} - iB_{1y}}{2C_2r} &= \frac{i\Delta x - \Delta y}{r}. \end{aligned}$$

Since $2C_2r = |B_2|_{@r}$, the expression can be rewritten as

$$\frac{(B_{1x} - iB_{1y})}{|B_2|_{@r}} = i\frac{\Delta x}{r} - \frac{\Delta y}{r}.$$

Equating the real and imaginary parts of the expression,

$$\frac{\Delta x}{r} = -\frac{B_{1y}}{|B_2|_{@r}} \quad \text{and} \quad \frac{\Delta y}{r} = -\frac{B_{1x}}{|B_2|_{@r}}. \quad (8.20)$$

This relationship is more easily shown in fig. 5.

Since the relationships rely on using the absolute values of the quadrupole fields, the sign conventions are suspect. If the quadrupole polarity is reversed, eq. (8.20) will give the wrong signs for the offsets. Also, whether the measured signals are

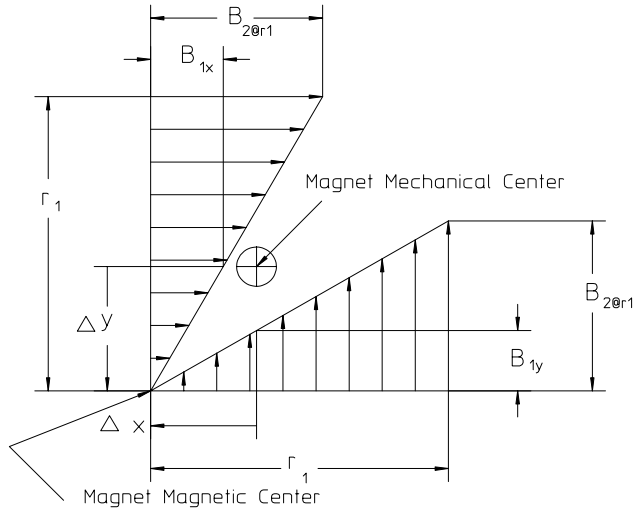


Figure 5 Quadrupole Magnetic Center

positive or negative depends on how the coil is wired into the integrator. The most reliable method of determining the signs is to intentionally offset the measurement coil from the mechanical center in a known direction, observe the polarities of the dipole signals for the required quadrupole polarity and adjust the sign of the algorithm accordingly.

8.4.2 Sextupole Magnetic Center

The same approach can be taken to locate the magnetic center of a sextupole magnet. In the case of the sextupole, the apparent *quadrupole* field characterizes the location of the magnetic center. The spilloff function of the complex variable written for the sextupole is

$$\begin{aligned} F &\approx C_3 (z^3 + 3z^2 \Delta z), \\ &\approx C_3 [z^3 + 3z^2 (\Delta x + i\Delta y)], \end{aligned}$$

and the fields are given by

$$\begin{aligned} B^* &= B_x - iB_y = iF' = iC_3 [3z^2 + 6z(\Delta x + i\Delta y)], \\ &= i3C_3 z^2 + i6C_3 z(\Delta x + i\Delta y) \end{aligned}$$

The magnetic field appears to consist of a dipole term and a quadrupole term

$$\begin{aligned} B_{2x} - iB_{2y} &= i6C_3z(\Delta x + i\Delta y) \\ \frac{B_{2x} - iB_{2y}}{6C_3z} &= i(\Delta x + i\Delta y). \end{aligned}$$

Evaluating at $|z| = r$ and dividing both sides of the equation by r

$$\frac{B_{2x} - iB_{2y}}{6C_3r^2} = \frac{i\Delta x - \Delta y}{r}.$$

Since $3C_3r^2 = |B_3|_{@r}$ for real values of C_3 , the expression can be rewritten as

$$\frac{(B_{2x} - iB_{2y})}{2|B_3|_{@r}} = i\frac{\Delta x}{r} - \frac{\Delta y}{r}.$$

Equating the real and imaginary parts of the expression,

$$\frac{\Delta x}{r_1} = -\frac{B_{2y}}{2|B_3|_{@r_1}} \quad \text{and} \quad \frac{\Delta y}{r_1} = -\frac{B_{2x}}{2|B_3|_{@r_1}}. \quad (8.21)$$

Again, as in the case of the quadrupole, the signs in eq. (8.21) are suspect and it is highly recommended to perform an experiment intentionally offsetting the measurement coil in a preliminary measurement to establish the proper sign convention for a magnet with the required polarity.

8.5 Rotating Coil Magnetic Measurements

The previous section developed the mathematics required to understand the measurement system using fundamental relationships. The difficulties in measuring the harmonic field errors in high quality magnets were demonstrated and a means of designing rotating coils with high sensitivities to small harmonic errors was suggested.

This section on measurements describes a data acquisition system which integrates the compensated rotating coil and its various components. The algorithms for computing the absolute amplitudes of the integrated fundamental fields and the relative amplitudes and phases of the integrated error multipole fields are developed. Finally, an example of a data presentation format useful for evaluating the magnet field quality is suggested.

8.5.1 The Measurement System

Fig. 6 is a schematic of a rotating coil magnetic measurement system.

The major components of this system are;

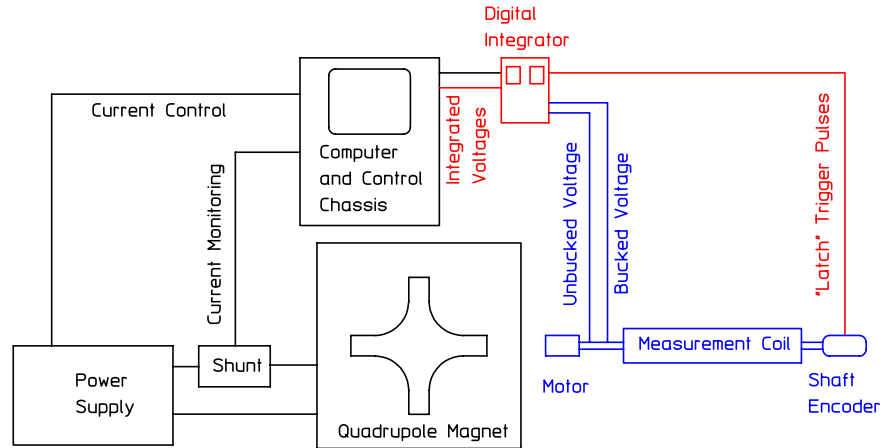


Figure 6 Rotating Coil Measurement System

- Computer/Control Chassis. The schematic shows one item. However, this component consists of many elements.
 - Computer with Control/Data Acquisition Software installed.
 - D/A Chassis required to control the power supply.
 - A/D Chassis to monitor current from a current transducer, labeled in the illustration as a Shunt.
 - Input/Output Channel for the Digital Integrator.
 - * Integrator Converts Electrical Voltage from the Measurement Coil to digital format and performs an integration with respect to time.
 - Input Channel for Shaft Encoder.
 - D/A Chassis to control the Motor.
- Digital Integrator
 - The Digital Integrator consists of two items. A voltage to frequency converter and an up-down counter. The v-to-f converter generates a signal whose frequency increases linearly with the input voltage (see fig. 7). The up-down counter counts the pulses. The sum of the counted pulses is proportional to the integrated voltage.
- Shaft Encoder

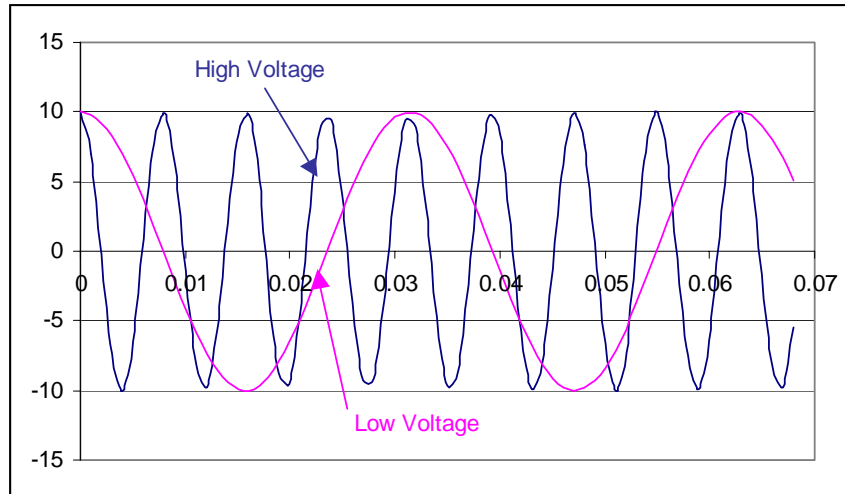


Figure 7 Voltage to Frequency Converter Output

- The Shaft Encoder is a digital device which puts out pulses as a function of angle. At given angle increments, the computer latches an output signal from the digital integrator.
 - Motor
 - On a signal from the computer, the motor starts and ends the coil rotation. Usually, three rotations are specified. The measurement is made during the second rotation. The first and last rotations ensure that the rotation is accelerated and decelerated uniformly so that the measurements are made while the coil is rotated at a uniform rate. Although, in principle, the integrated signal is independent of the rotation rate, a uniform rotation is desirable to eliminate the effect of a constant voltage noise source (described in the section on the Measurement Coil).
 - The Measurement Coil
 - The measurement coil described earlier in the chapter consists of two sets of coils, usually with many soldered joints. These joints are the junctions of dissimilar metals and thus constitute thermocouple leads and can generate small constant voltages. Because of this noise source, it is important to rotate the coil at a constant angular velocity. The constant rotation rate provides means of compensating for the effect of the thermocouple voltage prior to processing the data. Fig. 8 is an example of the typical measurement output. The graph illustrates the output from a quadrupole measurement. The integrator is zeroed before the start of measurement

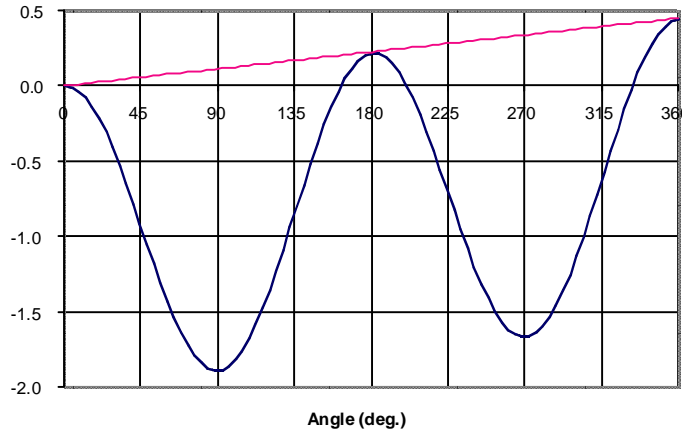


Figure 8 Voltage Output with Drift

and the graph displays the result of a linear drift due to DC voltage generated in the coil while measuring the integrated vector potential from a quadrupole magnet. This linear drift must be subtracted from each point prior to the data reduction process. If the angle is measured in degrees, the expression for the correction is, $V_{corrected} = V - \frac{Angle(^{\circ})}{360}V_{360}$. The corrected data are used in the Fourier analysis described in the next section.

8.6 Fourier Analysis

As in the case of the measurement using a coil with a single wire, the data collected with a coil can be Fourier analyzed and the output can be written as a sum of Fourier terms;

$$\int V dt = \sum (p_n \cos n\theta + q_n \sin n\theta)$$

Suppose the data are collected and Fourier analyzed for the measurement coil in two configurations and the coefficients for the two configurations are described by CAPITAL and lower case letters to differentiate among uncompensated and compensated measurements, respectively.

$$\begin{aligned} \left(\int V dt \right)_{uncompensated} &= \sum (P_n \cos N\theta + Q_n \sin N\theta) \\ \left(\int V dt \right)_{compensated} &= \sum (p_n \cos n\theta + q_n \sin n\theta) \end{aligned}$$

8.6.1 Uncompensated Signal

From eq. (8.15), the expression for the uncompensated integrated field is

$$\begin{aligned} \left(\int V dt \right)_{N \text{ uncomp.}} &= L_{eff} M_{outer} (|C_N| r_1^N S_N \cos(N\theta + \psi_N)), \\ &= L_{eff} M_{outer} \left(|C_N| r_1^N S_N \begin{bmatrix} \cos N\theta \cos \psi_N \\ -\sin N\theta \sin \psi_N \end{bmatrix} \right). \end{aligned}$$

Equating common terms for both the fundamental and spillover measurements;

$$P_{N-1} = L_{eff} M_{outer} |C_{N-1}| r_1^{N-1} S_{N-1} \cos \psi_{N-1}. \quad (8.22)$$

$$Q_{N-1} = -L_{eff} M_{outer} |C_{N-1}| r_1^{N-1} S_{N-1} \sin \psi_{N-1}. \quad (8.22)$$

$$\sqrt{P_{N-1}^2 + Q_{N-1}^2} = L_{eff} M_{outer} |C_{N-1}| r_1^{N-1} S_{N-1}. \quad (8.23)$$

$$P_N = L_{eff} M_{outer} |C_N| r_1^N S_N \cos \psi_N.$$

$$Q_N = -L_{eff} M_{outer} |C_N| r_1^N S_N \sin \psi_N.$$

$$\sqrt{P_N^2 + Q_N^2} = L_{eff} M_{outer} |C_N| r_1^N S_N, \quad (8.24)$$

$$\text{or } L_{eff} |C_N| = \frac{\sqrt{P_N^2 + Q_N^2}}{M_{outer} r_1^N S_N}. \quad (8.25)$$

Solving for the phase angles;

$$\tan \psi_{N-1} = \frac{\sin \psi_{N-1}}{\cos \psi_{N-1}} = -\frac{Q_{N-1}}{P_{N-1}} \implies \psi_{N-1} = -\arctan \frac{Q_{N-1}}{P_{N-1}}$$

$$\tan \psi_N = \frac{\sin \psi_N}{\cos \psi_N} = -\frac{Q_N}{P_N} \implies \psi_N = -\tan^{-1} \frac{Q_N}{P_N}$$

8.6.2 Compensated Signal

From eq. (8.16), the expression for the compensated integrated field is

$$\left(\int V dt \right)_{comp.} = L_{eff} M_{outer} \sum_n |C_n| r_1^n s_n \cos(n\theta + \psi_n)$$

All the signals except from the fundamental and the first spillover field are of interest since these signals have zero sensitivity in the compensated mode.

$$\begin{aligned} \left(\int V dt \right)_{uncomp.} &= L_{eff} M_{outer} \sum_{n \neq N-1 \text{ and } n \neq N} |C_n| r_1^n s_n \cos(n\theta + \psi_n) \\ &= L_{eff} M_{outer} \left(\sum_{n \neq N-1 \text{ and } n \neq N} |C_n| r_1^n s_n \begin{bmatrix} \cos n\theta \cos \psi_n \\ -\sin n\theta \sin \psi_n \end{bmatrix} \right) \end{aligned}$$

Rewriting the Fourier expressions for the measured signal from the uncompensated coil,

$$\left(\int V dt \right)_{comp.} = \sum_{n \neq N-1 \text{ and } n \neq N} p_n \cos n\theta + q_n \sin n\theta.$$

Equating common terms,

$$\begin{aligned} p_n &= L_{eff} M_{outer} |C_n| r_1^n s_n \cos \psi_n \\ q_n &= -L_{eff} M_{outer} |C_n| r_1^n s_n \sin \psi_n \end{aligned} \quad (8.26)$$

$$\sqrt{p_n^2 + q_n^2} = L_{eff} M_{outer} |C_n| r_1^n s_n \quad (8.26)$$

$$L_{eff} |C_n| = \frac{\sqrt{p_n^2 + q_n^2}}{M_{outer} r_1^n s_n} \quad (8.27)$$

Solving for the phase angles,

$$\tan \psi_n = \frac{\sin \psi_n}{\cos \psi_n} = -\frac{q_n}{p_n} \implies \psi_n = -\arctan \frac{q_n}{p_n}. \quad (8.28)$$

8.6.3 Expressions for the Integrated Multipole Fields

Using the expression for the complex conjugate of the magnetic field, $B_n^* = i n C_n z^{n-1}$, and recalling that C_n is generally a complex constant, expressions for the x and y components of field can be derived.

$$\begin{aligned} B_n^* &= B_{nx} - i B_{ny} = i n C_n z^{n-1} = i n |C_n| e^{i\psi_n} |z|^{n-1} e^{in\theta}, \\ &= i n |C_n| e^{i\psi_n} |z|^{n-1} e^{in\theta} = i n |C_n| |z|^{n-1} e^{i(n\theta + \psi_n)}, \\ &= i n |C_n| |z|^{n-1} [\cos(n\theta + \psi_n) + i \sin(n\theta + \psi_n)], \\ B_{nx} - i B_{ny} &= n |C_n| |z|^{n-1} [i \cos(n\theta + \psi_n) - \sin(n\theta + \psi_n)]. \end{aligned}$$

Therefore, evaluating at $|z| = r_1$,

$$\begin{pmatrix} B_{nx} \\ B_{ny} \end{pmatrix} L_{eff} = -L_{eff} n |C_n| r_1^{n-1} \begin{pmatrix} \sin(n\theta + \psi_n) \\ \cos(n\theta + \psi_n) \end{pmatrix}.$$

The amplitudes of the multipole fields evaluated at the radius of the measurement coil outer radius, r_1 are

$$|B_n| L_{eff} = L_{eff} \sqrt{B_{nx}^2 + B_{ny}^2} = L_{eff} n |C_n| r_1^{n-1}.$$

The amplitude of the fundamental field is

$$|B_N| L_{eff} = \sqrt{B_{Nx}^2 + B_{Ny}^2} = L_{eff} N |C_N| r_1^{N-1}.$$

Substituting for $L_{eff} |C_n| r_1^{n-1}$ and $L_{eff} |C_N| r_1^{N-1}$ from eqs. (8.27) and (8.25), we get, finally, expressions for the amplitudes of the integrated fields at the coil radius r_1 .

$$|B_n| L_{eff} = \frac{n \sqrt{p_n^2 + q_n^2}}{r_1 s_n M_{outer}}. \quad (8.29)$$

$$|B_N| L_{eff} = \frac{N \sqrt{P_N^2 + Q_N^2}}{r_1 S_N M_{outer}}. \quad (8.30)$$

Again, as in the discussion of the algorithms for the coil in the compensated configuration, the phase for the fundamental signal is given by

$$\Psi_n = -\arctan \frac{Q_n}{P_n}. \quad (8.31)$$

The expressions for the phases of the fields given by eq. (8.28) and eq. (8.31) are absolute angles with respect to the angle of the plane of the coil with respect to the magnet magnetic horizontal plane at the time the shaft encoder is zeroed.

8.6.4 Excitation and Transfer Function

The inevitable mechanical fabrication errors result in uncertainty of the radius of the center of the outer bundle of wires, r_1 , for the measurement coil. Thus, it is necessary calibrate the coil to obtain measurement values with sufficient precision for use for control of the magnet power supplies. A calibration method employed at SLAC for the determination of the excitation and transfer functions for quadrupoles and sextupoles was to compare the values computed from the rotating coil measurements $B' L_{eff}$ and $B'' L_{eff}$ for a quadrupole and sextupole to the results measured using a wire traversed across the center plane of the magnets. Another method is to rotate the coils in a dipole magnet whose fields have been carefully measured using a Hall probe scan and compare the rotating coil integrated dipole field with the results of the Hall probe scan.

Quadrupole Excitation and Transfer Function

Assuming that the rotating coils have been calibrated, for a quadrupole, the magnet excitation and transfer function is expressed in terms of the gradient.

$$|B_2| = B'r_1 \quad (8.32)$$

$$\text{Excitation} = B'L_{eff} = \frac{|B_2| L_{eff}}{r_1} = \frac{2\sqrt{P_2^2 + Q_2^2}}{r_1^2 S_2 M_{outer}}. \quad (8.33)$$

$$\text{Transfer Function} = \frac{B'L_{eff}}{I} = \frac{2\sqrt{P_2^2 + Q_2^2}}{Ir_1^2 S_2 M_{outer}} \left(\text{units} = \frac{T}{Amp} \right). \quad (8.34)$$

Sextupole Excitation and Transfer Function

Assuming that the rotating coils have been calibrated, for a sextupole, the magnet excitation and transfer function is expressed in terms of the sextupole gradient.

$$|B_3| = \frac{B''r_1^2}{2} \quad (8.35)$$

$$\text{Excitation} = B''L_{eff} = \frac{2|B_N| L_{eff}}{r_1^2} = \frac{6\sqrt{P_3^2 + Q_3^2}}{r_1^3 S_3 M_{outer}}. \quad (8.36)$$

$$\text{Transfer Function} = \frac{B''L_{eff}}{I} = \frac{6\sqrt{P_3^2 + Q_3^2}}{Ir_1^3 S_3 M_{outer}} \left(\text{units} = \frac{T}{m Amp} \right). \quad (8.37)$$

8.6.5 Relative Phases

Normally, the measurement coil is rotated counterclockwise with the motor at the near end and the horizontal plane of the measurement coil starting from the 3 o'clock position (the zero angle for the Cartesian coordinate system). Because of difficulties in precisely aligning the horizontal plane of the coil, the beginning angle may be rotated slightly with respect to the horizontal datum plane of the measured magnet. Therefore, the fundamental field phase angle will have a small finite value. In order to properly evaluate the phases of the error multipoles, it is necessary to recompute the phases of the error multipoles with respect to the zero phase of the fundamental field. For magnets with mirror symmetry about the centers of their poles, the allowed or systematic multipole errors will be real and their phases, $\psi_n \text{ allowed} \approx 0$ or π . The error spectra of magnets are normally dominated by the allowed multipole errors. For carefully fabricated and assembled magnets, $\left| \frac{B_n}{B_N} \right|_{\text{systematic}} \geq 5 \times \left| \frac{B_n}{B_N} \right|_{\text{random}}$. The error multipoles which are not systematic will be complex and their phase angles relative to the zero phase of the fundamental will generally $\neq 0$ or π . Since mechanical fabrication and assembly errors contribute the full spectrum of multipole indices, a phase error will also contribute to the allowed multipole spectrum and the phases for the allowed multipoles will differ by a small amount from $\psi_{n-\text{allowed}} = 0$ or π .

In order to fully understand the measurements, it is necessary to correct the absolute phase angles of the error multipoles by subtracting the absolute phase angle of the fundamental field. In order to do this properly, it is necessary to understand that the angle for the vector potential function is multiplied by the index number. Thus, $A_n L_{eff} \propto \cos(n\theta + \psi_n)$. Therefore, if the phase angle for the fundamental is subtracted from the angle, then $N\theta = -\psi_N$ or $\theta = -\frac{\psi_N}{N}$ must be added to the phase angle of the fundamental and each multipole error. Therefore, $n\theta = -\frac{n\psi_N}{N}$ must be added to the absolute phase of each multipole term to obtain the relative phase of each multipole error. The expression for the relative phase of each multipole error is given by

$$\Psi_n = \psi_n - \frac{n\psi_N}{N}. \quad (8.38)$$

From this expression, it can be seen that a relatively small coil alignment error will result in a relatively large error in the relative phase.

8.6.6 Units

The units for $|B_n| L_{eff} = T - m = \frac{Webers}{m^2}m = \frac{V\text{-sec}}{m}$. Therefore, since the units for $\frac{\sqrt{a_n^2+b_n^2}}{|r_1|} = \frac{V\text{-sec}}{m}$ and all the other terms in the expressions are unitless. The expressions give the integrated field amplitudes directly.

8.7 Measurements and Output

8.7.1 Measurement Plan

A measurement plan must be written for the individual magnets. Information required prior to developing a measurement plan is the maximum excitation and the range of excitations for particular families of magnets and their individual polarities. The maximum measurement current should be $I_{m \text{ max}} \geq 105\%$ of the maximum operating current, I_{max} . Normally, the precision required for the excitation of magnets is $< 0.1\%$ of the true value. Measurement variations for individual magnets exceeding this tolerance can result from saturation of the magnet steel and remnant field effects, resulting in magnet excitation on different legs of the steel B-H curve. Therefore, the measurement plan usually calls for a conditioning cycle prior to the actual measurement. The conditioning cycle requires at least three cycles from zero to $\geq 110\%$ of $I_{m \text{ max}}$ and back to zero at rates where the current ramps are ≥ 30 sec. This rate is sufficiently slow for magnets whose cores are assembled from thin ($\lesssim 2$ or 3 mm) laminations to avoid effects due to eddy currents, but should be decreased for solid core magnets or magnets assembled from laminations $\gtrsim 10$ mm. The conditioning and the subsequent measurements must be performed for the power supplies connected with the required polarity for the individual magnets in operation. Reversing the polarity will result in measured excitation curves on an entirely different leg of the magnet steel B-H curve than the anticipated operating point. This conditioning

cycle fixes (in theory) the operating point on the upper leg of the magnet steel B-H curve for all subsequent operations, resulting in reproducible excitation during the magnet lifetime. If the magnet operation exceeds the conditioning current or is operated (accidentally or intentionally) with the opposite polarity, the magnet should be reconditioned prior to operation.

The measurement plan includes computed currents at which measurements are taken. These currents, ($I \leq I_{m\ max}$), include values with the power supply increasing and decreasing so that measurements are obtained on both legs of the Hysteresis curve. Normally, if there are three or four operating currents for a magnet family, at least double the number of current values should be selected to obtain a smooth curve through these points.

8.7.2 Raw Data Output

Since it is difficult to repeat the experimental setup after a measurement is completed, information regarding the validity of the measurement is desired immediately. Measurements are valid if the amplitude of the drift is not excessive and the range of the measurements has not exceeded the maximum range of the voltmeter resulting in saturating the instrument. Graphs like fig. 8 for both the uncompensated and compensated coil measurements are desirable in real time to determine whether it is necessary to repeat the measurements before removing a magnet from the test stand. A graph will immediately reveal whether or not the integrator range was exceeded or whether or not the measurement suffered from excessive DC voltage noise.

- Integrator range saturation is characterized by a flattening of the curve at the extreme values.
 - The Fourier analysis of data where the curve is flattened due to saturating the range of the voltage integrator will produce large errors in the multipole amplitudes and their phases.
- Excessive DC voltage noise is indicated by a large drift, where the linear portion of the curve exceeds the sinusoidal amplitude by a large factor.
 - Since a large drift increases the range of the measurements, the sinusoidal portion of the collected data is reduced as a percentage of the full range and the precision of the computed Fourier coefficients will be reduced.

8.7.3 Bucking Ratio

The raw data output (described in the previous section) from the coil in the compensated configuration looks remarkably similar to the uncompensated measurement. This is because the compensation is not perfect and a large fraction of the signal from the fundamental field remains when the coil is in the compensated configuration. In general, a well made coil will have sufficient mechanical errors in the fabrication of

the coil substrate and in winding so that the signal from the inner coil will differ from the signal from the outer coil by $\approx 1\%$. Since the signal from the error multipoles for a well designed and well assembled magnet are $\leq 10^{-4}$ of the fundamental signal, the error multipole integrated voltage amplitude will still be about $\approx 1\%$ of the fundamental compensated coil signal. One way to evaluate the level of compensation is to compute a Bucking Ratio and present it as part of the reduced data output. The expression for the bucking ratio is;

$$R_{Bucking} = \frac{\sqrt{P_N^2 + Q_N^2}}{\sqrt{p_N^2 + q_N^2}}, \quad (8.39)$$

where (p_N, q_N) and (P_N, Q_N) are the Fourier coefficients of the fundamental signal from the uncompensated and compensated coils, respectively. An acceptable value is $R_{Bucking} \geq 100$. Lower values indicate that the signals from the higher order multipoles may be dominated by electrical noise. One can improve the bucking ratio for a coil by adding a voltage divider which can shunt some of the signal from either the outer or inner coil before combining their signals.

8.7.4 Normalized Multipole Errors

Using eqs. (8.29) and (8.30), one can write an expression for the multipole errors amplitudes normalized to the fundamental amplitude at radius r_1 ,

$$\frac{|B_n|_{r_1} L_{eff}}{|B_N|_{r_1} L_{eff}} = \frac{n S_N \sqrt{p_n^2 + q_n^2}}{N s_n \sqrt{P_N^2 + Q_N^2}}. \quad (8.40)$$

However, physics specifications normally require the evaluation of the spectrum of error multipoles at some arbitrary radius (usually the radius of the expected 10σ beam), different from the outer radius of the measurement coil. This can be the radius of the required good field region or the pole radius. In most cases, the radius of the good field region is larger than the measurement coil radius and, in all cases, the pole radius is larger than the measurement coil radius.

Fig. 9 illustrates the cross-section of a quadrupole measurement coil installed in the 35 mm. gap of a SPEAR3 quadrupole. The coil is wound on a epoxy fiber-glass mandrel and is mounted with its rotating axis precisely centered in a precision machined aluminum tube. This machined tube is necessarily smaller than the magnet aperture since any small magnet assembly error will prevent installation of a coil housed in a tube with the magnet aperture radius in the gap. In order to center the coil in the aperture, a pair of accurately machined half sleeve cylinders is placed around the machined tube in contact with the two upper poles. For an accurately assembled magnet, this four point support is nearly kinematic and repeatable. The coil is attached to the upper poles rather than the lower poles since the upper poles

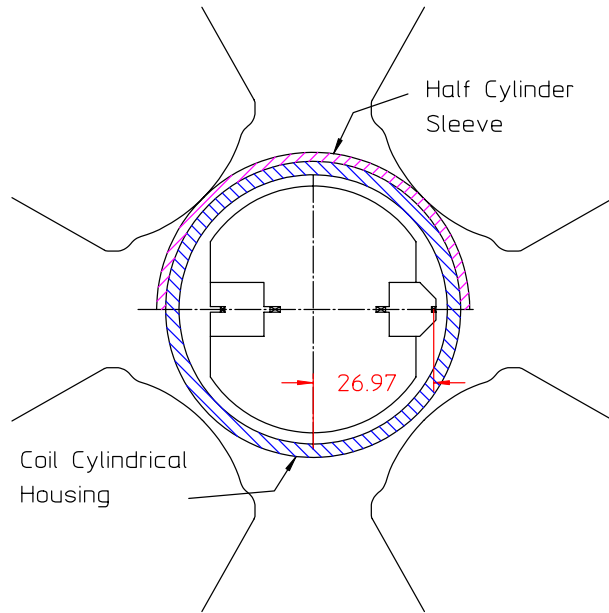


Figure 9 Quadrupole Measurement Coil

of the magnet are part of the upper yoke on which are mounted alignment targets. All the alignment coordinates are associated with the upper half of the magnet. This is important since one of the measurements made with the coil is the location of the axis of the magnet relative to the rotating axis of the measurement coil.

8.7.5 Error Spectrum Normalized to the Required Good Field Radius

In the case of the specific measurements illustrated in fig. 9, the coil radius is <27 mm., substantially less than the required 32 mm. good field radius specified by the Physics of the machine. Therefore, one needs to renormalize the error multipole for evaluation at the required radius. Eq.(8.41) is used for the expression of the field errors normalized to the fundamental at the required good field radius.

$$\begin{aligned}
 \left| \frac{B_n^*}{B_N^*} \right|_{gfr} L_{eff} &= \left| \frac{B_n^*}{B_N^*} \right|_{r_1} L_{eff} \left(\frac{r_{gfr}}{r_1} \right)^{n-N}, \\
 &= \frac{n S_N \sqrt{p_n^2 + q_n^2}}{N s_n \sqrt{P_N^2 + Q_N^2}} \left(\frac{r_{gfr}}{r_1} \right)^{n-N}.
 \end{aligned} \tag{8.41}$$

8.7.6 Magnetic Center

Eqs. (8.20) and (8.21) gives the expressions for the x and y magnetic center offset in terms of the magnetic fields. In order to use these expressions in the data reduction,

the expressions must be written in terms of the Fourier coefficients from the measured data. Since the coil sensitivity for the quadrupole and dipole fields are almost zero for the coil in the compensated configuration, the Fourier coefficients from the measured data collected with the coil in the uncompensated configuration are used. The general expressions for the magnetic center offsets for a coil with outer radius r_1 are given by

$$\frac{\Delta x}{r_1} = -\frac{B_{(N-1)y}}{(N-1)|B_N|_{@r_1}} = \frac{L_{eff}|B_{N-1}|\cos\psi_N}{L_{eff}(N-1)|B_N|_{@r_1}}.$$

Substituting the expressions written in terms of the Fourier coefficients,

$$\begin{aligned}\frac{\Delta x}{r_1} &= \frac{\frac{(N-1)\sqrt{P_{N-1}^2 + Q_{N-1}^2}}{r_1 S_{N-1} M_{outer}}}{\frac{(N-1)N\sqrt{P_N^2 + Q_N^2}}{r_1 S_N M_{outer}}} \times \frac{P_{N-1}}{\sqrt{P_{N-1}^2 + Q_{N-1}^2}}, \\ &= \frac{S_N P_{N-1}}{S_{N-1} N \sqrt{P_N^2 + Q_N^2}}.\end{aligned}$$

Similarly, $\frac{\Delta y}{r_1} = \frac{S_N Q_{N-1}}{S_{N-1} N \sqrt{P_N^2 + Q_N^2}}$.

Therefore, for the quadrupole;

$$\frac{\Delta x}{r_1} = \frac{S_2 P_1}{2S_1 \sqrt{P_2^2 + Q_2^2}} \quad \text{and} \quad \frac{\Delta y}{r_1} = \frac{S_2 Q_1}{2S_1 \sqrt{P_2^2 + Q_2^2}}, \quad (8.42)$$

and for the sextupole;

$$\frac{\Delta y}{r_1} = \frac{S_3 P_2}{3S_2 \sqrt{P_3^2 + Q_3^2}} \quad \text{and} \quad \frac{\Delta y}{r_1} = \frac{S_3 Q_2}{3S_2 \sqrt{P_3^2 + Q_3^2}}. \quad (8.43)$$

8.8 Measurement Output

The tabular example of the reduced data is a useful format for summarizing the results of rotating coil magnetic measurements for a quadrupole. A similar table can be devised summarizing the results of rotating coil sextupole measurements.

8.8.1 Tabular Output

Magnet Type		Serial No.		Polarity	
File Name		Meas. Current	(Amps)		
Coil Radius	(mm)	Norm. Radius	(mm)		
V/f Gain		Temperature			(°C)
N	$P_n \times 10^{-6}$	$Q_n \times 10^{-6}$	$\sqrt{P_n^2 + Q_n^2} \times 10^{-6}$	ψ_n	
	$V \text{ sec}$	$V \text{ sec}$	$V \text{ sec}$		
1	eq.(8.28)	
2	"	
n	p_n	q_n	$\sqrt{p_n^2 + q_n^2}$	ψ_n	$\left \frac{B_n^*}{B_N^*} \right _{gfr} L_{eff} \Psi_n$
2	eq.(8.28)	eq.(8.41)
3	"	"
4	"	"
5	"	"
6	"	"
7	"	"
8	"	"
9	"	"
10	"	"
11	"	"
12	"	"
13	"	"
14	"	"
...	"	"
n_{\max}	"	"
Magnet Excitation (T):		eq. (8.32)	Transfer Function $\left(\frac{T}{Amp} \right)$:	eq. (8.34)	
Bucking Ratio		eq. (8.39)			
Drift		page 230			
Δx (mm)		eq. (8.42)			
Δy (mm)		eq. (8.42)			
Date:		Time:		Operator:	

8.9 Analog Output (Iso-Error Plots)

Tabulated measurement data are often difficult to digest. The relative amplitudes of the normalized multipoles and their phases are a collection of numbers whose impact on the performance of the accelerator lattice requires complex and time consuming modelling. When faced with evaluation of the quality of the production quantity of many magnets, many sheets of tabulated results are difficult to digest and compare.

An analog means of presenting and comparing the measurement data can be useful. The multipole data are constructed into a field error map.

The algorithms used in MatLab[®] to construct an iso-error map are

$$\begin{aligned}\Delta B_n &= (\overline{\Delta B}_n)_{r_0} \left(\frac{z}{r_0} \right)^{n-1} \\ \Delta B_{nx} &= |\Delta B_n|_{r_0} \left| \frac{z}{r_0} \right|^{n-1} \cos((n-1)\theta + \Psi_n) \\ \Delta B_{ny} &= |\Delta B_n|_{r_0} \left| \frac{z}{r_0} \right|^{n-1} \sin((n-1)\theta + \Psi_n) \\ |B_2| &= |B_2|_{r_0} \left| \frac{z}{r_0} \right|.\end{aligned}$$

Therefore,

$$\begin{aligned}\frac{\Delta B_{nx}}{|B_2|} &= \left| \frac{\Delta B_n}{B_2} \right|_{r_0} \left| \frac{z}{r_0} \right|^{n-2} \cos((n-1)\theta + \Psi_n), \\ \frac{\Delta B_{ny}}{|B_2|} &= \left| \frac{\Delta B_n}{B_2} \right|_{r_0} \left| \frac{z}{r_0} \right|^{n-2} \sin((n-1)\theta + \Psi_n),\end{aligned}$$

and

$$\begin{aligned}\frac{\Delta B_x}{|B_2|} &= \sum_{n=3}^{n_{\max}} \left| \frac{\Delta B_n}{B_2} \right|_{r_0} \left| \frac{z}{r_0} \right|^{n-2} \cos((n-1)\theta + \Psi_n) = \sum_x \\ \frac{\Delta B_y}{|B_2|} &= \sum_{n=3}^{n_{\max}} \left| \frac{\Delta B_n}{B_2} \right|_{r_0} \left| \frac{z}{r_0} \right|^{n-2} \sin((n-1)\theta + \Psi_n) = \sum_y,\end{aligned}$$

where $\left| \frac{z}{r_0} \right| = \frac{\sqrt{x^2 + y^2}}{r_0}$ and Ψ_n is the phase of the multipole error relative to the fundamental field phase.

Finally, a contour map is computed using the function

$$\left| \frac{\Delta B}{B_2} \right| = \sqrt{\sum_x^2 + \sum_y^2}$$

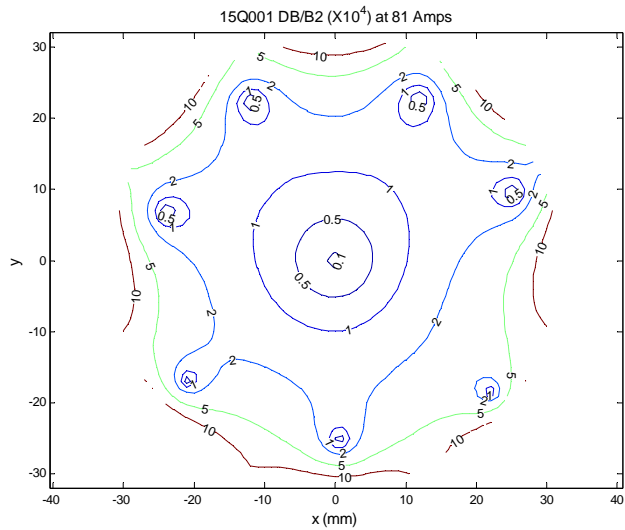


Figure 10 Iso-Error Field Distribution for a Measured Quadrupole

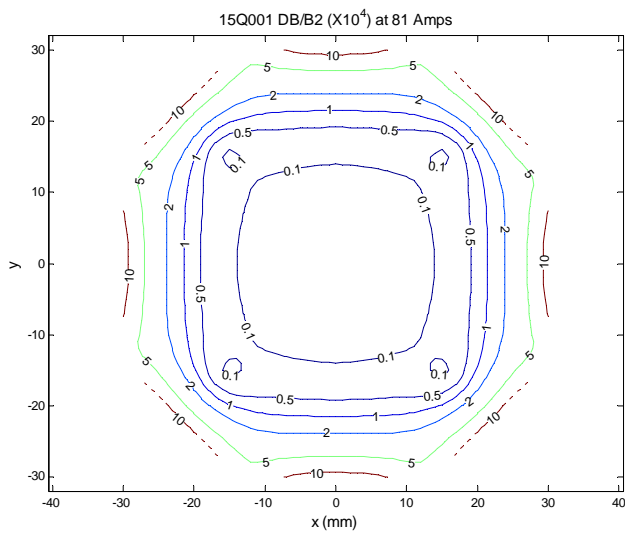


Figure 11 Iso-Error Curve for the SAME Quadrupole with Unallowed Multipole Errors Removed

The iso-error curves illustrated in figs. 10 and 11 are for the same measurements. The second curve is reconstructed using only the systematic multipole errors, $n = 1, 10, 14$ and 18 . From these figures, it can be seen that, although the amplitudes of the random error multipoles are substantially smaller than the amplitudes of the systematic error multipoles, the random error multipoles dominate the field quality. This points out the need to adhere to tight mechanical fabrication and assembly tolerances.

8.10 Chapter Closure

It is difficult and costly to develop and maintain a complete magnetic measurement infrastructure, especially since projects requiring many magnets occur at sporadic intervals. A measurement system may include means of three dimensional or two dimensional mapping of magnets using Nuclear Magnetic Resonance (NMR) techniques or Hall probes. In addition to the costs of the magnetic probes, the data acquisition electronics and computer hardware, mapping over a volume or an area require expensive precise mechanical stages with sufficient range to traverse the required volume/area. Another element in a magnetic measurement infrastructure may be a means of traversing a wire over a span through the magnetic field. Again, this requires the investment in at least two precision mechanical stages to move the ends of the wires. These two techniques represent measuring at a point (the probe) and the field integral over a two dimensional length (the wire). Both these techniques are tedious and time consuming when enough data is required to fully characterize the shape and the distribution of error fields within the volume or area eventually occupied by the charged particle beam. In addition to the measurement time, the magnets and probes must be precisely aligned so that the field distribution can be related to points or lines within the magnet aperture.

Another means of characterizing a magnet is to measure the field integral within a three dimensional volume. This is a more efficient way of characterizing the field distribution, requiring a simpler measurement system. The most challenging components of this system requires the design and fabrication of a rotating coil. This chapter is written to summarize the rotating coil measurements of magnets, which can characterize the integrated transverse fields of a magnet within a cylindrical volume. The chapter starts by laying the theoretical groundwork, relating the time-integrated voltage to the space integrated magnetic vector potential. A coil configuration is described which enhances measurement of the small field errors by means of rejecting the large signal from the fundamental field. A mechanical coil support cylinder is described which minimizes the time required to align the coil with respect to the datum coordinate system of multipole magnets (quadrupoles and sextupoles). The topology of a measurement system is suggested. The algorithms used to reduce the raw electronic data to parameters useful for the evaluation of magnet performance and quality are developed. Finally, a data summary format is suggested.

8.11 Problems

A rotating coil magnetic measurement system can be costly and difficult to assemble. In order to test ones understanding of the measurements and the algorithms used to characterize the properties of the tested magnet, one needs to actually design and assemble a rotating coil and a magnetic measurement system and operate it on a specimen magnet. Most students will seldom get an opportunity to test ones skill in this area. Moreover, a fictional problem spanning the theory and concepts covered in this chapter can be difficult to pose. However, a great many magnets have been fabricated and tested using the means summarized in this chapter. Therefore, to approximate the real world of magnetic measurements, an actual case study is presented so that the student can get an example of the raw data collected from a measurement of an actual magnet and perform the calculations using the algorithms presented in this chapter. The results of the calculations performed by the student can then be compared with the tabulated results generated by the data reduction part of the magnetic measurement system to determine whether the calculations performed by the students are correct and/or to determine whether the software written by the student to achieve the results have been correctly translated from the algorithms.

It is expected that the problem can be solved by the student when he/she has a fairly large block of time. The calculations can be tedious. It is hoped that the experience gained by the student performing these calculations will provide him/her with a familiarity of the techniques and a confidence to apply them when encountering an opportunity to perform “real” rotating coil magnetic measurements.

Problem 8.1 (Summary Solution)

The data are the actual raw output from the measurements of a SPEAR3 quadrupole. Two output files are presented, one with the coil in the uncompensated configuration and the second with the coil in the compensated configuration. Some of the data are reproduced in this section but are also copied onto a spreadsheet included with this text so the student can avoid the drudgery of copying a large number of data. The coil configuration is not the same as that summarized by the set of coil parameters given in eq. (8.17). Therefore, a new set of sensitivities S_N and s_n must be computed.

Coil Configuration The measurement coil and the magnet pole configuration are illustrated in fig. 9. The radii and number of turns for each set of windings schematically shown in fig. 2 are

$$\begin{aligned} r_1 &= 26.97 \text{ mm}, & r_3 &= 20.260 \text{ mm}, \\ r_2 &= 15.145 \text{ mm}, & r_4 &= 8.495 \text{ mm}, \\ M_{\text{outer}} &= 150 \text{ Turns}, & M_{\text{inner}} &= 300 \text{ Turns}. \end{aligned}$$

Problem 8.1a Compute β_1 , β_2 , ρ and μ for the coil.

Problem 8.1b Compute S_1 and S_2 .

Problem 8.1c Compute the spectrum of s_n 's for $1 \leq n \leq 18$.

Problem 8.1d Fig. 12 displays the digital output from the integrator for the uncompensated measurement of the SPEAR3 quadrupole, serial Number 34Q040, a 340 mm. long quadrupole with a 35 mm radius aperture, measured at 81.1246 Amps. In the figure, the data are displayed in six double columns, the first column of each double set displays the shaft encoder counts with $0 \leq \text{counts} \leq 256$ for rotation angle $0 \leq \theta \leq 2\pi$. These data are stored in an Excel[©] spreadsheet copied onto the enclosed CD under file name 34Q40.xls.

After subtracting the drift, compute the first two sets of coefficients for the Fourier series expansion for the voltage, p_1 , q_1 , p_2 , q_2 . Compute the amplitude and the phase of the fundamental signal ($n = 2$). Using the coefficients and the sensitivities (computed in Problem 8.1b) and the number of turns in the outer windings of the measurement coil, compute the integrated excitation expressed in terms of $\int B_{r1} dz$ $\int B' dz$. Compute the phases of the dipole and quadrupole field with respect to the zero angle of the shaft encoder.

Compute the magnetic center offsets Δx and Δy by looking at the ratio of the spilloff fields to the fundamental at the measurement radius.

Problem 8.1e Fig. 13 displays the graphical output from the integrator for the compensated measurement of the same SPEAR3 quadrupole, measured at 81.1033 Amps. The graphical presentation demonstrates the operation of the integrator. When the zeroeth encoder pulse is received, the integrator output is zeroed so that the cosine 2θ curve varies from $0 \leq \int V dt \leq -2 |\int V dt|_{\max}$ instead of $|\int V dt|_{\max} \leq \int V dt \leq 2 |\int V dt|_{\max}$. Since the maximum amplitude is substantially smaller than the uncompensated data, the drift due to the small constant thermocouple voltage generated by the coil joints results in a larger drift than the previous data. The data used to generate the graphical output are stored in an Excel[©] spreadsheet copied onto the enclosed CD under file name 34Q40.xls.

After subtracting the drift, compute the sets coefficients for the Fourier series expansion for the voltage, p_n , q_n for $2 \leq n \leq 18$.

Using the sensitivities computed in Problems 8.1b and 8.1c, compute the multipole amplitudes normalized to the amplitude of the fundamental field $\left| \frac{B_n}{B_2} \right|_{r_1}$. Suppose the good field radius for this 35 mm radius aperture quadrupole is 32 mm. Compute $\left| \frac{B_n}{B_2} \right|_{r=32mm} \dots$

=====															
0	0	43	-24558000	86	-24493000	129		2000	172	-25889000	215	-24407500			
1	6000	44	-25248000	87	-23782000	130	-47500	173	-26562000	216	-23622000				
2	-28500	45	-25911500	88	-23025500	131	-134000	174	-27213500	217	-22871500				
3	-101500	46	-26553000	89	-22277000	132	-260000	175	-27883500	218	-22084000				
4	-215000	47	-27205500	90	-21515500	133	-426000	176	-28484000	219	-21315500				
5	-365500	48	-27794000	91	-20756500	134	-639500	177	-29064500	220	-20530500				
6	-567500	49	-28359000	92	-19987000	135	-882500	178	-29610500	221	-19674000				
7	-794500	50	-28890000	93	-19154000	136	-1164500	179	-30123000	222	-18870500				
8	-1062000	51	-29393500	94	-18356000	137	-1478000	180	-30646000	223	-18049000				
9	-1364500	52	-29905000	95	-17563000	138	-1829000	181	-31097000	224	-17246500				
10	-1700000	53	-30347500	96	-16777000	139	-2242000	182	-31510000	225	-16436000				
11	-2105500	54	-30753500	97	-15982000	140	-2668000	183	-31889500	226	-15555000				
12	-2513000	55	-31126500	98	-15124000	141	-3122500	184	-32236000	227	-14733000				
13	-2956500	56	-31466000	99	-14323000	142	-3612000	185	-32569000	228	-13930500				
14	-3429000	57	-31792000	100	-13533000	143	-4135000	186	-32847500	229	-13130000				
15	-3938000	58	-32059500	101	-12755000	144	-4723000	187	-33075500	230	-12350000				
16	-4514500	59	-32284000	102	-11986500	145	-5304500	188	-33273500	231	-11505000				
17	-5079000	60	-32477000	103	-11168500	146	-5898000	189	-33433500	232	-10732000				
18	-5663500	61	-32630500	104	-10409500	147	-6529500	190	-33557000	233	-9989500				
19	-6277000	62	-32755000	105	-9692000	148	-7187000	191	-33638500	234	-9246000				
20	-6922000	63	-32832500	106	-8962000	149	-7917500	192	-33673000	235	-8528500				
21	-7638500	64	-32866000	107	-8263500	150	-8623500	193	-33674000	236	-7777500				
22	-8326500	65	-32866000	108	-7530000	151	-9321500	194	-33633500	237	-7088500				
23	-9018000	66	-32826500	109	-6866000	152	-10074500	195	-33545000	238	-6447000				
24	-9745500	67	-32739500	110	-6243500	153	-10828000	196	-33423500	239	-5803000				
25	-10487000	68	-32619000	111	-5612500	154	-11648500	197	-33265500	240	-5197000				
26	-11287000	69	-32463500	112	-5027500	155	-12429500	198	-33063500	241	-4588000				
27	-12055500	70	-32267500	113	-4432500	156	-13195000	199	-32829000	242	-4028000				
28	-12812500	71	-32035000	114	-3897000	157	-14012500	200	-32533500	243	-3523500				
29	-13602500	72	-31747500	115	-3405000	158	-14823000	201	-32219500	244	-3024000				
30	-14403500	73	-31435000	116	-2920500	159	-15682000	202	-31880000	245	-2565000				
31	-15234000	74	-31098000	117	-2479000	160	-16505000	203	-31485500	246	-2121000				
32	-16053500	75	-30712000	118	-2059500	161	-17293000	204	-31071000	247	-1715500				
33	-16829000	76	-30305500	119	-1676500	162	-18135500	205	-30590500	248	-1367000				
34	-17645000	77	-29842000	120	-1349500	163	-18943500	206	-30094000	249	-1039000				
35	-18440000	78	-29352000	121	-1037500	164	-19775000	207	-29580500	250	-758500				
36	-19258500	79	-28849500	122	-776000	165	-20595500	208	-29012500	251	-521000				
37	-20060000	80	-28298500	123	-546000	166	-21363000	209	-28446000	252	-329500				
38	-20821500	81	-27736500	124	-350500	167	-22169500	210	-27821000	253	-168500				
39	-21601000	82	-27130500	125	-206500	168	-22934500	211	-27172000	254	-35000				
40	-22352000	83	-26487000	126	-90000	169	-23698000	212	-26523000	255	56000				
41	-23106000	84	-25849500	127	-21000	170	-24477000	213	-25827500	256	100500				
42	-23859000	85	-25170500	128	10500	171	-25178500	214	-25133000						

Figure 12 Uncompensated Raw Data

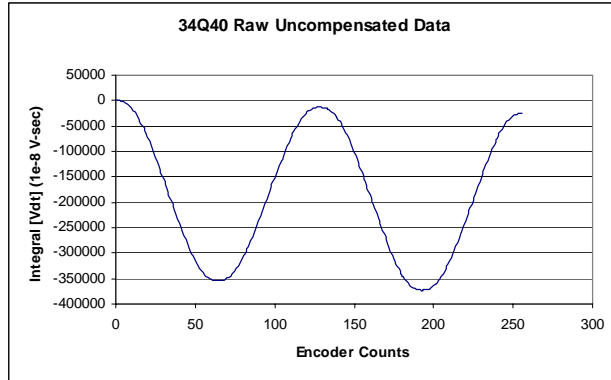


Figure 13 Graphical Compensated Raw Data

Problem 8.1f Compute the phases of each of the multipole error fields with respect to the zero angle of the shaft encoder. Compute the relative phases of each of the multipole field errors with respect to the zero phase angle of the fundamental field, $N = 2$. Compute the bucking ratio, eq. (8.39).

Chapter 9

MAGNET YOKE DESIGN AND FABRICATION

9.1 Introduction

The chapter on Perturbations discussed the introduction of errors in the magnet performance due to fabrication, assembly and pole excitation errors. Errors which appear to be due to pole excitation errors can be introduced by the iron saturation as well as mechanical fabrication errors. As shown in the chapter on perturbations, iron saturation can change the location of the magnetic center for assymetric multipole magnets, alter the fundamental field reproducibility of individual magnets in the same family and add to the multipole error spectrum of magnets.

The fields of the magnet fabricated with a yoke and pole contour resulting from the two dimensional design are three dimensional. Means for visualizing the three dimensional fringe field shapes contributing to integrated field errors and empirical techniques for correcting them are discussed.

This chapter is devoted to discussing and listing guidelines for the design of iron yokes for high quality magnets. It assumes that a pole contour satisfying two dimensional uniformity requirements has been selected. Fabrication and core assembly practices developed at different US National Laboratories are described which resulted in the manufacture of high quality magnets for the accelerators at those laboratories. These design practices include consideration of the iron saturation characteristics. The field errors due to the saturation of magnet iron depends not only on the magnetic properties of the iron, but how the material is distributed in individual magnets and among magnets of the same family.

The selection of magnet core designs using solid iron blocks or laminations are discussed. Because of magnet performance issues associated with solid core magnets and comparative costs, many modern accelerators have designed, assembled and installed magnets with yokes fabricated using stamped steel laminations. Issues associated with this type of fabrication are discussed.

9.2 Saturation

Although all the discussion so far has referred to construction of the magnet yoke from iron, most magnets use steel (iron with controlled Carbon impurities). The magnetic performance of steel is highly variable and affected by both the chemical

impurities in the iron and by its mechanical and thermal processing. The magnetic performance of steel is dominated by its Carbon content and, to a lesser degree, other chemical impurities. Because of this, most magnet steel is designated by its equivalent Carbon content. (The effect of other chemical impurities are incorporated into the steel designation as an equivalent Carbon content.) The magnetic performance is also affected by mechanical processing. Thus, rolled steel may have different directional magnetic properties. Isotropic properties can be restored by annealing the rolled steel at some temperature high enough to regrow the crystalline grain structure. Despite these mechanical effects, most rolled magnet steel is rolled at a high enough temperature so that it has isotropic magnetic properties and may or may not be annealed after rolling.

Selection of steel is important in some applications where extremely high fields are required or size constraints force less than ideal designs. Steel selection is also important for specialized applications where fringe fields are important. However, for the purposes of this text, it is assumed that special constraints do not apply and good design practices can be used to select pole and yoke shapes. Therefore, the discussion will refer to the design parameters limited by the properties of one of the most commonly used and easily available grades of magnet steel, 1010 steel. The designation describes the maximum equivalent maximum Carbon impurity as $\leq 0.10\%$ Carbon. A portion of the table of values for the BH relationship taken from the Poisson program for 1010 steel is reproduced here.

$H(\frac{A}{m})$	$B(Tesla)$	$H(\frac{A}{m})$	$B(Tesla)$	$H(\frac{A}{m})$	$B(Tesla)$
0.0000	0.0000	0.09533	1.2373	0.86938	1.6726
0.01257	0.1890	0.11461	1.3021	1.04522	1.7019
0.01510	0.2704	0.13779	1.3586	1.25664	1.7336
0.01816	0.3649	0.16566	1.4074	1.51080	1.7679
0.02184	0.4680	0.19916	1.4494	1.81639	1.8046
0.02625	0.5757	0.23945	1.4856	2.18378	1.8432
0.03157	0.6846	0.28788	1.5171	2.62549	1.8831
0.03795	0.7918	0.34610	1.5451	3.15654	1.9236
0.04563	0.8949	0.41611	1.5709	3.79497	1.9636
0.05485	0.9922	0.50028	1.5955	4.56258	2.0022
0.06595	1.0821	0.60146	1.6201	5.48541	2.0384
0.07929	1.1640	0.72312	1.6456		

The BH curve using the tabulated data is shown in fig. 1. The BH relationship becomes highly nonlinear at $B \leq 1.5$ Tesla and the material exhibits fully saturated behavior at $B \geq 2.0$ Tesla. (Fully saturated behavior is when the material permeability $\mu = \frac{\Delta B}{\mu_0 \Delta H} \rightarrow 1$.)

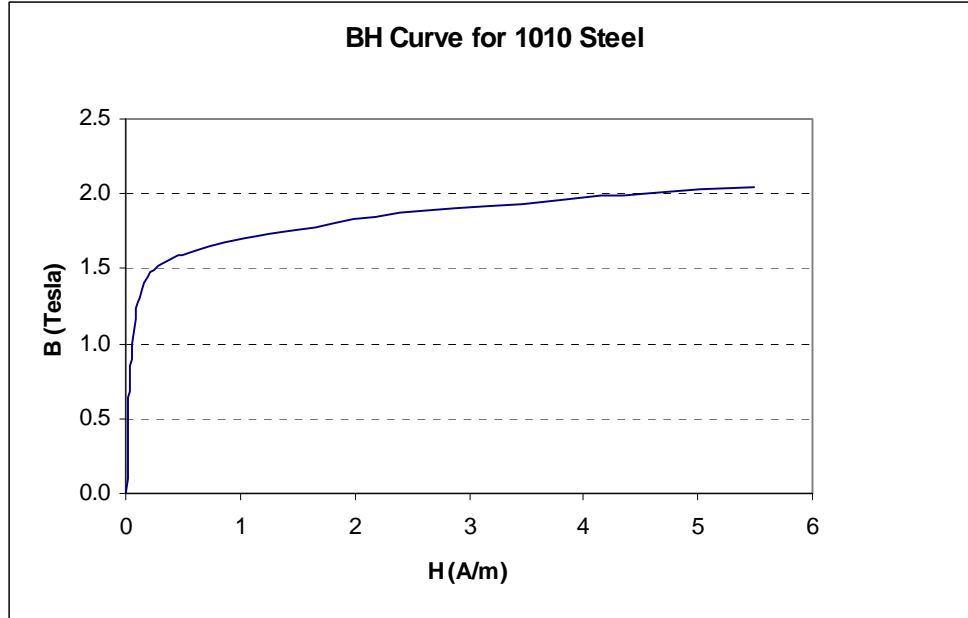


Figure 1 1010 Steel BH Curve

9.3 Two Dimensional Design

The discussion and example in this section is devoted to design practices for dipole magnets to minimize the effects of iron saturation. The principles are easily extended to quadrupole, sextupole and other magnet types. Fig. 2 illustrates an example of bad two dimensional dipole design practice contrasted with good practice.

The bad features in the left hand illustration improved in the right hand illustration are:

1. The pole edge is vertical resulting in equal width at the top and at the bottom of the pole. Transverse magnetic flux enters the pole through the coil resulting in higher flux at the top of the pole. At high fields, the top of the pole can saturate. The right hand figure illustrates a tapered pole which is wider at the top resulting in more uniform magnetic flux density over the pole area.
2. The coil is narrow and is installed in a narrow slot. The magnetic flux through the low reluctance path through the narrow coil results in high transverse field, adding to the saturation at the top of the pole. The right hand figure illustrates a wider coil with approximately the same area and a higher reluctance path and a lower transverse field due to both the wider coil slot and the tapered pole edge.
3. The corner of the pole has a sharp corner. Using the orthogonal analog principle, it can be seen that the flux lines will pile up in this region resulting in a

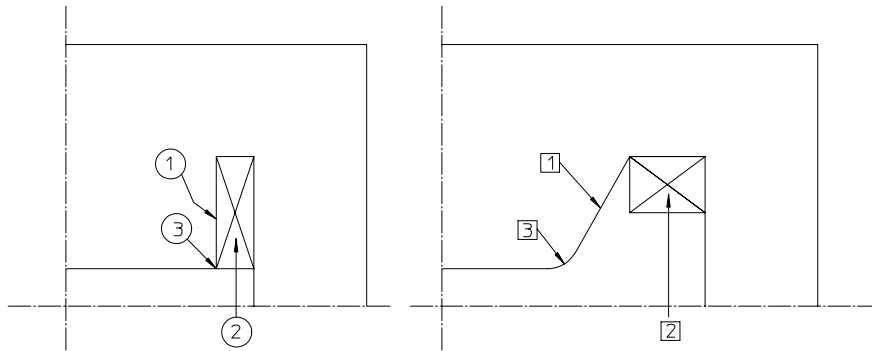


Figure 2 Alternate Dipole Two-Dimensional Designs

high iron magnetic field. The steel in this area is likely to saturate, resulting in a nonuniform field distribution along the horizontal centerline which will change with excitation. The right hand figure illustrates a radius at the pole corner, reducing this magnetic flux stress concentration.

The results of the listed improvements in the two dimensional design are magnets whose field remains uniform and whose excitation remains linear over a wider range of excitation. Also, for magnets in a power supply string, the magnet excitation reproducibility is less sensitive to variations in the BH curve of the steel used in the yokes. The improvements in the performance are not without costs. The more generous size of the improved designs results in heavier magnets requiring more steel sheet material for laminated magnets and larger steel blocks for solid core magnets.

9.4 Three Dimensional Design

Magnet uniformity specifications typically require the integrated field to be uniform, have a uniform integrated gradient or to have a uniformly parabolic field integral for the dipole, quadrupole or sextupole, respectively. Although the two dimensional field may have the desired properties, the distribution of the three dimensional fringe fields at the ends of the magnet is not uniform. A general rule of thumb is that the length of the fringe field beyond the edge of the steel pole tip is $= h$, $= \frac{h}{2}$, or $= \frac{h}{3}$, for the dipole, quadrupole or sextupole, respectively, where h is the dipole half gap, the quadrupole and the sextupole pole radius.

9.4.1 Dipole Fringe Field

In order to achieve a uniform field integral, it is necessary that the magnet effective length does not change with transverse position. The effective length is given by, $L_{eff} = \frac{\int Bdz}{B_{center}}$. The effective length of a magnet is measured by either making a Hall

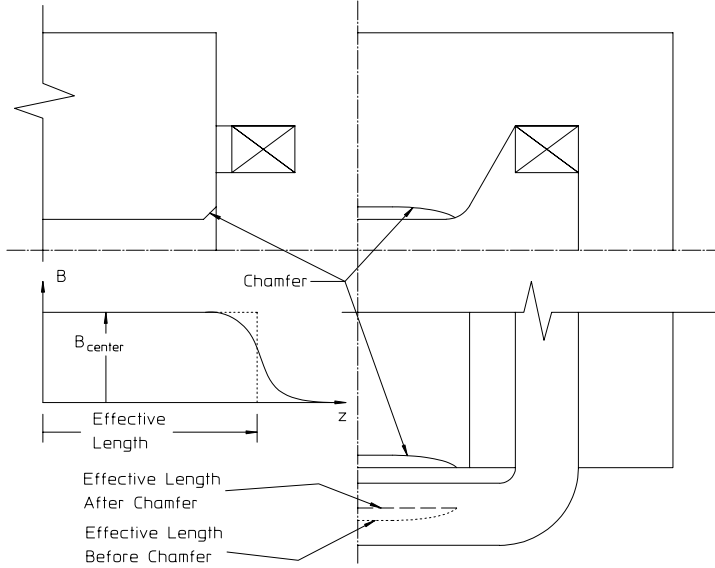


Figure 3 Dipole Fringe Field

probe map of the distribution of the vertical field on a grid on the dipole horizontal plane or measurements of the field integral using a stretched wire. Because of the finite width of the dipole pole, the distribution of the effective length of the magnet is maximum at the center and reduces in a nonlinear fashion transversely near the edge of the pole.

The distribution for a symmetric dipole can be fitted to a polynomial and has the form $L_{eff} = \sum_k A_k x^{2k}$. The allowed dipole multipole errors are $n_{allowed} = N(2m + 1)$, odd integers, where $m =$ all the integers starting from zero. Since the fields have indices $n_{allowed} - 1$, the allowed multipoles are even functions of the space variable. Therefore, the distribution of L_{eff} satisfies the rotational symmetry conditions for the dipole. The first term is quadratic (the sextupole term) and is usually the most serious error. The process of compensating for the shape of the fringe field is illustrated in fig. 3 and described in the following list of steps.

1. The field integral, $\int B dz$, is measured as a function of the transverse position, x .
2. The effective length, $L_{eff} = \frac{\int B dz}{B_{center}}$, is computed as a function of the transverse position, x .
3. The minimum effective length $L_{eff}(x_{grf} + \Delta x) = \frac{\int_0^{x_{grf}} B dz}{B_{center}}$, is established where x_{grf} , is the width of the required good field region and Δx is some arbitrary margin beyond the good field boundary.



Figure 4 Chamfer on Prototype Gradient Magnet Removeable Pole Ends

4. The distribution of the excess fringe field, $2\Delta z = L_{eff}(x) - L_{eff}(x_{gfr}) = \frac{\int_0^x B dz}{B_{center}} - \frac{\int_0^{x_{gfr}} B dz}{B_{center}}$, is computed as a function of x .
5. The four ends of the two pole are machined to a depth $\Delta z(x)$.
 - (a) The angle of the cut is unimportant. However, a 45° angle cut is convenient and distributes the same angle at two points and minimizes saturation effects due to the sharp corners.

The chamfer on the SPEAR3 gradient magnet prototype is shown in fig. 4. Since the gradient magnet superimposes both a constant dipole field with a linearly distributed quadrupole field, the chamfer was empirically developed to maintain a constant integrated gradient. In this figure, solid steel pieces, machined with the two dimensional pole contour, were bolted onto the pole ends. These pieces were removed, machined with the required distribution of the chamfer depth determined by the described iterative process and replaced. After replacement, the distribution of the field integral was measured. The final chamfer shape was achieved after two iterations. This shape was subsequently machined onto glued end packs which were then assembled with additional laminations to complete the core assembly for the production magnets .

9.4.2 Quadrupole Fringe Field

The length of the quadrupole fringe field varies with the “gap”. The quadrupole gap is approximated by the length along the vector equipotential lines which describe

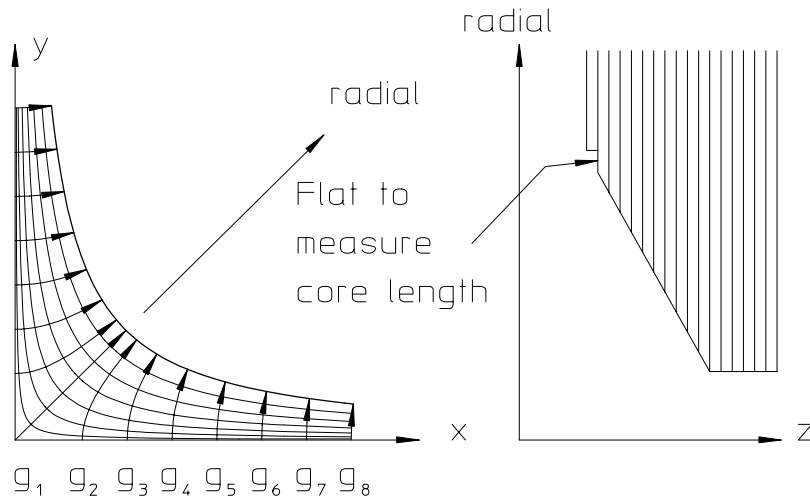


Figure 5 Quadrupole Fringe Fields

the directions of the flux lines. Fig. 5 illustrates the distribution of the effective quadrupole gaps and suggests a means of adjusting the pole lengths to compensate for the variation of the fringe field. In this figure, the quadrupole gaps decrease as the distance from the center of the pole. $g_1 > g_2 > g_3 > g_4 > g_5 > g_6 > g_7 > g_8$, which suggests that the center of the pole should be shortened more than the edge of the pole. The illustration shows a section taken through the radial centerline of the quadrupole pole and a straight angled machined cut at the end of the pole tip. This simple cut removes the most material from the center of the pole. The depth of the cut decreases as one nears the edge of the pole. Thus, $\Delta z_1 > \Delta z_2 > \Delta z_3 > \Delta z_4 > \Delta z_5 > \Delta z_6 > \Delta z_7 > \Delta z_8$, achieving the desired effect. The flat shown as part of the machined cut is a convenience since measurements of the angle cut at the end of the pole tip is difficult. This allows the machinist to measure the pole lengths to ensure that each of the four pole lengths are equal.

The chamfer cut is rotationally symmetric for pole angles at multiples of $\frac{\pi}{2}$ and the integrated field satisfies the allowed multipole principal described in an earlier chapter. The quadrupole allowed multipole indices are $n = 2, 6, 10, 14, \dots$ (see page 50). The first multipole error term is $n = 6$. The empirical method of determining the chamfer cut is usually performed on the magnet prototype. This cut is repeated for the production quantity of the magnet.

The steps used for the determination of the shape of the cut used for the Advanced Light Source Quadrupoles at LBNL were:

1. Measure the multipole spectrum at the operating gradient for the magnet and

note magnitude of $F_1 = \left| \frac{B_6}{B_2} \right|_{z=0}$.

2. Select the radial distance for the back of the cut and make the cut with depth z_1 .
3. Measure the multipole spectrum and note the magnitude of $F_2 = \left| \frac{B_6}{B_2} \right|_{z=z_1}$.
4. Compute the derivative $\frac{\partial F}{\partial z} = \frac{F_1 - F_2}{z_1}$.
5. Calculate a new depth z such that $\Delta F = F_2 = \frac{\partial F}{\partial z} \Delta z$.
 - (a) $\Delta z = \frac{F_2}{\frac{\partial F}{\partial z}} = \frac{F_2 z_1}{F_1 - F_2} \implies z_2 = z_1 + \frac{F_2 z_1}{F_1 - F_2}$.
6. Repeat steps 3 to 5 until $\left| \frac{B_6}{B_2} \right|_{r=r_0} \longrightarrow \leq \text{Specified Value}$.

At the end of this exercise, the multipole amplitude of the allowed multipole with the next highest index $\left| \frac{B_{10}}{B_2} \right|_{r=r_0}$ may be large. This is usually not a serious problem since $\left| \frac{B_{10}}{B_2} \right| \propto \left(\frac{r}{r_0} \right)^8$ and becomes very small at small radii.

Machining the End Chamfer

Magnet yoke structures are often assembled from thin steel laminations. The laminations at the two ends of the magnet are often assembled into end packs, glued from enough laminations for a thick enough structure to compress and support the balance of the laminations. In some cases, the entire yoke is glued. In other cases, the yokes are either welded or mechanically assembled with the glued end packs used as mechanical end plates holding the balance of the laminations sandwiched between them. In either case, the process for shaping the pole end chamfer should be carefully specified to avoid delaminating the glued end packs by the mechanical or thermal stress resulting from machining. Yoke end pack fabrication specifications should call for slow tool advance rate and multiple shallow cuts to avoid heat buildup. The machined surface should be cooled with an air stream. (Liquid coolants are often incompatible with glues.) In addition, a push cut should be specified. The push cut rotates the cutter toward the surface, rather than away from the surface, as the tool advances. This cut is illustrated in fig. 6. This type of cut avoids tearing the glued lamination away from the surface. (The opposite rotation direction is preferred by machinists since it enhances metal chip removal.)

The chamfer shown on fig. 7 illustrates the straight cut used on the SPEAR3 quadrupole. The small cut at the end further refined the chamfer to reduce the amplitude of the $n = 6$ multipole which grew at the maximum excitation due to local saturation of the iron.

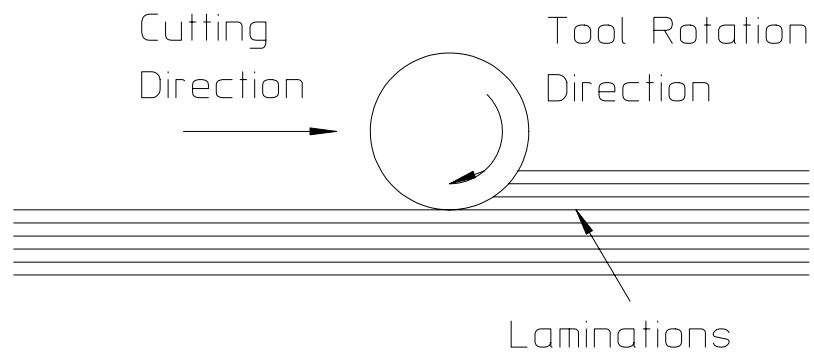


Figure 6 Push Cut

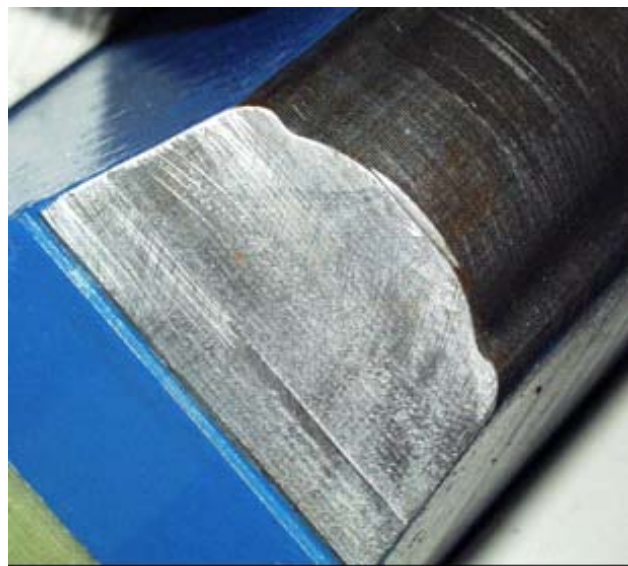


Figure 7 SPEAR3 Quadrupole End Chamfer

9.5 Solid Iron or Steel Laminations

Decisions to fabricate magnet yokes made from large, solid pieces of iron or steel or steel laminations hinge on a variety of requirements. Historically, the primary consideration for the choice was whether the magnet operated in a persistent mode or was cycled. Solid iron yokes support eddy currents and magnets using solid iron yokes cannot be cycled or pulsed rapidly. Except for booster synchrotrons, which accelerate low energy beam from an injector system to the required energy for injection into synchrotron light and storage ring accelerators, most synchrotron magnet applications do not require magnets to cycle rapidly. Based only on this consideration, magnet yokes fabricated from large solid pieces of iron or steel are acceptable. However, other issues need to be considered when making this choice.

9.5.1 Reproducibility and Symmetry

Synchrotron dipole magnets and families of quadrupoles and sextupoles are often connected in series with a single power supply. In this configuration, it is important that the magnetic fields for all the magnets in a family reproduce the same fields and/or gradients at the same excitation current. For magnets with individual power supplies, reproducibility among the magnets allows the use of the same algorithm for controlling the magnet field without the necessity of individually measuring all the magnets. For magnets whose yokes are assembled from several segments, symmetry requires that the material as well as the mechanical shapes of the individual pieces be identical.

The reproducibility and symmetry conditions require that the individual pieces making up the magnet yokes have identical iron properties. That is, the BH saturation characteristics of the iron or steel used to fabricate the individual yoke segments must be nearly identical.

Iron Properties

The magnetic properties of iron/steel depend on the chemistry and the mechanical and thermal history of the material. Typically, iron/steel pieces are fabricated from large cast billets from material melted in a furnace. The capacity of the furnace can range to several hundred tons. Material in the furnace stratifies, so that the properties of the steel from a single melt varies and can be expected to be uniform in the first, second and third pours from a single melt. This is typically referred to as the head, center and tail of the melt. Each portion may yield up to 100 tons of material with uniform chemistry and thermal history. Therefore, it is not difficult to secure sufficient material with identical properties to fabricate all the yoke pieces for the required number of magnets in a single family.

9.5.2 Solid Iron Cores

One can ensure that the individual yokes making up all of the yokes for a magnet family have reproducible magnetic properties if the corresponding pieces making up

the individual yokes are taken from pieces from the same portion of the same melt of a batch of iron or steel. This requires careful documentation of the fabrication/purchase specifications.

Eddy Currents

Because of the electrical conductivity of steel, eddy currents can be generated in solid magnet cores. Depending on the rate of change of field, these eddy currents can approach the current density of the coils used to excite the magnet fields. For solid transformer circuits with no gap, the eddy currents can be very persistent. A solid 15 cm. thick piece of steel will support an eddy current whose exponential decay time constant is 60 seconds if used as a transformer core. (The time constant for magnets with a few cm. gap fabricated with similar thicknesses of solid steel is measured in the range of a few seconds.) The eddy currents can generate local magnetic fields in the magnet yoke larger than the design fields. Therefore, rapid changes in the magnet field can generate hysteresis effects which locally change the *BH* characteristics of the iron or steel in isolated areas of the magnet yoke or pole tip. These effects can be very damaging to the operation of an accelerator since the *BH* iron characteristics affect magnet performance and field quality.

Hysteresis effects on the magnet circuit can change the excitation characteristics of individual magnets. Thus, if one develops a successful accelerator tune for an accelerator based on the current settings for individual magnets, changes in the *BH* characteristics of the magnet steel due to hysteresis can change the magnet excitations at tune currents and can delay the successful reproduction of the accelerator performance. In the same manner, changes in the *BH* characteristics of the magnet steel due to hysteresis at the edges of the magnet pole can change the field quality.

Normally, an accelerator whose magnets are fabricated from solid yoke pieces require programming the power supplies for slow, reproducible conditioning cycles and current settings. A typical conditioning cycles require the power supplies to ramp the current slowly to $\geq 110\%$ of the maximum operating current at least three times before slowly ramping the magnet current to the operating setting to ensure that all the magnets in the same family operate on the same hysteresis curves. Reconditioning of magnets is required after power supply crashes when eddy currents are generated by rapid decay of magnet currents.

9.5.3 Laminated Steel Cores

Since the time constant for pieces of solid steel varies at the square of the thickness, eddy currents for the typical lamination thickness ($\leq 1.5\text{ mm.}$) can only be generated for extremely fast power supply cycling rates or ramp times. Therefore, hysteresis effects are not important for magnets assembled using laminated cores. Reproducibility requirements among all the cores can be ensured for laminated cores by distributing all the steel from different sources (with different *BH* characteristics) among all the core segments for a magnet family.

Shuffling vs. Sorting

The procedure for distributing the steel properties among all the core segments has often been described as shuffling. Shuffling describes the process of random distribution. A better term used for distributing the steel properties among all the core segments is sorting. Sorting is the process of systematic distribution. The process for sorting the steel properties among all the magnet cores is listed as follows:

1. All the laminations stamped from a single batch of steel sheets sharing the same chemistry and thermal history is stacked separately.
2. Pallets are arranged for each core segment of a magnet family.
 - (a) If a family of magnets consists of 30 quadrupoles assembled from 2 core segments, 60 pallets are required.
3. As the lamination stamping from a single batch of steel sheets is completed, the laminations are distributed as evenly as possible among all 60 pallets.
 - (a) A few extra laminations are stacked on each pallet to ensure that sufficient laminations are available for each segment.
4. Core stacking and assembly can begin only after all the stacks are filled.

This procedure ensures that all the core segments of all the magnets in a family have reproducible magnet *BH* properties and simplifies the requirements for procuring the steel yoke material

9.5.4 Economics

A second consideration in selection of solid or laminated core structures is economics. The cost of machining solid iron yoke pieces for individual magnets must be compared with the cost of tooling for stamping laminations and stacking, compressing and assembling the cores.

Laminated Yokes

The cost of the die set for stamping laminations is one of the highest magnet manufacturing costs. Depending on the complexity of the cross section and size of the lamination, the US costs can be $\geq K\$60$. US stamping costs are currently $\approx \frac{\$1}{\text{lamination}}$. Thus, for a 0.5 meter long quadrupole constructed with a two piece yoke employing 0.5 mm. thick laminations, the cost of the stampings (exclusive of material costs) is $\approx \$2000.00$. The cost of additional hardware required for assembling the cores must be added to the material costs. The labor costs for stacking, compressing and assembling the cores might be 3-4 man-days per core segment and the cost of stacking and compressing fixtures may add $5K\$$ to the tooling costs.

Solid Core Yokes

Core machining costs are more difficult to isolate and evaluate. A simple flat pole (unoptimized) dipole core can employ simple machine tools. Quadrupole and sextupole cores demand the use of more complicated computer controlled machine tools such as 3 and 5 axis mills. The labor rates for the use of complex machine tools is more expensive and requires the addition of programming time. Typically, nearly half the material must be removed from a solid block of iron or steel in order to achieve the desired shape of a magnet core. The machining cost must also reflect the higher rates on more complicated and expensive machine tools.

Cost Comparisons

Typical undocumented studies have shown that the cost of fabricating a few (≤ 4) laminated magnet yokes is dominated by the tooling costs and exceeds the cost of machining the same number of yokes from solid blocks. However, these same studies have shown that the cost of machining exceeds the cost of fabricating laminated cores for the typical accelerator application where the tooling costs can be shared by the larger number of core segments.

9.5.5 Laminated Yoke Fabrication

In this section, it is assumed that a laminated yoke design is selected. Manufacturing and fabrication of laminated cores are discussed. The issues associated with selection of lamination material thickness and stamping tooling is discussed.

Although there are as many ways to assemble a laminated yoke as there are designers and engineers specifying magnet fabrication, only those used by the author are described. These methods are welding, gluing and mechanical assembly.

Lamination Thickness and Die Set Design

Two dimensional computer controlled machine tools can presently shape hardened steel bars used for punch and die tooling to within $\leq \pm 10 \mu m$ of the required contour. The clearance between the punch and die (the male and female parts of a die set) is selected by the diemaking and is proportional to the thickness of the material being shaped. For 0.5 mm. thick steel sheets, the clearance is sufficiently small so that the finished contour of the punched lamination closely reproduces the tolerance achieved in machining the tooling ($\leq \pm 10 \mu m$). As the thickness of the material increases, the clearance and thus the tolerance increases. The practical upper limit for the thickness of punched steel lamination appears to be about 1.5 mm. For this thickness, the clearance between the punch and die are sufficiently wide so that the edges of the cut are rougher and punching burrs occur. The precision of the cut edge for the thicker material is about $\leq \pm 25 \mu m$, still accurate enough for good magnet performance. However, the burrs which occur for this thickness material make stacking and compression of the collection of laminations more difficult and result in less precise

assemblies. Again, the lack of precision is not sufficient to compromise the magnetic performance of the individual yoke pieces. However, when the yoke requires the precise assembly of two or more yoke pieces using keys or other mechanical devices to locate the pieces accurately with respect to each other, small mechanical errors in the mating surfaces resulting from stacking the laminations with small burrs may contribute to larger mechanical assembly errors which can compromise the magnet performance.

Magnets comprise a large part of an accelerator perimeter. Thus, it is not unusual to require up to 50 meters of laminations to assemble the several yoke pieces to assemble 25 meters of magnets of one type. Thus, a die set may be required to stamp up to 100,000 $\frac{1}{2}$ mm. laminations. The tooling for a die set wears by either rounding or chipping the outside corner of the punch or the inner corner of the die. Also, laminations with sharp inside or outside corners require that these corners be machined in the tooling. The tooling in these corners wear quickly. The frequency of sharpening can be reduced by proper lamination design. Proper lamination design includes providing radii at sharp corners of the lamination. The punch and die are sharpened by machining off a small portion of their surfaces, restoring the sharp corners on the outside edge of the punch and the inside edge of the die. The hardened steel bars from which the tooling is machined must be sufficiently thick so that this sharpening can be performed a sufficient number of times to punch the full quantity of required laminations accurately. This is a process well understood by diemakers. However, some steel lamination material is coated with an inorganic coating for electrical insulation. This coating is abrasive and can accelerate tool wear. It is usually good practice to provide the toolmaker with a sample of the sheet material so that he can estimate the frequency of the sharpening procedure and provide the appropriate tooling thickness.

Figs. 8, 9 and 10 illustrate laminations for a gradient magnet, quadrupole and sextupole, respectively, using a die set manufactured in China.

9.6 Yoke Assembly/Fabrication Techniques

In a previous section of this chapter, comparisons were made among yokes fabricated from solid and laminated material. Although the author has been involved in the design of a limited number of magnets constructed with solid yokes, the vast majority of synchrotron magnet fabrications have involved assembling the yokes from laminations. This section is devoted to discussing techniques of laminated yoke construction which satisfy mechanical requirements leading to good magnet performance.

Physics requirements demand that magnets of the same family be reproducible, have predictable centers and have an error multipole spectrum with sufficiently low amplitude error harmonics. After the two dimensional pole contour has been developed, these requirements can be met with yokes whose mechanical shapes and sizes are precise. The mechanical fabrication and assembly tolerances needed to



Figure 8 Gradient Magnet Lamination

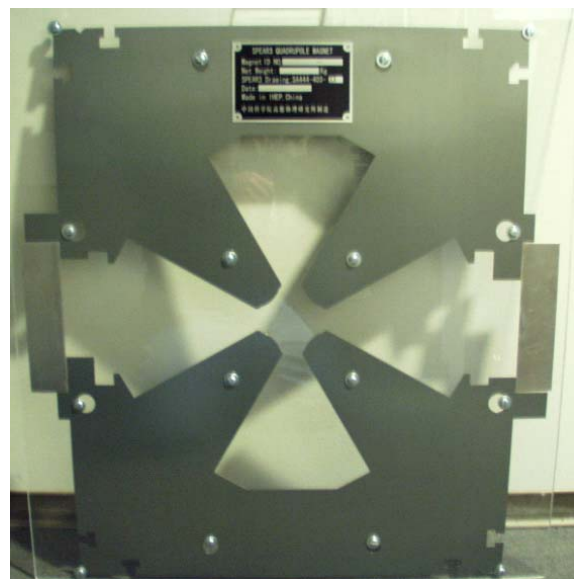


Figure 9 Quadrupole Laminations



Figure 10 Sextupole Laminations

achieve the required magnetic performance was discussed in the chapter on Perturbations. This discussion assumes that the magnet laminations have been stamped and sorted to assure the material reproducibility of the assembled yokes and that the stack and various parts have been fabricated for final yoke assembly. The three techniques discussed in this section are welding, gluing and mechanical assembly.

9.6.1 Gluing

For all three techniques of yoke assembly, welding, gluing and mechanical assembly, some lamination gluing is required. All three assembled yokes require two end plates, stacks of glued laminations with thickness designed for sufficient stiffness to support and hold the balance of the laminations compressed between them. The end plates are glued from the stacks of laminations previously sorted for each yoke.

Quadrupole Lamination

A typical yoke lamination for a quadrupole is illustrated in fig. 11.

Some of the features in the lamination cross section are listed as follows:

1. Rectangular key slots are provided at the bottom of the two vertical legs. These slots receive rectangular keys for transverse alignment of the two yoke halves.
2. The angled shoulder at the two edges of the lamination provide surfaces for the installation of mechanical clamps to attach the upper half of the magnet to the lower half.

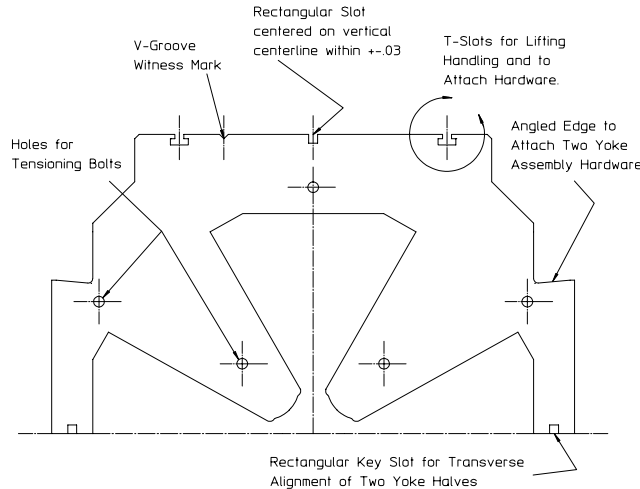


Figure 11 Quadrupole Yoke Lamination

3. A rectangular slot centered on the vertical centerline is used to install an alignment ball for the top yoke and to transversely align the magnet using a rectangular key on the bottom yoke.
 - (a) This is a feature of a generic fiducialization scheme. The generic scheme will be contrasted with a pedigreed fiducialization scheme in a later chapter. (See page 319.)
4. A V-groove witness mark is provided on one side of the vertical centerline to break the symmetry of an otherwise symmetric design.
 - (a) The witness mark is provided to demonstrate that the laminations are periodically flipped about their vertical centerlines during the stacking procedure. (The witness mark creates short v-grooves on each side of the assembled yoke.) The flipping enhances the symmetry since any errors in the stamping die set or assymmetries in the iron properties can be equally distributed to the two poles.
5. T-slots are provided for the installation of bars with threaded holes.
 - (a) Lifting fixtures can be attached using these threaded holes.
 - (b) Plates for attaching bussing hardware and water cooling manifolds and electrical termination strips can be attached using these holes.
6. Holes are stamped into the laminations at the centers of the two poles and in the yoke area.

- (a) These holes are provided to install and secure bolts which maintain compression on the yoke structure and prevent delamination along weak glue joints. Because of the weight of the iron yokes (typically $\geq 500\text{ kg}$), a glued structure without mechanical support can separate during lifting and handling.
 - (b) Holes are located in the yoke section of the lamination since this area is the heaviest and requires the most support.
 - (c) Two holes are located at radially centered locations near the ends of the two poles. Since the pole tip fields for a well designed quadrupole are ≤ 0.6 Tesla, the hole is made sufficiently small so that the steel does not saturate in this area. Bolts are required in these locations since the balance of the tensioning bolts are located far from the pole ends. The bolts support and prevent delamination at the ends of the long poles.
7. The components of the fasterner system which secures the yoke structure through the bolts holes is illustrated in fig. 12.
- (a) The illustrated fastener system is electrically shorted to one end of the core and electrically insulated from the other end of the core. This configuration opens the electrical circuit due to several tensioning bolts enclosing the magnetic flux and prevents the generation of eddy currents during changes in currents. Transient currents occur when magnets are excited to their required currents or when their excitations are changed.
 - i. A metal washer and an insulating washer is attached below the bolt head.
 - ii. A metal washer is attached below the nut.

Glued Core Stacking Fixture

Fig. 13 illustrates a core stacking fixture similar to the fixture designed and fabricated at LBNL for the ALS quadrupoles and at IHEP for the SPEAR3 quadrupoles.

The fixture is used to assemble the parts, compress the laminations and to cure the epoxy. The curing cycle for the yoke assembly involves installing the assembled and compressed yoke into an oven. Therefore, all the fixture material must be compatible with the curing temperature of the selected epoxy. This tooling is built robustly and consists of several parts.

1. Baseplate
 - (a) The baseplate is fabricated from material that resists abrasion and must be longer than the longest magnet of a given family. Extra length is

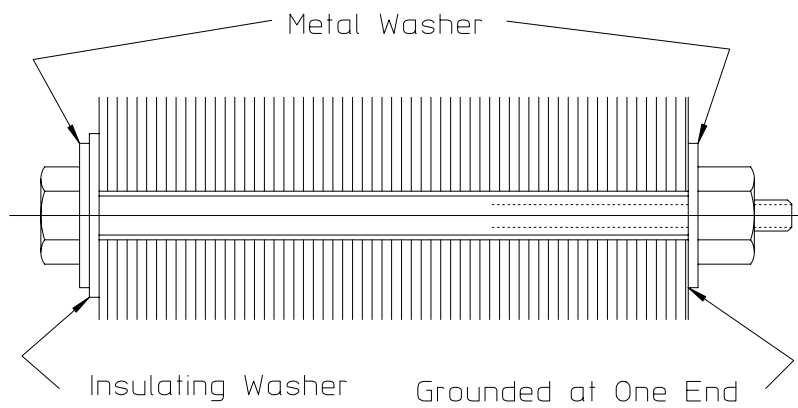


Figure 12 Yoke Fastener System

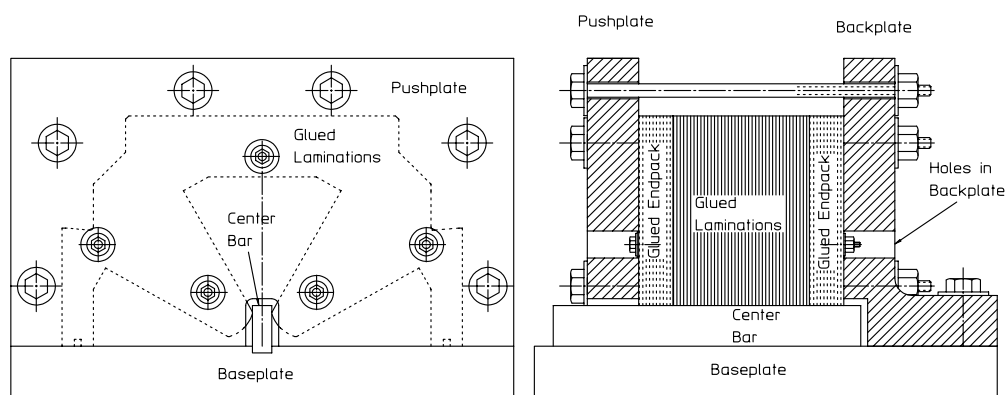


Figure 13 Glued Quadrupole Yoke Stacking Fixture

provided so that laminations can be inserted before the structure is compressed. The baseplate upper surface is ground flat and a groove is accurately machined along its longitudinal centerline to receive the center bar.

2. The Center Bar

- (a) The center bar is fabricated from material that resists abrasion. Its width is designed approximately $25 \mu m \leq$ the horizontal gap between the poles. Holes are provided so that it can be secured to the baseplate with fasteners.

3. Backplate

- (a) The backplate is fabricated from an L-shaped piece of steel and machined so that its vertical and bottom surfaces are precisely normal to each other. Holes are provided for the tensioning bolts. Additional holes are provided so the fasteners permanently attached to the yoke can be installed and tightened after final compression of the assembled yoke assembly. A cavity is machined into the backplate front face so that the center bar can be recessed behind its front surface. The backplate is permanently bolted and keyed to the baseplate, perpendicular to the axis of the center bar, with fasteners and dowels.

4. Pushplate

- 5. The pushplate is machined so that its vertical and bottom surfaces are precisely normal to each other. Additional holes are provided so the fasteners permanently attached to the yoke can be installed and tightened after final compression of the assembled yoke prior to installing into the curing oven. A slot is machined through the pushplate so that the push place can slide around the center bar.

6. Tensioning Fasteners

- (a) The tensioning fasteners consist of bolts, nuts and washers. The tensioning bolt lengths must be compatible with the length of the baseplate. Since it will be used repeatedly during the course of assembly of numerous yoke assemblies, the threads should be machined for smooth operation.

Glued Yoke Stacking and Compression Procedure

Yoke gluing is employed for magnet yokes ≤ 0.6 meters long requiring precise mechanical accuracy (tolerance $\leq 50 \mu m$). The stacking and compression procedures

for glued, welded and mechanically assembled yokes are similar. The major difference is that the laminations between the endpacks for the welded and mechanically assembled yokes are not coated with epoxy. The epoxy used to coat the laminations must have a long pot life at room temperature to avoid premature curing. The following procedures assume that the glued endpacks have been assembled and their chamfers have been machined.

1. Assemble the fixture and install the back glued end pack.
2. Coat the laminations and install a fraction of the laminations between the end packs. The installed laminations are flipped about their vertical centerlines in 2-5 cm. increments to enhance symmetry. The positions of the witness marks on the top of the assembled yokes indicate the frequency of flipping. Several 2-5 cm. stacks can be installed before the first compression cycle.
 - (a) This procedure is repeated until the final length is achieved under compression. The force required for the final compression cycle is described in fig. 14 and is characterized by three stages. These stages are common for all the methods of yoke assembly, gluing, welding and mechanical assembly.
 - i. Stage 1 - A small force results in a large displacement due to the removal of the spaces between the adjacent laminations.
 - ii. Stage 2 - A larger force is required for a smaller displacement due to the flattening of the laminations and squeezing out of the excess epoxy between the laminations.
 - iii. Stage 3 - A very large force is required for a very small displacement. Only a thin film of epoxy remains and the displacement is a combination of straining the metal and removal of any small space between the laminations. At this stage, the effective elastic modulus ($E = \frac{Force/Area}{\Delta Length/Length}$) of the stack of laminations, $E_{Stage3} \approx 500,000 \text{ psi} = 34,000 \text{ atm} = 3,400 \text{ MPa}$.
 - iv. The operating line is the maximum pressure on the lamination stack. Usually for Pressure = $\frac{Force}{Area} \geq 30 \text{ psi} = 2 \text{ atm} = 0.202 \text{ MPa}$, the stack starts to squirm and it becomes increasingly difficult to keep the laminations in contact with the baseplate. Often, it becomes necessary to add bars across the top of the stacking/compression fixture to hold the laminations down against the baseplate.
 - (b) The ratio of the final stacking pressure to the modulus is the elastic strain. $\varepsilon = \frac{\Delta L}{L} = \frac{\text{Pressure}}{E_{Stage3}} = \frac{2 \text{ atm}}{34,000 \text{ atm}} \approx 5 \times 10^{-4}$. Therefore, it is expected that the springback, the recovery of the length after the fixture pressure is released, should be $\approx 5 \times 10^{-4}$, sufficiently small to avoid magnet errors.

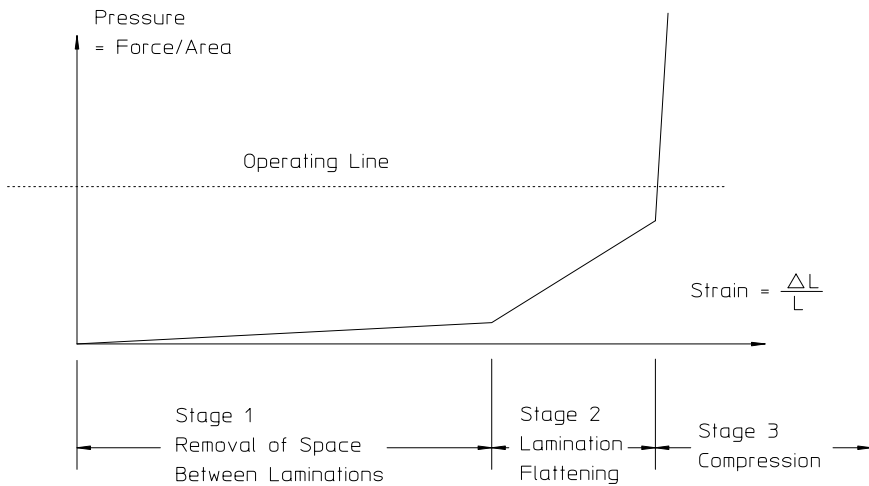


Figure 14 Typical Compression Force Diagram

3. Additional laminations are added and step 2 is repeated until the desired yoke length, after the front glued end pack is installed, is achieved under compression.
 - (a) After the final compression, the lengths of the top and bottom of the stack or the lengths of the left and right side of the stack may be different. A few cut laminations may be added in order to make the structure square. It is usually more important to recover left and right symmetry rather than top and bottom equality in length.
 - i. Differences in the lengths of the poles contribute to field errors.
 - (b) At LBNL, the yoke was stacked dry (without epoxy), to predetermine the number of required laminations and cut laminations to achieve the desired yoke squareness and length. The epoxy coating was added and the procedure repeated.
4. The yoke fastener system, illustrated in fig. 12 is installed and the entire core and fixture are installed in a curing oven to undergo the temperature cycle required for epoxy curing.
5. The cured yoke is removed from the oven and the fixture. The excess epoxy is removed from critical areas (the pole tip, mating surfaces and keyways at the bottom of the legs and any area used for magnet fiducialization or alignment).

Glued End Pack Stacking and Compression Procedure

The procedure is exactly the same as described in the previous section, except that the number of laminations required for the two endpacks (usually making up enough laminations to build up a pair of 3 to 5 cm. thick stacks) are removed from each stack of laminations for each yoke segment and glued using the stacking fixture. In order to accelerate production, several pairs of end packs can be assembled in a single gluing step. The laminations are coated with epoxy, each end pack is separated from each other with mylar or other material whose adhesion to cured epoxy is poor, and the end packs are compressed and cured using the same procedure used for the core assembly. The finished endpacks are removed from the curing oven, separated, cleaned and paired. The lamination from each paired endpack are from a single sorted stack. Since the laminations from each sorted stack are identical, the paired end packs from any stack can be assembled with the laminations from any other stack.

9.6.2 Welded Laminated Yokes

The PEPII Low Energy Ring quadrupole and dipole yokes were constructed using techniques which combined glued endpacks and welded construction. Mechanical precision comparable to glued construction can be obtained for welded yokes up to 0.6 meters long if proper weld design, techniques and practices are observed. Internal stresses due to weld bead shrinkage accumulate so that longer yoke structures tend to bend and warp, contributing to poor magnet performance. Except for the endpacks, welded yokes avoid the cleanup problems removing excess epoxy from crucial areas of the yoke. Welded yokes require more parts and some craftsmanship. The features of a welded yoke are illustrated in fig. 15. Some of the features of the lamination and the additional parts are listed:

1. In addition to the rectangular slot, the V-groove witness mark and the holes for the tensioning bars common to both the glued and the welded laminations, grooves are added near the lamination surfaces in contact with the angle plate. These grooves limit heat transfer to the bulk of the core resulting in less power requirements for the weld.
2. The same groove design is incorporated in the steel corner pieces.
3. Thick end plates are fabricated to which the corner pieces are welded with heavy weld beads for strength. The end plates and corner pieces comprise the frame in which the laminations are compressed and secured.
 - (a) The end plates do not cover the poles. The poles are secured against delamination using the same type of fasteners described for the glued yoke structure.
 - (b) The end plates do not cover the rectangular grooves on the two legs.

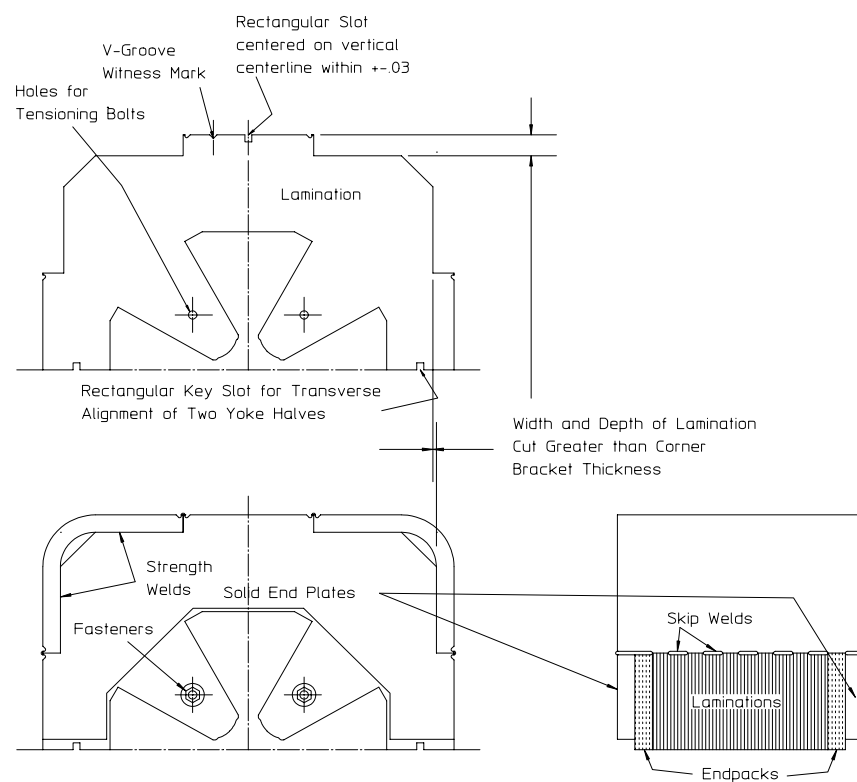


Figure 15 Welded Quadrupole Core

Some of the design and welding techniques contributing to precise mechanical yokes are listed as follows:

1. Welds require substantial heat and their shrinkage contributes to internal stresses and can result in distortions.
 - (a) The previously described heat sink grooves help minimize heating due to welding.
 - (b) Bars to lamination weld bead sizes are minimized.
 - (c) Skip welds are employed.
 - i. The weld lengths are staggered so that each lamination is secured by at least two welds.
2. Welding is a craft requiring proper training and a great deal of experience.
 - (a) Good welds between the endpacks and the yoke structure can be difficult to obtain because of the presence of glue which burns and smokes at the required welding temperatures.
 - (b) High quality small welds required to limit the heating and thermal distortions with sufficient strength to contain the lamination compression forces are difficult to make. Limiting the heat may result in cold welds, which are brittle and have a tendency to crack.
3. Welds need to be applied symmetrically in order to avoid unbalanced thermal stresses which can bend and/or warp the structure.
 - (a) Symmetric welding requires balanced procedures employing two welders, welding simultaneously on both sides of the yoke structure and trading places at frequent intervals.
4. Welding is performed while the yoke is confined in the stacking/compression fixture. The quality of the finished welded yoke is often unknown until the fixture is removed, transferring the internal compression and thermal distortion forces to the welded frame.

9.6.3 Mechanically Assembled Laminated Yokes

The fabrication technique described in this section was originally developed in response to the challenges associated with the fabrication and assembly of large, high quality quadrupoles for the final focus for the PEPI electron/positron collider interaction regions. To maximize the luminosity at the collision point, the multipole error tolerance for these magnets was extremely small. Preliminary perturbation calculations for the design showed that the required field quality for the 1.5 and 2

meter long magnets demanded construction of yoke pieces which were straight and flat within $\leq \pm 50 \mu\text{m}$ along their entire length. Welded prototypes quickly demonstrated that machining limitations and weld distortions resulted in mechanical errors which exceeded this limit by a wide margin. With accurate fixtures, laminations can be stacked and compressed to meet the straightness requirements. However the long 1.5 and 2 meter long steel bars could not be machined to the tight tolerances demanded for small, uniform weld beads. Good quality welds require uniformly small gaps between the bars making up the mechanical support structure and the stacked laminations. The long heavy bars distorted during machining because of the release of internal rolling stresses. Consequently, welds were not uniform and frequently needed to be large to fill the gap between the bars and the laminations, contributing to weld distortion due to shrinkage. The results were welded assemblies which warped beyond the mechanical precision required for good magnet performance.

The mechanical yoke assembly procedures, resulting in the successful fabrication of high quality magnets for PEPI, were subsequently used to assemble high quality magnets for other projects. The 0.75 meter long ALS Gradient Magnets and the 1.45 and 1.09 meter long SPEAR3 Gradient magnets were constructed using the same methods developed for the PEPI final focus quadrupoles and described in this section. The design of the 2.1 meter long Australian Light Source gradient magnets (currently under construction) also adopted the same construction techniques.

The Straight Gradient Magnet Yoke Design

The gradient magnets for the Advanced Light Source (ALS) in Berkeley, SPEAR3 at SLAC and the Australian Light Source in Melbourne were designed with straight rather than curved yokes. The straight yoke design was selected rather than a curved yoke because of the anticipated difficulty in assembling a curved yoke which follows a precise uniform arc. Any transverse error in the placement of magnet laminations contributes to field errors because of the field gradient. The orbit through a gradient magnet curved at the anticipated radius of the beam follows a uniform radius arc. Since a gradient magnet is really a section of a quadrupole with the beam traversing an orbit far from the quadrupole magnet origin, the orbit follows an orbit which approximates the hyperbolic cosine curve through a defocusing quadrupole. The hyperbolic cosine approximation is a result of the solution of the linear differential orbit equation through a quadrupole. The solution of the nonlinear differential equation,

$$\frac{x''}{[1 + (x')^2]^{\frac{3}{2}}} = \frac{e}{p} B_y(x, z) = Kx, \quad (9.1)$$

gives an exact characterization of the beam orbit. In eq. (9.1), $p = e B\rho$ is the momentum of the particle with $B\rho$ the magnet rigidity, x' and x'' signify the first and

second derivatives of the beam displacement with respect to z and K is the quadrupole coefficient in units of length^{-2} . The derivation of the nonlinear expression is included in the chapter appendix on page 284. The linear approximation assumes that the average slope, $x' \approx 0$ and reduces eq. (9.1) to $x'' = Kx$, whose solution is the hyperbolic sine or cosine curve. (Knowledge about the zero slope at the longitudinal center of the magnet requires an even function, the hyperbolic cosine curve.)

Exact knowledge regarding the orbit through the SPEAR3 magnets was required since the two lengths of magnets required for the SPEAR3 racetrack configuration needed to be precisely aligned with respect to each other. Furthermore, the orbit through the straight gradient magnets is flatter than the uniform radius arc through a curved gradient magnet, shortening the path length through the magnet resulting in a shorter closed ring orbit. This shorter orbit results in a shorter transit time around the SPEAR3 ring requiring a slightly higher RF frequency. For these reasons, a great deal of effort was invested in the numerical integration of the nonlinear differential equation to accurately predict the orbit through the straight gradient magnet. This numerical integration included using Hall probe magnetic measurement data to characterize the longitudinal distribution of the fringe fields at each end of the magnet. These calculations are summarized in a paper to be published in a future issue of Nuclear Instruments and Methods in Physics Research by Yoon[16] et al.

Lamination and Bar Designs

Fig. 16 illustrates the SPEAR3 gradient lamination, tension bar and front and back plate and end plate designs. The engineering design of the tension bar and front and back plate requires sufficient rigidity of the assembled structure for acceptable deflection due to the yoke weight with the anticipated magnet support system. The structural stiffness is determined by the product, EI , where E is the effective elastic modulus of the structure and I its moment of inertia. The effective EI product is computed in the usual way, except that the stiffness contributed by the lamination uses an elastic modulus $E_{\text{lam}} \approx \frac{E_{\text{steel}}}{60}$. This is approximately the slope of the final $\frac{\text{Pressure}}{\text{Strain}}$ compression curve for the laminations. The expression for the structural stiffness is;

$$EI = E_{\text{lam}} I_{\text{lam}} + \sum_{\text{bars}} E_{\text{steel}} (I_{\text{bar}} + A_{\text{bar}} \times \bar{y}^2), \quad (9.2)$$

where the I 's are the expressions for the individual moments of inertia about the centerlines of each bar, A 's are the areas and \bar{y} 's are the distances from the assembly centerline to the centerline of the individual bars.

Some of the features of the designs are listed as follows:

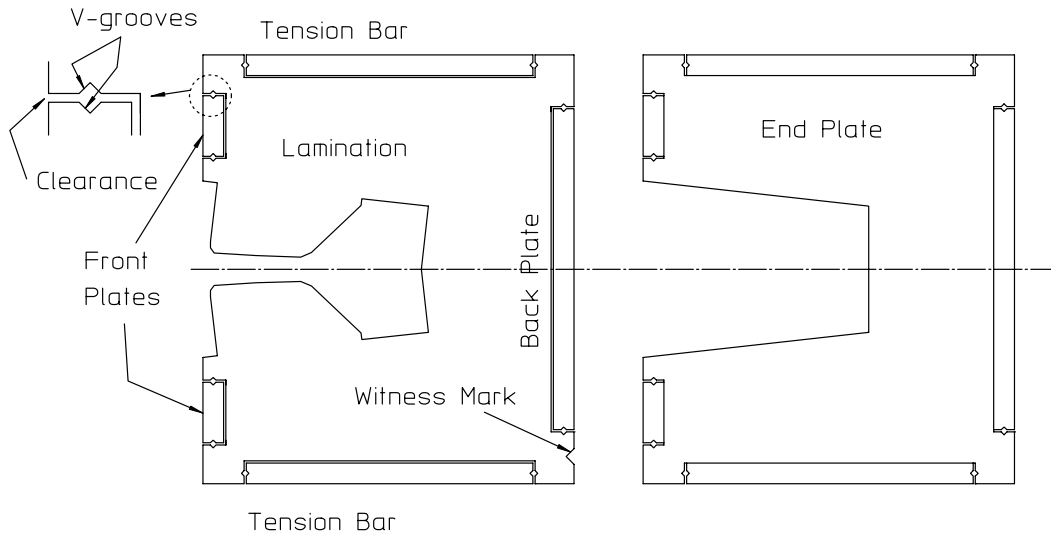


Figure 16 Bars, Laminations and End Plates

1. In addition to the overall shape of the lamination, cutouts are provided for the installation of the tension bars and back and front plates.
 - (a) The cutouts are sized to provide substantial clearance ($\gtrsim 3 \text{ mm}$) between the bars and the laminations.
 - (b) V-grooves are cut in the laminations at both edges of the cutouts for each bar.
 - (c) A witness mark is provided so that, when the laminations are flipped about their horizontal centerlines, the flipping will be indicated on the yoke assembly.
2. V-grooves are machined on the edges of all the bars corresponding to the v-grooves in the laminations.

End Plate Design

The end plates are fabricated from flat grounded solid steel plate. They have substantially the same cross section as the lamination except that the pole tips are absent and the cutouts for the tension bars and front and back plates have the same depth as the plate and tension bar thicknesses. With this configuration, when the structure is assembled, the end plate cutouts ensure clearance is maintained between the laminations and the tension bars and the front and back plates.

Core Assembly

The mechanical core assembly procedure can be described with the aid of several illustrations. Fig. 17 illustrates the stacking of the SPEAR3 gradient magnet laminations face down on a granite surface plate. Granite straight edges are used for transverse alignment. This tooling was selected because large, precise ground granite tooling can be purchased since granite tooling has long been used for optical and mechanical metrology. Figs. 18, 21 and 20 illustrate the steps described below:

1. The magnet back plate and two tension plates are assembled (permanently bolted and dowelled). The compression end plate and the magnet front end plate are then assembled and bolted.
 - (a) The magnet back and front end plates are fabricated from solid steel and do not extend to the pole contour. This is a similar design to the end plates for the welded quadrupole yoke, described earlier.
 - (b) The tension plates and the front and back frame plates (which are assembled later) can be machined with generous tolerances. This is because the clearance between the straight stacked laminations is large.
2. Hydraulic jacks are installed symmetrically between the compression end plate and the magnet front plate.
3. The tension plates are drilled with a series of holes so that the compression end plate can be moved as more laminations are stacked in the frame and the assembled yoke grows to its final length.
4. The glued end stacks and a portion of the laminations are stacked between the tension plates and the front and back end plates and compressed.
 - (a) As described in the stacking, compression and gluing of the quadrupole yokes, the laminations are added in small length increments and occasionally flipped about their centerline and recompressed so that the entire core does not have to be compressed at once.
 - (b) Partial laminations can be inserted occasionally to ensure that the lengths of the edges of the compressed core are equal.
5. When the final core length is achieved under the final compression load, the end plate is permanently bolted and doweled to the tension plates.
6. Since the lamination compression load has been transferred to the tension plates by bolting and dowelling, the hydraulic jack pressure can be released and the jacks removed without altering the geometry.

7. The two tension bars and the front and back end plates are parts of a rigid frame to which the laminations can be secured. The laminations are secured to the tension plates by filling the space between the laminations and the bars, provided by the v-grooves in the bars and in the laminations, with steel loaded epoxy (trade name Devcon^(R)).
 - (a) The steel loaded epoxy is extruded into the space provided by the v-grooves in the laminations and in the tension bars using a pneumatic applicator.
 - i. A tube is installed on the applicator.
 - A. The ease or difficulty in extruding the steel loaded epoxy in the space provided by the v-grooves depends on both the length and internal diameter of the tube and the viscosity of the steel loaded epoxy. A viscous mixture is preferred since a more fluid mixture will leak out of the space. There was no problem extruding a viscous mixture in the short (0.75 meter long) ALS gradient magnet since a 0.4 meter tube could be employed when applying from both ends of the core. However, there was a great deal of difficulty in extruding the viscous material in the longer (1.45 meter long) SPEAR3 gradient magnet. A less viscous material was selected and means of temporarily providing barriers to prevent the leakage of the material was employed.
 - B. For longer magnets, it is suggested that a large v-groove size be used so that a larger diameter extrusion tube can be inserted. Experiments can be performed prior to completing the design of the v-groove to determine the size required to ensure that extrusion of the viscous steel loaded epoxy can be accomplished for the required length of magnet.
 - ii. Transparent tape is affixed to the external space, covering the gap between the bars and the laminations.
 - iii. The tube is inserted in the space from the end of the magnet and the steel loaded epoxy is extruded as the tube is withdrawn.
 - (b) The steel loaded epoxy is allowed to cure at room temperature.
 8. After curing, the combination of the end plates, tension bars and the laminations are sufficiently rigid so that the structure can be rotated.
 9. After rotation, the front and back plates are installed, bolted and dowelled and step 7, the filling of the v-groove spaces with steel loaded epoxy, is repeated in the spaces between the front and back plates and the laminations.
 10. After all the epoxy has cured, the ends of the tension bars are sawed or machined off.

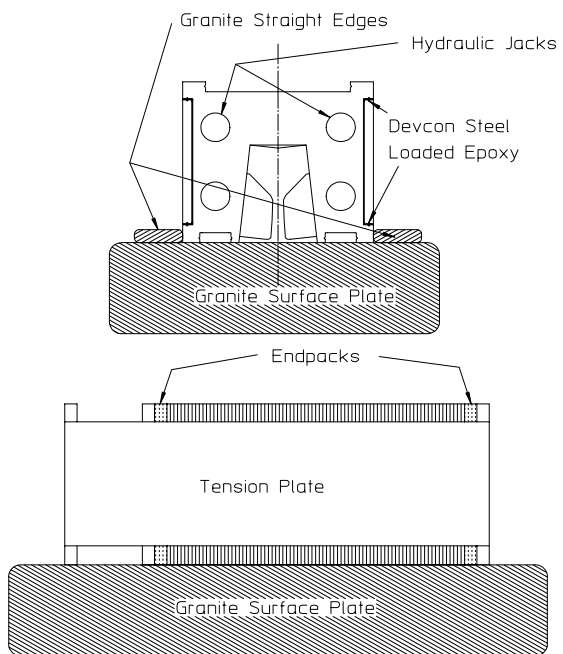


Figure 17 Assembly on Granite Surface Plate

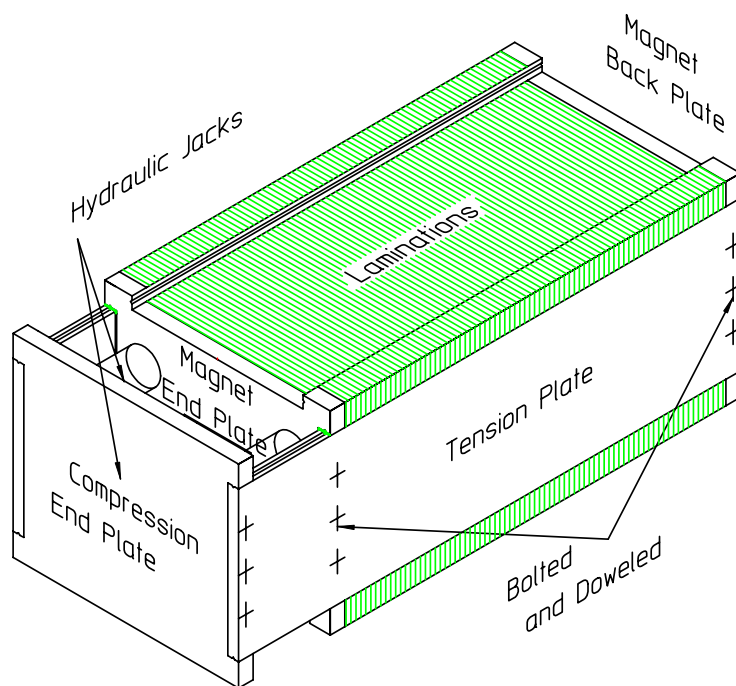


Figure 18 Core Compression

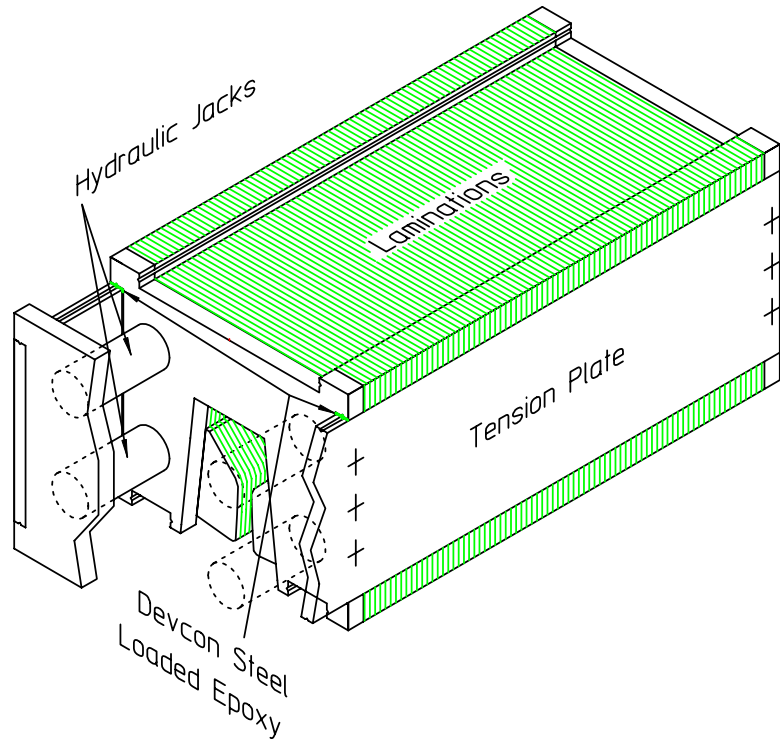


Figure 19 Schematic Assembly Showing Hydraulic Compression Jacks

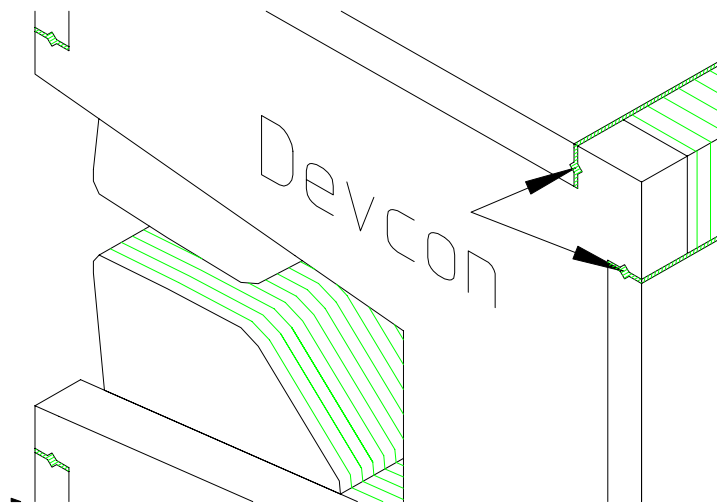


Figure 20 Steel Loaded Epoxy "Dowels"

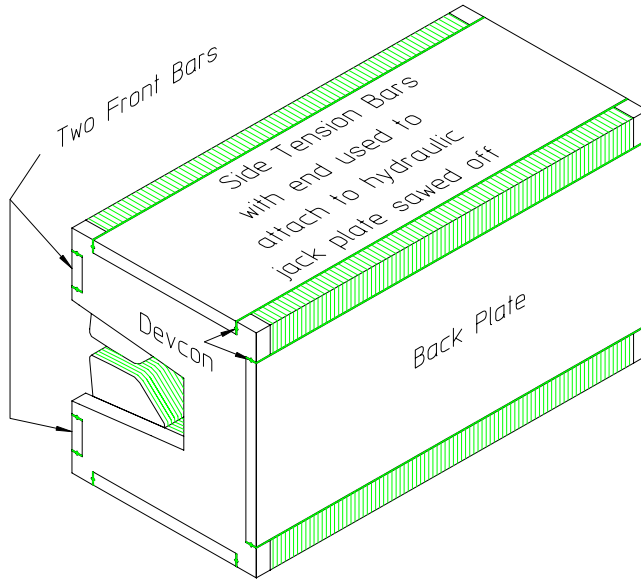


Figure 21 Assembled Gradient Magnet Core

9.7 Core Grounding

Safety and operating issues need to be addressed, not only for the magnet assembly, but for its components. Safety rules require that all non-powered accelerator components be grounded to prevent the buildup of static charge. It is usually good practice to identify a single grounding point and attach grounding straps from the magnet core to this point. In order to ensure that a single point on the yoke can be identified for attachment of the grounding strap, all the yoke components must be electrically connected. For glued and mechanically assembled cores, a small weld bead is added to the outside surface of the yoke so that each of the individual laminations are electrically connected. The weld is illustrated in fig. 22.

9.8 Chapter Closure

Physics specifications for accelerator magnets require excitation reproducibility and a spectrum of small amplitude integrated multipole errors. These field properties are dominated by the properties of the fabricated magnet yokes. Good magnet performance require the iron properties of the magnets to be symmetric and reproducible. Although symmetry and reproducibility can be achieved for yokes fabricated from both solid and laminated steel, these properties are more easily achievable with laminations by sorting. Sorting is also possible with the pieces used to fabricate solid steel yokes. However, even if magnetic steel properties of solid steel yoke pieces for a single family of magnets can be made identical, eddy currents, caused by rapid changes in excitation, can locally excite small regions of the magnet and cause these regions to

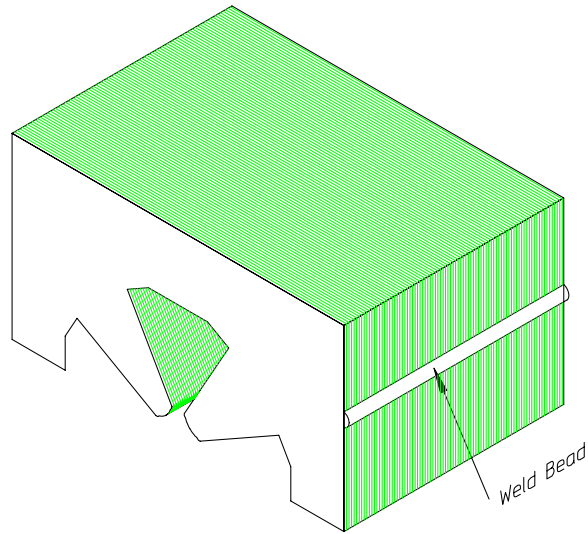


Figure 22 Grounding Weld Bead

locally undergo large hysteresis excursions and change the magnet properties of the steel. When solid core magnets undergo very fast excitation changes (ie. due to accidental power supply shutdown), the magnets must be reconditioned at currents much higher than their required excitation to restore all the steel properties so that all the yoke steel will operate along the same hysteresis curve. Because of these issues, most modern accelerator magnets are fabricated using stamped laminations. Most of the chapter is devoted to magnet yokes fabricated using laminated steel.

Previous chapters discussed the two dimensional design of magnets. Three dimensional fringe fields, which can compromise the integrated magnet uniformity, are discussed. Means of visualizing the dipole and quadrupole fringe fields are discussed. The shapes of pole end chamfers and the empirical process of developing the shapes and depths of these three dimensional cuts are listed.

In addition to the steel properties and three dimensional fringe fields, mechanical yoke fabrication and assembly errors can contribute to random integrated multipole errors. The multipole errors resulting from mechanical fabrication and assembly errors can be far more serious than those associated with iron and three dimensional effects. Random multipole errors have low indices (which do not reduce quickly near the center of the magnet) and can have skew as well as real components. Because of the potential seriousness of these errors, it is imperative that magnet yokes be made with high mechanical precision. Three yoke assembly methods are discussed. All three methods can result in precise yoke assembly resulting in magnets with high quality fields. Welding and gluing are employed for shorter magnets. A great deal of the discussion is devoted to describing the mechanical yoke fabrication

processes, which were developed to respond to the needs for fabricating mechanically precise yokes for larger (≥ 0.6 meters) magnets.

9.9 Chapter Appendix

Derivation of the Nonlinear Equation

The expression for the bend angle in a charged particle beam orbit is

$$B\rho\theta = \int Bds,$$

where s is the parameter describing the particle beam path. Differentiating the expression,

$$B\rho \frac{d\theta}{ds} = B(x, z), \quad (9.3)$$

where the coordinates, (x, z) , are the space coordinates along the horizontal plane. For a straight gradient magnet, $B(x, z) = B'x$ (the field varies linearly with the transverse coordinate, x). Using the lattice nomenclature for the quadrupole, the gradient is described by the k factor where $B' = B\rho K$. The units for K are expressed in units of $length^{-2}$ for the quadrupole. Substituting into eq. (9.3),

$$\begin{aligned} B\rho \frac{d\theta}{ds} &= B\rho Kx, \\ \text{or rewriting, } \frac{d\theta}{ds} &= Kx. \end{aligned} \quad (9.4)$$

The angle can be expressed trigonometrically as

$$\begin{aligned} \theta &= \tan^{-1} \frac{dx}{dz}, \\ \text{and } \frac{d\theta}{dz} &= \frac{\frac{d^2x}{dz^2}}{1 + \left(\frac{dx}{dz}\right)^2}. \end{aligned} \quad (9.5)$$

But,

$$\frac{d\theta}{ds} = \frac{d\theta/dz}{ds/dz}, \quad (9.6)$$

and

$$\begin{aligned} ds &= \sqrt{dz^2 + dx^2} \\ \frac{ds}{dz} &= \sqrt{1 + \left(\frac{dx}{dz}\right)^2}. \end{aligned} \quad (9.7)$$

Substituting eqs. (9.5) and (9.7) into (9.6), the expression for $d\theta/ds$ is given by

$$\begin{aligned} \frac{d\theta}{ds} &= \frac{d\theta/dz}{ds/dz} = \frac{\frac{d^2x}{dz^2}}{1 + \left(\frac{dx}{dz}\right)^2} \frac{1}{\sqrt{1 + \left(\frac{dx}{dz}\right)^2}}, \\ &= \frac{\frac{d^2x}{dz^2}}{\left[1 + \left(\frac{dx}{dz}\right)^2\right]^{\frac{3}{2}}}. \end{aligned}$$

Substituting into eq. (9.4) yields, finally, the nonlinear differential equation

$$\frac{\frac{d^2x}{dz^2}}{\left[1 + \left(\frac{dx}{dz}\right)^2\right]^{\frac{3}{2}}} = Kx, \quad (9.8)$$

which can be solved by numerical integration.

Note that if one assumes dx/dz is small, the differential equation simplifies to the linear expression

$$\frac{d^2x}{dz^2} = Kx,$$

whose solutions are the hyperbolic sine and cosine. For even functions (those symmetric about $x = 0$), the approximate solution is the hyperbolic cosine function.

Chapter 10

MAGNET COIL FABRICATION

10.1 Introduction

Laboratories and manufacturers have different preferred fabrication techniques. One can usually obtain lower cost coils by allowing manufacturers to develop bids using their preferred techniques and practices. However, it is always useful to understand the different techniques and their strengths and limitations so that one can make informed choices for the acquisition of magnet coils satisfying unique accelerator and/or facility constraints or needs. It is also useful to understand that winding configurations are constrained by practical limitations to avoid specifying a coil which cannot be physically realized.

Occasionally, coil designs are completely developed and fabrication techniques are fully specified to ensure that certain unique needs are satisfied. This technique is called building to print. While assuring that coil fabrication techniques satisfy the end needs of the coil, building to print can potentially release the vendor of the responsibility for the design. Moreover, if the specified fabrication technique differs from the standard technique employed by the manufacturer, high costs may result.

Certain minimum performance requirements are required for magnet coils. A description of measurements and tests performed on coils is listed for inclusion in specifications for acquisition of manufactured coils. Decisions for the means used to acquire coils can be difficult. Example coil designs and coil manufacturing processes are described in order to enhance the understanding of the design and manufacturing processes and reduce this difficulty.

The following are examples of coil fabrication techniques, processes and tests. These examples assume that coil engineering designs and parameters have been developed and specified by the magnet engineer/designer.

10.1.1 Conductor Size and Turn to Turn Insulation

The conductor size is selected by the magnet engineer/designer based on magnet requirements and power supply, power distribution and cooling constraints for the required facility. Convectively cooled magnet coils made with solid conductors are usually wound from round or square copper conductors up to 3 mm. maximum cross section. This size conductor is usually preinsulated with a baked on plastic coating (Formvar[®] or Polythermaleze[®]). Normally, the conductor catalogue will list the

maximum dimension of the insulated conductor so that the final wound coil size can be accurately predicted.

Water cooled conductors can be wound from square or rectangular hollow copper conductor, divided among two size ranges. Smaller hollow copper conductor ($\leq 6\text{ mm}$. maximum dimension) is used to wind individually powered, low current magnet coils. Magnet coils using these conductors are most efficiently wound if the conductor is preinsulated. The conductors used for ALS, PEPII and SPEAR3 quadrupole and sextupole magnet coils were preinsulated with a combination of Dacron^(R) and glass fiber. There are several US and European manufacturers who specialize in a technique of wrapping small conductors with these fibers. These same manufacturers will inform the buyer that they will not insure the integrity of insulation for conductors with dimensions $> 6\text{ mm}$. The fine fibers break and the insulation flakes off when larger conductors are bent around a tight radius when winding coils. This is due to the growth in the vertical dimension at the inside radius of the conductor when winding around a tight radius (keystoning). The insulation manufacturer will specify the final insulation thickness for the smaller conductor sizes so that the final wound coil size can be accurately predicted.

Square and rectangular hollow conductors with dimensions $> 6\text{ mm}$. are employed for higher current magnets and are usually insulated by wrapping the conductor in two layers half lapped adhesive mylar tape and woven glass or Dacron tape as the conductor comes off the spool and before winding on a mandrel. (Half lapped is a term to describe the partial overlap of the previous insulation winding by the following winding to ensure that no gaps remain.) Woven Dacron tape is often substituted for glass tape when the conductor must be pounded in order to ensure tight bend radii around a winding mandrel. Woven glass tape often disintegrates under these conditions. The mylar tape is used to ensure that a continuous insulator is present between the individual conductors so that intermittent turn to turn shorts are avoided. Many coil designers eliminate the mylar insulation and insulate only with the woven tape. The woven tape provides a network for the distribution of the epoxy used to encapsulate the coil assembly. The thickness for this insulation system should be computed as a bit more (say 125%) of twice the thickness of the adhesive mylar tape and woven fabric tape to predict the final wound coil size. (Twice the thickness since the layers of tape are overlapped.)

10.1.2 Coil Winding

Impractical coil configurations can be specified by the magnet engineer/designer not familiar with winding techniques or limitations. When laying out a coil, a natural tendency is to assume that a simple two dimensional configuration can be wound within a simple three dimensional projection of the two dimensional shape. This is not true. Layer to layer and row to row transitions require additional space. Moreover, row to row transitions precess around a coil so that they take up more longitudinal room than anticipated. Designs of row to row transitions often assume that the transitions stack one above the other. Typically, a coil has one more layer

or one more row at one end where transitions take place (usually the lead end of the wound coil) than the two dimensional cross-section. Also, if a tapered coil is required, the magnet engineer/designer can easily forget that the coils are wound under tension and it is extremely difficult to wind down a slope (from a wider turn to a narrower turn). The wider turn tends to move down the taper when wound under tension unless each turn is temporarily supported until the following turn is wound. Tapered coils are nearly always required for quadrupole magnets.

Fig. 1 of a 36 turn quadrupole coil and the following descriptions are included to provide an example to illustrate a coil winding process. This example is wound in two layers, with each layer wound up the taper in opposite directions.

1. The length of the required conductor is estimated and about half is coiled off to the side of the winding mandrel.
2. Layer 1 is wound from the center of the length of conductor and is wound up the tapered mandrel in the clockwise direction (when viewed from above) until half (18) of the required turns are wound.
 - (a) A spacer is placed under the first row to provide room for the conductor to transition from layer 1 to layer 2.
 - (b) After each bend around a corner, the conductor must be set using a bakelite (or other non-metallic tool) and a hammer to avoid elastic springback.
 - (c) The conductor should always be kept under tension when winding to minimize elastic springback and to ensure that the conductor is wound tightly and the coil package falls within the mechanical limits of the design.
3. The reserved coiled conductor is straightened out and the second layer is wound in the counterclockwise direction (when viewed from above) up the taper over the first layer until all of the required number of turns (36) have been wound.
4. After all the windings have been completed, a ground wrap is of woven fiberglass tape is wound around the completed coil to secure its shape.

The actual illustrated quadrupole coil requires 72 turns. The remaining 36 turns are wound in layers 3 and 4 in the identical manner as used for layers 1 and 2 over the first two layers. The leads are brazed together after the coil is vacuum impregnated to create a single coil with the required 72 turns.

Keystoning

Keystoning is a term used to describe the growth of the conductor dimension in the perpendicular direction to the bending plane when the conductor is bent in a tight radius. It is caused by the vertical growth in the conductor on the inside radius of the

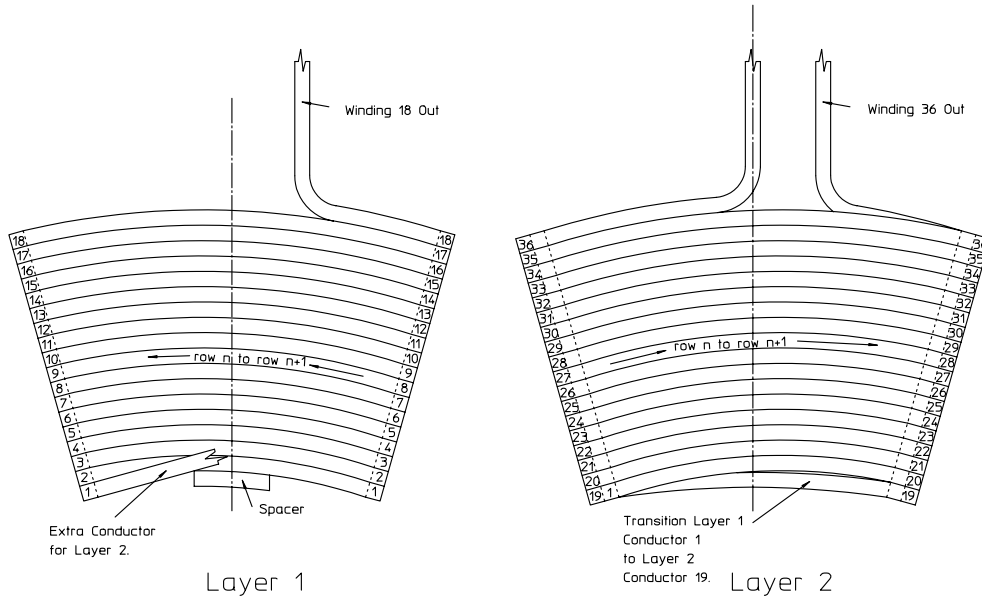


Figure 1 36 Turn Quadrupole Coil

bend compensating the longitudinal compression of the material on the inside radius of the conductor. In general, if a conductor is bent with an inside bending radius $\leq 3 \times$ conductor width, the conductor height will increase. Although curves for this effect exist, they are a bit difficult to scale. Larger conductors and rectangular conductors bent the hard way (in the plane of the wider dimension) undergo greater growth than smaller square conductors. A good conservative constant factor often used to anticipate the geometric growth of the coil is to assume a 5% growth in one dimension of the conductor. This growth must be factored into the final size of the assembled coil, especially if the coil is vacuum impregnated and a coil mold is fabricated.

Mirror Image

The electrical current in the coils for adjacent poles of a magnet reverse directions. There is a natural tendency to want to develop layouts for magnets using mirror image coil configurations for alternate poles. This is an unneeded manufacturing complication resulting in doubling the inventory of coil designs and increasing the potential for assembly errors. Identical coils can be installed on all the poles of the magnets using the coil to coil electrical bussing to alternate directions of the electrical current for adjacent poles.

10.1.3 Coil Potting (Encapsulation)

Once the coil is wound, some means must be employed to maintain its shape and to protect the conductor from dirt and moisture which can cause electrical shorts. Manufacturers use several methods for coil encapsulation. Some of the techniques and their advantages and disadvantages are described in the following sections.

Simultaneous Epoxy Impregnation and Winding (Wet Layup)

This method is employed for coils wound from small solid conductors with baked on plastic insulation. Uncured epoxy is painted on the surface of the coil as it is being wound. A few turns of woven fiberglass tape is wound around the completed coil and this ground wrap is painted with uncured epoxy. The assembled coil is then cured in an oven.

B-stage Epoxy Encapsulation

Woven fiberglass tape can be purchased impregnated with thermo-setting epoxy. If using this method for large conductors ($\geq 6\text{ mm.}$), the individual conductors are wrapped with the impregnated fiberglass tape prior to winding. A final layer of this tape is wrapped around the wound coil and secured. The tape becomes a ground insulation for the coil. The wrapped coil is installed in an oven and cured using the appropriate thermal cycle specified by the B-stage[®] tape supplier.

This method is the cheapest of the hollow conductor coil encapsulation techniques. However, the encapsulation is porous. Dirt and/or moisture can contaminate the coil and can potentially cause turn to turn shorts. This method is not recommended for magnets operating in a dirty or humid environment. Moisture can condense on a cooling coil after the power is turned off and migrate into the epoxy pores.

Cocooning

Cocooning is similar method to B-stage epoxy encapsulation. The difference is that the winding is performed using insulated conductor without the B-stage material impregnation. For small conductors, the Dacron[®]-glass fiber insulated conductor is used. For larger conductors, the mylar tape plus woven glass tape insulation is used. A layer of the B-stage impregnated glass tape is wound around the completed coil to form a water-tight skin. This skin is partially cured so that the coil with its skin forms a volume containing the wound coil. The volume is then filled with a epoxy mixture and cured. This method results in a less porous product. However, voids can still be present and the coil is subject to a lesser degree of the same potential contamination as the B-stage encapsulated coils.

Both the B-stage and cocooning methods result in coils whose final mechanical dimensions are unpredictable. Therefore, if the coil size and/or shape are crucial

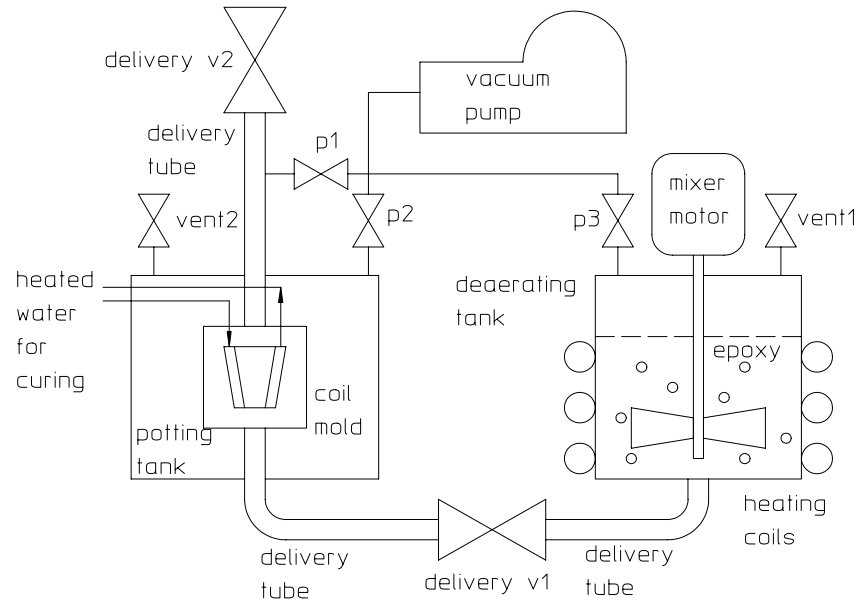


Figure 2 Vacuum Impregnation System Schematic

to installation (for instance between the poles of a two piece quadrupole), or if limited clearances are available between the coil and other mechanical constraints (for instance a vacuum chamber), these method may present potential problems.

Vacuum Impregnation

Vacuum impregnation results in the most robust product with the most predictable mechanical shape. It is also the most expensive process since it requires the fabrication and assembly of tooling and equipment. For accelerator magnet coils, the tooling and equipment can be capitalized over the large numbers of coils fabricated using the equipment. Vacuum impregnation has been used for the ALS and SPEAR3 magnet coils. These magnets required tight mechanical tolerances for coil installation between the poles of the yokes. The tight mechanical tolerances were also needed since the magnets are installed with minimum clearances between their elements and the vacuum chamber and other accelerator components. The PEPII Low Energy Ring magnets also employed vacuum impregnated coils. The PEPII tunnel environment can be humid and dirty. Fig. 2 is a schematic of a vacuum impregnation system.

The major elements of the vacuum potting system are:

1. The epoxy deaerating tank.

- (a) The deaerating tank is fitted with mixing vanes connected through a vacuum seal to a mixing motor.
 - (b) Some epoxy formulations require heating when mixing the components. A heater is attached to the tank so that the epoxy can be mixed and deaerated at warm temperatures.
2. The potting tank.
- (a) Small potting molds are sometimes difficult to seal since space for gaskets is limited. These molds are constructed water tight, so that they can hold the epoxy fluid but cannot be adequately evacuated. Water tight molds are installed in a potting tank so that they can be thoroughly evacuated.
 - (b) Potting molds for larger coils can be sealed with gaskets and evacuated. For larger coils, the potting tank is often eliminated.
3. The assembled coil mold.
- (a) The cavity size for the coil mold defines the outside geometry of the completed coil.
 - (b) At least two holes for the delivery of the epoxy should be provided. The input hole must be drilled at the lowest point in the mold cavity and the output hole must be drilled at the highest point in the mold cavity.
 - (c) The coil illustrated in the figure is a quadrupole coil with a tapered inside surface. The ends of the wound coil are flat. A slight taper must be machined into the outside surface of the inner mold piece and the inside surface of the outer mold piece at the ends to facilitate the removal of the cured coil from the mold.
 - (d) The schematic figure illustrates heated water connections to the assembled coil mold. This configuration assumes that the thermo-setting epoxy is cured by circulating heated water through the coil water passage(s).
4. A mechanical vacuum pump.
- (a) Valves are attached so that the vacuum pump can be connected to the deaeration tank, the potting tank and the coil mold output delivery tube.
5. Delivery tubes.
- (a) The delivery tubes should be transparent so that transfer of the uncured epoxy can be monitored.

- (b) The delivery tube connected to the top of the mold should be at least a meter long before the vacuum valve, p1. Since the epoxy shrinks during the cure, the excess delivery tube length on the mold exit acts as a reservoir, providing excess epoxy during the curing process and ensuring that there are no voids in the encapsulated coil.

Epoxy Formulation

The choice of the epoxy formulation depends on the application. Epoxy formulations with low uncured viscosity is preferred for vacuum impregnation to ensure complete filling of all the pores in the glass tape insulation. Mixing a heated formulation often reduces the viscosity and enhances the deairation. Formulations with a long uncured pot life and higher cure temperatures are preferred since higher curing temperature is often accompanied by better radiation resistance. Frequently, magnets are operated in very high radiation environments. For coils for these magnets, powder alumina can be mixed with the epoxy to enhance the radiation resistance of the organic potting compound.

Vacuum Potting Procedure

Numerous accelerator magnets require many coils and so several potting molds are built for each type of coil. Normally, the volume of epoxy encapsulant per coil is small. Often, many coils are encapsulated simultaneously to reduce the labor of mixing and deaerating the epoxy. The following is a summary of the procedure developed over several years at LBNL for in house fabrication of magnet coils using vacuum potting techniques. The same process was used at IHEP in China for the manufacture of the coils for the PEPII and SPEAR3 magnets.

1. The inside surfaces of the mold cavity are coated with a parting compound to enhance removal of the cured coil.
2. The wound and ground wrapped coil is placed and sealed in the mold. The sealed mold assembly is placed in the potting tank.
 - (a) Silicone rubber or other sealant compound will be needed to locally seal the coil leads exiting the mold.
3. The components of the epoxy formulation are measured and mixed together and the mixture is poured into the deairation tank.
4. The deairation tank is covered and the mixture is mixed using the electric motor attached to the mixing vanes.
 - (a) If the formulation requires heating during the mixing process, the heating coils may be energized during the mixing and deairation process.

5. The deeration tank is evacuated by opening the valve p3 to the mechanical vacuum pump.
 - (a) Dearation is indicated by bubbles forming in the mixture and coming to the surface of the epoxy as a foam.
 - (b) Dearation can often be enhanced by cycling. That is, the vent valves are opened and the tank is reevacuated several times.
 - (c) Dearation is complete when generation of bubbles nearly stops and the foam layer on the surface of the epoxy disappears.
6. The potting tank and the coil mold are evacuated by opening valves p1 and p2 to the mechanical vacuum pump.
 - (a) Larger coils can be installed in gasketed molds which are vacuum tight. These molds need not be installed in a vacuum potting tank and can be evacuated by opening the valve p1 which connects the mold to the vacuum pump.
7. The dearedated epoxy formulation is transferred under atmospheric pressure to the mold by simultaneously opening delivery v1 and the deeration tank vent1.
8. Transfer is complete when all the transfer tubes are filled. The transfer tube connected to the top of the mold should be nearly filled to the pump valve p1 before p1 is closed.
9. After filling the mold, delivery v2 and vent2 are opened to bring everything up to atmospheric pressure.
10. The epoxy is cured at elevated temperatures.
 - (a) Heated water can be circulated through the coil.
 - (b) The filled mold can be removed from the potting tank and placed in a curing oven.
 - i. The delivery tubes at the top and bottom of the mold are cut off and raised so that the surface of the epoxy in the tubes is above the highest point in the mold.
 - ii. After cure is complete, it will be noted that the surface of the cured epoxy has receded into the tube because of shrinkage during the cure. The lengths of the transfer tubes provide a small reservoir for the uncured epoxy to replace the volume of the cured epoxy shrinkage in the mold.

Coil Finishing

A finished coil, ready for installation on the magnet yoke, requires additional parts. These parts include water fittings, flags for the connection of electrical busses and a mounting plate for the installation of thermal interlocks. Good practice requires these parts to be attached to the coil leads robustly enough so that they cannot be accidentally broken off. Water fittings need to be attached with leakproof joints. Electrical connection flags require low electrical resistance joints. Thermal interlock mounting plates require low thermal resistance joints. All these parts have historically been attached to the coil leads using high temperature brazing material (silver solder). High temperature material rather than low temperature lead-tin solders have been specified for these joints because of the inevitable need to repair broken joints. Broken joints originally made using high temperature brazing material can be repaired using lower temperature compounds. Eventually, low temperature solders can be used to repair joints which have been repeatedly broken and repaired. Because of the need to use high temperature solders for the initial installation of these parts and the high thermal conductivity of the copper conductor, it is necessary to protect the organic encapsulation compound from the conducted heat. This is done using the same technique used to braze copper plumbing by keeping some distance between the brazing area and wrapping the area that needs to be protected by a damp cloth wrapped around the conductor. Brazing of parts to the finished coils requires some craftsmanship to secure sound joints while simultaneously isolating the heat from the thermally sensitive parts of the encapsulated coil.

Fig. 3 illustrates some of the points of the finished coil.

1. The water fittings are soldered at the ends of the leads. The illustration indicates the water flow direction.
 - (a) The water fittings are different sizes with the water outlet fitting slightly larger than the water inlet fitting. This feature avoids the possibility of connecting both ends of the circuit to the same manifold, "deadheading" the circuit. For small conductors, this is often not possible and the hoses for the outlet and inlet sides of the circuit must be clearly labeled to avoid misconnecting both ends of the coil to the same water manifold.
2. The flags for connecting the coil to coil busses are soldered close to the water fittings. The busses are convectively cooled and thus are limited to $j \leq \frac{1.5 \text{ Amps}}{\text{mm}^2}$ compared to the water cooled allowable current density, $j \leq \frac{10 \text{ Amps}}{\text{mm}^2}$. The heavier copper pieces used for the busses are mechanically attached to the yoke to avoid mechanical strain on the coil leads. Copper bussing supports close to the water fittings can reduce the bending stresses on the conductors due to the water tubes.

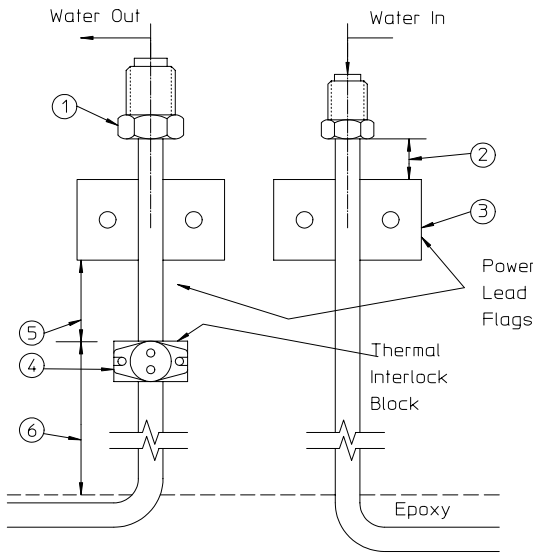


Figure 3 Brazing of Coil Parts

3. Slots machined in the power lead flags to receive the conductor ensure mechanical support during brazing and a good joint to the conductor.
4. The thermal interlock block must be located in a current carrying region of the conductor between the coil and the power lead flag. A thermal interlock located outside of the busses will not experience I^2R heating. The thermal interlock block is brazed to the water output leg of the hydraulic circuit where it can sense excessive water temperature rise or loss of water flow through the coil.
 - (a) A thermal interlock attached to the water input leg of the hydraulic circuit cannot sense high water temperature temperature due to the resistive heating of the coil.
5. Sufficient distance between the thermal interlock block and the power lead flags must be provided so that the thermal resistance between the conductor and the flag and power lead heat sink does not reduce the temperature rate of rise.
6. The distance between the closest brazed joint and the epoxy surface must be sufficiently large so that the brazing heat can be intercepted and prevented from damaging organic insulation.
 - (a) This distance also enhances the elastic compliance between the installed coil and the bus connection. This compliance makes it easier to install the

rigid bus connection and enhances the mechanical and electrical contact between the flags and the bus bars.

10.2 Coil Failures

Magnet coils can potentially fail in several different ways. Mechanically, the manufacturer may wind too many or too few turns or the completed coil outside envelope may not satisfy dimensional tolerances. Hydraulically, the water passage may leak or be partially or completely blocked. Electrically, the insulation system may be poor or incomplete resulting in intermittent or complete turn to turn shorts or shorts to ground. Manufacturing specifications are written to supplement the mechanical layouts or drawings which make up the package of documentation for the acquisition of magnet coils. The specifications describe the minimum manufacturing requirements reducing the chances of product failure. Required tests and measurements are included in the specification to ensure and document that coil performance requirements are achieved.

10.2.1 Specifications

The specifications list the computed values of the coil parameters such as the resistance and anticipated hydraulic flow at a specified pressure drop. These computed values can be later compared with measured values for completed individual coils. Specifications also include minimum shop and fabrication requirements, listed to ensure that failures are minimized. Some of these requirements are listed.

1. Coils should not be wound in a machine shop environment.
 - (a) Metallic chips in a machine shop can contaminate the coil during winding later causing intermittent or complete turn to turn shorts.
 - (b) Machining lubricant can contaminate the insulation, potentially jeopardizing the encapsulant bond and the insulation performance.
2. A single hydraulic circuit must be wound from a continuous unspliced length of conductor.
 - (a) Discontinuities in the hydraulic passage due to a conductor splice can cause blockage in the hydraulic circuit due to particulate contamination of the coolant. If the joint is in the middle of the circuit, it is very likely buried in the encapsulated coil and impossible to repair.
 - i. Splices may be difficult to locate in a spool of conductor from a manufacturer. A test involving blowing a ball $\leq 60\%$ of the coolant hole diameter in the length of conductor prior to winding is occasionally required.

Many more requirements are listed in a typical coil fabrication specification. These requirements can be obtained from public domain specifications previously published by different laboratories to purchase magnets and their coils.

10.2.2 Measurements and Tests

Measurements are compared with computed coil parameters. Tests are performed to verify that minimum requirements are satisfied.

Hydraulic Measurements and Tests

Flow measurements made at the design pressure drop are made and recorded for each water circuit for each coil. The water temperature at the time of the measurement as well as the flow rate and pressure drop should be recorded. The water temperature is important since water kinematic viscosity changes. The measurements are compared with flow computations made using the kinematic viscosity at a fixed temperature.

Leaks usually occur at brazed water fitting joints. Leaks are normally detected by pneumatically pressurizing a sealed water circuit and monitoring the pressure for some fixed time. Leaks are indicated by rapid or gradual loss of pneumatic pressure in the sealed circuit.

Electrical Measurements and Tests

1. The ambient temperature is recorded and coil resistance is measured with a bridge.
 - (a) The measured resistance is corrected to the resistivity temperature for comparison to the coil resistance computation.
 - (b) A bridge is used since other devices, such as voltmeters, require a small current which can change the coil temperature and the material resistivity.
2. Insulation to Ground (HiPot Tests)
 - (a) Different tests are performed depending on the means used to insulate the completed coil. The general requirements for the test is that the isolated coil should be capable of holding twice the operating voltage plus 1 kV. At this test voltage, leakage current to ground should not exceed $2 \mu A$.
 - i. Coils insulated using the wet layup, B-stage and cocooning techniques should be wrapped in aluminum foil, the aluminum coil grounded and the coil leads connected together raised to the test voltage.
 - ii. Coils which are vacuum impregnated can withstand a more severe test by immersing the potted region of the coil in salted water and raising the coil leads connected together to the test voltage.

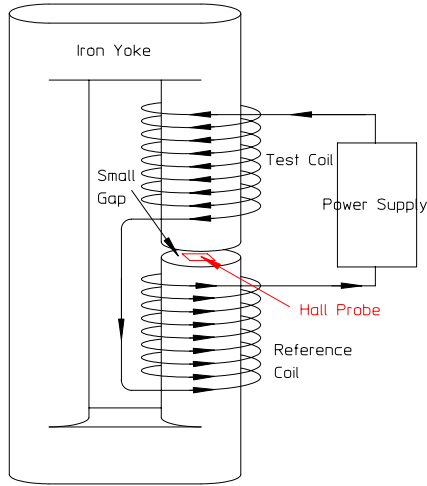


Figure 4 Coil Null Measurement Schematic

- iii. As in all high voltage operations, adequate safety equipment and procedures should be provided to protect the test personnel.
3. Dead turn to turn shorts.
- (a) Dead turn to turn shorts for coils with many turns are difficult to detect using resistance measurements. Resistance changes due to variations in the conductor cross-sectional area can be larger than the resistance change due to the effective change in the conductor length due to a dead turn to turn short.
 - i. A null measurement with two coils in a magnetic circuit can reveal differences in the number of turns in two otherwise identical coils. A schematic of the null connection is shown in fig. 4. A reference coil and the test coil are connected in opposite polarities. The errors in the number of turns can be measured using a Hall probe.

$$\begin{aligned}
 B &= \frac{\mu_0 NI}{gap} = \frac{\mu_0 (NI_{reference} - NI_{test})}{gap} \\
 &= \frac{\mu_0 I [N - (N - \Delta N)]}{gap} \\
 \Delta N &= \frac{B \times gap}{\mu_0 I}
 \end{aligned}$$

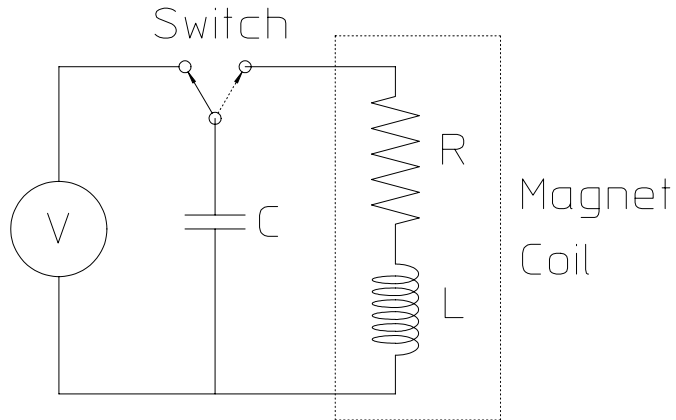


Figure 5 Impulse Test System

- (b) Resistance measurements are a more reliable means of detecting a dead turn to turn short for coils with fewer turns.
4. Intermittent turn to turn shorts can be measured using an impulse test.
- (a) To detect intermittent turn to turn shorts, it is necessary to generate many times the turn to turn voltage expected during operation. Since the impedance of a coil is primarily a low resistance and inductance, imposing a high voltage across the leads will lead to a high current and power which can damage the coil. Therefore, a dynamic rather than static test has been devised.
 - (b) The electrical parameters for a coil are its inductance and resistance. The coil inductance is changed by the presence of steel since its value depends on the magnetic stored energy of the magnet circuit. It is also changed by the presence of metallic objects which can support eddy currents since the eddy currents represent a circuit coupled by the magnetic field generated by the coil. Therefore, impulse tests must be made with the coil isolated from metallic or permeable material.
 - (c) The impulse test system schematic system is shown in fig. 5. In this system, a voltage source is used to charge the capacitor. The switch then connects the charged capacitor to the test coil while simultaneously isolating the power supply. The current then circulates in the closed circuit and the electrical energy stored in the capacitor is dissipated and reflected by the coil resistance and inductance.
 - (d) The differential equation describing the voltage for the continuous current

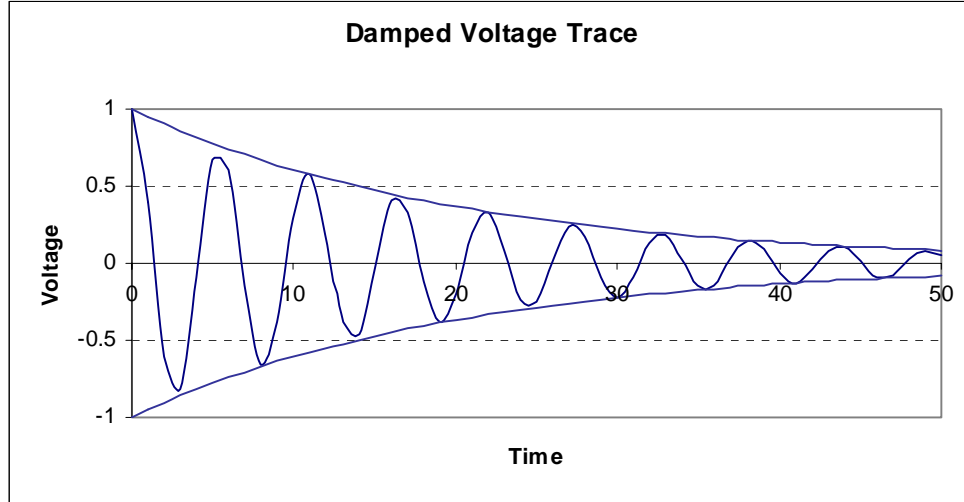


Figure 6 Underdamped Sinusoid

around the RLC circuit is

$$L \frac{dI}{dt} + RI + \frac{1}{C} \int I dt = 0 \implies \frac{d^2I}{dt^2} + \frac{R}{L} \frac{dI}{dt} + \frac{1}{LC} I = 0$$

- (e) The general form for the solution to this second order differential equation for an underdamped system is

$$I = e^{-\alpha t} (B_1 \cos \omega t + B_2 \sin \omega t),$$

where $\alpha = \frac{R}{2L}$ and $\omega = \frac{1}{(LC)^{1/2}}$.

- i. The complex or natural frequencies for this system are $s_1, s_2 = -\alpha \pm \sqrt{\alpha^2 - \omega^2}$. The system is underdamped only if $\alpha < \omega$ and the expression for the frequencies is complex. The size of the capacitor is selected so that an underdamped response can be obtained.

- (f) For the underdamped test system, the voltage response across the coil is

$$V(t) = V_0 e^{-\alpha t} \cos \omega t,$$

a damped sinusoid whose exponential damping time, $\tau = \frac{2L}{R}$, can be determined from the test voltage trace.

- (g) The typical signal is shown in fig. 6
5. The Impulse test procedures are as follows:
- (a) The coil is connected to the test equipment and a scope is connected to monitor the voltage signal across the leads of the test coil.

- (b) The voltage across the capacitor is raised to some low voltage, say 10 Volts. The voltage is switched across the test coil and the voltage trace is stored and photographed.
- (c) The voltage is raised at some arbitrary voltage increment and the test and scope trace photographs are repeated.
 - i. During the tests, the scope gain is adjusted so that the maximum scope amplitude of the damped signal is maintained.
- (d) The voltage is finally raised to the equivalent of 100 volts per turn or a maximum of approximately 1kV and the final test is performed.
 - i. A good coil will display the identical scope trace at all voltages.
 - ii. A coil with intermittent turn to turn shorts will display the identical scope trace until the turn to turn voltage exceeds some breakdown value. At some voltage level, the signal trace will change. In some cases, hash (static) will appear at the peaks of some of the first few sinusoidal traces. In other cases, the sinusoid frequency and/or the damping rate will suddenly change. The photograph of the stored scope image at the breakdown voltage can be compared with the photograph at the low starting voltages.

10.3 Chapter Closure

Unless a laboratory has an extensive engineering and manufacturing infrastructure, accelerator magnets are acquired by purchasing from manufacturers specializing in magnet or electrical equipment manufacture. One can select the coil geometry which optimize the purchase and operation of power supplies and power distribution systems and satisfy hydraulic cooling constraints without understanding detailed design or the manufacturing process. Fully developing mechanical detailed coil designs and their specifications to ensure delivery of a robust coil system is more difficult and can only be accomplished if one is familiar with the manufacturing and quality assurance processes. This chapter is written to describe methods used in past successful projects to acquire magnet coils which satisfied quality and reliability requirements for magnets installed in the challenging environment of large accelerators for reliable operation over the long operating life of typical accelerators.

The chapter describes the winding, encapsulation, measurements and testing of magnet coils. A sample quadrupole winding is described to illustrate the layer to layer and row to row transitions which must be anticipated. Different conductor insulation systems are described. The strengths and weaknesses of different coil potting techniques are listed and the vacuum encapsulation processes are described. Failure modes are described and means of developing specifications, measurements and tests to avoid these failure modes are listed.

Chapter 11

MAGNET ASSEMBLY

11.1 Introduction

Previous chapters covered the fabrication of the main magnet components, the yokes and the coils. A completed magnet requires the assembly of these major components, fabrication and assembly of electrical busses connecting the separate coils, provision of terminations for magnet power cables, assembly of the water cooling tubes to separate or integral water manifolds, installation and wiring of protective interlock systems and provision for any personnel safety related parts. This chapter reviews the methods employed in the past to complete the magnet assembly. It includes principles of design for the busses, the interlock system, the cable terminations and the hydraulic circuit to protect the and ensure long operating life for the magnet and its components. Bussing topologies are introduced which avoid unwanted magnetic fields.

Finally, safety rules and design principles applied to ensure personnel safety are listed.

11.2 Coil Supports and Bussing

Coils are normally assembled and mechanically secured to the yoke segment before the yoke segments are assembled. Previous examples of laminated quadrupole and sextupole yoke designs included holes through their poles for installation of bolts to ensure that the laminations do not separate. These bolts can be exploited to secure parts used to hold the coils in their coil slots. This releases the space radially outside of the coil and reserves this room for the bussing, cooling tubes and thermal interlocks. Quadrupole and sextupole magnets are typically smaller than dipole magnets. Their numerous coils require more bussing and cooling elements than the dipole coils. The radial area outside of the quadrupole and sextupole coil can become congested. Dipole magnets, on the other hand, are larger and coil supports can be anchored above the upper coil and below the lower coil. Coil supports are designed primarily to resist gravitational loads. Magnetic external loads are typically small and internal loads are generally directed radially outward.

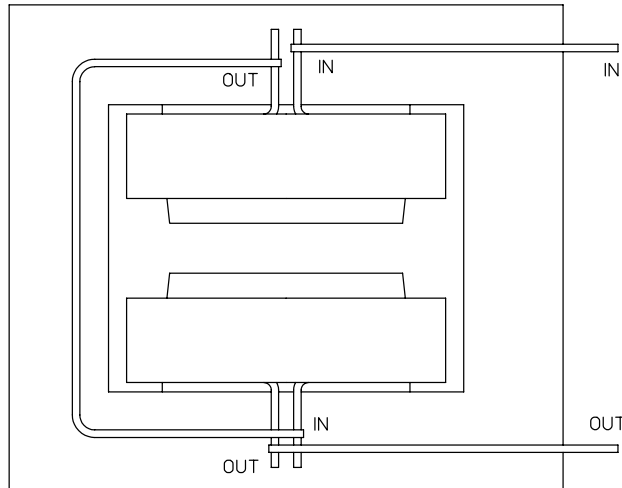


Figure 1 Incorrect Bussing Topology

11.2.1 Bussing

Bussing between the separate coils in a magnet normally uses solid copper bars and are convectively cooled. The copper bar cross-sectional area must be sized so that the maximum current density satisfies the current density limit for convectively cooled copper conductors, $j \leq \frac{1.5 \text{Amps}}{\text{mm}^2}$. Occasionally, when large currents need to be carried, water cooled conductor similar to the coil conductor is used for coil to coil bussing.

Bussing Topology

The topology and the support of the parts used to carry current from one coil to another is important. Fig. 1 illustrates the wrong topology for bussing a dipole. The conductor connecting the two coils wraps a one turn current carrying circuit around the beamline. This configuration generates a small but measureable solenoidal field. A solenoidal field can rotate the beam and mix the horizontal and vertical beam phases.

Fig. 2 illustrates the correct bussing topology for a dipole. Figs. 3 and 4 illustrate the correct bussing topologies for the quadrupole and sextupole, respectively. The routing of the busses returns the current in the opposite direction and avoids the solenoidal field. Good bussing practice places the busses near to each other.

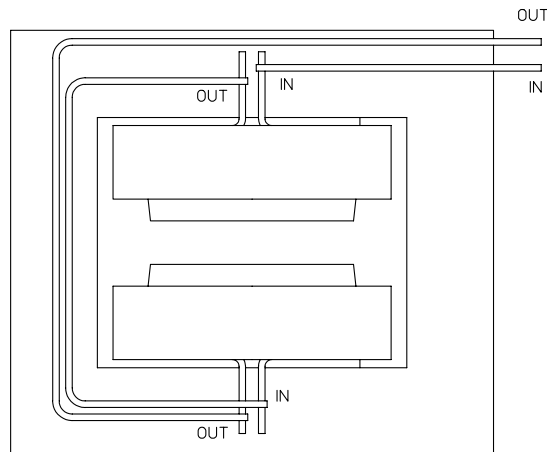


Figure 2 Correct Dipole Bussing Topology

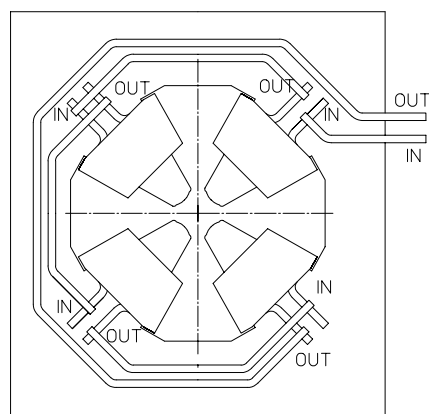


Figure 3 Correct Quadrupole Bussing Topology

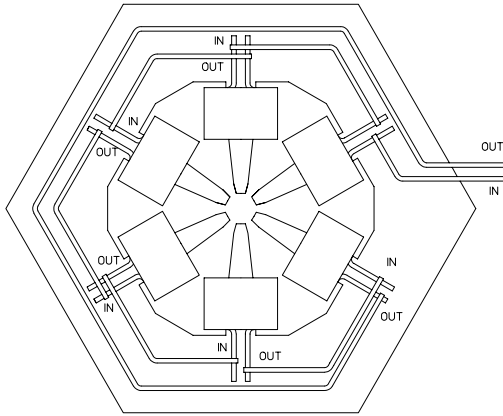


Figure 4 Correct Sextupole Bussing Topology

Electrical and Thermal Connections

Good practices must be followed in connecting the electrical bussing and attaching the thermal interlocks. Fig. 5 illustrates some of these practices.

1. Thermal interlocks are thermal switches which are normally closed.
 - (a) The thermal interlock purchased for the SPEAR3 magnets at SLAC open at temperature $175^{\circ} \pm 5^{\circ}F$ ($80^{\circ} \pm 3^{\circ}C$) and reset at $155^{\circ} \pm 5^{\circ}F$ ($68^{\circ} \pm 3^{\circ}C$).
 - i. Thermal interlocks are usually tested using an instrumented heating plate prior to installation on a coil.
 - (b) Thermal interlocks are always attached to the current carrying portion of the conductor (inside of the electrical busses) and always on the water output portion of the hydraulic circuit.
 - i. In this location, I^2R heating is measured directly rather than by thermal conduction from the current carrying portion of the conductor.
 - ii. The placement of the interlock on the water output portion of the hydraulic circuit ensures that excessive temperature rise due to reduced water flow caused by partial or complete blockage of the hydraulic circuit is sensed.
 - (c) One thermal interlock is required per water circuit. If an individual coil is fabricated with N water circuits, N thermal switches are required per coil.

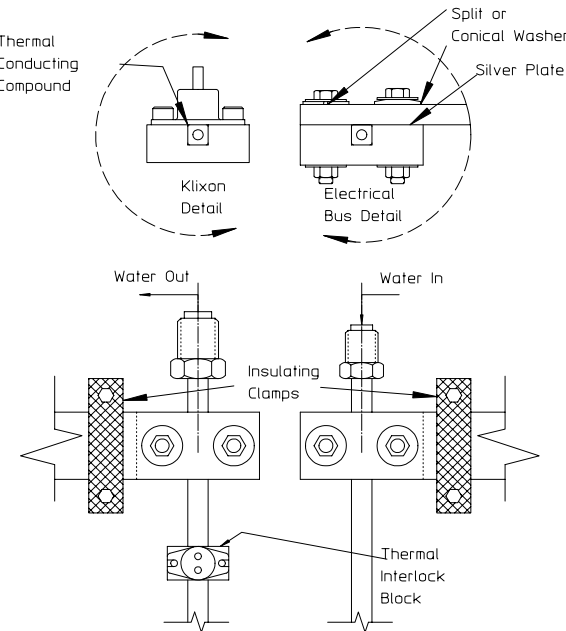


Figure 5 Interlock and Bussing Connections

- (d) The dipole will have at least $2N$ thermal interlocks, a quadrupole at least $4N$ thermal interlocks and a sextupole at least $6N$ thermal interlocks. These interlocks are connected in series to a terminal block attached to the yoke on each magnet. The series connected interlocks are connected to the power supply and wired so that the power supply shuts down and cannot be turned on when the circuit is open.
 - (e) When several magnets are connected in series, the series connected interlocks for the individual magnets are connected in series and are connected to the power supply and wired so that the power supply shuts down and cannot be turned on when the circuit is open.
 - (f) Thermal conducting compound is placed between the thermal switch and its mounting plate.
2. Electrical connections between the solid bus bars and the blocks brazed to the coil conductors must be made reliably.
- (a) Loose joints constitute a high electrical resistance path resulting in local I^2R heating. Heated fasteners expand and further loosen the joint, causing an unstable situation.

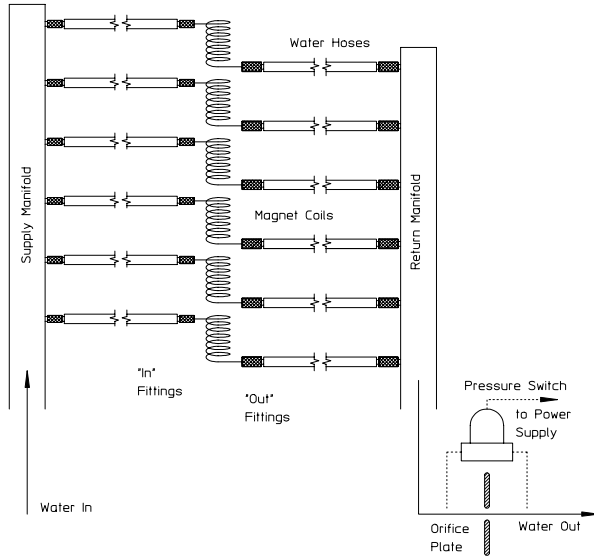


Figure 6 Hydraulic Connection Practices

- i. The mating surfaces of the bus bars and the blocks brazed on the coils are either coated with an electrically conductive compound or are silver plated.
 - ii. The fastener system used to connect the bus bars to the blocks consist of a bolt, a nut, two flat washers and either a conical or split washer. The conical or split washers are used to ensure some mechanical stored energy to prevent the fasteners from loosening.
- (b) The busses are secured to the yoke using insulating blocks and fasteners.
- i. Securing the busses isolates the mechanical load from the coil leads and ensures that they are not bent or broken.

Hydraulic Connections

Magnets may or may not be supplied with separate water manifolds. Occasionally, water manifolds are provided by the user and are attached to the magnet girder to supply water for several magnets. Fig. 6 illustrates several examples of good hydraulic design practice and can be applied to magnets supplied with water manifolds or for manifolds attached to the magnet girder.

1. Flow Interlocks

- (a) The components of a flow interlock are an orifice plate or a venturi connected to an electrical pressure switch. The pressure switch is normally closed and opens when it senses a reduced or zero pressure drop due to reduced or no flow through the hydraulic circuit. The pressure switch is connected to the magnet power supply and is wired to shut the power supply off when the switch is open.
- (b) The flow interlock is always connected to the output of the return manifold. An interlock at the input manifold will not detect interrupted flow in the magnet due to leaks or breaks in coil cooling circuits.
- (c) Flow interlocks are usually not attached to individual magnet manifolds since they are costly.

2. Water Hoses

- (a) The water hoses should be at least 1 meter long and assembled from electrically insulating material. Often, water hoses use rubber material filled with carbon powder. This type of hose is not acceptable since it is slightly conductive and represents a current loss mechanism resulting in errors in magnet excitation.
- (b) For anticipated long service in radiation environments, the water hoses should be made from material which can resist radiation damage.

3. Fittings

- (a) A quadrupole requires at least eight water hoses, four supply and four return. A sextupole requires at least twelve. It is very easy to misconnect the hoses resulting in "deadheading" a circuit. Deadheading a circuit refers to the error of connecting both ends of the coil hydraulic circuit to the same manifold, resulting in no flow. This error occurs quite frequently, especially since magnet hydraulic circuits are often disconnected and connected repeatedly during testing, magnetic measurements and at installation.
- (b) A means of avoiding deadheading is to use two different size water fittings, the larger for the return hose and manifold and the smaller for the supply hose and manifold.
 - i. Two different size water fittings are often not practical for magnets wound using small conductors. When the same size fittings are required, the hoses must be clearly labeled. The hoses may also be different colors.
 - ii. Another means of preventing deadheading for coils requiring the same size fitting is to use right and left handed threads for the connections.

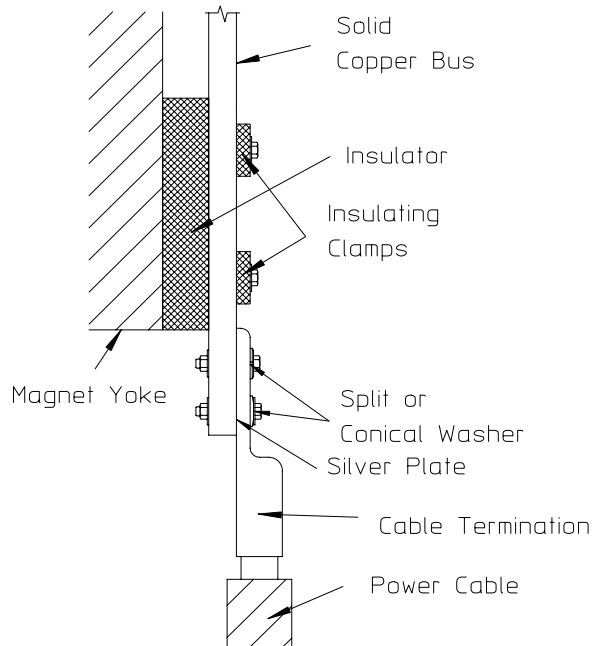


Figure 7 Power Lead Connections

Although this prevents misconnections, it requires doubling the inventory of different size water fittings.

Power Lead Connections

Power cables are typically constructed from braided copper, heavily insulated and are fitted with standard terminations. Since power cables are heavy and typically quite long, the mechanical weight must be transferred to the yoke. Fig. 7 illustrates some examples of good practice in terminating the bussing in the magnet so that power leads can be connected safely to the magnet. The magnet busses are securely connected to the yoke using insulators to prevent the mechanical load from the heavy cable from stressing the magnet coil components.

Again, as in the bus connections to the magnet coils, the fasteners used to secure the cable termination to the ends of the busses include split or conical washers to ensure elastic stored energy and silver plated surfaces to ensure a high conductivity electrical joint.

Safety

Since magnet testing requires crew presence in the vicinity of powered magnets, personnel safety rules must be observed. In the US, a facility is not allowed to operate an accelerator until documentation is supplied and reviewed indicating that all safety

rules have been observed and all personnel safety devices have been implemented. The rules for different countries vary. Some of the US electrical personnel safety rules are reviewed.

1. Coil covers and/or careful taping of all current carrying components is required to prevent direct personnel contact with any magnet conductor or bus connection under the following conditions:
 - (a) $IV > 150 \text{ V-Amps}$, $I > 30 \text{ Amps}$, $V > 130 \text{ Volts}$ or when the magnet stored energy is $> 5 \text{ joules}$.
2. Coil covers are recommended for all magnets regardless of their operating condition since it is difficult to audit safety practices when many different magnets are installed in the typical accelerator and/or beamline.
 - (a) The coil cover or taping must include the lead ends of the water circuit fittings which operate at the coil voltage.
 - (b) Safety rules require that any removable section of a coil cover must be attached by at least four fasteners.
3. Power cables exceeding 600 Volts must be distributed in separate conduits.
 - (a) This situation occurs when magnets are connected in power supply strings. It can often be mitigated by center-tapping the power supply. That is, the full voltage is split so that the power supply leads are at a $\pm \frac{V_{string}}{2}$ potential and one of the leads of the the center magnet in the string is grounded.
4. All magnet elements designed to operate at ground potential must be connected to a single ground point. A grounding strap must be connected from this ground point to the facility ground.

11.2.2 Magnet Tests

Once a magnet has been completed, tests and measurements are made to ensure that magnets satisfy physics and operation requirements.

Magnetic Measurements

Physics requirements include field quality and excitation reproducibility among magnets of the same family. Performance can be predicted by the precision of the fabrication and assembly of the yoke. Fabrication precision is determined by mechanical measurements of fabricated parts and comparison with mechanical fabrication tolerances. Assembly precision is determined by measuring the displacements and

rotations of one part of a yoke with respect to the other and comparison with mechanical assembly tolerances. Although inspection of parts is required to ensure that fabrication tolerances are met, assembly precision can be far more difficult to measure. It involves measurement of displacements along three different coordinate axes and rotations about those same three axes of the yoke elements which dominate magnet performance. The yoke elements dominating magnet performance are the poles which often do not have convenient datum surfaces for mechanical measurements. A far better means to ensure that physics requirements are met is to perform magnetic measurements. Typically, the effort to make magnetic measurements is dominated by the setup. This includes gathering the elements, power supplies, water cooling infrastructure and the measurement coils and data acquisition system. Setup also includes installing and connecting the magnet to the power supply and hydraulic circuit and installing the measurement coil. Once the setup is completed, the actual measurement can be performed quite quickly for individual magnets. The effort required for repeated measurements of other magnet in the same family is dominated by the removal of one magnet and installation of a new magnet. Again, the measurement time is small in comparison to the setup. A final magnetic measurement of all the magnets can quickly reveal the results of yoke assembly errors. It will also quickly reveal any coil fabrication errors such as turn to turn shorts or errors in the number of turns which were overlooked during the individual coil testing process.

Electrical and Hydraulic Tests and Measurements

Electrical and hydraulic tests are similar to those required for individual coils. Resistance and hydraulic measurements should be compared with computed values.

1. Resistance Test

- (a) This measurement should be performed with a bridge connected across the power lead terminals.

2. Hipot Test

- (a) Normally, the completed magnet, including installed thermal interlocks, is tested.
 - i. The interlock wires are insulated from the housing. The interlock insulation is not designed for high voltage. Therefore, it is recommended that the interlock wires and the wiring to the interlock manifold be connected to the coil circuit prior to performing the high voltage test.
- (b) Both power supply connection leads are connected to a voltage source while the yoke is grounded.
- (c) Maximum voltage $\leq 2 \times V_{operating} + 1 \text{ kV}$.

- (d) Maximum leakage current must be $\leq 2 \mu A$ at the maximum voltage.

3. Hydraulic Test

- (a) Measure the total water flow across the water manifolds at the anticipated operating pressure differential Δp . The water temperature at the time of the water flow test should be recorded.

11.3 Chapter Closure

A completed magnet requires more than the fabrication and assembly of the major components. Various components must be designed, fabricated and assembled in order to distribute the current from coil to coil, terminate power leads, distribute the cooling water and provide for equipment safety. Other components must be designed, fabricated and assembled to ensure personnel safety. Personnel safety issues are easily overlooked, but can be crucial to facility operation. Certification for facility operation cannot be granted without documented assurance that all personnel safety devices have been installed and implemented.

Tests are performed and measurements are made of the individual magnet components. A list of final tests and measurements of the assembled magnet is presented to ensure that the completed magnet will satisfy physic, operational and safety needs. This chapter lists and describes the design, fabrication, assembly and tests for a completed magnet.

Chapter 12

MAGNET INSTALLATION AND ALIGNMENT

12.1 Introduction

Accelerator lattice and beam transport magnet locations are defined in terms of the locations and acceptable errors of the local magnet coordinate system in relation to a lattice or transport global coordinate system. In order to ensure accurate magnet alignment, it is necessary to clearly define the magnet local coordinate system. The local magnet coordinate transverse and vertical (x and y) axes origins are centered in the magnet gaps and the longitudinal (z) axis origin is located on a line through the transverse and vertical center of the magnet gap midway between the front and back faces of the magnet yoke. Physics specifications for magnet installation require the origins of these magnet axes be aligned within some specified tolerance in the lattice or transport system u, v, w coordinate system with the magnet vertical (y) axis aligned with the lattice v coordinate and the longitudinal (z) axis rotated in the direction prescribed by the lattice shape. Typical accelerator tolerances require magnets to be aligned transversely and vertically (Δx and Δy) within $\leq \pm 200 \mu m$ of their ideal positions. Typical magnet longitudinal alignment tolerances are a more generous $\Delta z \leq \pm 500 \mu m$ of their ideal positions. Roll tolerance (rotation about the z or longitudinal axis) is typically $\leq \pm 0.5 \text{ mrad}$ and pitch and yaw tolerance (rotation about the x and y axes, respectively) is typically $\leq \pm 1.0 \text{ mrad}$. With modern optical alignment and laser interferometry equipment coupled to computer data acquisition/reduction systems, measurement of the locations of accelerator components within these tolerances is easily accomplished. Magnet alignment within these tolerances either requires means for making precise adjustments after installation or requires precise fabrication of magnet support structures. Some of the advantages and disadvantages of an adjustable alignment technique employing kinematically installed struts are discussed. The adjustable system is compared with a system where the support structure is designed to ensure correct alignment at installation.

Since the charged particle beams in a lattice or beam transport system traverse through the magnet gaps and since vacuum chambers occupy this space, optical targets used for magnet alignment cannot be placed at the local magnet coordinate system origin. Because of this, means for identifying the location of external magnet features with respect to the local magnet coordinate system is crucial to magnet alignment measurement and/or adjustment. The measurement of the coordinates

of external features used for optical alignment is called fiducialization. Different means for the fiducialization of magnets have been employed. Two fundamentally different fiducialization techniques rely either on design or on measurements. The two techniques are arbitrarily described as the generic and pedigreed techniques.

This chapter is written to summarize techniques for magnet installation and alignment and to describe means for magnet fiducialization. Different mechanical magnet and girder support systems along with survey and alignment techniques are described in a chapter written by Dr. Robert Ruland in ref. [4]. The type of magnet fiducialization consistent with the means for support and/or alignment are discussed. Although earlier chapters discussed designs for magnet yokes independent of means for installation and/or alignment, installation/alignment issues are important for the design of magnet yoke external features and should be integrated into the design at the earliest possible design stage.

12.2 Magnet Support

The choice of magnet support systems depends on the needs of the accelerator and/or the limitations of the fabrication processes or alignment capabilities. The support systems described in this section are those for the installation of magnets on girders, which make up major accelerator lattice subassemblies. Local coordinate system axes are associated with the girder subassemblies. Eventually, these girder subassemblies need to be installed and the girder subassembly coordinate axes need to be aligned with respect to the global lattice coordinate system.

12.2.1 Predetermined Alignment

Support systems, currently favored by many synchrotron light facilities (especially in Europe), respond to the need for experimental photon line stability. The most common source of photon instability is resonant coupling with sources of environmental vibrations affecting the electron beam orbit. Small amplitude electron beam excursions are caused by mechanical motions of the synchrotron magnets. Synchrotron magnets move as a resonant response to environmental vibrations whose largest amplitude components are in the low frequency region of the vibration spectrum. Sources of low frequency environmental vibrations are motors, pumps, water flow in cooling pipes, traffic on nearby roads, etc. Therefore, magnet support systems whose resonant frequency is $\geq 25\text{ Hz}$ and/or is critically damped are favored for heavy magnet support systems. (Damping of support structures is often impractical since it requires the use of viscoelastic material which are mechanically unstable.)

Since the natural frequency of a mechanical structure is $\propto \sqrt{\frac{k}{m}}$ where k and m are the spring constant of the support and the mass of the load, respectively, it is important that k be made as large as possible (a stiff structure). The mass of the magnet cannot be easily adjusted since it is usually determined by magnetic design requirements limiting the minimum size of the yoke carrying the magnetic flux.

The predetermined alignment system places the magnets directly onto rails

machined on a support girder. This is the stiffest support since all the load is carried over a wide area across a very short support compression member. It relies on the manufacture of the magnet support structure to precise mechanical tolerances. Magnet installation using this technique is usually limited to beamlines ≤ 3 meters. Support structures longer than this are difficult to fabricate to the required mechanical precision because of machining limitations. The support structure design must be sufficiently stiff so that elastic deflection under magnet load does not exceed the alignment tolerance. Because of these limitations, the predetermined alignment system is usually limited to groups of quadrupoles and/or sextupoles aligned along a straight line between dipole magnets in a synchrotron lattice. Fig. 1 illustrates the support of a quadrupole and sextupole using the predetermined alignment technique. Some of the features of this system and the means of fiducialization are listed as follows:

1. The fabricated substand must be perfectly level prior to installation of the magnets.
2. The laminations for different magnet types are approximately the same height so that the combined height of the substand and the lamination centerline can be made identical.
3. A center slot is provided in the laminations for the insertion of alignment bars directly below the centerlines keyed to slots in the support bars on the required centerline. This slot also provides means for centering an alignment target directly over the magnet centerlines.
4. The target is placed so that its center is over the $x = 0$ and $z = 0$ coordinate origins. The y coordinate value for each magnet type is fixed.
5. The lamination is designed so that the top and bottom are parallel to the horizontal axes of the magnets.
6. The assembled magnet roll (rotation about the local z axis) and pitch (rotation about the local x axis) can be measured with precision levels placed on the tops of the magnets.

12.2.2 Generic Fiducialization

The magnet fiducials described in the previous section for the predetermined alignment system is an example of generic fiducialization. The local x , y and z coordinates of the center of the alignment target are determined by the design of the lamination and the yoke and are identical for all magnets in a family. In this example, a single target defines the x , y and z coordinate origins. The pitch and roll, rotations about the x and z local coordinate axes, are measured with levels placed across the width and along the length of the top of the magnets. The yaw, rotation about the y local

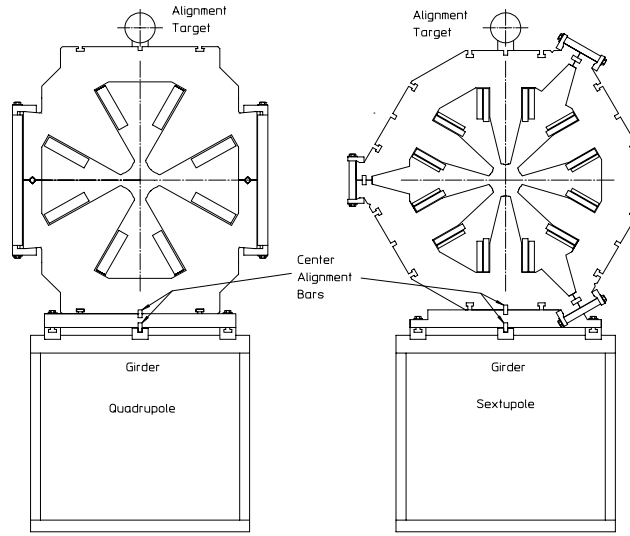


Figure 1 Predetermined Alignment Supports

coordinate axis, is determined by the keys on the magnet base and is not measured. If verification of the yaw is desired, two targets can be placed on the top of the magnet using keys for alignment along the longitudinal magnet axis.

12.2.3 Adjusted Alignment

For some accelerator applications, adjusted alignment is required. This is true when the bend magnets and the multipole magnets are installed on the same girder. For these applications, a straight line between the anticipated beam orbits through the installed and aligned bend magnets establish a straight datum axis for the alignment of the quadrupoles and sextupoles installed between them. The first adjusted alignment system developed for the Advanced Light Source (ALS) and subsequently used for the PEP II Low Energy Ring magnets and the SPEAR3 magnet and vacuum chamber supports employed a six strut support system. The supports using six struts are kinematic with the number of struts matching the six degrees of freedom, translation in the x, y and z local coordinate directions and rotations about the x, y and z local coordinate axes. This kinematic system requires all six struts and becomes mechanically unstable when any single support is omitted. Fig. 2 illustrates an example of the locations of the six struts providing adjustments in all six degrees of freedom.

In the following calculations, it is assumed that the rotations occur at an axis origin translated to the bottom of the magnet at the transverse and longitudinal center of the magnet so that the translations due to the rotations use the vertical distance between the bottom of the magnet and the magnet center as a "moment

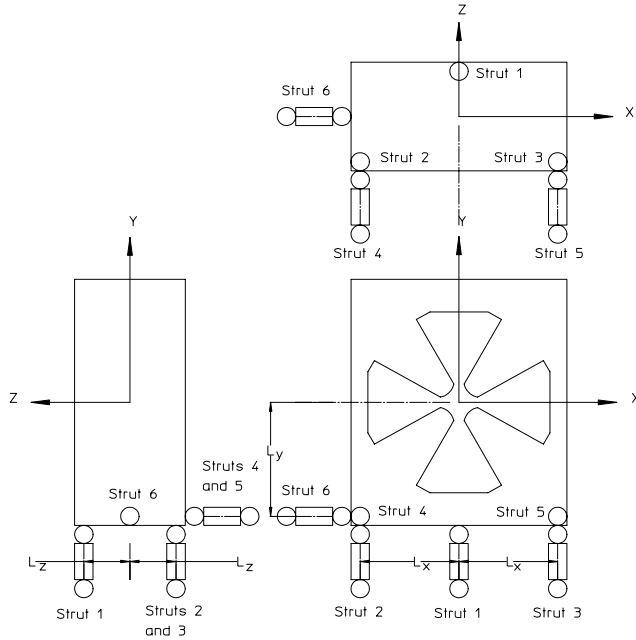


Figure 2 Six Strut Supports

arm". The expressions for the six motions are

$$\begin{aligned} Pitch &= \theta_x = \frac{s_1}{l_z} - \frac{s_2 + s_3}{2l_z} \\ Yaw &= \theta_y = -\frac{s_4}{l_x} + \frac{s_5}{l_x} \\ Roll &= \theta_z = \frac{s_2}{l_x} - \frac{s_3}{l_x}, \end{aligned}$$

$$\begin{aligned} \Delta x &= s_6 + l_y \theta = s_6 + l_y \left(\frac{s_2}{l_x} - \frac{s_3}{l_x} \right) \\ \Delta y &= \frac{s_1 + s_2 + s_3}{3} \\ \Delta z &= \frac{s_4 + s_5}{2} - l_y \theta_x = \frac{s_4 + s_5}{2} - l_y \left(\frac{s_1}{l_z} - \frac{s_2 + s_3}{2l_z} \right). \end{aligned}$$

The expressions for the rotations are rewritten as follows so that all the perturbations have length units;

$$\begin{aligned} l_y \theta_x &= \frac{l_y s_1}{l_z} - \frac{l_y (s_2 + s_3)}{2l_z} \\ l_y \theta_y &= -\frac{l_y s_4}{l_x} + \frac{l_y s_5}{l_x} \\ l_y \theta_z &= \frac{l_y s_2}{l_x} - \frac{l_y s_3}{l_x}. \end{aligned}$$

The six equations in six unknowns can be written more conveniently in matrix form;

$$\begin{pmatrix} 0 & \frac{l_y}{l_x} & -\frac{l_y}{l_x} & 0 & 0 & 1 \\ \frac{1}{3} & \frac{1}{3} & \frac{1}{3} & 0 & 0 & 0 \\ -\frac{l_y}{l_z} & \frac{l_y}{2l_z} & \frac{l_y}{2l_z} & \frac{1}{2} & \frac{1}{2} & 0 \\ \frac{l_y}{l_z} & -\frac{l_y}{2l_z} & -\frac{l_y}{2l_z} & 0 & 0 & 0 \\ 0 & 0 & 0 & -\frac{l_y}{l_x} & \frac{l_y}{l_x} & 0 \\ 0 & \frac{l_y}{l_x} & -\frac{l_y}{l_x} & 0 & 0 & 0 \end{pmatrix} \begin{pmatrix} s_1 \\ s_2 \\ s_3 \\ s_4 \\ s_5 \\ s_6 \end{pmatrix} = \begin{pmatrix} \Delta x \\ \Delta y \\ \Delta z \\ l_y \theta_x \\ l_y \theta_y \\ l_y \theta_z \end{pmatrix}.$$

This simple matrix equation can be rewritten;

$$(M)(s) = (\Delta),$$

where (M) is a 6×6 square matrix with unitless values and (s) and (Δ) are six term column matrices with values having units of length.

The error deflections and rotations are measured and the struts are adjusted to remove the errors. The matrix expression for the required strut adjustments is;

$$(s) = -(M)^{-1}(\Delta),$$

where (s) is the six element column matrix whose values are the required adjustments.

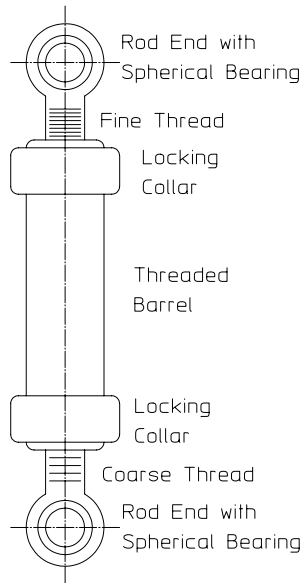


Figure 3 Adjustable Struts

12.2.4 Adjustable Struts

The adjustable strut used by ALS and PEPII Low Energy Ring magnets is illustrated in fig. 3. Each strut consists of a barrel, two rod ends and two locking collars. The spherical bearings in each rod end allows the ends of the supports to rotate. The rotation is required for the pinned end of a kinematic support. The rod ends are both right hand thread, but one has a fine thread and the other has a coarse thread. Each rotation of the barrel adjusts the strut lengths by an amount equal to the difference in the pitches of the two threads. The adjustments are much more precise than a turnbuckle, employing right and left hand threaded rod ends whose adjustment is the sum of the pitches. The locking collars provide sufficient friction to reduce backlash and to ensure that unwanted adjustments are avoided. With the locking collars tightened, it takes a great deal of effort to rotate the threaded barrel.

Natural Frequencies

One of the reasons that newer synchrotron light source accelerators presently avoid struts for installing and aligning magnets is the relatively low natural frequencies of strut supported magnet structures. If struts are used to support magnets, the engineer/designer must have some means of estimating the the structure natural frequencies. Although many computer programs are available for performing dynamic analysis of elastic systems, understanding the analytic expressions for the estimation

of natural frequencies is useful for determining the sensitivities of the natural frequencies to mechanical parameters. If magnets are installed on rafts, the rafts must be installed and aligned. Although predetermined alignment can be used for magnet supports, it is not practical for raft adjustments. Raft supports usually incorporate adjustable struts. An example for estimating the natural frequencies for a simple kinematically supported system uses the strut supported magnet structure to develop the relationships. This example can be used as a guideline for estimating the natural frequencies of larger raft structures and/or to design the raft struts with adequate stiffness to avoid resonances with low frequency mechanical vibration sources. The equations of motion for magnets supported by struts can be written and have the general form

$$\begin{aligned} m\ddot{x} &= \text{Force} \\ \text{and } mI_p\ddot{\theta} &= \text{Torque}, \end{aligned}$$

where m and I_p are the mass and polar moment of inertia of the load (the magnet in this example). A series of equations similar to the equations for computing the strut adjustments are written. For these calculations, both the rotations and displacements are computed at a set of coordinate axes translated from the magnet center to a point on the center of the bottom of the magnet. The resulting motion equations have a similar form to the displacement equations developed earlier. The rotation equations are

$$\begin{aligned} mI_{xx}\ddot{\theta}_x &= l_z ks_1 - l_z \left(\frac{ks_2 + ks_3}{2} \right), \\ mI_{yy}\ddot{\theta}_y &= -l_x ks_4 + l_x ks_5, \\ mI_{zz}\ddot{\theta}_z &= l_x ks_2 - l_x ks_3, \end{aligned}$$

where I_{xx} , I_{yy} and I_{zz} are the polar moments of inertia about the transverse, vertical and longitudinal axes, respectively, with an origin at the center of the bottom of the magnet. The polar moment of inertia for a rectangular prism about a central axis not at the centroid of the prism is given by;

$$mI_p = m \frac{a^2 + b^2}{12} + m\bar{y}^2,$$

where a and b are the width and height of the prism and \bar{y} is the vertical distance from the axis to the centroid of the mass. For this example, assume that the magnet can

be approximated as a rectangular prism with width, height and length (dimensions along the x, y and z coordinate axes) = W , H and L , respectively. Then;

$$\begin{aligned} I_{xx} &= \frac{H^2 + L^2}{12} + \left(\frac{H}{2}\right)^2 \\ I_{yy} &= \frac{W^2 + L^2}{12} \\ I_{zz} &= \frac{H^2 + W^2}{12} + \left(\frac{H}{2}\right)^2. \end{aligned}$$

For more complex shapes, the polar moments of inertia, centroids and areas are computed by most computer aided design (CAD) programs.

Rewriting the rotation equations;

$$\begin{aligned} l_y \ddot{\theta}_x &= \frac{l_y l_z k s_1}{m I_{xx}} - l_y l_z \left(\frac{k s_2 + k s_3}{2 m I_{xx}} \right) \\ l_y \ddot{\theta}_y &= -\frac{l_y l_x k s_4}{m I_{yy}} + \frac{l_y l_x k s_5}{m I_{yy}} \\ l_y \ddot{\theta}_z &= \frac{l_y l_x k s_2}{m I_{zz}} - \frac{l_y l_x k s_3}{m I_{zz}}. \end{aligned}$$

The translation equations are;

$$\begin{aligned} m \ddot{x} &= k s_6 = k s_6 \\ m \ddot{y} &= k \frac{s_1 + s_2 + s_3}{3} \\ m \ddot{z} &= k \frac{s_4 + s_5}{2} = k \frac{s_4 + s_5}{2}. \end{aligned}$$

The six equations in six unknowns can be written more conveniently in matrix form;

$$\left(\begin{array}{cccccc} 0 & 0 & 0 & 0 & 0 & \frac{k}{m} \\ \frac{k}{3m} & \frac{k}{3m} & \frac{k}{3m} & 0 & 0 & 0 \\ 0 & 0 & 0 & \frac{k}{2m} & \frac{k}{2m} & 0 \\ \frac{l_y l_z k}{m I_{xx}} & -\frac{l_y l_z k}{2 m I_{xx}} & -\frac{l_y l_z k}{2 m I_{xx}} & 0 & 0 & 0 \\ 0 & 0 & 0 & -\frac{l_y l_x k}{m I_{yy}} & \frac{l_y l_x k}{m I_{yy}} & 0 \\ 0 & \frac{l_y l_x k}{m I_{zz}} & -\frac{l_y l_x k}{m I_{zz}} & 0 & 0 & 0 \end{array} \right) \begin{pmatrix} s_1 \\ s_2 \\ s_3 \\ s_4 \\ s_5 \\ s_6 \end{pmatrix} = \begin{pmatrix} \ddot{x} \\ \ddot{y} \\ \ddot{z} \\ l_y \ddot{\theta}_x \\ l_y \ddot{\theta}_y \\ l_y \ddot{\theta}_z \end{pmatrix}.$$

The natural frequencies of the strut supported structure in this example are = $\sqrt{\text{eigenvalues}}$ of the square matrix.

12.2.5 Adjustable Support Blocks

Application of the previous example for the computation of the dynamic response for a strut supported magnet system can demonstrate that low natural frequencies of a strut supported magnet system can be avoided only by very robust design of the struts. Operation at ALS revealed that the ALS magnet supports resonated at low natural frequencies. Because the load was carried across the small area of the threaded barrel over the length of the strut, the mechanical compliance of the struts paired with the magnet masses resulted in low natural frequencies. Because of this, a more rigid support system is described which supports the magnet at three points with three short supports loaded in compression. Fig. 4 illustrates the kinematic adjustable support system consisting of three assembled elements, a flat block, and edge block and a corner block.

1. Small buttons (shims) are assembled and screwed onto each of the blocks.
 - (a) Shim 1 assembled on the flat block provides adjustment in the vertical (y) direction.
 - (b) Shim 2 assembled on the corner block provides adjustment in the vertical (y) direction.
 - (c) Shim 3 assembled on the edge block provides adjustment in the vertical (y) direction.
 - (d) Shim 4 assembled on the corner block provides adjustment in the longitudinal (z) direction.
 - (e) Shim 5 assembled on the edge block provides adjustment in the longitudinal (z) direction.
 - (f) Shim 6 assembled on the corner block provides adjustment in the transverse (x) direction.
2. The magnet is installed with a set of starting shims and the three displacement and three rotation errors are measured.
3. The differences in the shim thicknesses are computed by solution of the six linear equations in six unknowns (matrix inversion).
4. New shims with the required adjusted thicknesses are installed and steps 2 to 4 are repeated.
 - (a) It is expected that conversion to alignment within the required tolerances should be achieved with 2 iterations.

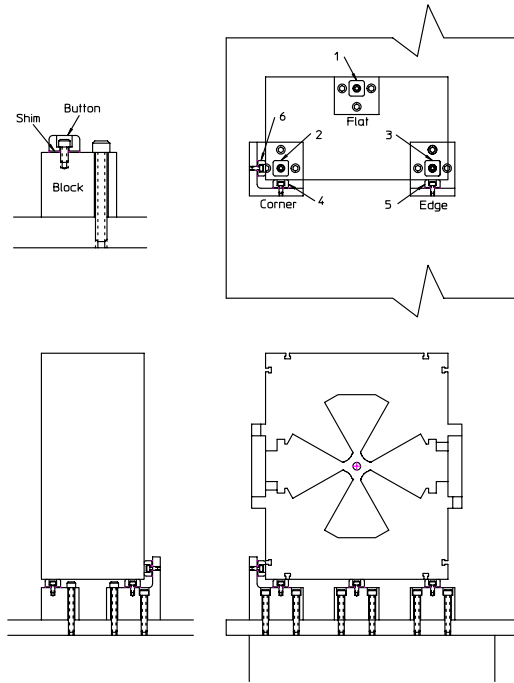


Figure 4 Adjustable Support Blocks

Again, as in the computations for the motions due to the struts, it is assumed that the rotations occur at an axis origin translated to the bottom of the magnet at the transverse and longitudinal center of the magnet so that the translations due to the rotations at the magnet center use the vertical distance between the bottom of the magnet and the magnet center as a “moment arm”. The displacement equations are identical to the displacement equations written for the strut system. Although the location of shim 6 is not centered along the centerline as in the strut system, because it is the only adjustment in the x direction, it does not introduce a rotation around the y axis.

Since the error deflections and rotations are measured, the button thicknesses must be adjusted to remove the errors. The matrix expression for the required button thickness adjustments is

$$(s) = - (M)^{-1} (\Delta),$$

where (M) is an identical matrix as used for the six struts and (s) is the six element column matrix whose values are the required changes in the button thicknesses.

Generic fiducialization can be employed for a magnet installed and aligned using a strut adjustable or block adjustable support system. However, it requires at

least two optical targets in addition to the transverse and longitudinal levels. Two optical targets, at least one located at the $x = z = 0$ coordinate location at the top of the magnet with a second located on the same y plane at some fixed separation δ will establish the yaw or ω_y rotation of the magnet.

12.2.6 Pedigreed Fiducialization

Pedigreed fiducialization has been used for the ALS and SPEAR3 magnets. This method refers to the measurement of fiducial targets installed on individual magnets. The results of this fiducialization method is a set of target coordinates unique for each individual magnet. Thus, it requires the maintenance of a large database.

This fiducialization method does not rely on design features of either the yoke lamination or yoke assembly. Its precision is limited by measurement precision of the instrument used to measure the coordinates and does not rely on mechanical fabrication or assembly tolerances. It is especially useful when optical lines of sight for alignment are congested or limited since it allows the location of fiducial targets on any arbitrary surface as well as the flat magnet top surface. This method is more difficult and expensive than the generic fiducialization technique. It requires careful definition of the datum coordinate system according to conventions used in mechanical metrology. It also requires a three dimensional coordinate measurement system robust enough to support the weight and large enough to measure the maximum span of the fiducialized magnet. Large coordinate measurement machines (CMM's) have been employed in the past. However, it is also possible to employ a laser interferometer measurement system as a portable CMM.

Briefly, the process for pedigreed fiducialization is to measure the three dimensional Cartesian coordinates, in the CMM coordinate system, of features on the magnet, devices installed in the magnet gap and the fiducial targets. The coordinates of the magnet features and the devices are then used to define the coordinate system of the magnet. The final step is to mathematically transform the fiducial target coordinates by rigid body translations and rotations to the coordinate system of the magnet. An example of the fiducialization of a quadrupole magnet, shown in fig. 5, is presented as an illustration of the process. Metrology practices require that coordinate systems be defined in three steps by carefully defining a principal plane, a principal line on that plane, and a principal point on that line. The following measurement and computation steps reflect this rigid practice.

1. A machined cylinder with radius $< h$ (pole radius) is placed in the magnet gap with a split sleeve with radius $= h$ in contact with the upper two poles.
 - (a) Because of inevitable small fabrication and/or assembly errors, a machined cylinder with radius $= h$ may not fit in the magnet aperture.
2. In the Coordinate Measuring Machine (u , v , w) coordinate system, the following measurements are made.

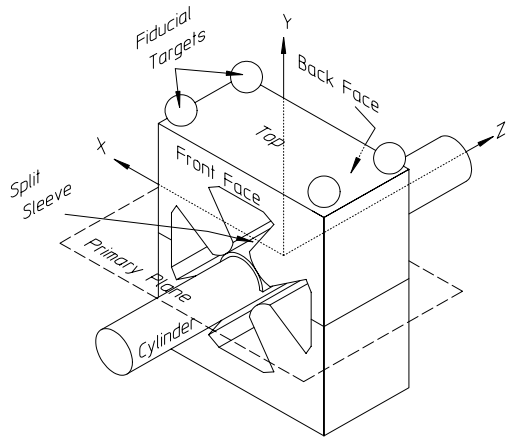


Figure 5 Quadrupole “Pedigreed” Fiducialization

- (a) Several points on the top plane of the magnet yoke.
 - (b) Several points on the front face of the magnet yoke.
 - (c) Several points on the back face of the magnet yoke.
 - (d) Several points on the surface of the cylinder.
 - (e) The (u, v, w) coordinates of the centers of each of the fiducial targets.
 - i. Three fiducial targets are required to fully and uniquely describe the magnet coordinate origin. Four targets are usually employed for redundancy and to protect against having to repeat the measurements if one target is damaged. Often, more than four targets are installed to provide more flexibility for viewing the targets with optical or laser instruments in the congested accelerator environment.
 - ii. If the fiducial targets are balls, several measurements are needed in order to compute the least square fit to a sphere.
3. Computations using the results of 2a, 2b, 2c and 2d are used to establish the magnet (x, y, z) coordinate system.
- (a) A least square fit of the measurements on top of the magnet yoke establishes a plane parallel to the principal magnet plane.
 - (b) A least square fit of the measurements on front face of the magnet yoke establishes the front face plane of the magnet.
 - (c) A least square fit of the measurements on back face of the magnet yoke establishes the back face plane of the magnet.

- (d) A least square fit of the measurements on surface of the cylinder establishes a magnet axis.
 - (e) The point midway between the intersection of the front face plane and the back face plane with the magnet axis establishes the origin of the coordinate system, $(x, y, z) = (0, 0, 0)$.
 - (f) The plane established in step 3a is translated parallel to itself to coincide with the $(x, y, z) = (0, 0, 0)$ coordinate origin. This is the magnet principal plane.
 - (g) The perpendicular projection of the cylinder axis, established in step 3d, on the principal plane is the magnet z coordinate axis.
 - i. Ideally, the cylinder axis will lie in the plane. Actually, small errors due to the cylinder contact at high points on the poles of the assembled yoke result in the axis intersecting the plane at a small angle.
 - (h) The line perpendicular to the principal plane at the coordinate origin is the magnet y coordinate axis.
 - (i) The line perpendicular to both the y and z coordinate directions with the positive direction established by the right hand rule for the vector cross product, $\vec{x} = \vec{y} \times \vec{z}$ at the coordinate origin is the magnet x coordinate axis.
4. The fiducial ball (x, y, z) coordinates are computed by rigid body translation and rotation of the (u, v, w) fiducial ball coordinates.

12.3 Chapter Closure

Magnet design is not complete until means for installation/alignment are integrated with the design. It is extremely difficult to retrofit support points and alignment features into a magnet designed and built ignoring these needs. This chapter describes some of the means used in the past for magnet support, installation, fiducialization and alignment. The examples illustrate some of the design features which need to be integrated into the magnet design. These descriptions also illustrate some of the strengths and weaknesses of the various installation/alignment techniques and allows informed decisions to be made regarding some of the choices. Computations for calculating the adjustments required for alignment after translational and rotational errors have been measured are described. Other computations illustrate that mechanical natural frequencies can be estimated without employing complex computer codes. Parameters in the algorithms employed for the estimation of natural frequencies can be adjusted to improve the behavior of the support system. The sensitivities of the values of the natural frequencies to these parameters can be evaluated. Computer codes can then be employed to refine the estimates.

Solutions

Solution 1.1

$$\begin{aligned} |\vec{F}| &= \text{coulombs} \times \frac{m}{\text{sec}} \times \text{Tesla}, \\ &= \frac{\text{coulombs}}{\text{sec}} \times m \times \frac{\text{Webers}}{m^2}, \\ &= \text{Amps} \times m \times \frac{V \text{ sec}}{m^2} = \frac{\text{Watt sec}}{\text{meter}}, \\ &= \frac{\text{joules}}{m} = \frac{N \text{ m}}{m} = N. \end{aligned}$$

Solution 1.2

Because the field from one current is perpendicular to the first current and parallel to the second current. The expression for the force magnitude is,

$$\begin{aligned} |\vec{F}| &= |e \vec{v} \times \vec{B}|, \\ &= ev \frac{\mu_0 I}{2\pi d} \sin 0 = 0. \end{aligned}$$

Solution 1.3

The force per unit length is given by

$$\begin{aligned} \frac{\vec{F}}{\text{length}} &= \vec{I} \times \vec{B}, \\ \frac{F}{\text{length}} &= |\vec{I} \times \vec{B}| = I_1 \frac{\mu_0 I_2}{2\pi d} = \frac{\mu_0 I_1 I_2}{2\pi d}. \end{aligned}$$

The units for the force per unit length are

$$\begin{aligned}
 \frac{F}{\text{length}} &= \frac{\mu_0 I_1 I_2}{2\pi d}, \\
 &= \frac{T \text{ m}}{\text{Amps}} \frac{\text{Amps}^2}{m} = \frac{\text{Webers}}{m^2} \text{ Amps}, \\
 &= \frac{V \text{ Amps sec}}{m^2} = \frac{W \text{ sec}}{m^2} = \frac{\text{joules}}{m^2}, \\
 &= \frac{N \text{ m}}{m^2} = \frac{N}{m}.
 \end{aligned}$$

Solution 2.1

For a real quadrupole,

$$xy = \frac{35^2}{2}, \text{ where } x \text{ and } y \text{ have units of mm.}$$

For a skew quadrupole,

answer to be supplied by the student.

Solution 2.3

If the coefficients for the multipole error function is complex, it can be expressed as the magnitude of the coefficient multiplied by a complex unit vector

$$\begin{aligned}
 F(\theta) &= |C_n| e^{i\psi} e^{in\theta}, \\
 &= |C_n| e^{i(\psi+n\theta)}.
 \end{aligned}$$

For a function symmetrical about the pole centerline at $\theta = \frac{\pi}{2N}$,

$$\begin{aligned}
 \operatorname{Re} F\left(\frac{\pi}{N} - \theta\right) &= -\operatorname{Re} F(\theta) \\
 \text{and } \operatorname{Im} F\left(\frac{\pi}{N} - \theta\right) &= \operatorname{Im} F(\theta).
 \end{aligned}$$

The real parts of the function, the vector potentials, are opposite sign on each side of the line of symmetry if the vector potential along the pole centerline is set at zero. The imaginary parts, the scalar potentials, are the same sign on each side of the line of symmetry. The student should determine from the ideal flux plots for some of the generic magnets illustrated in the first part of this chapter that the signs indicated in this example are correct.

$$\begin{aligned}
 F\left(\frac{\pi}{N} - \theta\right) &= |C_n| e^{i\psi} e^{in\left(\frac{\pi}{N} - \theta\right)}, \\
 &= |C_n| e^{i\left(\psi + \frac{n\pi}{N} - n\theta\right)}.
 \end{aligned}$$

We know that the “allowed” multipoles must satisfy eq. (2.34) due to rotational symmetry

$$\begin{aligned} n_{\text{allowed}} &= N(2m+1) \\ \frac{n_{\text{allowed}}\pi}{N} &= \frac{N(2m+1)\pi}{N} \\ &= (2m+1)\pi \\ &= \text{odd integer } \times \pi. \end{aligned}$$

Therefore;

$$\begin{aligned} F\left(\frac{\pi}{N} - \theta\right) &= |C_n| e^{i(\psi+(2m+1)\pi-n\theta)} \\ &= |C_n| e^{i(2m+1)\pi} e^{i(\psi-n\theta)} \\ &= -|C_n| e^{i(\psi-n\theta)}. \end{aligned}$$

Symmetry about the pole center requires

$$\begin{aligned} \text{Re } |C_n| e^{i(\psi+n\theta)} &= -\text{Re } [-|C_n| e^{i(\psi-n\theta)}] \\ \text{Im } |C_n| e^{i(\psi+n\theta)} &= \text{Im } [-|C_n| e^{i(\psi-n\theta)}]. \end{aligned}$$

Equating the real and imaginary parts of the exponential portion of the expressions and rewriting the expressions for the cosines and sines of the combined angles,

$$\begin{aligned} \text{Re}(e^{i(\psi+n\theta)}) &= \cos(\psi + n\theta) = \cos\psi \cos n\theta - \sin\psi \sin n\theta, \\ -\text{Re}(-e^{i(\psi-n\theta)}) &= \cos(\psi - n\theta) = \cos\psi \cos n\theta + \sin\psi \sin n\theta, \\ \text{Im}(e^{i(\psi+n\theta)}) &= \sin(\psi + n\theta) = \sin\psi \cos n\theta + \cos\psi \sin n\theta, \\ \text{Im}(-e^{i(\psi-n\theta)}) &= -\sin(\psi - n\theta) = -\sin\psi \cos n\theta + \cos\psi \sin n\theta, \end{aligned}$$

which satisfy the required conditions if and only if $\psi = 0$.

Solution 3.4

Use figures 12 and 13. For the unoptimized case, $\frac{y_c}{h} = 0.32$ and $\frac{B_{\text{corner}}}{B_{\text{pole}}} \approx 1.63$. $B_{\text{pole}} = B'h = 12 \times 0.05 = 0.6 \text{ T}$. $y_c = 0.32 \times 50 = 16 \text{ mm}$. The width between adjacent poles is 32 mm. Therefore, a coil whose width is < 32 mm can be installed between the poles. The maximum pole tip field at the edge of the pole is $B_{\text{corner}} = 1.63 \times 0.6 = 0.98 \text{ T}$. The calculations for the optimized pole tip is left for the student.

Solution 4.1

For the sextupole ($n = 3$) error

$$\begin{aligned}\varepsilon_l &= \frac{\Delta l}{l} = \frac{5 \text{ mm.}}{500 \text{ mm.}} = 0.01 \\ \left| \frac{B_3}{B_2} \right|_h &= \frac{n}{N} \Delta C_n(l) = i \varepsilon_l \frac{n}{N} \frac{\Delta C_n(l)}{i \varepsilon_l} \text{ where } \begin{array}{l} n = 3 \\ N = 2 \end{array}\end{aligned}$$

From the table in 99,

$$\frac{n}{N} \frac{\Delta C_n(l)}{i \varepsilon_l} = -2.22 \times 10^{-1}.$$

Therefore,

$$\begin{aligned}\left| \frac{B_3}{B_2} \right|_h &= \frac{n}{N} \Delta C_n(l) = i \times 0.01 \times 2.22 \times 10^{-1}, \\ &= i 2.22 \times 10^{-3},\end{aligned}$$

and

$$\begin{aligned}\left| \frac{B_3}{B_2} \right|_{r_0} &= \left| \frac{B_3}{B_2} \right|_h \left(\frac{r_0}{h} \right)^{n-N} = i 2.22 \times 10^{-3} \left(\frac{40}{50} \right)^{3-2} \\ &= i 1.78 \times 10^{-3}, \text{ a skew sextupole error.}\end{aligned}$$

Solution 4.1a For the center shift

$$\left| \frac{B_1}{B_2} \right|_h = \frac{n}{N} \Delta C_n(l) = i \varepsilon_l \frac{n}{N} \frac{\Delta C_n(l)}{i \varepsilon_l} \text{ where } \begin{array}{l} n = 1 \\ N = 2 \end{array}$$

From the table in 99,

$$\frac{n}{N} \frac{\Delta C_n(l)}{i \varepsilon_l} = 2.83 \times 10^{-1}.$$

Therefore,

$$\begin{aligned}\left| \frac{B_1}{B_2} \right|_h &= \frac{n}{N} \Delta C_n(l) = i \times 0.01 \times 2.83 \times 10^{-1}, \\ &= i 2.83 \times 10^{-3}.\end{aligned}$$

Since the field is imaginary,

$$\left| \frac{B_{1x}}{B_2} \right|_h = 2.83 \times 10^{-3}.$$

From eq.(4.9),

$$|\Delta y| = h \left| \frac{B_{1x}}{B_2} \right| = 50 \text{ mm} \times 2.83 \times 10^{-3} = 0.14 \text{ mm}.$$

Solution 4.1b From 4.3.4, the amplitudes of the coefficients are identical to the coefficients used to compute the solutions for problems 4.1a and 4.1b. However, the denominator for the expressions are real and not imaginary. From eq. (4.10), $\varepsilon_a = 0.01$ for $\eta = 0.98$. Therefore, the amplitude of the sextupole error field is the same as computed for problem 4.1a, but is real. The dipole field is real, therefore $\left| \frac{B_{1y}}{B_2} \right|_h = 2.83 \times 10^{-3}$ and the center displacement is horizontal and $|\Delta x| = 0.14 \text{ mm}$.

Solution 5.3

For the sextupole $B_{poletip} = \frac{B''h^2}{2}$. Therefore, the sextupole gradient is $B'' = \frac{2B_{poletip}}{h^2}$. From eq. (5.13), the required excitation is

$$NI = \frac{B''h^3}{6\eta\mu_0} = \frac{2B_{poletip}h^3}{6\eta\mu_0h^2} = \frac{B_{poletip}h}{3\eta\mu_0}.$$

Substituting,

$$\begin{aligned} NI &= \frac{B_{poletip} h}{3\eta\mu_0}, \\ &= \frac{0.3 \text{ T} \times 0.045 \text{ m}}{3 \times 0.98 \times 4\pi \times 10^{-7} \frac{\text{Tm}}{\text{Amp}}}, \\ &= 3654 \text{ Amps}. \end{aligned}$$

The “canonical” current density is

$$j = 10 \frac{\text{Amps}}{\text{mm}^2} = \frac{NI}{f A}.$$

Therefore,

$$\begin{aligned} A &= \frac{NI}{f j}, \\ &= \frac{3654 \text{ Amps}}{0.50 \times 10 \frac{\text{Amps}}{\text{mm}^2}} = 730 \text{ mm}^2. \end{aligned}$$

From eq. (5.18),

$$\begin{aligned}
 P_{sext} &= \rho \frac{B'' h^3}{\eta \mu_0} j l_{ave}, \\
 &= \rho \frac{2B_{poletip}}{h^2} \frac{h^3}{\eta \mu_0} j l_{ave}, \\
 &= \rho \frac{2B_{poletip} h}{\eta \mu_0} j l_{ave}, \\
 &= 1.86 \times 10^{-8} \Omega m \frac{2 \times 0.3 T \times 0.045 m}{0.98 \times 4\pi \times 10^{-7} \frac{T m}{Amp}} 10 \times 10^6 \frac{Amps}{m^2} 0.5 m, \\
 &= 2040 \Omega Amp^2 = 2.04 kW.
 \end{aligned}$$

Solution 5.4

The conductor length is NL_{ave} , where $L_{ave} = 50 \text{ cm}$. The resistance per coil can be computed using

$$\begin{aligned}
 R &= \frac{\rho L}{a} = \frac{\rho N L_{ave}}{a}, \\
 &= \frac{1.86 \times 10^{-8} \Omega m \times 20 \times 0.50 m}{20.323 \times 10^{-6} m^2}, \\
 &= 9.15 \times 10^{-3} \Omega.
 \end{aligned}$$

The power per coil and for the magnet are

$$\begin{aligned}
 P_{coil} &= I^2 R = 200^2 Amps^2 \times 9.15 \times 10^{-4} \Omega, \\
 &= 366.1 W. \\
 P_{magnet} &= 6P_{coil} = 2.20 kW,
 \end{aligned}$$

which compares with the solution of Problem 5.3.

The length of a hydraulic circuit for a single coil is $L = NL_{ave} = 20 \times .50 = 10 \text{ m}$. Performing the spreadsheet calculation for one water cooling circuit per coil ($d = 3.6 \text{ mm}$, $L = 10 \text{ m}$, $P_{circuit} = 0.366 \text{ kW}$), the flow velocity is approximately $v = 5 \frac{\text{m}}{\text{sec}}$ and the water temperature rise, $\Delta T \approx 1.7^\circ C$. The flow is a bit high (hydraulic vibrations occur at velocities $\geq 5 \frac{\text{m}}{\text{sec}}$) and the temperature rise is small. A second iteration combines three coils into a single hydraulic circuit. For case 2, ($d = 3.6 \text{ mm}$, $L = 30 \text{ m}$, $P_{circuit} = 1.098 \text{ kW}$), the spreadsheet results are shown in the Excel® graphs shown in fig. 6. The flow velocity is a more comfortable

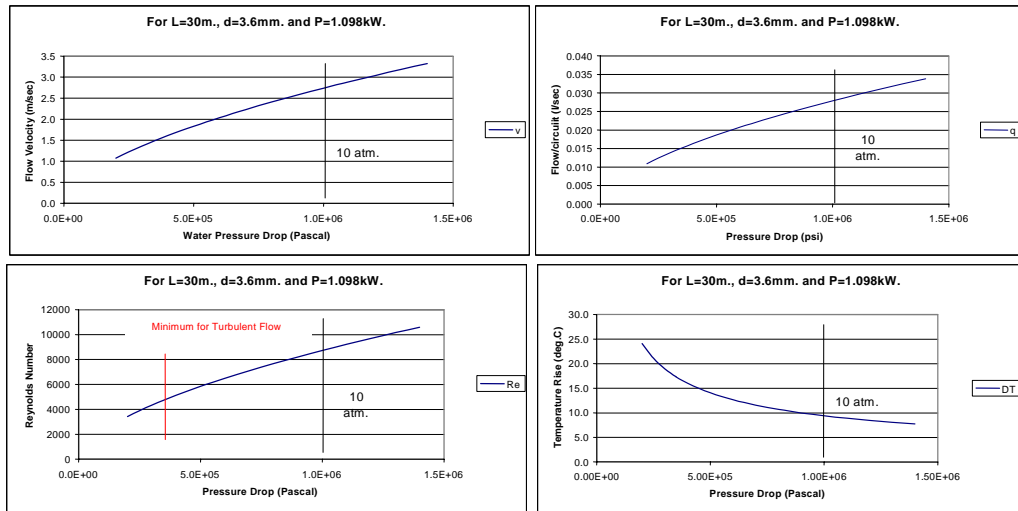


Figure 6 Problem 5.4 Hydraulic Calculation Results

$v = 2.7 \frac{m}{sec}$ and the water temperature rise, $\Delta T \approx 9^\circ C$. For three coils in series, the sextupole has two water circuits with

$$q = 0.028 \frac{l}{sec. \text{ per circuit}}.$$

Thus, the total coolant flow required is

$$q_{magnet} = 0.056 \frac{l}{sec.} = 3.36 \frac{l}{min.}.$$

Solution 7.1

The maximum field on the horizontal centerline below the edge of the pole is

$$\begin{aligned} B_{\max} &= B'x = 5 \frac{T}{m} \times 0.10 \text{ m}, \\ &= 0.5 \text{ T}. \end{aligned}$$

Solution 7.1a Magnetic force distribution is proportional to the field distribution squared. Since the field distribution in a quadrupole is linear, the force distribution per unit length is parabolic. The force per unit length of the magnet for $0 \leq x \leq 0.10 \text{ m}$ is parabolic with a maximum amplitude of 1 atmosphere = $0.1 \frac{MN}{m^2}$. (See 7.2.2).

Solution 7.1b The pressure curve is proportional to B^2 . Since B is linear, the pressure curve is parabolic.

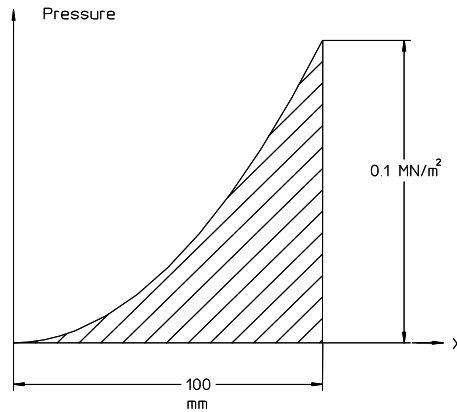


Figure 7 Pressure Distribution

Solution 7.1c The force per unit length of the magnet for $0 \leq x \leq 0.10 \text{ m}$ is the integral of the parabolic curve shown in fig. 7. The area under a parabola is

$$\begin{aligned}\frac{\text{Force}}{\text{Length}} &= \int_0^w P(x) dx = \int_0^w P_{\max} \frac{x^2}{w^2} dx = P_{\max} \frac{x^3}{3w^2} \Big|_0^w = \frac{P_{\max} w}{3}, \\ &= \frac{1}{3} \times 0.1 \text{ m} \times 0.1 \frac{\text{MN}}{\text{m}^2} = 0.0033 \frac{\text{MN}}{\text{m}}.\end{aligned}$$

The attractive force between the two halves of a 0.3 meter long quadrupole is twice the $\frac{\text{Force}}{\text{Length}}$ computed in the previous paragraph since the magnet width is $-0.10 \text{ m} \leq x \leq 0.10 \text{ m}$.

$$\begin{aligned}\text{Force} &= 2 \times 0.0033 \frac{\text{MN}}{\text{m}} \times 0.3 \text{ m}, \\ &= 0.002 \text{ MN}.\end{aligned}$$

Solution 7.3a The numerical solutions for the subsections of Problem 7.3 carry the units. It is usually good practice to carry the units through and derive the resulting units. This practice provides confidence that the computations are being correctly executed.

Using eq. (5.8) and solving for the field

$$\begin{aligned}B &= \frac{\eta \mu_0 N I}{g}, \\ &\approx \frac{4\pi \times 10^{-7} \frac{\text{T m}}{\text{Amp}} \times 40 \times 1000 \text{ Amps}}{0.05 \text{ m}}, \\ &\approx 1.0 \text{ T} \text{ (approximate assuming } \eta \approx 100\%).\end{aligned}$$

Solution 7.3b Using eq. (7.4)

$$\begin{aligned}
 U_{gap} &= \frac{B^2}{2\mu_0} (V)_{gap}, \\
 &= \frac{1.0 \text{ } T^2}{2 \times 4\pi \times 10^{-7} \frac{T \text{ } m}{Amp}} \times 0.1 \text{ } m \times 0.5 \text{ } m \times 0.05 \text{ } m, \\
 &= 995 \text{ } T \text{ } Amp \text{ } m^2 = 995 \frac{\text{Webers}}{m^2} \text{ } Amps \text{ } m^2, \\
 &= 995 \text{ } V \text{ sec } Amp = 995 \text{ } W \text{ sec} = 995 \text{ joules}.
 \end{aligned}$$

In this example problem, it is helpful to carry the units to verify the calculation.

Solution 7.3c Using eq. (7.5)

$$\begin{aligned}
 U_{coil} &= \frac{B^2}{6\mu_0} (V)_{coil}, \\
 &= \frac{1.0 \text{ } T^2}{6 \times 4\pi \times 10^{-7} \frac{T \text{ } m}{Amp}} \times 0.1 \text{ } m \times 0.5 \text{ } m \times 0.05 \text{ } m, \\
 &= 332 \text{ joules}.
 \end{aligned}$$

Solution 7.3d The stored energy in the magnet includes the stored energy in the gap, the two coils, the iron yoke and the three dimensional fringe field. The magnet fringe field length is approximately a half gap ($\approx 0.025 \text{ m}$) at each end. The field changes approximately linearly along this length. One can estimate the stored energy in this small volume. However, the fringe field stored energy is small compared to the stored energy in the gap and coils and adds very little to the total stored energy.

The stored energy in the iron yoke is $U = \frac{1}{2} \int BHdv$ where $H_{iron} = \frac{B}{\mu\mu_0}$ so that

$$\begin{aligned}
 U &= \frac{1}{2} \int \frac{B_{iron}^2}{\mu\mu_0} dv, \\
 &\approx \frac{1}{2} \frac{B_{iron}^2}{\mu\mu_0} (Vol)_{yoke}.
 \end{aligned}$$

For a well designed magnet where the iron is not saturated and $\mu \approx 1000$. If the volume of the iron yoke is approximately ten times the volume of the air gap, the iron stored energy is $\approx 1\%$ of the gap stored energy. Therefore,

$$\begin{aligned} U_{magnet} &\approx U_{gap} + 2U_{coil}, \\ &\approx 995 + 2 \times 332 = 1659 \text{ joules}. \end{aligned}$$

Solution 7.3e Using eq. (7.6)

$$L = \frac{2U}{I^2} = \frac{2 \times 1659}{1000^2} = 3.32 \times 10^{-3} \text{ h} = 3.32 \text{ mh.}$$

Using eq. (5.15)

$$\begin{aligned} R &= \frac{\rho L}{a} = \frac{\rho N L_{ave}}{a}, \\ &= \frac{1.86 \times 10^{-8} \Omega \text{ m} \times 40 \times 1.3 \text{ m}}{100 \times 10^{-6} \text{ m}^2} = 0.0097 \Omega \end{aligned}$$

Solution 7.3f Using eq.

$$\begin{aligned} V &= RI + L \frac{dI}{dt}, \\ &= RI_{\max} \sin \omega t + LI_{\max} \frac{d}{dt} \sin \omega t, \\ &= RI_{\max} \sin \omega t + LI_{\max} \omega \cos \omega t. \end{aligned}$$

Rewriting

$$\frac{V}{V_{\max}} = \frac{RI_{\max}}{V_{\max}} \sin \omega t + \frac{LI_{\max} \omega}{V_{\max}} \cos \omega t,$$

where

$$V_{\max} = \sqrt{(RI_{\max})^2 + (LI_{\max} \omega)^2}.$$

The frequency at 1 Hz is $\omega = 2\pi \text{ sec}^{-1}$. The amplitude of the inductive voltage is

$$\begin{aligned} V_{inductive} &= LI_{\max} \omega, \\ &= 3.32 \times 10^{-3} \text{ h} \times 1000 \text{ Amps} \times 2\pi \text{ sec}^{-1}, \\ &= 3.32 \times 10^{-3} \frac{\text{joules}}{\text{Amp}^2} \times 1000 \text{ Amps} \times 2\pi \text{ sec}^{-1}, \\ &= 209 \frac{\text{joules}}{\text{Amp sec}} = 209 \frac{\text{W sec}}{\text{Amp sec}} = 209 \text{ V}. \end{aligned}$$

The amplitude of the resistive voltage is

$$V_{resistive} = RI_{\max} = 1000 \text{ Amps} \times 0.0097 \Omega = 9.7 \text{ V.}$$

Therefore, the maximum voltage is

$$V_{\max} = \sqrt{(9.7)^2 + (209)^2} = 209.2 \text{ V.}$$

The expression for the normalized voltage can be rewritten

$$\begin{aligned} \frac{V}{V_{\max}} &= \frac{LI_{\max}\omega}{V_{\max}} \cos \omega t + \frac{RI_{\max}}{V_{\max}} \sin \omega t, \\ &= \sin A \cos \omega t + \cos A \sin \omega t = \sin(A + \omega t). \\ \text{But } \tan A &= \frac{\sin A}{\cos A} = \frac{\frac{LI_{\max}\omega}{V_{\max}}}{\frac{RI_{\max}}{V_{\max}}} = \frac{L\omega}{R}, \\ \text{and } A &= \tan^{-1} \frac{L\omega}{R}. \end{aligned}$$

The expression for the voltage is

$$V = \sqrt{(RI_{\max})^2 + (LI_{\max}\omega)^2} \sin(A + \omega t),$$

and the voltage must lead the current by an angle

$$\begin{aligned} A &= \tan^{-1} \frac{L\omega}{R} = \tan^{-1} \frac{3.32 \times 10^{-3} \frac{\text{joules}}{\text{Amp}^2} \times 2\pi \text{ sec}^{-1}}{0.0097 \Omega}, \\ &= \tan^{-1} 2.15 \frac{\frac{W \text{ sec}}{\text{Amp}^2} \text{ sec}^{-1}}{\Omega} = \tan^{-1} 2.15 \frac{\Omega}{\Omega} = 1.135 \text{ rad} = 65^\circ. \end{aligned}$$

Solution 7.4

Consider a dipole with half gap $h = 25 \text{ mm}$ with a vacuum chamber whose horizontal surfaces has a thickness of $t = 3 \text{ mm}$ and halfwidth $b = 50 \text{ mm}$, the skin depth δ is

$$\delta = \sqrt{\frac{2}{\omega \mu_0 \sigma}},$$

where $\omega = 2\pi f$ and f is the frequency in Hz (sec^{-1}). Consider the range of frequency $1 \leq f \leq 60 Hz$. (Because of magnet inductance, only small magnets can be cycled at $60 Hz$.) For stainless steel ($\sigma = \frac{1}{\rho} = \frac{1}{70 \times 10^{-8} \Omega m}$), the skin depth at the minimum frequency is

$$\begin{aligned}\delta &= \sqrt{\frac{2}{2\pi (sec^{-1}) \times 4\pi \times 10^{-7} \frac{T m}{Amp} \times \frac{1}{70 \times 10^{-8} \Omega m}}}, \\ &= \sqrt{\frac{0.18 Amp \Omega m sec}{T m}} = 0.42 \sqrt{\frac{Amp \Omega m sec}{\frac{Weber}{m^2} m}}, \\ &= 0.42 \sqrt{\frac{Volt m sec}{\frac{Volt sec}{m^2} m}} = 0.420 m.\end{aligned}$$

The normalized half width of the plate is $\beta = \frac{b}{\delta} = \frac{0.050 m}{0.42 m} = 0.119$. The normalized plate thickness is $\tau = \frac{t}{h} = \frac{3 mm}{25 mm} = 0.12$. The maximum attenuation at the center of the magnet given by eq. (7.40) is

$$\begin{aligned}\frac{B_a}{B_0} &= \frac{1}{1 - \tau} \left[1 - \tau \frac{\cosh \beta \cos \beta - i \sinh \beta \sin \beta}{\cosh^2 \beta \cos^2 \beta + \sinh^2 \beta \sin^2 \beta} \right] \\ &= \frac{1}{1 - 0.12} \left[1 - 0.12 \frac{\cosh 0.119 \cos 0.119 - i \sinh 0.119 \sin 0.119}{\cosh^2 0.119 \cos^2 0.119 + \sinh^2 0.119 \sin^2 0.119} \right] \\ &= \frac{1}{1 - 0.12} \left[1 - 0.12 \frac{1 - 0.142 i}{0.9999 + 0.0002} \right]. \\ \text{Re } \frac{B_a}{B_0} &\approx 1 \quad \text{Im } \frac{B_a}{B_0} \approx\end{aligned}$$

Solution 8.1

The summary table for the quadrupole is shown in fig. 8. The column for the sensitivities have values normalized to the sensitivity for the fundamental, S_2 . Neither the integrated fundamental field, $\int B_{r1} dz$, nor the gradient, $\int B' dz$, are displayed in this summary table. However, one can compare the computed values with theoretical values based on the parameters for the magnet

$$h = 35 mm, \quad N = 124 \frac{\text{turns}}{\text{pole}} \text{ and } L_{eff} \approx 0.34 m.$$

One can learn a great deal from the results of the magnetic measurements. The performance of this magnet, as reflected by the illustrated tabular results, is

typical of the performance for most well constructed quadrupoles. Note that the offset of the magnetic center from the mechanical center is $< 100 \mu m$. Some of this amount is real, but a part of it reflects the difficulty of aligning the measurement coil with its axis precisely along the magnet mechanical axis. Note further that the amplitudes of the dominant error terms are for multipole indices, 6, 10, 14 and 18, the “allowed” harmonics. Furthermore, the relative phases of these allowed harmonics is approximately $\frac{\pi}{2}$. The allowed harmonics are dominated by the design and are real. Thus they are either in phase or 180° out of phase with the fundamental. The “unallowed” harmonics, those due to mechanical fabrication or assembly errors have random phases. These random phases are also reflected in small differences from 0° and 180° for the allowed harmonics.

Table1:SPECTRUM DISPLAY
(Normalized to the Standard Excitation)

Magnet ID: 34Q-040 **polarity:** F
File Name: a344081t2
Norm.I(A): 81

n	PHI[n] (*10E-08 V.S)	Angle (dgr.)	PHI[n]/PHI[2]	Coil Coeffi[n]	B[n]/B[2]	Reltative Phase (dgr.)
u1	394832.933	272.421	2.37400E-2	1.04000E-1	2.46251E-3	
1	2800.808	262.755				
u2	16635043.82	1.503	1.00000E+0	1.00000E+0	1.00000E+0	
2	178113.857	1.255				
3	1287.359	30.481	7.73884E-5	7.60020E-1	5.88170E-5	28.2265
4	767.136	217.461	4.61157E-5	2.45047E+0	1.13005E-4	214.455
5	144.547	90.697	8.68931E-6	1.60306E+0	1.39295E-5	86.9395
6	1135.794	167.022	6.82772E-5	3.39993E+0	2.32138E-4	162.513
7	72.071	159.455	4.33246E-6	3.22454E+0	1.39702E-5	154.1945
8	136.585	148.144	8.21070E-6	5.50157E+0	4.51717E-5	142.132
9	88.034	140.554	5.29208E-6	6.02694E+0	3.18950E-5	133.7905
10	1101.983	183.637	6.62447E-5	9.07477E+0	6.01156E-4	176.122
11	54.699	194.001	3.28819E-6	1.06309E+1	3.49563E-5	185.7345
12	54.741	198.185	3.29072E-6	1.48552E+1	4.88844E-5	189.167
13	48.542	183.175	2.91806E-6	1.79778E+1	5.24603E-5	173.4055
14	295.898	187.825	1.77877E-5	2.40027E+1	4.26952E-4	177.304
15	35.801	216.841	2.15212E-6	2.94960E+1	6.34789E-5	205.5685
16	34.781	219.539	2.09084E-6	3.82787E+1	8.00346E-5	207.515
17	24.851	215.416	1.49387E-6	4.73399E+1	7.07194E-5	202.6405
18	207.067	192.648	1.24476E-5	6.03298E+1	7.50962E-4	179.121

Gain:	100	Room Temp(°C):	27
Reference Radius(cm):	3.2		
Bucking Ratio:	93.4		
Delta X(mm):	-0.002	Delta Y(mm):	0.079
Drift(*10e-8V.s):	-24160	Relative Drift:	-0.065
Operator:	LLI,YJLI	Delta R(mm):	0.079
Test Time:	6/29/2001		14:39

Figure 8 Summary Information from Measurements

References

1. John J. Livingood, *Principles of Cyclic Particle Accelerators.* D. Van Nostrand Company, Inc., 1961.
2. H. Wiedemann, *Particle Accelerator Physics, Basic Principles and Linear Beam Dynamics.* Springer-Verlag, 1993.
3. S. Y. Lee, *Accelerator Physics.* World Scientific, 1999.
4. Herman Winick, Editor, *Synchrotron Radiation Sources - a Primer.* World Scientific, Singapore, New Jersey, London and Hong Kong, 1995.
5. K. Halbach, *Private communications.*
6. K. Halbach, "First order perturbation effects in iron dominated two dimensional symmetrical multipoles," *Nuclear Instruments and Methods*, Vol. 74, pp 147-164, 1969.
7. K. Halbach and R. Yourd, "Tables and graphs of first order perturbation effects in iron dominated two dimensional symmetrical multipoles." LBNL Internal Publication, UCRL-18916 and UC-34, 1969.
8. R. Peters, *Friction Loss in Pipes, LBNL Design Data 10A.*
9. F. Kreith, *Principles of Heat Transfer.* Intext Educational Publishers, New York and London, 1973.
10. R. Holsinger and K. Halbach, "Los Alamos National Laboratory Poisson Superfish Program Poisson written by Ron F. Holsinger in collaboration with Klaus Halbach. The original Poisson Superfish codes were developed by Ron F. Holsinger in collaboration with Klaus Halbach. These programs are provided as a service to the accelerator community by the Los Alamos Accelerator Code Group (LAACG).," (c) Copyright 1985-2002, by the Regents of the University of California. This software was produced under U. S. Government contract W-7405-ENG-36 by Los Alamos National Laboratory, which is operated by the University of California for the U. S. Department of Energy. Neither the Government nor the University makes any warranty, express or implied, or assumes any liability or responsibility for its use, or represents that use of this software would not infringe privately owned rights. Unpublished - rights reserved under Copyright Laws of the United States., 2002.
11. Lawrence Berkeley National Laboratory, 1 Cyclotron Road, Berkeley, CA 94720.
12. Los Alamos National Laboratory, P.O. Box 1663, Los Alamos, NM 87545.
13. James H. Billen, Phone: 1 505 667 6627. Email: jbillen@lanl.gov.

14. G. Lambertson, *Private communication.*
15. J. George B. Thomas, *Calculus and Analytic Geometry*. Addison-Wesley Publishing Co., Inc., Cambridge, Mass., 1953.
16. M. Yoon, J. Corbett, M. Cornacchia, J. Tanabe, A. Terebilo, "Analysis of a storage ring combined-function magnet: trajectory calculation and alignment procedure," *Nuclear Instruments and Methods*, to be published, 2004.

Index

Index

- alignment, 317
 - adjusted alignment, 320, 321
 - adjustments, 321–323
 - fiducialization, 328
 - generic, 320
 - pedigreed, 329, 330
 - predetermined alignment, 318–320
 - support blocks, 326, 327
 - adjustments, 327
 - supports
 - vibration, 318, 323, 326
- assembly, 305
 - bussing, 306, 308–310
 - topology to avoid solenoidal field, 306–308
 - coil supports, 305
 - flow interlocks, 310
 - hydraulic connections, 310, 311
 - fitting sizes used to avoid dead-heading circuits, 311
 - personnel safety, 312
 - power lead connections
 - stored energy, 312
 - thermal switches, 308
- Automesh code, 149
 - boundary conditions and constraints, 152
- geometry, 155, 157, 158, 185
 - example-Collins quadrupole, 158–162
 - line boundary, 161
 - using the spreadsheet, 157
- Tape35, 150
- textfile input, 150
- vector potential edit
- dipole, 162, 163, 165
 - using edit values as boundary conditions, 164, 166–168
- average turn length, 129
- beam dispersion, 23
- beam stiffness, 15
- Billen, James, 148
- Biot-Savart law, 20
- bump magnet, 25, 26
- Cauchy-Riemann conditions, 38
 - satisfied for B^* but not for B , 39
- $C_n z$ to the nth power, 40, 46
 - complex constant C_n , 40
 - coordinate axes, 40
 - ideal field, 40
 - magnetic fields calculated from the function
 - dipole field, 46
 - quadrupole field, 47
 - sextupole field in Cartesian coordinates, 47
 - sextupole field in polar coordinates, 47
- coil design, 125
 - as related to power distribution cables, 128
- current density, 126, 144, 335, 336
 - canonical values, 129
- magnet power as a function of requirements and current density, 128
 - power, 126
 - voltage and current relations, 128

- coil fabrication, 287
conductor and insulation, 287
encapsulation, 291
B-stage, 291
cocooning, 291
vacuum impregnation, 292, 294, 295
wet layup, 291
failure modes, 298
finishing, 296
electrical terminations, interlocks and water fittings, 296, 297
electrical terminations-maximum current density, 296
manufacturing specifications, 298
quality assurance, 299
electrical measurements and tests, 299
hipot test, 299
hydraulic tests, 299
impulse test, 301–303
null test, 300
resistance measurement, 301
winding, 288, 289
keystoning, 289
mirror image, 290
transitions, 289, 290
colliders, 60
complex extrapolation
as a means of determining the pole contour, 45
complex variable
function of, 34
scalar potential (imaginary part), 34
vector potential (real part), 34
vector potential (real part)
as applied to magnetic measurements, 214
conformal maps, 51
as applied to the septum quadrupole, 60, 62
as used in the Poisson code, 167, 170, 172, 175
dipole optimization, 176
optimized dipole mapped into the quadrupole, 177–179
optimized dipole results, 179
other uses of the vector potential boundary, 178, 180–183
vector potential boundary condition, 169, 172–174, 185
dipole to gradient magnet map, 54
dipole to quadrupole map, 52
dipole to sextupole map, 53
gradient magnet to dipole map, 54
mapping functions, 52
quadrupole to dipole map, 52
quadrupole to dipole maps, 186
sextupole to dipole map, 53
continuity
parallel H field, 114
perpendicular B field, 34
corrector, 19, 20, 24, 25
current density, 126
for convectively cooled coils, 128
for water cooled coils, 129
cycled magnets, 192, 210, 340
dipole magnet, 20
cosine wound coil, 120, 121
force direction, 22
gradient dipole, 17, 22
beam orbit, 274, 275, 284, 285
conformal map, 71, 76
yoke fabrication, 274–277, 279–281
PEPII dipole, 17
eddy currents, 26, 27
field amplification, 201
field attenuation, 193, 198, 210, 341
due to semi-infinite vertical plates, 198

- in a closed rectangular metallic vacuum chamber, 200
- in a semi-infinite plate, 194
- efficiency, 101, 115
- equipotentials, 40
 - curvilinear squares, 40
 - dipole scalar and vector equipotentials, 41
 - quadrupole scalar and vector equipotentials, 42
 - scalar equipotentials as boundary conditions, 40
 - sextupole scalar and vector equipotentials, 44
 - polar coordinates, 42
 - vector equipotentials as flux lines, 40
- excitation, 113
 - dipole, 116, 210, 338
 - cosine distribution, 120
- efficiency, 116
- quadrupole, 122, 185, 234
 - cosine distribution, 124
 - transfer function, 234
- reproducibility, 102
- sextupole, 125, 234
 - transfer function, 234
- field uniformity, 64, 85
 - dipole uniformity, 186
 - graphical presentation, 66
 - optimization procedure, 66
 - optimized, 65
 - pole overhang factor, 65
 - unoptimized, 65
 - gradient magnet - mapping an existing optimized pole, 74
- gradient magnet uniformity
 - conformal mapping spreadsheet, 75
 - dipole space, 72
 - quadrupole space, 72
- using conformal mapping, 71
- quadrupole uniformity, 185
- optimized and unoptimized poles, 70, 71
- using conformal mapping, 67, 68
- Fourier analysis, 216, 230
 - coefficients, 216
 - related to Cn's, 216, 217, 231, 232
 - related to field components, 217, 218, 233
 - related to harmonic phases, 217, 231–233
 - fringe field, 26, 27
- H-dipole, 62, 63
- Halbach, Klaus, 147
- Holsinger, Ron, 147
- inductance, 191, 210, 340
- installation, 317
 - supports, 318, 320, 321, 327
- Lambertson, Glen
 - eddy current calculations, 193
 - septum magnet, 27, 119
- Laplace's equation, 37
 - function of a complex variable, 35
 - scalar potential, 35
 - solution as a function of the complex variable z, 37
- solution as a function of vector and scalar potentials, 38
 - complex conjugate of the field vector, 38
 - vector potential, 35
- light source accelerators
 - ALS, 274
 - Australian Light Source, 274
 - SPEAR3, 16, 277
- magnetic fields
 - 2D fields in a vacuum, 36
 - from the function of a complex variable, 36

- in three dimensions, 35
- in two dimensions, 35
- magnetic force, 21, 31, 331
 - force on coils, 187
 - force on poles, 189, 209, 338
 - one atmosphere pressure, 190
 - pressure on coils, 189
 - pressure on poles, 189, 190, 209, 337
- magnetic measurements, 213, 313
 - bucking ratio, 236, 237
 - integrated voltage, 216, 217
- magnet center
 - quadrupole, 239
 - sextupole, 239
- measurement output, 240
 - iso-error plots, 240, 242
- measurement plan, 235
- normalized multipole errors, 237
 - corrected to required good field radius, 238
- raw data output, 236
- relative phases, 234, 235, 247, 342
- rotating coil
 - output voltage, 218, 219
- rotating compensated coil, 220, 238, 244
 - parameters, 221, 222, 245, 342
 - sensitivities, 221–223, 245, 342
- spilldown, 223, 224
 - as related to the magnetic center, 224–227
- system, 227, 228
 - computer and interfaces, 228
 - digital integrator, 228, 229
 - motor, 229
 - shaft encoder, 228
 - voltage drift, 229, 230
- magnetostriction, 28
- Marks, Dr. Neil, 16
- Maxwell's equations
 - integral form, 114
- steady state, 33
- Mulhaupt, Dr. Gottfried, 25
- multipole errors, 37, 48
 - error multipoles expressed as fields, 51
- systematic error multipoles, 49, 50
 - dipole errors, 50
 - quadrupole errors, 50
 - rotational symmetry, 49
 - sextupole errors, 50
 - symmetry about pole center, 56, 332
- Taylor's series of $C_n z$ to the nth power, 48
- multipoles, 36, 40
- orthogonal analog model, 57, 84, 85, 333
 - as applied to a conductor dominated magnet, 58
 - as applied to an H dipole, 62
 - as applied to the window frame magnet, 58
- orthogonality, 103
- orthogonal analog model, 186
- packing fraction, 127, 129
- pancake coil, 62, 126
- Pandira code, 147, 149
 - Outpan.txt, 151
- PEPII, 16
- permeability
 - relative permeability of soft magnetic material, 114
- perturbations, 87
 - algorithm for the use of coefficients, 89
 - individual pole designations, 90
 - lamination sorting to assure symmetry of core segments, 97
- quadrupole individual pole error coefficients, 88

- sexupole individual pole error coefficients, 88
- two piece quadrupole, 91
 - assymetry, 92
 - calculation of mechanical assembly tolerances, 100
 - coefficient table for different perturbations, 99
 - errors leading the excitation errors, 102
 - errors leading the multipole field errors, 102
 - errors leading to magnet alignment errors, 100
 - illustration of assembly error modes, 99
 - length difference between two halves, 94
 - orthogonality of error multipole spectra, 103
- Poisson code, 147, 149
 - documentation, 150
 - Outpoi.txt, 151
 - problem flow, 150, 151
 - Tape35, 151
- Poisson's equation, 36
- polarity, 20, 28
 - alternate definition, 29
 - corollaries, 29
 - force directions, 22
 - magnetostriiction, 28
- pole contours
 - contours extrapolated from required field
 - gradient magnet example, 45
- dipole pole design, 57
- gradient magnet
 - as a part of a larger quadrupole, 46
- ideal contours from the scalar potential
- quadrupole pole, 56, 332
- ideal contours from the scalar potentials, 43
- dipole contour, 44
- quadrupole pole, 44
- sextupole pole, 44
- pole design, 57
- pole cutoff, 67
 - horizontal, 70
 - vertical, 70
- power
 - coil, 127
 - dipole, 128
 - quadrupole, 128
 - sextupole, 128
- ProCons, 150
- pulsed magnets, 192
- quadrupole, 18
 - cosine wound coil, 123
 - F quadrupole for positively charged beams, 23
 - field distribution, 20
 - PEPII quadrupole, 18
 - polarities, 22
 - skew quadrupole, 24, 25
 - two-piece, 91
 - yoke fabrication, 264, 265, 267, 272, 282
- real magnets, 43
 - dipole, 44
 - quadrupole, 44
 - sextupole, 44
- resistance, 210, 340
- resistance, coil, 127
- saddle coil, 58
- septum magnet
 - current carrying septum, 26
 - fringe field, 26, 27, 119
 - eddy current, 26, 27
 - Lambertson septum
 - fringe field, 119

- vertical steering, 27, 28
- sexupole, 19
 - F sextupole for positively charged beam, 23, 24
 - field distribution, 20
 - polarities and field distribution, 23
- skew magnets, 43
 - imaginary constant, 43, 48
- sorting, 97
- Stoke's theorem, 114
- stored energy, 190, 210, 339
- Superfish family of codes, 149
- Taylor's expansion, 48
- tests, 313
 - electrical
 - hipot, 314
 - resistance measurement, 314
 - hydraulic, 315
- tolerances, 100–103, 111, 333–335
- trim windings, 104
 - all trim modes
 - multipole spectra, 107
 - horizontal steering trim, 106
 - multipole spectra
 - sensitivity to required good field radius, 107
 - orthogonality with the primary field, 104
 - sextupole trim winding configurations, 108
 - skew quadrupole, 19, 20, 106
 - trim excitations, 109
 - vertical steering trim, 105
- units, 31, 133, 331
 - as related to magnetic measurements, 235
- English, 135–138, 140
- MKS, 21, 34, 131, 137, 139, 140
- pressure
 - units for 1 atmosphere, 134
- vectors, 20, 33–35, 187, 330
 - curl, 34
 - divergence, 34
- water cooled coils, 129, 144, 336
 - flow velocity, 130, 131
 - maximum recommended value, 135
 - surface roughness, 135
- friction factor, 130
 - laminar flow, 130
 - turbulent flow, 130, 131
- hydraulic calculations, 137
 - sensitivities, 141
 - spreadsheet, 138, 139
- pressure drop, 130, 142
 - convenient values, 134
- Reynolds number, 130
 - kinematic viscosity, 135
- temperature rise
 - maximum recommended value, 135
 - recommended value for light source accelerators, 135
- volume flow, 134, 136
- Wfsplot code, 149
- window frame dipole, 58, 59
- yoke, 249
 - 2D design, 251, 252
 - 3D design, 252
 - canonical fringe field lengths, 252
 - chamfer machining, 257
 - dipole chamfer, 252–254
 - quadrupole chamfer, 255, 257
 - quadrupole fringe field, 254
- iron saturation, 249, 251, 252
 - 1010 steel BH curve, 250, 251
- laminated
 - die set, 261
 - dipole lamination, 263
 - quadrupole lamination, 263, 265
 - sexupole lamination, 264
 - sorting, 260
- laminated-fabrication techniques, 261

electrical grounding, 281
gluing, 264, 266–268, 270, 271
mechanical assembly, 273, 275–
277, 279–281
welding, 271–273
laminations or solid, 258
economics, 260
eddy currents, 259
reproducibility and symmetry, 258